Multimodal Electrochemical Guided Mode Resonance Biosensors

Stephen Thorpe

Doctor of Philosophy

University of York

Biology

September 2019

Abstract

Biosensing technology currently uses a single transduction mode, restricting the systems the technology can be applied to and the information that can be gained. Multimodal biosensing combines multiple transduction technologies to probe different properties simultaneously, increasing the range of measurable interactions, the amount of information that can be extracted, and the detection accuracy.

Guided mode resonance sensors are one dimensional periodic grating structures that measure the local refractive index at the grating surface, and have been used extensively for label-free biosensing assays. Electrochemical biosensors measure the activity of chemical reactions through changes in electrical current. Combining refractive index and electrochemical sensing allows for the parallel interrogation of the presence and activity of biomolecules.

A multimodal electrochemical guided mode resonance (EGMR) sensor based on a 1D GMR grating structure with a layer of indium tin oxide is presented. Simulation of the GMR structure was used to inform the EGMR design for the best compromise between electrochemical and optical sensing performance. The fabricated device is characterised optically and electrically, with an optical sensitivity of 83 nm/RIU. Combined electrochemical and optical sensing measurements were demonstrated in parallel to characterise a redox active molecule.

The electrochemical chirped GMR (ECGMR) was applied to developing a low cost multiplexed label-free biosensor. The chirped GMR sensor converts the spectral response of the GMR to spatial information allowing binding to be measured using a monochromatic source and a camera. A biocompatible antibody electrografting protocol was demonstrated for creating a multiplexed antibody array of sepsis biomarkers using the ECGMR. Parallel label-free detection of CRP, IgG and *Escherichia coli* was demonstrated. The limit of detection was 60 pg/mL CRP and 5 x 10^2 CFU/mL of *E. coli*.

This work is the first example of a multimodal GMR, and progresses the use of biosensing technology for point-of-care applications.

Contents

List of Tables

List of Figures

8

9

Acknowledgements

I would first like to thank my supervisors Dr. Steve Johnson, Professor Thomas Krauss and Professor Gavin Thomas for all their help and support. Thank you also to my TAP panel members Professor James Moir and Dr. Alison Parkin for their input into this work.

There are many colleagues that I would like to thank for sharing their knowledge with me, supporting my work and for just generally contributing to making the labs such a great place to work in these last few years. Special thanks go in particular to Dr. Giampaolo Pitruzello for teaching me to fabricate the GMR sensors, a vital first step for completing this thesis. From the Photonics group thanks to Dr. Yue Wang, Dr. Chris Reardon, Dr. Donato Conteduca, Dr. Kezheng Li, Isabel Barth, George Duffet, Lewis Reeves, Alex Drayton, Josh Male, Manuel Deckart Adam Stroughair. From the Bio inspired technologies group, Dr. Jose Juan-Colas, Dr. Casper Kunstmann, Dr. Matt Simmons, Dr. Lisa Miller, Dr. Eleni Koutsoumpeli, Dr. Katherine Dunn, Callum Silver, and all other members of both groups past and present. It's been a privilege to work with such talented scientists and I have thoroughly enjoyed being a part of the Physics/Electronics community that we have created.

From the Biology department my thanks to Dr. Michelle Rudden, Dr. Emmanuelle Severi, Dr. Sophie Rugg, Caroline Pearson and Reyme Herman in particular, but thank you everyone for letting me absorb your biological wisdom, for suffering through my endless drawings of photonic crystals on whiteboards and for making an engineer feel so welcome.

Thanks to everyone in the CIDCATS programme, particularly Helen, Shoumit, Rosie and Karinna who this all began with. It's been an incredibly interesting journey from the first day of learning what a pipette is and I would like to think we all know a little more about what disease is now.

Finally thank you to Bex for being there through everything. Without your constant support and friendship none of this would have been possible.

Author declaration

I declare that this thesis is a presentation of original work and I am the sole author. This work has not previously been presented for an award at this, or any other, University. All sources are acknowledged as References.

All contributions are acknowledged where appropriate in the text.

Abbreviations

APP: Acute Phase Protein

BSA: Bovine Serum Albumin

CRP: C Reactive Protein

CV: Cyclic Voltammetry

CVD: Chemical Vapour Deposition

DNA: Deoxyribonucleic Acid

EBL: Electron Beam Lithography

ECGMR: Electrochemical Chirped Guided Mode Resonance

EC-OWLS: Electrochemical Optical Waveguide Lightmode Spectroscopy

EC-SERS: Electrochemical Surface Enhanced Raman Spectroscopy

EGMR: Electrochemical Guided Mode Resonance

EIS: Electrochemical Impedance Spectroscopy

E-QCMD: Electrochemical Quartz Crystal Microbalance and Dissipation

FET: Field Effect Transistor

FF: Filling Fraction

FWHM: Full Width Half Maximum

GMR: Guided Mode Resonance

IgG: Immunoglobin G

IL: Interleukin

IPA: Isopropyl Alcohol

ISFET: Ion Sensitive Field Effect Transistor

ITO: Indium Tin Oxide

KPi: Potassium Phosphate buffer

LB: Lysogeny Broth

LMR: Lossy Mode Resonance

LOD: Limit of Detection

LPFG: Long Period Fibre Bragg Grating

LSPR: Local Surface Plasmon Resonance

MALDI-TOF MS: Matrix-Assisted Laser Desorption/Ionization-Time Of Flight

MB: Methylene Blue

MZI: Mach-Zehnder Interferometer

NB: Nile Blue

OD: Optical Density

OWLS: Optical Waveguide Lightmode Spectroscopy

PCEM: Photonic Crystal Enhanced Microscopy

PCF: Photonic Crystal Fibre

PCT: Procalcitonin

PECVD: Plasma Enhanced Chemical Vapour Deposition

PEDOT: poly3,4- ethylenedioxythiophene

POC: Point Of Care

Q: Quality Factor

QCM: Quartz Crystal Microbalance

QCMD: Quartz Crystal Microbalance and Dissipation

RCWA: Rigorous Coupled Wave Analysis

RIE: Reactive Ion Etching

RIU: Refractive Index Unit

RNA: Ribonucleic Acid

SERS: Surface Enhanced Raman Spectroscopy

SPR: Surface Plasmon Resonance

SWV: Square Wave Voltammetry

TCO: Transparent Conductive Oxide

TE: Transverse Electric

TM: Transverse Magnetic

μTAS: Micro Total Analysis System

WGS: Whole Genome Sequencing

Chapter 1

Introduction

The human body contains many sensing systems to help interpret the world around us. From the five basic senses we can find and taste food, smell aromas in the air and feel the heat from the sun on our skin. Much of this sensing capability is not consciously available for us to interpret however. For example, our immune system detects the presence of foreign bodies that can cause illness and disease, while within our cells complex sensing systems can detect the presence of single molecules that regulate and coordinate critical cellular processes.

Biosensing technology is our attempt to leverage the vast sensing apparatus available from the natural world to measure and interpret biological and chemical molecules. In its simplest form a biosensor consists of a bioreceptor and a transducer, that is coupled to a readout system [1]. The bioreceptor will interact with the target
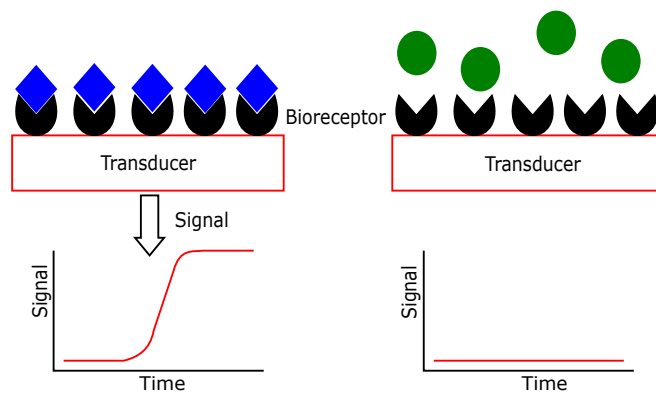
Figure 1.1: Schematic showing the principle of a generic biosensor. The transducer is functionalised with a bioreceptor to give specificity. When the bioreceptor binds to the target biomolecule, the transducer produces a measurable signal. If the specific molecule is not present the transducer signal should remain unchanged.

molecule and provides specificity. Bioreceptors are typically bound on to the surface of the transducer. When the bioreceptor binds to its target molecule it will induce a response in the transducer. The response from the transducer is measured and converted to a signal that can interpreted by the user such as a colour change or an electrical signal to a computer.

1.1   Current Molecular Detection Technology

The most widely used assays for detecting protein biomarkers are the enzyme linked immunosorbance assay (ELISA) and lateral flow assay (LFA).

ELISA are the most widely used tests for detecting proteins and molecular biomarkers. Antibodies that have been immobilised on to a polystyrene microwell plate capture the target analyte from the sample [2]. The plate is washed to remove non-specifically bound targets then the capture antigens are labelled with a secondary antibody that has modified with a fluorescent or enzymatic tag. The measured fluorescence intensity or enzymatic activity is proportional to the concentration of the labelled secondary antibody and consequently the target antigen concentration. ELISA assays have a low limit of detection, in the order of picograms, and can give quantifiable measurements of antigen binding when used with appropriate titration curves. highly effective in terms of sensitivity, specificity and the range of analytes that can be detected, the ELISA protocol consists of multiple steps, needs specialised equipment for result readout and requires trained operators to perform the assay, restricting their use to laboratories that have the necessary facilities and personnel to perform them.

LFAs consist of a nitrocelluose membrane with strips of antibodies printed on to the surface and a reservoir of nanoparticle labelled secondary antibodies [3]. When the end of the membrane is dipped into the sample, the sample is wicked along the membrane towards the antibody strips. If the target antigen is present it will bind to the antibody strip on the membrane surface, the labelled secondary antibodies will bind to the captured antigen, causing a colour change of the strip that is observable by eye. LFAs do not require any specialist training and have been widely commercialised for use in pregnancy tests. The limit of detection for a LFA is significantly higher than that of an ELISA however. LFA measurements can be semi-quantitative but are better treated as a presence absence indicator of the antigen in question.

Currently, the ELISA and LFA each fill a specific niche, the ELISA a quantitative

and highly sensitive assay but is slow, technically complex expensive. The LFA is rapid, cheap, and easy to use, but lacks the sensitivity and quantification required for many applications. There is a need for new biosensing technology that combines the sensitivity of ELISA with the practicality and cost effectiveness of LFA [4].

1.2   Bioreceptors

The bioreceptor gives the biosensor specificity and sensitivity towards the target analyte. There are many different types of bioreceptor including antibodies, DNA, enzymes or even whole cells. There are many mechanisms by which a bioreceptor can interact with its target.

Affinity binding sensors use affinity target molecules that bind specifically to the target antigen. The most common affinity binding molecule is an antibody, which are generated by the adaptive immune system in response to an antigen. Polyclonal antibodies are antibodies that have been purified from a living animal that has been exposed to the target antigen. Using the animals immune system as the selection mechanism simplifies the selection process [5]. Using animals limits the range of targets that can be selected against as the animal must be able to raise an immune response. For example, antigens that are too toxic can kill the animal before antibodies can be produced.

Monoclonal antibodies are antibodies that have been produced by an *in vitro* cell line [6]. Antibody producing cells from the animal exposed to an antigen are hybridised with a tumour cell line to create an immortal cell line known as hybridoma capable of producing antibodies. The advantages are increased specificity compared to polyclonal antibodies and more reliable production as the hybridoma cell lines can be kept almost indefinitely. Monoclonal antibodies are however significantly more expensive than polyclonal antibodies because of the *in vitro* purification steps required.

There are several alternative affinity binding agents to antibodies including DNA aptamers or synthetic antibodies mimetics such as affimers [7]. These have an number of advantages over antibodies. Aptamers and affimers can be selected against almost any target, as they are selected *in vitro*. Synthetic binding molecules have also been shown to be more stable than antibodies. Aptamers in particular also promise to be cheaper to produce than antibodies as they can be produced used synthetic chemistry as opposed to purifying them from an animal. Selecting an

aptamer or affimer against a specific target is however significantly more expensive compared to antibodies as the selection process must recreate the role of an animals immune system.

Enzymes can also be used as bioreceptors. When exposed to the target antigen the enzyme will catabolise the antigen into its product. Enzymatic degradation of the target molecule leads to physical changes such as the release protons or electrons, the generation of heat or changes in colour, that can be subsequently quantified using a transducer. One of the most commercially successfully biosensors, the glucose biosensor, uses an enzyme as its bioreceptor [8]. Here, glucose oxidase immobilised on to a conductive electrode catabolises glucose into gluconolactone and hydrogen peroxide, generating a current. The magnitude of current is proportional to the concentration of glucose in the sample.

1.3   Transducers

The transducer responds the binding of the bioreceptor to its target analyte and translates this to measurable signal. Transducers used for biosensing include optical, electrochemical, and mechanical.

Photonic biosensors are nanoscale structures that shape and control light to detect biomolecules typically within a hundred nanometres of the surface. Optical resonances are fundamental to the operaton of photonic biosensors [9]. The optical resonance generates an evanescent field that it is sensitive to the refractive index of the media local to the sensor. A change in refractive index of the media results in a change in the propagation of light within the structure due to the interaction with the evanescent wave. This change in propagation leads to a change in the optical resonance that be measured and quantified by monitoring the wavelength or intensity of light propagating through the structure. These photonic biosensors are made from high refractive index materials such as Si. One of the key advantages of photonic biosensors is that the manufacturing processes are identical to those used in the semiconductor fabrication industry [10]. This leads to the potential of very low unit costs for each of the sensors.

There are several types of photonic biosensors that use different structures to guide light. Microring resonators shown in figure 1.2a are circular waveguides that incite a resonance by constructive interference of light propagating around the ring shaped waveguide [11]. The resonance results in a drop in transmission at the resonance
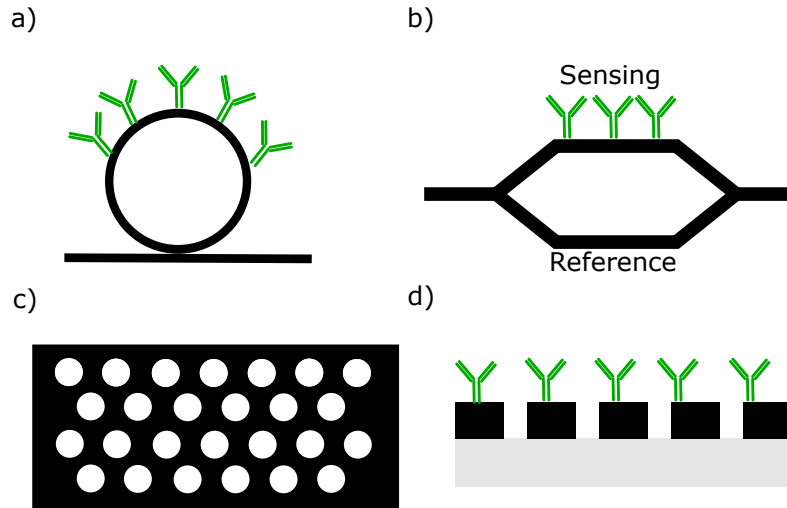
Figure 1.2: **a)** Microring resonator with coupling waveguide **b)** Waveguide Mach-Zenhder inferometer **c)** Two dimensional photonic crystal **d)** Guided mode resonance grating structure on glass substrate.

wavelength that shifts in wavelength as biomolecules bind to the sensor surface. Mach-Zenhder inferometers in figure 1.2b use a Y-shaped waveguide consisting of a sensing arm and a reference arm [12]. The sensing waveguide is in contact with the media while the reference arm is encapsulated and thus does not make direct contact with the media. Binding of an analyte on the sensing arm causes a change in phase in the light propagating in the sensing arm, which in turn leads to a change in interference between the two arms of inferometer that can be measured to quantify the concentration of the analyte. Photonic crystals, shown in figure 1.2c, are structures of periodic refractive index [13]. The periodicity of the structures confines the light, preventing propagation through the structure. The periodicity can be in one, two, or three dimensions and can be formed from arrays of circles or other geometric shapes The confined light excites a resonance leading to areas of high intensity electric fields in the structure which can be used for biosensing.

The work in this thesis focuses on 1D resonant photonic grating structures shown in figure 1.2d. The periodicity of the grating is key for confining the light and inciting the resonant behaviour [14]. An advantage of using a grating is that the resonance can be created using out of plane light, simplifying the optical measurement system in comparison to other photonic crystal biosensors.

Electrochemical biosensors measure electrical changes in; current (amperometric), voltage (potentiometric), or impedance (impedimetric) in response to a target analyte [15]. Electrochemical sensors are typically constructed from three electrodes, a working electrode a counter electrode and a reference electrode. The working electrode is the transduction element where the target analyte is detected. The reference

electrode provides a stable voltage against which to measure the working electrode voltage. The counter electrode completes the electrochemical circuit allowing the flow of current. The electrodes are made from conductive inert materials such as Au, Pt or carbon. The electrodes can be microfabricated using thin film deposition processes or printed with conductive inks using screen printing.

An amperometric sensor measures electrical current arising from reduction oxidation (redox) reactions which occur during biological processes [16]. The redox activity is typically from a surface immobilised enzyme where enzymatic catabolism of the target molecule results in electron transfer producing a measurable current. Redox active probes such as ferrocene or methylene blue can also be used with amperometric sensors. Here, the redox activity of the electrochemically active probe will change in response to changes in pH or the electrostatic interaction with other molecules.

Potentiometric sensors measure electrical potential due to ionic concentration. Enzymatic activity can be measured by the change in proton concentration. Alternatively the electrode can be made specifically sensitive to a certain type of ion. Direct detection of the surface potential from the binding of molecules to the surface has been recently demonstrated [17].

Impedimetric sensors measure the change in electrical impedance due to the presence of a biological molecule [18]. In electrochemical impedance spectroscopy, a sinusoidal voltage at a range of frequencies is applied to the working electrode while the resulting current is measured as used to calculate the electrode impedance. Impedance measurements have been used widely in affinity biosensors, where binding of the analyte to a surface immobilised affinity binding agent changes the measured impedance of the electrode.

The work in this thesis primarily uses amperometric sensing using voltammetic techniques such as cyclic voltammetry and square wave voltammetry.

1.4   Multimodal Biosensors

Multimodal sensing integrates multiple transduction technologies into a single device. Using multiple transduction technologies extends the possible range of measurable interactions compared to a single technology alone. The combination of measurements also allows for more information to be extracted from the system being measured and gives greater confidence in the measured results.

The majority of multimodal sensing technology has been focused towards measuring physiological parameters, such as movement speed, heart rate or blood oxygen concentration [19]. These have been already integrated into a number of commercially successful technologies such as the FitBit. The combination of multiple sensing types allows for the analysis of complex actions such as sports performance, which would be impossible to understand using a only a single sensing modality. The inherent complexity of biology makes it impossible to use only a single biosensor type to measure every biomolecule. Applying multimodal sensing paradigm to biosensors is aimed at increasing the total number of interactions within a single biosensing device [20].

1.5   Lab on a Chip

Micro total analysis systems (μTAS) aim to integrate biosensors with sample preparation fluidics to perform assays completely on chip [21]. The design philosophy of μTAS is "sample in answer out" so that complex biosensing assays directly from the sample itself can be performed without intervention. A review by Patabidge et al. provides impressive examples of the current complexity of existing μTAS systems for performing biosensing assays [22].

Wearable and implantable biosensors are being investigated for continuous sampling of a patient instead of discrete sampling. This leads to the concept of "closed" loop drug delivery' where the injection of a drug is directly controlled by an implanted biosensor to maintain the optimum concentration of the drug within the patient [23]. Beyond this there is the potential of using implantable sensors for continuous diagnostics for the early detection of diseases such as cancer [24]. The actual use of implantable biosensors for this application is however still years away (to the possible relief of some readers).

1.6   The Role of Biosensors

Biosensors in medical applications are perhaps the most recognisable and commercially successful application of the technology, including glucose sensing for diabetes monitoring and pregnancy test strips. Despite these successes there has been limited uptake of biosensor technology for more complex medical challenges. There are significant challenges in both the developed and underdeveloped medical settings.

In low and middle-income countries where access to healthcare facilities is limited, biosensor technology has the potential for making routine lab testing available for all and to provide diagnosis of conditions that are unique to underdeveloped countries such as neglected tropical diseases [25].

In the developed world, biosensor technology is required for improving the quality and provision of healthcare. For example, increasing aged populations place additional strain on healthcare services, increasing the demand for diagnostic testing. Further challenges such as the increase in drug resistant infections demand changes to clinical practice and associated technology to better manage the prescription of antibiotics [26]. Here, biosensing technology can be used to increase the speed and accuracy of the diagnostics ensuring the right antibiotic at the right time. There is also the potential to move from the current lab based diagnostic methodology, to one where diagnostic tests are performed at the point of care, for example at the GP surgery or at the bedside [27].

Environmental monitoring for the detection of toxic chemicals is vital to protect the environment and associated ecosystem. However detection of these environmental contaminants remains laborious, time consuming and expensive due to a continued reliance on manual sampling methods coupled with laboratory based analysis techniques [28]. Biosensors for direct monitoring of toxins, pesticides and pharmaceuticals are required for improved monitoring for public health. Biosensors for monitoring ocean contamination are also required for continued monitoring of sea wildlife and biodiversity [29].

The rising population has placed increased demand on food production throughout the world. There is a need to increase the productivity and efficiency of current farming practices. Precision agriculture uses a data driven approach towards agriculture to better control farming techniques such as the informed use of pesticides or fertilisers [30]. There is demand for biosensing technology for monitoring soil conditions, identification of disease in both plants and animals, and to measure contamination of foods to improve food safety.

1.7   Challenges

It is clear that there are numerous sectors that would benefit from biosensing technology. Yet the uptake of biosensing technology remains limited. There remain numerous challenges to making a biosensor after demonstrating it successfully in

a laboratory. For example, the manufacturing processes needed to fabricate the sensors must be economically viable, while for use in medical applications or food safety there are stringent regulatory requirements that can require extensive testing and validation prior to commercialisation

There also are very few (arguably no) problems that have no outright solution other than an on chip biosensing technology. The existing methods may be slow, expensive, inconvenient or insensitive but on some level they do the job they are intended to do. Changing the workflow of how these techniques work is a risk, whether that be to the health of an individual or the financial viability of a business.

1.8   Scope of this Thesis

This thesis focuses on the fabrication and characterisation of a multimodal electrochemical guided mode resonance (EGMR) sensor, combining electrochemical and refractive index sensing modalities.

In chapter 2, a review of existing multimodal biosensing technology is presented beginning with generic exemplar multimodal technology before focusing specifically on multimodal biosensors that combine electrochemical and refractive index sensing technology. In chapter 3, the operating principles of guided mode resonance sensors are explored along with discussion of how GMR sensors compare with other existing photonic biosensors.

Chapter 4 gives a detailed description of the fabrication processes and techniques used to the manufacture the EGMR. The principles of electrochemical measurements are also discussed along with the optical measurement systems used to operate and characterise the EGMR.

Chapter 5 presents the characterisation of the EGMR sensor in both optical and electrochemical modalities, including optimisation of electrically conductive indium tin oxide (ITO) thin films. Simulation of the EGMR is presented to underpin the design and fabrication choices. The effect of applied bias voltage to the resonance of the EGMR is investigated and combined with simulations to examine the physical origin of the observed resonance changed. The combined optical and electrochemical sensitivity of the EGMR is explored by measuring varying concentrations of NaCl in a microfluidic flow cell. Finally the chapter concludes with an example of parallel optical and electrochemical measurements of a redox active molecule.

In chapter 6, I demonstrate the potential of the EGMR for multiplexed, label free diagnostics. The EGMR is modified to use a variant of GMR sensors known as a chirped GMR, that allows the measurement of optical resonance using a simplified optical setup that is compatible with a inexpensive mass production, known as electrochemical chirped GMR (ECGMR). A method of selectively functionalising the ECGMR surface by electrochemical grafting of antibodies modified with diazonium salts is provided. Finally a proof of concept of a rapid diagnostics of sepsis is demonstrated, showing that both molecular markers and bacteria can be detected simultaneously and at concentrations that are clinically relevant.

Chapter 2

Multimodal biosensors

2.1 Introduction

This chapter reviews the existing multimodal biosensor techniques. The first section details the concept of multimodal biosensor before discussing examples of multimodal sensors that combine a range of transduction techniques. The second section will focus specifically on multimodal devices that combine electrochemical and optical techniques, particularly refractive index sensing photonic and plasmonic structures.

2.2 Overview of Multimodal Biosensing Techniques

Multimodal biosensors combine multiple transduction techniques into a single device. Multiple modalities can significantly extend the capabilities of a biosensor compared to technologies that employ a single mode sensor. Firstly the measurements from the different modalities can be directly compared and combined to extract greater information about the system being measured [20]. Multimodal sensors can also expand the range of systems that can be measured using a single device. For example, one mode may be used to measure the presence and concentration of a particular analyte, while the other mode can be used to measure biological function such as the the activity of an enzyme which catabolises the detected molecule [31]. Secondly multimodal sensors open the possibility of allowing information to flow

in both directions across the biology-transducer interface; one mode to control a biomolecule while the second mode can simultaneously monitor the induced change.

The inherent disadvantage of multimodal sensors is that they combine the cost and practical challenges of performing two biosensing techniques. Additionally, in many multimodal sensors the integration of the techniques can result in a degradation in the sensing performance of the individual sensor modalities. This may account for the prevalence of multimodal sensors that integrate electrochemical measurements with other techniques. All that is required to integrate electrochemical analysis with a second sensing modality is the integration of a conductive surface, a common feature of many biosensing technologies. In addition, a high quality research level potentiostat can be purchased for a few tens of thousands of pounds, with many cheaper alternatives available [32].

2.2.1 Quartz Crystal Microbalance Biosensors

Quartz crystal microbalance (QCM) is a technique for measuring the deposition of mass on to a piezoelectric sensor. A radio frequency voltage induces expansion and contraction of the piezoelectric crystal creating a transverse acoustic wave across the crystal. By exciting the crystal at the correct frequency a resonant standing wave is induced when the acoustic wavelength is twice the thickness of the QCM sensor [33]. The resonant frequency is sensitive not only to the sensor geometry but also on the mass deposited on to the crystal. For a rigid material, the change in resonance frequency due to additional mass can be described using equation 2.1, known as the Sauerbury relation, which predicts that change in resonant frequency is linear with change in mass. QCM was first used in vacuum deposition systems for measuring the amount of deposited material, however QCM sensors integrated into a fluidic cell can be used for biosensing.

$$\Delta m = -\frac{C \Delta F}{n} \qquad (2.1)$$

For biosensing, deposition of the biological material on the QCM sensor causes the same change in mass as with a metallic film and corresponding change in resonant frequency. By following the change in frequency over time the mass of the biological material can be calculated. This time dependent measurement can be exploited to quantify the kinetics of biological interactions, for example the kinetics of association between an antigen and an antibody immobilised on the surface of a QCM sensor.
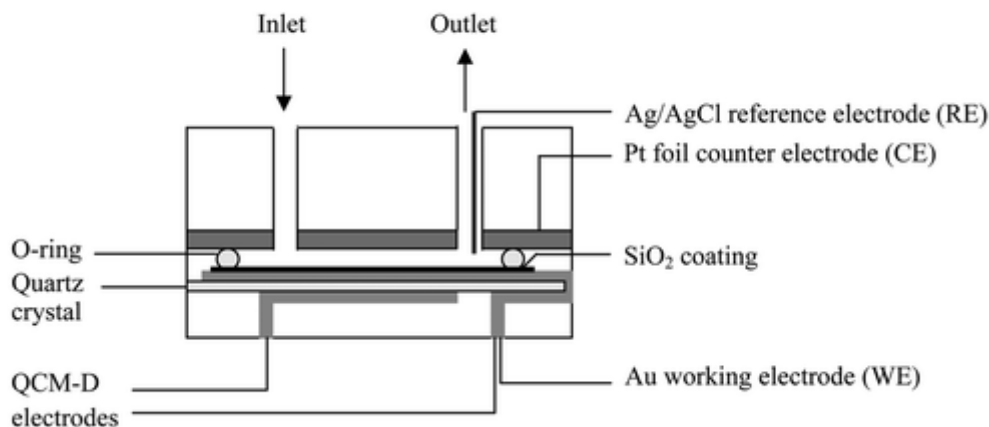
Figure 2.1: Schematic of an electrochemical QCMD setup for combined electro-chemical impedance spectroscopy and mass measurements. The QCMD working electrode is used to both drive the resonance frequency of the piezoelectric crystal and perform the EIS measurements. Coating the top surface in the platinum foil ensures a large surface area of the counter electrode. Adapted from [34].

QCM also provides information about the rigidity of the deposited biomolecules by monitoring the energy dissipated by the resonant sensor (known as quartz crustal microbalance with dissipation, QCMD). After turning off the RF voltage the oscilla-tion of the QCMD sensor will decay exponentially and the oscillation will be damped by the material that is deposited on QCMD sensor surface. If the material is rigid i.e. has a low viscoelasticity, it will continue to oscillate with the QCMD sensor so the damping will be minimal. If the material is soft however, energy from the oscillation will deform the material and cause a more rapid decay in the oscillation of the QCMD sensor.

2.2.2 Electrochemical QCMD

QCM sensors are typically made using gold electrodes to drive the oscillation of the piezoelectric quartz crystals. As Au is a material commonly used for electrochem-ical sensing, this had led to the development of Electrochemical QCMD (EQCMD) where an Au coating deposited on the QCMD sensor is used as the working electrode and a counter and reference electrode is inserted into the fluidic cell. It must be noted that the application of bias voltages to the QCM sensor typical for voltam-metric experiments can influence the frequency response of the piezoelectric sensor.

Anodic adsorption of charged molecules such as a poly-L-lysine has been studied

using EQCMD [35]. Here, the Au electrode on the QCMD sensors was held at a range of bias voltages in order to monitor the adsorption kinetics as a result of the charge of the molecule. A combined QCMD and electrochemical impedance spectroscopy (EIS) setup shown in figure 2.1 has also been used to characterise pore formation in lipid bilayers showing that real time measurements of both mass change and impedance could be made [34]. Similarly, morphological changes in protein film adsorption has also be explored [36]. I note, the resonance of the QCM crystal is not significantly affected by application of the bias for EIS as the voltages employed in EIS are typically only one to ten millivolts in amplitude.

EQCMD has also been used not just for combined measurements but also for the active control of surfaces such as electrically switchable surfaces where the electrochemical functionality enables control of surface functionalisation, and the response to the applied electric field is measured using the QCMD mode [37].

2.2.3 Localised Surface Plasmon Resonance (LSPR) QCMD

QCMD sensors have been patterned with Au nanodisks to induce local surface plasmon resonance (LSPR) for combined mass and refractive index sensing (a detailed discussion of surface plasmon resonance (SPR) is given in section 2.3.2). Here, SiO_2 is typically deposited on to the QCM electrode to serve as the substrate for the Au nanostructures [38]. Electron beam lithography is then used to define the nanodisks structures into a section of the QCM crystal as shown in figure 2.2a. The response is measured by monitoring the change in transmitted or reflected light intensity and gives quantitative information on surface binding kinetics that is complementary to the QCMD signal [39].

The QCMD sensing wave propagates more than 300 nm into the medium and so typically probes the entire of a deposited material on the surface [40]. The LSPR sensing area however is limited to within 100 nm of the sensor surface. Combining the techniques together allows for decomposition of surface and bulk effects [41].

LSPR QCMD has been used for the characterisation of extracellular vesicles, one to ten micron sized spheres of lipids [42]. By combining the change in frequency, dissipation and LSPR response to the surface it is shown possible to distinguish between; vesicles binding the surface and changes in conformation, for example due to swelling or vesicle collapse in response to steric effects as the vesicles pack densely on the surface.
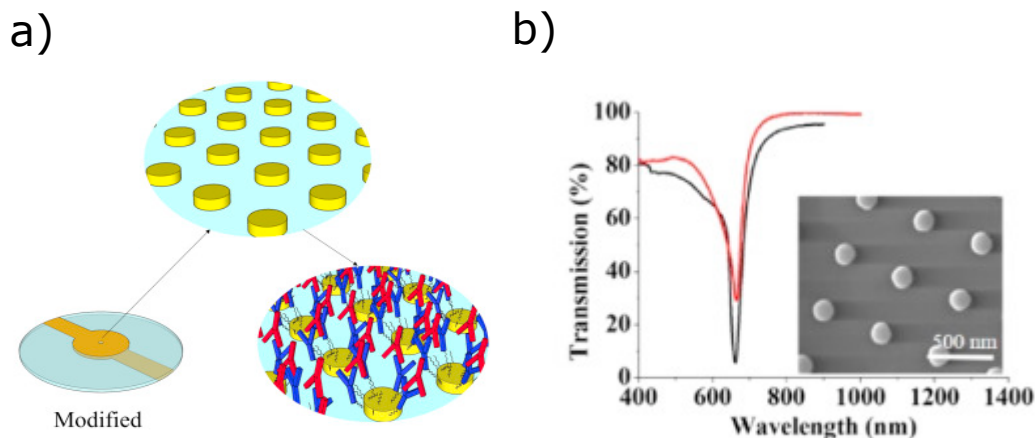
Figure 2.2: **a)** Schematic of the Au nanodisks patterned on to the centre of a QCMD sensor. The LSRP nanodisks can then be functionalised with biorecognition molecules such as antibodies for combined mass and LSPR affinity sensing assays **b)** Transmission spectra of showing the drop in transmission due to the LSPR. Adapted from [38].

2.2.4 Ion Sensitivity Field Effect Transistors

A field effect transistor (FET) is an electronic device that acts as voltage controlled current source. An FET consists of three terminals, known as the source, drain and gate electrodes. In typical use, the flow of current from the source to the drain is controlled by the application of bias voltage to the gate electrode. In the ion sensitive field effect transistors (ISFET), the gate electrode is modified such that it is sensitive to the concentration of a specific ion in solution [44]. Aggregation of these ions at the surface of the modified gate electrode results in an increase in local charge density, and thus a corresponding change in source-drain current. To make the FET responsive to ions, the metal layer on the gate is replaced with an ion sensitive layer such as SiO_2 or Si_3N_4 which is sensitive to the concentration of protons. [43] The gate terminal is then connected to a reference electrode such as an Ag/AgCl reference to hold the gate at a constant voltage. ISFETs have been most commonly used as pH sensors where the ion sensitive layer can protonate/ deprotonate as a function of pH, leading to a corresponding change in the source drain current. Ion sensitive layers that are sensitive to a range of different ions have been demonstrated [45]. The ISFET surface can also be functionalised with biorecognition molecules such as antibodies, aptamers, affimers or enzymes in order to probe biological interactions [46].

Although electrical in nature they are distinguished from electrochemical biosensors because they do not apply voltage to a working electrode with respect to the reference electrode. However, since an ISFET already employs a reference electrode, it
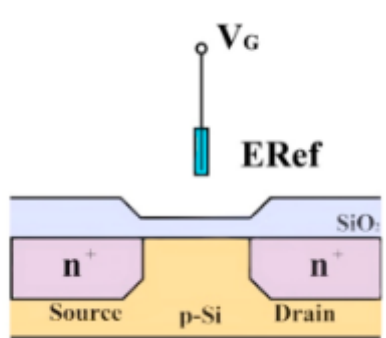
Figure 2.3: Schematic of an ion sensitive field effect transistor. Flow of current from the source to the drain is restricted by the depletion region generated by the PN junction. The depletion region can be tuned by applying bias voltage Vg to the gate. The charge of on the SiO2 layer changes with the ionic concentration of the media, causing a change in the voltage Vg which is reflected by the current flow between the source and the drain. Adapted from [43].

is relatively trivial to integrate a metal working electrode and a counter electrode for simultaneous electrochemical measurements.

Although ISFETs have not been widely used for multimodal sensing, combined enzymatic activity measurements using cyclic voltammetry combined with ISFET based pH sensing has been demonstrated using a switchable ISFET system [47]. One notable example is the integration of an ISEFT with a SPR nanodisk array. The combined device was capable of measuring refractive index change using the SPR array, along with chemiluminescence, ion sensing and electrical enzymatic activity [48].

2.2.5 Raman Electrochemistry

Raman spectroscopy is an optical chemical analysis technique. All objects, regardless of size, scatter photons. The majority of the photons are elastically scattered; the photons have the same energy after scattering. Raman scattering collects inelastically scattered photons that have lost energy on scattering with a molecule. The amount of energy lost is characteristic of the scattering molecule. The sensitivity of Raman spectroscopy is limited by the number of inelastically scattered photons that can be collected. Increasing the incident light intensity increases the number of photons that can be collected but at the cost of the damaging the material being analysed due to the high incident power.

Surface enhanced Raman spectroscopy (SERS) uses nanostructured metal surfaces to enhance the Raman signal. To briefly explain, the incident light excites a plas-

monic field leading to an amplified electric field at the metal surface. Molecules close to the metal interact with the enhanced electric field which increases the amount of scattering and consequently the intensity of the Raman signal [49].

Electrochemical SERS (EC-SERS) has been used extensively since the 1980s, with an excellent review provided of the numerous biological systems investigated by De Win et al [50]. There have also been recent efforts to expand EC-SERS from a research tool to point of care (POC) diagnostics, with recent work demonstrating that EC-SERS can be performed on a fabric printed electrode to create a wearable EC-SERS surface [51] [52].

Raman spectroscopy has also been combined with Au cantilever based microresonators for combined Raman and mass sensing [53]. Here, the Au resonator was struc- tured to create a textured surface to support a SERS signal. When illuminated with an incident 663 nm laser, the change in mass could be measured due to the induced thermal oscillation of the cantilever while simultaneously measuring the SERS signal.

2.3 Dual Electro-Optical Techniques

This section will discuss combined electrochemical and refractive index sensing, focusing specifically on photonic and plasmonic nanostructures as the refractive index sensor. From early work on combined surface plasmon resonance with electrochemical measurements, the field has seen a recent upsurge in interest with a number of different methods being published in the last three to four years.

2.3.1 Optical Waveguide Lightmode Spectroscopy

Optical waveguide lightmode spectroscopy (OWLS) is an optical evanescent field based refractive index sensing technique. The OWLS structure consists of a grating coupler patterned on to a planar optical waveguide; a thin dielectric film that has a higher refractive index than the substrate and the surrounding media [54]. When illuminated at a specific incidence angle with a polarized, monochromatic light source, the light will couple into the grating and excite a guided mode in the planar waveguide. This results in an evanescent wave that propagates into the media at the waveguide-media interface. Changes in the refractive index of the media will interact with this evanescent field, causing a change in the coupling incidence
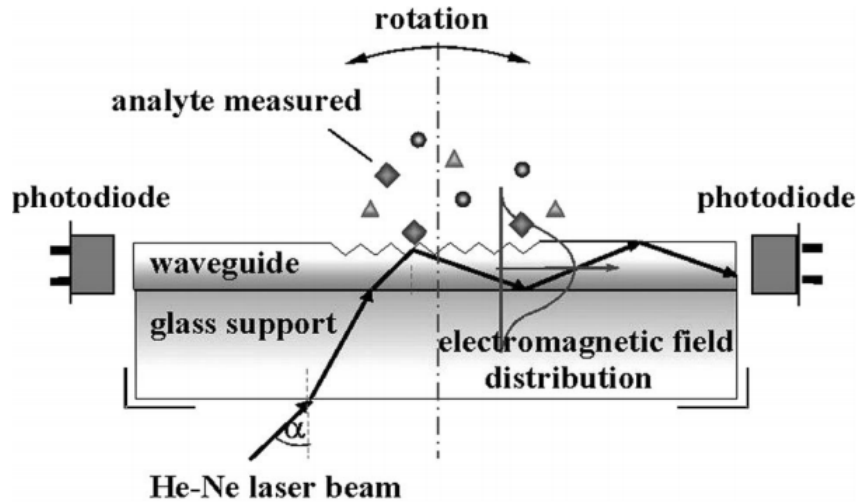
Figure 2.4: Schematic of an optical waveguide lightmode spectroscopy setup. The incident light is coupled into the waveguide by the grating coupler. The evanescent guided mode is detected by the photodiode on each side of the waveguide. Changes in refractive index change the angle of incidence for coupling to the occur. Adapted from [55].

angle.

The refractive index of the media surrounding the waveguide can be measured by recording the incidence angle that maximises the intensity of the guided mode which is coupled out of the edge of the planar waveguide and measured by a photodiode. Continuously monitoring the change in incidence angle allows for label free measurement of changes of refractive index at the waveguide surface. The incidence angle is also dependent on the polarisation resulting in different incidence angles for transverse electric (TE) or transverse magnetic (TM) polarised light. Measuring TE and TM modes simultaneously allows for quantification of both the refractive index and thickness of a layer adsorbed on the waveguide surface.

OWLS has been used to investigate corrosion of dieletric thin films, quantum dots, and deposition of proteins and lipid bilayers [56]. Critically, OWLS provides high refractive index sensitivity enabling bioassays that employ OWLs have to have low limits of detection. For example, an assay for the malaria drug artemether showed a limit of detection of 0.05 ng/mL [57]. However, changing the incidence angle requires a precision stepper motor as the angle only changes within a few degrees for measuring biologically relevant changes in refractive index. In addition, the laser light source also needs to be highly stable as measuring the change in refractive index assumes that the wavelength of light is constant. Both of these requirements mean that the measurement system requires moving parts and expensive optical compo-
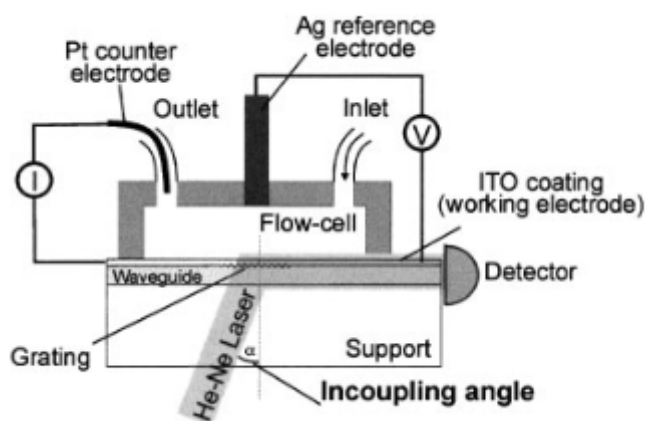
Figure 2.5: Electrochemical optical waveguide lightmode spectroscopy experimental setup. The waveguide has been coated in ITO to serve as the working electrode. A Pt wire counter electrode and an Ag reference electrode are inserted into the fluidic channel to complete the electrochemical circuit. Adapted from [58].

nents and are more complex than that of many competing photonic techniques.

Electrochemical optical waveguide lightmode spectroscopy

In electrochemical optical waveguide lightmode spectroscopy (EC-OWLS), the grating coupler and planar waveguide are coated with a thin layer of indium tin oxide (ITO) for combined electrochemical and refractive index sensing. ITO has a high refractive index, high conductivity and low optical losses in the visible spectrum. The ITO layer serves as the working electrode, while Pt and Au wires are used typically as the counter electrode and pseudo reference electrode, respectively. The EC-OWLS chip can also be used within a microfluidic chamber for combined optical and electrochemical measurements under continuous flow.

Much of the literature has used EC-OWLs to study and understand the surface-adsorption of materials, such as poly-L-lysine [59] and layer-by-layer film deposition under applied dc bias voltage conditions [60]. EC-OWLS has also been applied to more complex electrochemical systems, for example cyclic voltammetry has been used to characterise the redox active molecule toludine blue [61]. The adsorption and electrochemical properties of cyctochrome c, a redox active protein, have also been measured simultaneously using an ITO based planar waveguide based on the EC-OWLS experimental setup [62]. Electrochemical impedance spectroscopy has also been applied within EC-OWLS to characterise the formation of supported lipid bilayers [63]. Finally, there have also been some studies on the growth of bacteria using EC-OWLS. The growth of *Lactobacillus plantarum* was measured while im-

mobilised to the surface by application of bias voltage to the EC-OWLS working electrode [64].

2.3.2   Surface Plasmon Resonance

Surface plasmon resonance (SPR) uses the interaction of light with free electrons in a metal thin film to excite an evanescent plasmon wave at the metal media interface. A plasmon is a quasiparticle of the plasma oscillation from the free electrons in metals [65]. The incident light must be coupled into the metal to excite a surface plasmon. This is typically performed using the Kretschmann configuration, consisting of a prism with a thin metal film deposited on the surface [66]. At the critical angle, the incident light in the prism will be reflected by total internal reflection. An evanescent wave from the incident light will decay into the metal thin film on the surface of the prism, exciting a single mode transverse magnetic polarised surface plasmon at the metal dielectric interface [67]. The incident light coupling to the surface plasmons results in a reduction in reflectance at the photodetector. The wave-vector of the plasmons is dependent on the refractive index of the media such that changing the refractive index will require a different incident angle in order to excite the surface plasmon. By tracking the change in the reflectance peak with respect to incidence angle, binding events to the metal surface can be monitored [68].

Alternative SPR configurations use grating couplers and optical fibres to couple the light into the metal. These simplify the optical setup by removing the need for a prism or a rotatable light source to measure the SPR. SPR based devices provide a higher refractive index sensitivity than many photonic sensors, as more of the evanescent wave is present in the media than the metal, decaying several hundred nanometres in the media but only 20-30 nm into the metal [69].

Imaging can also be performed using an SPR sensor by replacing the photodetector with a camera. In this configuration, the incidence angle and wavelength remain fixed, so the refractive index shift across the metal surface is measured by the change in intensity on the resulting image [71]. This allows spatial changes in refractive index to be measured over time. The spatial resolution is dependent on the propagation length of the plasmon, which is primarily limited by the losses of the metal layer itself.
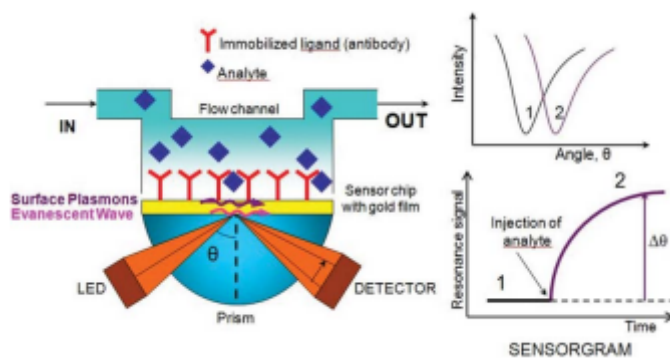
Figure 2.6: Schematic of affinity biosensing using SPR in the Kretschmann configuration. As the incident angle is varied the SPR is the excited by the evanesecent wave at the metal prism interface at a particular angle. Changes in refractive index at the metal-media interface caused by antigen binding cause a change in the incident angle required to excite the SPR. Tracking the change in incident angle over time allows for measurement of binding kinetics to the sensor surface. Adapted from [70].

Electrochemical SPR

The metal film in SPR sensors is usually Au, a material commonly used as a working electrode for electrochemical systems. There has thus been a significant body of work using SPR sensors for combined optical and electrochemical measurements; a technique known as electrochemical SPR (EC-SPR) [72].

A notable example of EC-SPR is the combined optical and electrochemical measurements of glucose oxidase in which the complementary measurement modes can be used to account for non-specific binding target molecules to the sensor surface [73]. Glucose oxidase was immobilised using layer-by-layer electrostatic adsorption of PEDOT and its enzymatic activity was confirmed using amperometric detection. Simultaneous monitoring of the change in thickness of the surface immobilised layer via the SPR signal was used to remove non-specific adsorption to the sensor surface. There was not however any quantifiable attempt to show that this approach improved the specificity of glucose detection compared to a single mode sensor.

A similar approach has been used for the simultaneous detection of glucose and human IgG (14 mM glucose and 14 μg/mL human IgG) using a combined anti-IgG and glucose oxidase surface functionalisation [74]. Carboxylated polymers were electropolymerised on to the SPR sensor surface, allowing for a two-step functionalisation of the polymerised films. The surface was first functionalised with glucose oxidase before a second electropolymerisation step with anti-IgG. The current generated by the turnover of glucose to glucolactone was detected amperometrically,

while IgG binding was monitored using the SPR signal.

Electro-assisted thiol functionalisation of an EC-SPR sensor was used for the apatmeric detection of ampicillin with a limit of detection of 1 nM/mL in buffer [75]. Although the electro-assisted functionalisation reduced the time to immobilise the aptamer, this method of functionalisation is more complicated than using a thiol based self assembled monolayer alone. Electro-assisted deposition has also been investigated to direct the adsorption of proteins using plasmonic nanowires. The surface of the Au SPR was modified using electrodeposition of Au to create localised surface plasmon resonance structures. The LSPR structure enhanced the sensitivity of the device and the charge dependent deposition of the proteins bovine serum albumin and lysozyme was characterised [76]. Similarly, the electrodeposition effect was exploited to the improve the sensitivity of a biosensor for troponin, a cardiac health marker [77]. EC-SPR has also been used for phenotypic studies of prokaryotes by monitoring the growth of electro-active biofilms using SPR simultaneous with electrochemical measurements of electron transfer in the electroactive bacterial films. In addition, EC-SPR imaging of eukaryotes, here human basal epithelial cells, has been demonstrated combined with electrochemical measurements [78].

In addition to the development of EC-SPR for biosensors, the multimodal technique has also been used for more fundamental chemical analysis. For example, spectroelectrochemical measurements using EC-SPR were used to show the wavelength dependence refractive index of surface adsorbed methylene blue films under bias voltage conditions [79]. Surface modification of an SPR sensor with graphene was shown to improve the electrochemical stability under acidic conditions and to reduce non faradaic background currents [80]. Finally, electrochemical control of plasmonic nanohole transmission using a surface immobilised electroactive polymer polypyrrole has demonstrated, the polypyrrole can be switching from a conducting to an insulating material using applied bias voltage correspondingly lowering and increasing the plasmonic transmission [81].

2.3.3   Lossy Mode Resonance

Lossy mode resonance (LMR) biosensors are similar to SPR sensors but use a lossy dielectric thin film instead of a metal layer on top of an optical waveguide as shown in figure 2.7 [82]. For the LMR to be observed two conditions must be met; the permittivity of the thin film must be greater than zero, and the refractive index of film must be greater than the waveguide [83]. When illuminated with white light, optical modes will be guided in both the optical waveguide and the dielectric thin
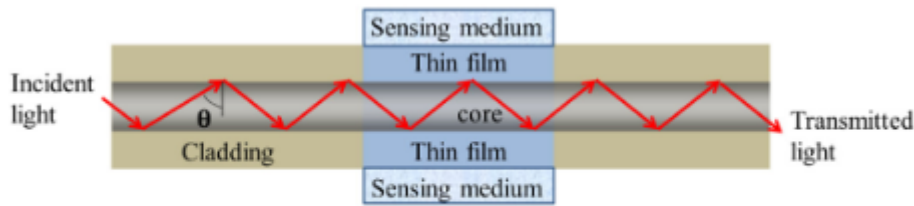
Figure 2.7: Schematic of a lossy mode resonance fibre sensor. A portion of the cladding is removed for deposition of a thin film such as ITO. The LMR is due to the coupling of optical modes in the film and modes in the fibre. Adapted from [82].

film. The LMR occurs when the mode in the waveguide couples with the mode in the thin film, resulting in a transmission dip. The peak attenuation wavelength is dependent on several factors; the refractive index contrast between the thin film and the waveguide, the thickness of the lossy thin film, and the incidence angle [84].

Increasing the thickness of the thin film layer allows for multiple modes to be guided in the thin film and therefore multiple attenuation peaks will appear. The multiple attenuation peaks can be used for sensing however greater refractive index sensitivity is used when a single mode fibre is used [85].

Unlike SPR which can only be observed using TM polarised light, LMR is polarisation independent and can be observed with both TE and TM polarised light or white light with no polarisation at all. The polarisation independence makes LMR attractive because it simplifies the optical setup by removing polarising elements. The trade-off however is that the TE and TM LMR will interfere with each other, resulting in a broadening of the resonance peak. This makes it more challenging to track the change in mode leading to a decrease in sensitivity.

LMR can be induced most effectively as the incidence angle approaches 90°, where the effective refractive index of the waves in the thin film becomes equal to the substrate [86]. A LMR can be induced on a thin film on any substrate and has been demonstrated using the Kretchsmann configuration of SPR [87]. It is simpler however to use an optical fibre for the waveguide as the incidence angle of the light propagating through the fibre is already approximately 90°. Practical LMR sensors therefore almost exclusively use optical fibres in which the cladding can be removed from a standard optical fibre for coating with high refractive index films such as TiO_2 or In_2O_3 using standard thin film deposition processes [82] [88]. LMR sensors have been shown to have high refractive index sensitivity. For example, a sensitivity of over 300,000 nm/RIU has been demonstrated using a LMR sensor, but this was only present for a very narrow range of refractive index changes [85].

Alternative fibre structure such as D-shaped fibres have been investigated experimentally. These fibre configurations tend to have greater sensitivity than standard LMR on optical fibres as the evanescent tail of the mode propagates further into the media [89]. Theoretical works have also examined the potential of LMR biosensors in which the resonance is induced in photonic crystal fibres (PCF), which have periodic air fibre refractive index changes within the fibre core [90]. PCF-based LMR sensors can theoretically achieve very high refractive index sensitivity ($> 10^6$ nm/RIU) but their complex fabrication process and fragility means that there are significant challenges for PCF-based sensors to achieve widespread use.

Alternative fibre structure such as D-shaped fibres have been investigated experimentally. These fibre configurations tend to have greater sensitivity than standard LMR on optical fibres as the evanescent tail of the mode propagates further into the media [89]. Theoretical works have examined LMR induced in photonic crystal fibres, which have periodic air fibre refractive index changes within the fibre core [90]. PCF-based LMR sensors can theoretically achieve $> 10^6$ nm/RIU refractive index sensitivity but their complex fabrication process and fragility means that there are significant challenges for PCF-based sensors to achieve widespread use.

Electrochemical LMR

Despite many LMR sensors using conductive oxides such as ITO in their fabrication, the combination of electrical and optical measurements using LMR is very limited. For example, the optical response of the LMR under bias voltage conditions has been shown to be dependent on both the properties of the ITO and of the surrounding electrolyte while electropolymerisation of isatin, a drug precursor compound, was monitored electrochemically, using cyclic voltammetry, and optically using a LMR fibre sensor [91] [92]. The electrical sensitivity of an ITO based LMR sensor has been shown to be improved with electropolymerisation of poly(3,4-ethylenedioxythiophene) polystyrene sulfonate (PEDOT:PSS) on to an ITO coated LMR fibre [93]. Application of the PEDOT reduced the Ohmic drop of the electrochemical cell compared to ITO alone, reducing the peak to peak separation and the non-faradaic background when measuring a redox active molecule.

2.3.4   Fibre Gratings

Fibre Bragg gratings are optical fibres that have a small area of periodic refractive index along the length of the fibre. Fibre gratings are divided into two categories
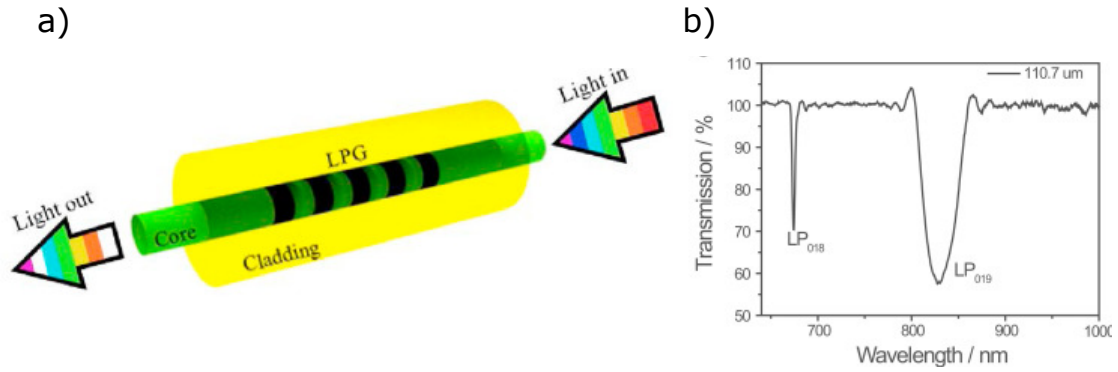
Figure 2.8: **a)**Schematic of the long period Bragg fibre grating. **b)** Transmission profile of a LPFG. Adapted from [94].

based on the length of the grating period [94]. Sub wavelength fibre gratings demonstrate peak reflectance at a wavelength determined by the Bragg reflectance due to the coupling of the forward and counter propagating modes in the fibre [95]. There are currently no published works on multimodal sensing using sub wavelength fibre gratings. In contrast, long period gratings, as shown in figure 2.8, use gratings that have a periodicity of greater than 100 microns. Here, a transmission dip will occur due to coupling between the mode propagating in the core and a mode propagating in the cladding. The resonance of the fibre grating is dependent on the physical parameters of the grating such as the period of the grating, the refractive index contrast of the grating,and the stress on the optical fibre [96]. Fabrication of the grating, is typically achieved by modifying the refractive index of the fibre at specific locations by exposure to high power UV light.

Combined optical and electrochemical investigations have been performed using long fibre gratings coated in ITO and it was found that application of voltage to the ITO caused significant changes in the resonance due to the increase in carrier density in the ITO and the electrical change of the electrochemical double layer [97]. Diamond coated long fibre gratings doped with boron have also been demonstrated and applied to combined optical refractive index sensing and electrochemical measurements of ferrocene [98].

2.3.5 Electrophotonic Ring Resonator Silicon Biosensors

A ring resonator is a waveguide that loops back on it itself. Light is typically coupled into and out of the sing-shaped waveguide via a coupling, linear waveguide fabricated close to the ring [99]. The waveguide will resonate at frequencies at which an integer number, m, of wavelengths fit within the length (circumference), L, of the waveguide (Eq. 2.2). This results in multiple resonant frequencies separated
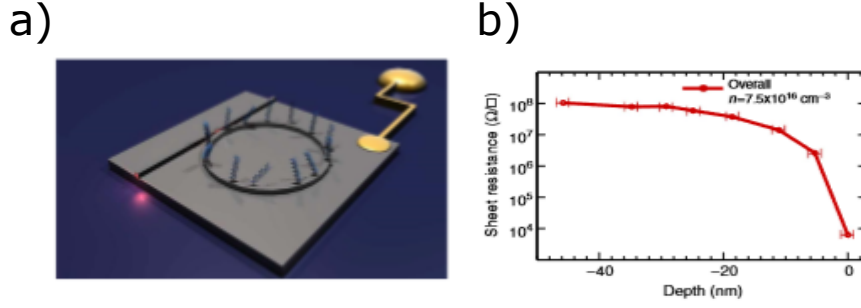
Figure 2.9: **a)** The electrophotonic silicon ring resonator with a Au contact electrode **b)** Sheet resistance against depth of the silicon demonstrating that only the surface of ring resonator is highly doped. Below 20 nm the Si behaves as an intrinsic semiconductor. Adapted from [103].

by the free spectral range (Eq. 2.3), where n_g is the group refractive index of the waveguide. At resonance, the light continues to propagate around the ring resonator, resulting in multiple dips in optical transmission dips at the output of the coupling waveguide. An alternative coupling method uses a second waveguide, which couples the light from the resonator to a second output, resulting in a transmission peak. There is no inherent sensitivity advantage in this strategy, but it does provide an opportunity to couple resonators together, one serving as a reference and the second as the analyte detector [100].

$$\lambda_{res} = \frac{n_{eff} L}{m} \tag{2.2}$$

$$FSR = \frac{\lambda^2}{n_g L} \tag{2.3}$$

The radius of the ring-shaped waveguide is limited by how well the light can be confined within the waveguide, but for high refractive index materials such as Si the loop radius can be as small as 3 μm [101]. One of the challenges facing the manufacture of Si ring resonators is the need to ensure sharp and vertical edges of the waveguide in order to reduce scattering of light out of the waveguide. Si ring resonators are typically used with TE polarised light as this polarisation has the least optical loss. The TM mode can provide higher sensitivity however because it is confined at the top of and bottom of the waveguide [102]. This provides a greater overlap between the evanescent field and the surrounding media, and consequently more interaction with biomolecules on the sensor surface. It also means the confined mode will interact less with the vertical edges of the waveguide, leading to reduced scattering from roughness on the waveguide.

Electrophotonic silicon biosensors are a Si ring resonator structure that has a high extrinsic doping of around 10^{20} carriers/ cm^3 within 20 nm of the waveguide surface [103]. When used in TE mode, the majority of the light is confined within the undoped area of the waveguide. Optical losses are therefore minimised while still retaining a conductive surface. The ring resonator can be integrated into an electrochemical cell for combined electrochemical and optical measurements.

To date, few experimental measurements have been performed using the combined electrochemical and refractive index sensitivity of the electrophotonic ring resonator. The conformational change of methylene blue labelled surface immobilised DNA following hybridisation with its complementary strand was examined using the electrophotonic sensor [104]. The reduction in electron transfer from the methylene blue after hybridisation showed that the methylene blue had physically been moved from the surface by the straightening on the DNA after binding. Combining this with the refractive index shift shows that the reduction in faradaic current from the methylene blue is not due to interference from the hybridising DNA strand itself. Multiplexed DNA sensing using a electrophotonic microarray has also been performed where the selective functionalisation of the sensor surface was achieved by electrografting of diazonium salts to provide spatial control over the surface functionalisation.

2.4   Summary

In this chapter I have reviewed existing multimodal biosensing technologies that promise to extend the capabilities of more traditional, single modal sensors. While there are many examples of multimodal biosensors using a range of transduction methods, this chapter has focused largely on multimodal sensors that combine electrochemical and optical transduction. Perhaps the most established of these multimodal technologies is EC-SPR that has been applied to a large number of measurements system to extend the capabilities of single modal SPR both for applications in diagnostics and for fundamental chemical and biological research. Recently, the field of multimodal sensors has been increasing and today there are several emerging technologies that combine electrochemical measurements with photonic structures. While many of these have been characterised experimentally, the technology has yet to be adopted widely outside of academia.

Chapter 3

Guided Mode Resonance

3.1 Introduction

This chapter discusses the guided mode resonance (GMR) sensor used in this work. First a general overview of GMR sensors and their use in biosensing will be given. A detailed discussion of the physical origin of the optical resonance will be presented along with fabrication techniques and methods of interrogating the GMR resonance for biosensing applications. The use of GMR for photonic crystal enhanced microscopy will be discussed before concluding with a comparison of GMR sensors with alternative photonic structures.

3.2 GMR Sensors

GMR is an optical phenomenon in periodic nanostructured dielectrics. Interference and diffraction of modes guided by the nanostructured grating can be engineered to give up to 100% reflection of the incident light. Since GMR was first observed over 100 years ago there has been substantial theoretical and experimental characterisation of grating structures. GMR structures have been developed for use in many applications such as optical filters, polarisers, laser cavity mirrors and wavelength division multiplexers [105] [106] [107] [108]. A comprehensive review of the application of GMR structures is provided by Quaranta et al. [109].
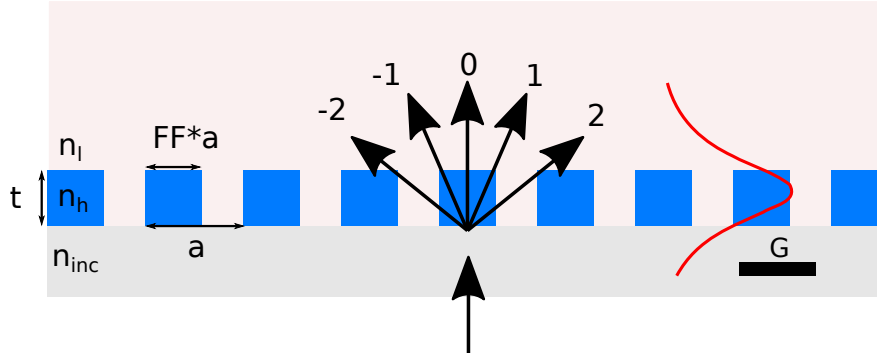
Figure 3.1: Schematic of a GMR nanostructure. The GMR structure of thickness t with refractive index n_h, period a, filling fraction FF on a glass substrate with refractive index n_{inc}. The media has a refractive index n_l. When the incident light is at angle $0\,°$, diffracted modes with angle θ_m are produced. The evanescent sensing wave is shown decaying into both the media and the glass substrate. The direction of the grating vector G is indicated by the black bar.

More recently, research initially driven by Cunningham and Magnusson saw the development of GMR structures for applications in biosensing [110] [111]. GMR biosensors are a label free optical sensing technology that has been demonstrated for the selective detection of biomolecules. An important advantage of GMR sensors is that they can be illuminated with normal incidence light, simplifying optical integration compared to the in plane optical coupling used in other photonic biosensors.

Typically, a GMR structure is made from a thin film (100 - 200 nm) of a high refractive index dielectric material that is deposited on to a glass substrate. The dielectric material is patterned into a one dimensional periodic grating structure, shown figure 3.1, which acts as both a diffraction grating and a waveguide layer. When illuminated with incident white light normal to the grating structure, a particular wavelength of light λ_{res} will resonate within the grating structure and be reflected back towards the light source.
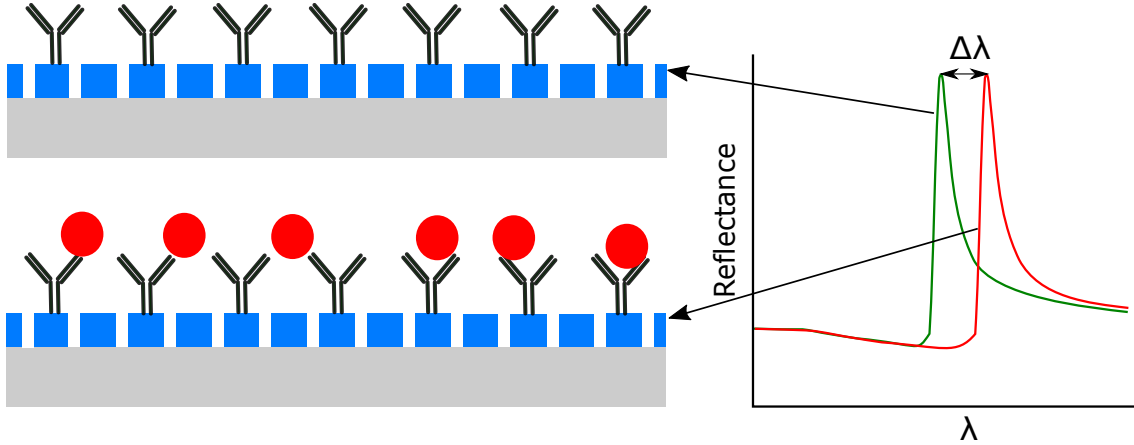
Figure 3.2: Biosensing using a GMR sensor. When functionalised with antibodies the GMR will have a reflectance peak at λ_{res}. Upon binding the target analyte the resonance wavelength will shift by $\Delta\lambda$.

The resonant light within the structure is known as a "leaky mode" as it is not totally confined within the grating but instead includes an evanescent wave that decays approximately 200 nm into the surrounding media. The resonance wavelength λ_{res} is dependent on the periodicity and material properties of the grating but most importantly on the refractive index within the extent of the evanescent field. Consequently, a change in the refractive index of the media local to the GMR surface causes a change in λ_{res} as shown in figure 3.2. By monitoring the change in λ_{res}, the GMR structure operates as a refractive index sensor. By functionalising the surface of the GMR with a bioreceptor, such as an antibody or affimer layer, the GMR can be used to specifically measure the refractive index change due to the binding of an analyte.

3.3   Resonance Conditions

There are two conditions that must be met for GMR to occur within a 1D periodic grating structure. First the effective refractive index n_{eff} must be greater than substrate refractive index for the grating to act as a waveguide (Eq. 3.1). As a first approximation for the TE mode n_{eff} can be considered as the magnitude of the refractive index of the grating structure n_g and the medium n_m surrounding it (Eq. 3.2). For application in biological sensing, the media refractive index will typically be similar to water ($n = 1.33$) which is lower than the RI of glass ($n = 1.46$). A high refractive index n grating material such as Si_3N_4 ($n = 2$) or TiO_2 ($n = 2.6$) is

used for fabricating the grating structure to meet the condition in equation 3.1.

$$n_{inc} < n_{eff} \tag{3.1}$$

$$n_{eff} = \sqrt{n_h^2 + n_l^2} \tag{3.2}$$

$$sin(\theta_m) = \frac{n_{inc}}{n_{eff}} sin(\theta_{inc}) - \frac{m\lambda}{n_{eff}a} \tag{3.3}$$

$$\frac{\lambda_0}{n_{eff}} < a < \frac{\lambda_0}{n_{inc}} \tag{3.4}$$

The behaviour of the grating can be described by equation 3.3, the general diffraction grating equation, where θ_m is the diffraction angle of the mth order, θ_{inc} is the angle of incident light, m is the order of the diffracted light, a is the grating period and λ is the wavelength of light. The second condition for GMR in equation 3.4 is that the grating is larger than the wavelength of light in the grating but smaller than the wavelength in the glass substrate. As a general rule to meet this condition, $\frac{\lambda}{a}$ should be approximately 1 to 1.6. For periods smaller than incident wavelength, the contribution of $\frac{\lambda}{a}$ is so large that the only solution is the 0th order modes. In this case the grating effectively becomes a thin film, with no diffraction and only the thin film resonance is observed. For grating periods greater than the incident wavelength, the grating equations reduces to Snell's law, and behaves as a standard diffraction grating.

$$sin(\theta_m) = m \tag{3.5}$$

If the resonance condition is met and assuming $\theta_{inc} = 0$, then the grating equation reduces to equation 3.5, where m can only be 0, 1 or -1. The 0 mode is not diffracted and continues at 0 °. In contrast, the 1 and -1 mode however are diffracted at 90° into the grating itself and are supported by the waveguide. Due to the periodic structure of the grating these modes are reflected and scattered at each interface between the grating and the media. The scattering into the medium is the origin of the evanescent decaying wave which is used for the refractive index sensing shown in figure 3.1. By tuning the material parameters of the grating including the period, the filling fraction and thickness of the film, the leaky resonant mode can destructively interfere with the 0th order transmitted light, resulting in up to 100% reflection of

31

the resonant light at a resonance wavelength λ_{res}. Measuring the reflected light with a spectrometer shows a high peak reflectance with an asymmetric line shape i.e a Fano resonance shown in figure 3.2. The origin of the asymmetry is that the reflectance is the product of the thin film reflectance of the dielectric layer and the Bragg reflectance of light guided by the grating.

3.3.1 Polarisation

The GMR reflectance is dependent on the polarisation of the incident light as the grating structure is not uniform in all directions. The TE mode is defined as the mode in which the electric field $\mathbf{E}$ is parallel with the grating vector G while for the TM the electric field is perpendicular to the grating vector. The two modes therefore experience a different effective refractive index as the grating is periodic in only one direction. The difference in effective refractive index therefore leads to the TE and TM modes resonating at different wavelengths.

The TE mode is characterised by a high reflectance but low quality factor Q where as the TM is typified by a lower reflectance but higher Q. The Q factor, defined as the ratio of the resonant frequency to the resonance linewidth at full width half maximum, is a critical quantity in resonant biosensors. The higher Q associated with the TM mode is advantageous for biosensing, as it ensures greater confinement within the waveguide layer, which increases the interaction of the evanescent leaky mode with the surrounding the media [112]. The difference in mode profile of the TE and TM mode has been exploited to determine the thickness of films deposited on the GMR [113].

3.3.2 Angle of Incidence

When illuminated with an incident angle of 0°, the -1 and 1 modes are guided equally within the grating structure. Changing the incident angle from 0° results in different diffraction angles for the two modes. The change in angle means the modes experience a different periodicity leading to the production of two resonances. As the resonance condition for these two modes would be different, this could be potentially exploited for measuring the thickness of the layer forming on the GMR surface [104]. This is not typically required for standard biosensors assays however so the incidence angle of light is kept at 0°. As the GMR is so sensitive to the angle of incidence, the light is collimated to prevent any unwanted resonance from the other modes.

3.4 Fabrication Techniques

For the GMR to operate in the near infrared region with a resonance wavelength of 800-850 nm, the grating period will be approximately 500 nm. The filling fraction will be between 70 and 80%, giving a grating groove width of approximately 100 nm. There are a number of nanofabrication techniques that can be used to create features with this spatial resolution that have been used for the fabrication of GMR gratings.

Electron beam lithography is a direct write nanofabrication technique used to produce structures into electron sensitive resist layers using a high energy electron beam [114]. Electron beam lithography is the main fabrication used in this thesis and will be discussed in greater detail in chapter 4. Laser interference lithography uses diffractive interference from a grating slit to project the pattern of the GMR on to the substrate. Laser interference lithography has been used for patterning a GMR sensor into a UV photoresist layer deposited on to a flexible substrate [115]. Laser ablation is a technique for removing solid material from a substrate using a high powered laser. Laser ablation using a 187 nm UV laser has been used for fabricating 50 nm deep sub wavelength GMR structures in TiO_2 [116]. Focused ion beam milling, which uses ions to physically etch away the substrate, has also been used for the fabrication of GMR gratings [117]. The direct write nature and need to physically remove the material means both laser ablation and ion beam milling are not suitable for high throughput manufacturing. They are however more suitable for patterning GMR structures on to non-standard substrates such as the tip of an optical fibre, which would be difficult to manipulate using lithographic methods.

A technique that is becoming increasingly popular for the fabrication of GMR structures however is nanoimprinting. Nanoimprinting is a soft lithography technique for producing nanostructures using PDMS moulds. First, a "master" of the GMR structure is produced using conventional nanofabrication techniques such a E-beam lithography or focused ion milling. A PDMS mould of the master is then produced to give the inverse of the structure. For structures which are greater than 100 nm a standard 10:1 mixture of PDMS can simply be poured on to the master and left to cure. For sub 100 nm structures such as those for high filling fraction GMR gratings, the feature resolution can be improved by spin coating on a dilute PDMS layer on to the master prior to making the full moulds [118].

The substrate to be patterned is then prepared by spin coating on a UV curable liquid resist layer. The PDMS mould is then pressed into the resist layer and exposed

to UV light. Once the mould is removed the imprint of the mould is left in the now hardened resist layer. The GMR structure can then be made by depositing a high refractive index dielectric layer on top of the cured structure using methods such as plasma sputtering or chemical vapour deposition (CVD) [119]. The advantage of nanoimprint lithography is that the fabrication time is independent of the device surface area, allowing whole wafers to be patterned more rapidly than conventional nanofabrication techniques.

3.5   Measurement Methods

Several methods have been proposed for measuring the response to changes in refractive index from a GMR biosensor.

3.5.1   Wavelength

The most common approach for tracking changes in the resonance of the GMR is to measure the wavelength of the resonant reflectance peak using a spectrometer. Such measurements can be performed as a function of time in order the quantify the kinetics of a reaction. The measured spectra is typically fitted mathematically to a standard reflectance profile such as the Fano equation to extract the resonance wavelength and increase sensitivity compared to a simple peak intensity extraction. The sensitivity of the wavelength resonance measurement is theoretically limited only by the Q factor of the grating, higher Q factor meaning improved sensitivity by being able to better resolve the resonance peak [14]. In practice however the measurement sensitivity is also limited by the spectral resolution of the spectrometer to measure such a high Q resonance. The cost of the spectrometer is also a significant hindrance for future commercialisation of GMR based diagnostics.

3.5.2 Intensity
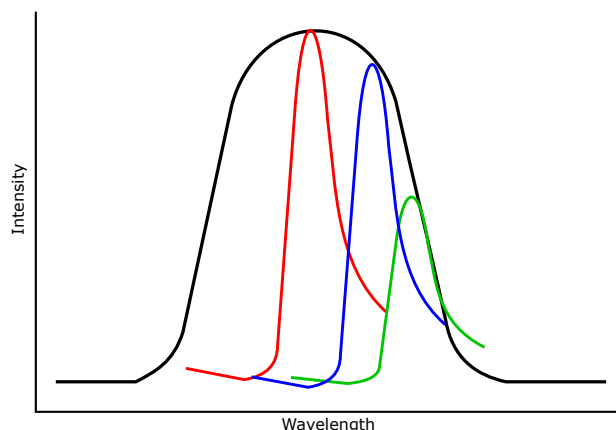
Figure 3.3: Intensity based measurement of GMR reflectance. The GMR is illuminated with by an LED with the transmission profile shown in black. The intensity of the GMR reflectance decreases with increasing resonance wavelength due to the spectral profile of the LED illumination.

Intensity based measurements use a monochromatic light source such as an LED, and monitors the change in intensity as the resonance wavelength overlaps with the incident light as shown in figure 3.3. The advantage of measuring intensity is that a camera rather than a spectrometer is used for measuring the GMR signal, reducing the costs of the measurement setup. GMR sensors integrated within 96 well plates demonstrates that the intensity based technique has the potential for multiplexed measurements similar to those performed in a conventional ELISA assay [120]. Measurements reported using this strategy to detect targets such as CD40 or epidermal growth factor (EGF) have been restricted to μg/mL concentration, which is above clinical relevance. The lack of sensitivity is due to the emission spectrum of the LED being broader (FWHM $\approx$ 10 nm) than the resonance shift of the GMR ($\Delta\lambda$). The change in reflected intensity is therefore minimal for anything other than very high target concentrations. Intensity measurements are also highly sensitive to the stability and noise of the incident light source, so reduction in cost for removing the spectrometer is offset by the the requirement for a high stability light source.

3.5.3 Phase

Interferometric sensors such as Mach Zehnder interferometers (MZI) have been shown to have vastly superior RI sensitivity (10^{-9} RI/nm) compared to that of GMR sensors. There are few attempts to incorporate interferometric style measurements into GMR measurements for sensing applications. One approach using a
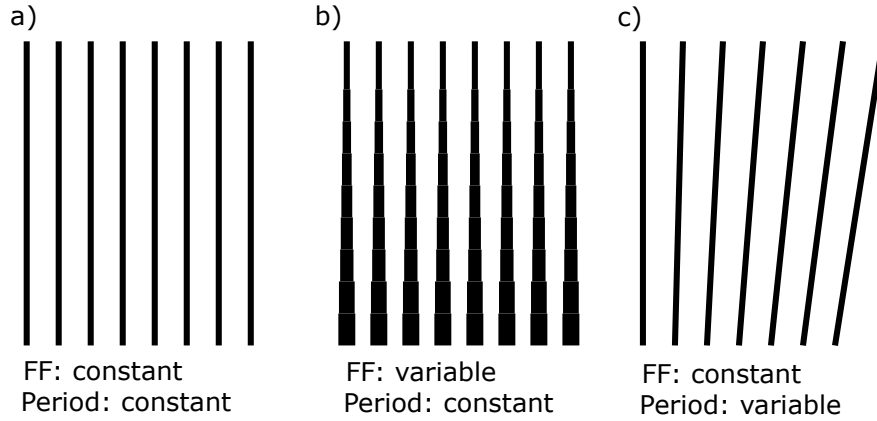
Figure 3.4: **a)** Schematic of a standard GMR grating with a constant filling fraction (FF) and period. The filling fraction is shown in black. **b)** Schematic of a chirped GMR grating by changing FF with constant period. **c)** Schematic of the "fan" chirped GMR with constant FF and changing period.

heterodyne interferometer was shown to resolve a minimum 1.98×10^{-7} RIU while a simpler MZI style optical setup achieved a minimum 3.98×10^{-7} RI/nm [121] [122]. Although this is significantly more sensitive that intensity or wavelength shift measurements, the increased sensitivity comes at the cost of experimental complexity. The expense of these methods is likely to preclude them from POC diagnostic applications, limiting their future use. Furthermore the monolithic integration of the phase measurement used in techniques such as MZI has been replaced with a less practical free space optical setup.

3.5.4 Chirped GMR

One of the challenges facing commercialisation of photonic sensors is that complex and expensive optics are required for measuring the output of the sensor. The chirped GMR is a resonant grating sensor where one of the physical parameters of the grating changes spatially across the sensor resulting in a grating that resonates at different wavelengths across the grating. The first work on the chirped GMR grating achieved this change by modulating the filling fraction, as shown in figure 3.4b. Here, the filling fraction was modulated by changing the exposure dose to under and over expose the resist in certain areas, causing an increase and decrease in the filling fraction respectively.

Tuning the period for creating the chirped GMR was initially challenging due to exposure grid resolution of the electron beam lithography system. The period could only be tuned by approximately one nanometre, give a minimum of resonance wavelength change of 1.25 nm per period change. This limitation has been overcome by

improving the patterning parameters to reduce the grid exposure, enabling greater resolution of the GMR period. Using the fan shaped structure in figure 3.4c gives a continuous change in the period with a constant filling fraction rather than discrete steps from directly setting the period in the lithography system. The resonance from the fan shape chirped GMR will be experimentally characterised in chapter 6.
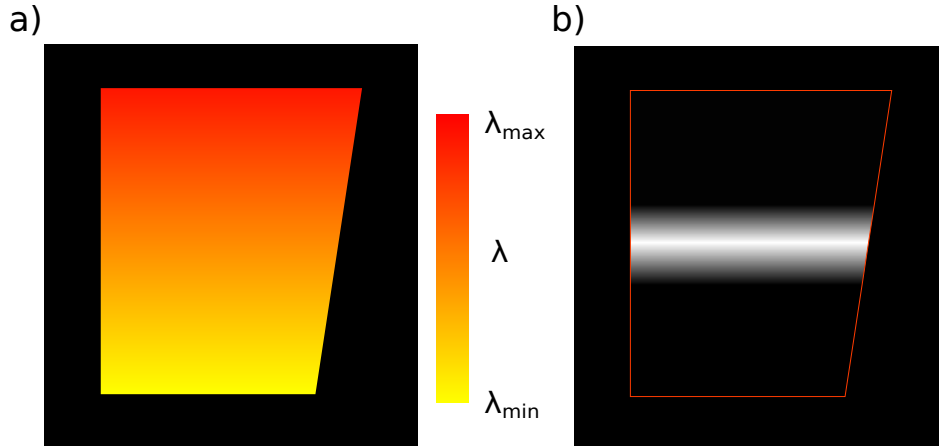
Figure 3.5: **a)** Schematic of the fan chirped GMR resonance wavelength. The resonance wavelength increases with the period. **b)** Schematic of the reflectance bar of the chirped GMR when illuminated with monochromatic light.

The resonance wavelength of the chirped GMR can be visualised using hyperspectral imaging as shown schematically in figure 3.5a. When illuminated with a monochromatic light source there will be an area of the grating where the period matches the resonance condition for the refractive index currently on the grating. A region of high reflectance can be observed across the grating at the period that matches the condition as shown in figure 3.5b. Increases in the refractive index, for example due to antigen binding changes the resonance condition moving the region of high reflectance towards the shorter period as shown in 3.6.

The change in refractive index has been converted from spectral change to a spatial change. This can be measured using a monochromatic light source such as an narrowband LED and imaged with a camera as opposed to using a spectrometer, significantly decreasing the costs of a prospective final device. The magnitude of the resonance wavelength position is dependent on the length of each filling fraction area.

The sensitivity of the chirped GMR for the detection of the IgG was estimated at 40 ng/mL from the measured shift of 500 ng/mL, assuming that the resonance position shift was linear [123]. The use of a chirped GMR as a spectrometer for a standard GMR sensor has also been reported [124][125]. This method is not as elegant as
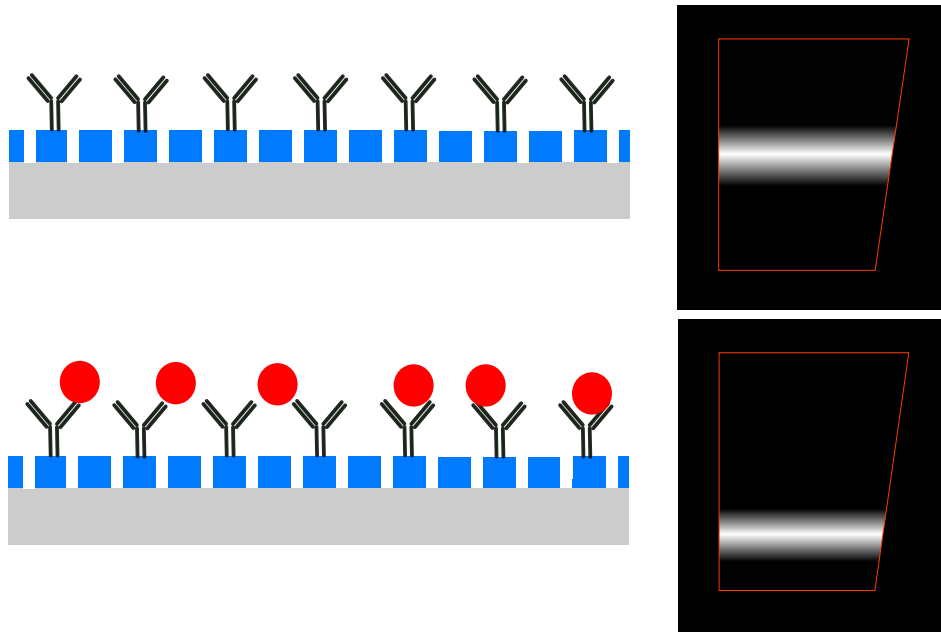
Figure 3.6: Schematic of biosensing with the chirped GMR. When functionalised with antibodies the white high reflectance region is tuned to the centre of the GMR structure. Antigen binding causes the reflectance region to shift towards the shorter period section of the grating.
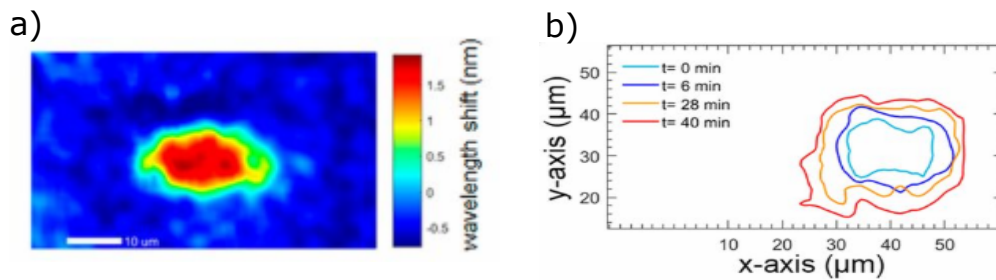
Figure 3.7: **a)** Photonic crystal enhanced resonance imaging of HepG2 cells expressing thrombopoietin (TPO). The grating was functionalised anti-TPO antibodies **b)** Visualisation of the TPO over time. Adapted from [126].

using the chirped GMR itself as the sensor however requiring a second GMR sensor, with no particular gain.

3.6 Hyperspectral Imaging

GMR sensors can be used for imaging of the resonance wavelength across the surface of the grating similar to SPR imaging. To produce a resonance image, the grating is illuminated with monochromatic light and the wavelength of the incidence light is scanned. Plotting the wavelength with the maximum reflectance for each pixel gives an image of the resonance wavelength.

3.6.1 Spatial Resolution

The spatial resolution of the GMR is asymmetric. Parallel to groove of the grating, the resolution is diffraction limited. Perpendicular to the grating the spatial resolution is limited by the propagation length of the mode within the grating. The propagation length is inversely proportional to the FWHM of the resonance such that increasing the spatial resolution of the grating leads to a corresponding decrease in the spectral resolution and consequently the detection sensitivity.

The asymmetry of the spatial resolution is due to the direction of the propagating mode. The resonant mode only propagates with the grating vector perpendicular to the grooves of the grating. The incident light has only a component normal to the grating vector, but is blurred by the resonant light propagating parallel to the grating vector. As there is no resonance propagating perpendicular to the grating vector, the spatial resolution remains limited by diffraction. The spatial resolution has been characterised by either etching away parts of the grating or by fabricating structures on top of grating using lithographic processes [127].

Depositing structures on top of the grating also allows investigation into the effect of the media refractive index on the spatial resolution. The refractive index contrast between the object being measured and the background media determines the spatial resolution [128]. If there is no contrast between the object and the media the resonance wavelength will be the same and therefore the object cannot be differentiated from the background media. The spatial resolution dependence on refractive index contrast was used for the imaging of 600 nm metal nanoparticles [129]. The high index contrast between the nanoparticle and the surrounding media allowed for imaging beyond the diffraction limit of conventional optical microscopy.

GMR based imaging is also known as photonic crystal enhanced microscopy (PCEM) where the resonance wavelength can provide greater image contrast compared to other microscopy techniques such as phase contrast microscopy. PCEM has been used for imaging cellular secretion as shown in figure 3.7, where the surface was functionalised with specific antibody enabling time course images of the secretion of molecules, here cytokines, from individual cells [126] [130]. PCEM has been also used for investigating antibiotic resistance in biofilms [131]. As the GMR senses 200 nm into the biofilm it is possible to detect if an antibiotic has disrupted the entire biofilm or just bacteria on the biofilm surface.

3.6.2 Evanescent Field Penetration Depth

The penetration depth of the evanescent wave into the media has been characterised by placing a lens on the surface of the grating [128]. At the centre of the lens, the resonance wavelength will be highest and then decay with the curvature of the lens until it returns to the resonance wavelength of the background. The penetration depth of the evanescent wave was shown to be approximately 200 nm. The penetration depth is dependent on the high refractive index of the lens ($n = 1.51$) however, for a biological material such as a cell the penetration depth will be lower due to cell's lower refractive index compared to the lens.

3.7 Comparison with Alternate Technologies

Understanding the sensitivity of a biosensing technology is critical for applying it to real world applications. For a photonic sensor there are two types of sensitivity that a pertinent to sensitivity, the bulk sensitivity and the surface sensitivity. The bulk sensitivity refers to the shift in resonance wavelength for a refractive index change of the entire media layer n_m, throughout the entire extent of the evanescent decaying mode (Eq. 3.6).

Experimental measurement of the bulk sensitivity is performed by recording the wavelength shift for solutions of increasing refractive index typically using solutions of glucose, ethanol, or NaCl. The shift in resonance wavelength is subsequently plotted as a function of refractive index and the gradient of the line of best fit gives the bulk sensitivity in nm/refractive index unit (nm/RIU). The limit of detection (LOD), the smallest refractive index change that can be measured, is evaluated by dividing the sensitivity by 3σ, where σ is the standard deviation of the resonance wavelength for the starting buffer (Eq. 3.7). The bulk sensitivity primarily serves as a measure of the potential performance as a sensor and is useful for comparing the performance of optical biosensor technologies.

$$S = \frac{d\lambda}{dn} \tag{3.6}$$

$$LOD = \frac{S}{3\sigma} \tag{3.7}$$

GMR resonance sensors have been demonstrated as having a refractive index LOD

of approximately 10^{-4} RIU/nm. Other photonic crystal technologies such as ring resonators, photonic crystals or bimodal waveguides routinely achieve LOD of 10^{-6} - 10^{-7} nm/RIU with the theoretical LOD being close to 10^{-9} RIU/nm [132]. Although the GMR LOD can be improved using interferometric approaches as discussed in section 3.5.3 this has only been demonstrated using free space optics, which is more complicated than than monolithically integrated sensors demonstrated using other photonic techniques.

Despite the apparent lack of optical sensitivity, GMR sensors have been used successfully for detecting protein, viral and bacterial pathogens at levels that are either at or approaching clinical relevance. A summary of some relevant examples is provided in table 3.1. The apparent contradiction between high biological sensitivity and low optical sensitivity is explained when considering that the sensitivity of the transducer is not the only element that is important in a biosensor. If the bioreceptors are not appropriately immobilised or the biofouling from unwanted biolmolecules is not controlled, the sensitivity of the assay will be poor regardless of the optical sensitivity.

Table 3.1: Clinically relevant targets measured using GMR sensors and the measured limit of detection.

Analyte	Concentration	Reference
Thrombin	190 nM	[133]
Cardiac troponin, Creatine kinase, Myoglobin	0.05, 0.1, 35 ng/mL	[134] [135]
β actin	255 ng/mL	[136]
Ryanodine receptor 3	<50 ng/mL	[137]
Staphylococcus aureus	10^3 CFU/mL	[138]
IgG	40 ng/mL	[123]
Glycosylated hemoglobin	5% total hemoglobin	[139]
HIV	10^4 copies/mL	[140]
Interleukin 1β	100 ag/mL	[141]
TNF α	5 pg/mL	[142]

3.8 Summary

In this chapter I have described the GMR structure and how it can be applied as a biosensor. I have introduced the physical origin of the resonance and its dependence on the material properties of the grating structure. The varying methods of fabricating a GMR sensor were discussed along with methods of measuring the change in resonance from a GMR sensor. Finally I have compared GMR sensors with other photonic biosensors and how the GMR remains a valid biosensing tool despite the

significant difference in optical performance.

Chapter 4

Fabrication and Experimental Methods

The fabrication and characterisation of the electrochemical GMR has been a significant aspect of this thesis. In this chapter I will describe the fabrication processes used for the EGMR in chapter 5 and the chirped EGMR used in chapter 6.

During my PhD I have made a number of contributions to the fabrication and measurement facilities at the University of York. On starting my PhD, the electron beam evaporator had numerous technical faults that rendered it unusable. During my PhD I have rectified all of these faults so that the machine now works reliably and have characterised the deposition of different materials such as Au, Ti, Al, ITO, Ni, Cr and Ge. I have also assisted with developing the photolithography protocols using the direct write laser system that was installed during my PhD which are being used by other members of the lab group. I have also constructed a new optical setup with the assistance of Dr Jose Juan-Colas and Dr Chris Reardon for performing hyperspectral imaging of GMR sensors and monochromatic imaging of chirped EGMR. The optical setup has also been recently used for elasticated resonator interferometric stress microscopy in collaboration with University of St Andrews.

The GMR design and fabrication parameters were initially optimised by Dr. Graham Triggs, with contributions also made by multiple members of the Photonics Group at the University of York. The "fan" chirped GMR design and fabrication parameters were optimised by Dr. Kezheng Li from the Photonics group, University of York.

4.1 Materials

4.1.1 Si$_3$N$_4$

Silicon nitride (Si$_3$N$_4$) is a high refractive index dielectric material ($n = 2$) with a negligible extinction coefficient within the range of visible light, making it an ideal material for photonic biosensors. Si$_3$N$_4$ has also been shown to have high biological compatibility and can be used with a number of surface chemistry modification processes such as silanisation for the covalent binding of antibodies or other antigen binding molecules [143]. Si$_3$N$_4$ is however electrically insulating with a resistivity of 10^{15} Ωcm so cannot be used on its own to make an electrophotonic structure [144]. Doping Si$_3$N$_4$ with Al during chemical vapour deposition has been shown to increase the conductivity, this however would likely require a significant re-optimisation of the GMR structure fabrication process as the underlying substrate has changed [145]. Instead creating a hybrid structure that retains the original Si$_3$N$_4$ grating with a conductive layer. A potentially alternative material is TiO$_2$, which due to have higher refractive index (2.6), can provide greater confinement of light with in the GMR structure and consequently improve the refractive index sensitivity.

Using Si$_3$N$_4$ had two practical advantages over using other materials. Firstly low surface roughness 150 nm thicknes Si$_3$N$_4$ is commercially available, removing the need to deposit the material ourselves prior to fabrication. Secondly the fabrication protocol for making GMR gratings using Si$_3$N$_4$ was also highly optimised so it was logical to take advantage of this existing knowledge within the group.

4.1.2 Indium Tin Oxide

Combining electrochemical measurements with photonics requires compromising between conflicting requirements. Electrochemistry is performed using highly conductive materials such as Au, Pt or glassy carbon. Photonic structures are fabricated from electrically insulating dielectric materials to minimise optical losses. A conductive photonic structure is a trade off between maximising conductivity for optimal electrochemical sensitivity while minimising optical losses for optimum operation of the photonic sensor.

Transparent conductive oxides (TCO) are compound semiconductor materials that have the unusual combination of both high visible light transmission and high conductivity. Indium tin oxide (ITO) is a heavily doped n$-$type semiconductor that is

widely used for optoelectronics in devices such as solar cells, light emitting diodes and touchscreen technologies [146]. ITO consists of a ternary mix of Sn, In and O_2 with a 9:1 In_3O_2:Sn being most widely used for deposition processes. ITO has a band gap of approximately 4 eV, making it transparent at visible wavelengths of light with transmission over 90%. The films are degenerately doped to a carrier concentration of $10^{20} - 10^{21}$ cm^{-3} with the Fermi level E_f being above the conduction band. ITO thin films have been shown to have resistivity as low as 10^{-4} Ωsq [147]. The electrical properties are highly dependent on the crystalline structure and thickness of the ITO film. Depositing TCO thin films is much more challenging compared to depositing metals as the deposition parameters have a large influence on the final quality of the film, and must be carefully optimised to achieve the best results. The material properties of ITO are primarily influenced by thickness, O_2 concentration, Sn dopant concentration, and the film crystallinity [148].

The incorporation of O_2 within the film is critical for high conductivity and optical transmission. The fabrication processes used for depositing ITO things typically remove O_2 from within the crystal structure of the film. A high concentration of O_2 within the material is necessary for the creation of O_2 vacancies [149]. The presence of O_2 vacancies is important for achieving high conductivity as they act as donors for the Sn dopant creating available energy states close to the conduction band edge E_c [150]. The O_2 concentration is also important for grain boundary formation, with higher O_2 concentrations in the film promoting larger grain boundary formation [151]. This assists optical transmission by reducing light scattering and increases conductivity by decreasing electron grain boundary scattering. To control O_2 concentration in the film, O_2 is leaked into the vacuum chamber to react with the depositing material. Without sufficient O_2 during the process, the films typically have a very dark brown colour and high sheet resistance. Deposition processes incorporating hydrogen using RF sputtering have shown to further increase conductivity compared to O_2 only deposition procesess [152].

It can be difficult to fully retain the O_2 required for high conductivity and optical transmission even when including O_2 in the deposition atmosphere. Furnace annealing has been widely used to increase the conductivity and optical transmission of ITO thin films [153]. Improvement by annealing in visible and near infrared transmission is thought to be due to the Moss-Burstein effect, where the lower energy states of the conduction band are filled effectively creating a larger band gap [154]. Annealing in temperatures of up to 500°C improves the ITO conductivity by releasing carriers from the Sn dopant [155]. The annealing can performed in a variety of different atmospheric conditions, including air, Ar, N, O_2, H or mixes of these gases. Rapid thermal annealing can be used in place of furnace annealing, where the

annealing process can be shortened from several hours to only a few seconds [156].

It has been previously shown that there is a non linear dependence conductivity with respective to the thickness in ITO films thinner than 60 nm [157]. The increase of conductivity with thickness is due to the improved crystallinity of the films, which reduces the number of grain boundaries.

ITO films can be fabricated using all of the common vacuum thin film deposition techniques including; electron beam evaporation, thermal evaporation magnetron plasma sputtering, plasma enhanced chemical vapour deposition and laser pulse deposition [158][159][160][161][162]. Optimisation of these processes can yield material characteristics that are all similar to each other in terms of conductivity and optical transmission. Sputtered films have been shown to have improved surface roughness however. Electron beam evaporation and plasma sputtering are the most widely used techniques for depositin g ITO films in the literature but this more likely represents the ubiquity of sputterers and electron beam evaporators instead of any quantitative improvement in ITO film quality compared to other processes. Solution based processes such as sol-gel formation of ITO thin films can also produce films of equal quality to that of vacuum based deposition systems [163]. These techniques are intended to reduce manufacturing costs compared to vacuum based deposition processes, but makes them incompatible with multi-layer film structures such as in solar cells.

ITO surface have been used for culturing both eukaryotic and prokaryotic cells, combining both optical microscopy and electrochemical techniques for analysis of cell growth and adherence, demonstrating that ITO films can be used for a wide variety of biological assays [161] [164]. The increasing scarcity of indium is driving research into new TCOs to bring down production costs. Aluminium zinc oxide is a popular alternative for replacing ITO in solar cells and has been shown to have a resistivity of 10^{-5} Ω/m when grown as monocrystalline material [165]. The thickness must be at least 200nm to achieve this resistivity however, making it unsuitable for use in the EGMR which is demonstrated in chapter 5.

4.2   Fabrication

A detailed understanding of the fabrication processes used in the fabrication of the EGMR is vital for achieving the optimal performance of the sensor. To summarise briefly, the EMGR is fabricated using electron beam lithography to pattern the pe-
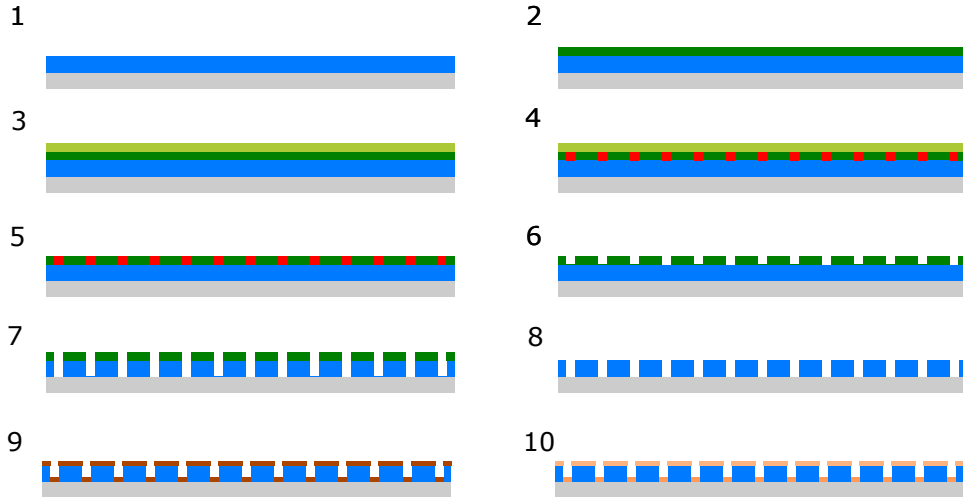
Figure 4.1: Fabrication process for producing the electrochemical GMR. 1) Clean Si3N4 substrate. 2) Spin coat ARP-13 3) Spin coat ARP-C 4) Electron beam exposure 5) Remove ARP-C 6) Develop exposed ARP-13 7) Etch structure with RIE 8) Remove remaining ARP-13 9) Deposit ITO using electron beam evaporation 10) Anneal ITO in furnace.

riodic structure into an electron sensitive resist layer. The GMR structure is then etched into the Si_3N_4 substrate using reactive ion etching. A thin film of ITO is deposited on to the GMR using electron beam evaporation then the sensor is furnace annealed to achieve maximum conductivity and transmission in the ITO film. The entire fabrication process of the EGMR is shown schematically in figure 4.1. The chirped EGMR used in chapter 6 uses the same GMR fabrication process for fabricating a chirped GMR, only the pattern written by the electron beam lithography system is changed. ITO electrodes are defined by photolithography using direct write laser lithography before using a lift off process to deposit the ITO thin film, shown schematically in figure 4.4.

4.2.1 Si_3N_4 Substrate Preparation (Step 1)

Wafers of 150 nm thick Si_3N_4 deposited by plasma enhanced chemical vapour deposited on to borosilicate glass substrate was cleaved using a Discodad wafer saw into 15 mm^2 pieces. The wafer was cleaned using O_2 plasma ashing for 10 minutes to remove any organic matter. To describe plasma ashing briefly, the sample is placed on the bottom aluminium plate in a vacuum chamber, which is vented to 0.2 mbar. O_2 is introduced into the chamber to pressure of 4 mbar, a 13.56 MHz voltage is applied across the top and bottom plates, causing ionisation of the O_2 within the chamber and ignition of a plasma. The activated species within the O_2 plasma break down organic chemical bonds such as carbon bonds, cleaning the sur-

face of the substrate. Plasma ashing is a safer alternative to piranha cleaning, a mixture of sulphuric acid and hydrogen peroxide, that is volatile in the presence of organic solvents such as acetone or propan-2-ol (IPA). After ashing, the substrate is cleaned by sonication for 3 miuntes in acetone followed by IPA to remove any residual particles then dried with N_2. The substrate is baked for 5 minutes on a hotplate at 90°C to dehydrate the surface.

4.2.2 Electron Beam Resist and Charge Dissipation (Step 2+3)

ARP 6900.13 electron-beam resist was spin coated on to the cleaned Si_3N_4 substrate at 5000 RPM for 60 seconds then baked for 7 minutes at 180°C. When exposed to a high energy electron beam the solubility of the exposed ARP regions will increase, allowing for selective removal of the exposed areas of resist using developers such as xylene.

Si_3N_4 has a high electrical resistance, which results in charging when exposed to an electron beam for scanning electron microscopy or electron beam lithography causing over exposure of SEM images or electron sensitive resists. To prevent this a charge dissipation layer is deposited on to the Si_3N_4. This was initially performed by thermal evaporation of approximately 20nm of Al using a Mantis Hex evaporator but was later changed to a spin coated conductive polymer. The first polymer to used was poly3,4-ethylenedioxythiophene-polystyrenesulfonate (PEDOT), which has been previously used as a charge dissipation layer for E-beam lithography [166]. It was found however that the PEDOT was difficult to remove reproducibly and its optical transparency made it challenging to identify when it had been removed. The charge dissipation layer was changed to AR-PC 5090, which is removed by soaking in DI water for 3 minutes. The substrate is a noticeably different colour with and without the AR-PC layer, giving a clear indication when the layer has been removed correctly. Using a spin coated charge dissipation layer simplifies the fabrication process compared to using the thermal evaporator with a negligible increase in charging compared to the Al thin film.

4.2.3 Electron Beam Lithography (Step 4)

Electron beam lithography (EBL) is a direct write nanofabrication technique used for maskless patterning of devices into electron sensitive resist layers. Similar to

scanning electron microscopy, EBL takes advantage of the decreased wavelength of high energy electrons to go beyond the diffraction limit of optical lithography. A 50 kV electron source is used to generate the electrons, which are focused on to the sample using an electrostatic column. The position of the beam can be steered using the electrostatic column for directly writing the pattern into the sample. The beam current is controlled by the aperture, which also controls the spot size of the beam.

The resolution of EBL is not limited by the wavelength of the electrons or by the optics used to focus the beam, but is instead limited by the interaction of the electrons with the resist layer. Exposure of the resist is due to the incident electrons and the secondary electrons generated by the incident electrons as it enters the sample. The forward scattering due to the incident electrons is low at the high electron energies used in EBL and is not considered a factor in the exposure. The scattering from the secondary electrons is significantly higher however, leading to the widening of the exposed areas. The resolution is also dependent on the step size of the write which is the distance the beam will be moved before exposing the next spot. A high step size means less spots will be used, lowering the resolution but increasing the write speed. Another important effect is the proximity effect, where due to electron scattering the pattern at the centre will receive a higher dose than at the edges. This is effect is reduced by the EBL software itself and is also not as important for a 1D structure such as the GMR as the edges of the GMR have a negligible contribution to the total reflectance.

The beam dose is the amount of electrons per area that the sample is exposed to, expressed in $\mu C/cm^2$. The dose is defined by the user using the beam current and the exposure time to give the intended beam dose. The dose is also affected by the material properties of the sample and the electron scattering. Too low a dose will result in underexposed features so the resist layer will not be cleared after development. Too high, and small features will be destroyed as all of the resist around the features is exposed along with the intended area. Each new sample requires optimisation to find the dose required for the sample material and feature size. I performed these optimisation experiments for attempting to fabricate the GMR gratings into ITO and silicon on sapphire substrates, but ultimately did not use these substrates for the work presented in this thesis.

The geometry of the GMR structure was optimised previously by Dr. Graham Triggs to give a resonance wavelength of 850 nm using a 550 nm period grating with an 0.7 filling fraction and a 150 nm thickness of Si_3N_4. The EBL parameters used here were optimised by other members of the group.

A 1 mm^2 GMR structure was patterned into the ARP-13 layer using a Voyager electron beam lithography system using a 130 μC base dose, a beam current of 0.7nA and a step size of eight nm. The Voyager system has a direct write field area of 500 μm^2, so a 1 mm^2 grating is "stitched" from four 500 μm^2 write field areas. This can cause errors in the write where the four sections do not match up exactly, leaving a small but noticeable gap in between the sections, but this does not have any noticeable effect on the GMR performance. Due to the experimental variability in producing the resist films for exposure, multiple copies of the GMR are written into the same substrate at increasing doses in steps of 10% from the base dose. Having this range of structures provided greater confidence that a successful GMR structure would be made from each write.

The chirped EGMR structures used in chapter 6 were patterned into the ARP-13 layer using a base dose of 130 μC using a 0.045nA beam current. An asymmetric step size of 0.5 nm by 4 nm is used to maximise the period resolution while minimising the total write time. Following exposure, the substrate was immersed in room temperature DI water for three minutes to remove the ARP-C charge dissipation layer. The exposed ARP-13 was developed for two minutes in xylene, creating the GMR structure within the exposed ARP-13 resist layer. The excess xylene was removed first using DI water then by quickly rinsing in IPA and drying with N$_2$.

4.2.4   Reactive Ion Etching (Step 5-8)

Reactive ion etching is a vacuum dry etching technique that uses a combination of physical and chemically selective etching processes to remove material from the substrate. The etching mechanism is a chemically reactive plasma which is ignited using a 13.56 MHz RF power supply from gases leaked into the vacuum chamber as shown in figure 4.2. The physical etch is caused by ionised particles bombarding the surface of the substrate, giving a highly uniform anisotropic etch across the substrate. Chemical etching occurs when reactive species in the plasma form volatile compounds with the substrate giving a selective but isotropic etch. Fabricating a GMR grating using purely physical etch would result in sharp walls of the grating but significant surface roughness as the masking resist would also be removed by the etch. A purely chemical etch would mean only the Si$_3$N$_4$ would be etched but the walls of the GMR structure would be rounded. By varying the pressure and RF power within the RIE chamber, the balance of physical to chemical etching can be controlled to achieve selective anisotropic removal of the substrate.

Prior to etching the RIE was cleaned using an O$_2$ plasma with a 500V DC bias
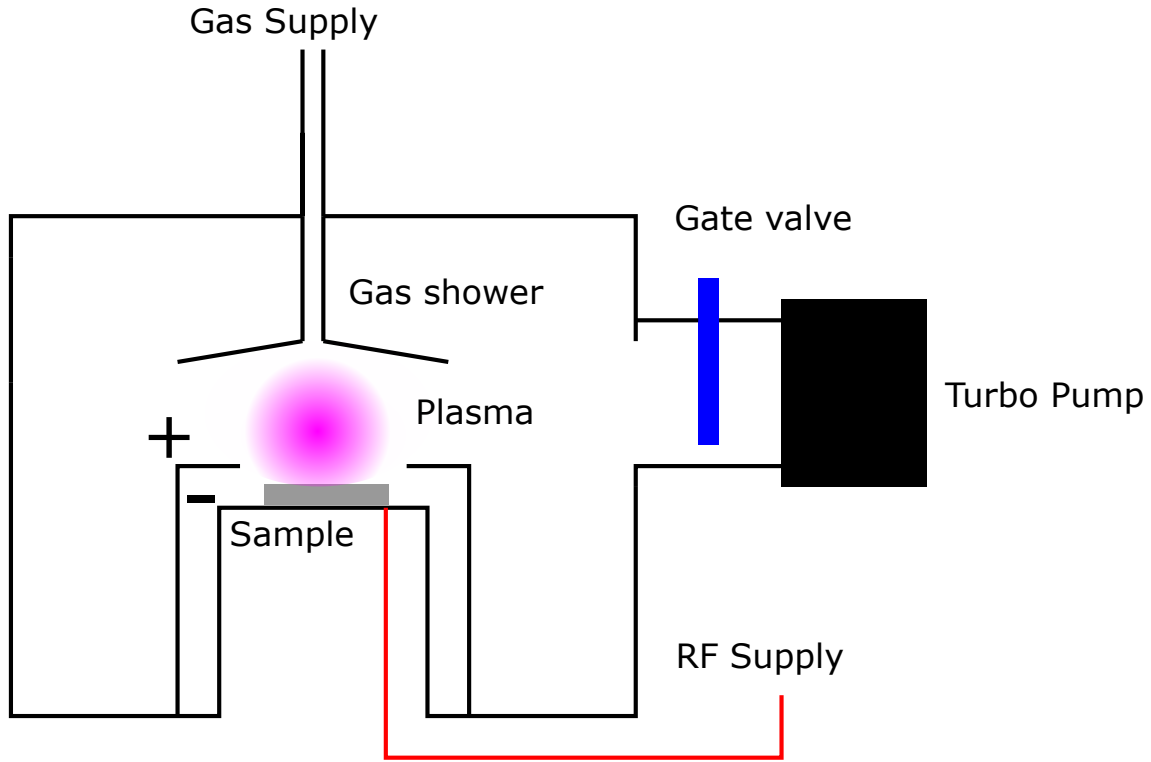
Figure 4.2: Schematic of the reactive ion etching system. The sample is placed on a carbon stage that is biased by the RF power supply. Gas for the plasma can be injected by the gas shower to ensure an even coverage of gas across the sample. The atmospheric pressure is controlled by the adjustable gate valve.

at 1.9×10^{-1} mbar for five minutes to remove any impurities from previous etches. The GMR structure was etched into the Si_3N_4 using a 29:1 ratio of CHF_3: O_2 at 4.8×10^{-2} mbar for seven minutes. Maintaining a DC bias voltage of 340V during the etching process gives an etch depth of 150 nm at an etch rate of approximately 21 nm/minute. The remaining ARP-13 resist layer was removed by two minutes sonication in 1165 microposit remover followed by acetone, IPA then dried with N_2.

4.2.5 Electron Beam Evaporation (Step 9 -10)

Electron beam evaporation is a physical vapour deposition technique used for depositing metal and dielectric thin films, shown schematically in figure 4.3. The target material is placed inside a crucible and bombarded with electrons from a heated tungsten filament. The electrons are steer from the filament on to the material by using an electromagnetic field. A second electromagnetic is then used to modulate the position of the electron beam within the crucible to ensure even heating of the material. The heated material will then begin to evaporate and deposit on to the substrates which are held above the crucible on a substrate holder. Unlike
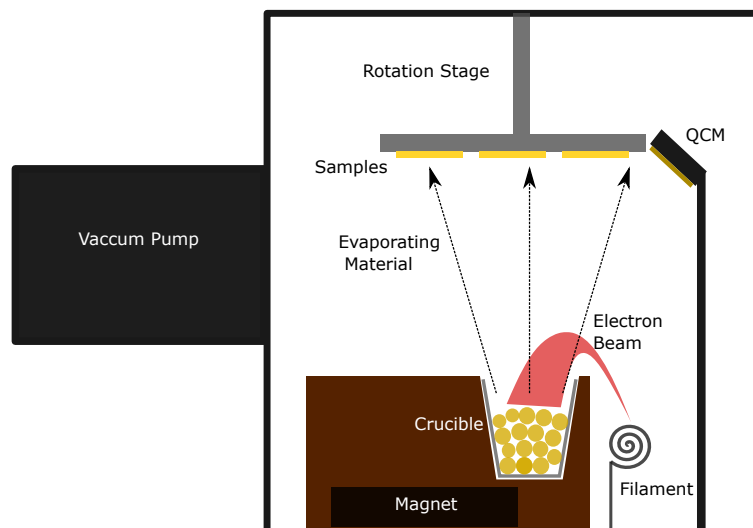
Figure 4.3: Schematic of the electron beam evaporation system. Electrons from the filament are guided on to the material in the crucible. The heated material evaporates on to the samples that are suspended above the crucible on a rotating stage. The thickness of the films is measured by a QCM sensor next to the stage. A shutter is placed in front of the rotation stage when the desired thickness of material has been reached to prevent further material deposition.

thermal evaporation, it is not typically necessary to melt all of the material within the crucible for evaporation or sublimation to begin, meaning that deposition of materials with high metal temperatures such as Ti or Ni can be achieved more readily and at lower power compared to thermal evaporation. The target substrates are typically placed on a rotating stage for even deposition of material across the entire substrate holder. Electron-beam evaporation is typically performed in high vacuum, at pressures less than 10^{-5} mbar. Gases such as O_2 or N_2 can be introduced during the evaporation process for reactive deposition.

A custom MBraun electron beam evaporation system was used for deposition of the ITO thin films. The system consists of a SmartBeam 10 kV electron beam source and a six crucible rotating hearth. A BeamTrek evaporation controller is used to control the electron beam source power and for modulating the position of the beam. An Inficon SQC-310 deposition controller is used for controlling deposition processes, which provides fully automated control over the initial rise and soak times, deposition rate and final thickness.

ITO deposition was performed using In_2O_3-SnO_2 90-10wt% pellets from Testbourne. Optimisation of the ITO deposition parameters is discussed in chapter 5. After deposition the films were annealed in an O_2 atmosphere at 400°C for one to three hours. Au and Ti pellets for fabricating contacts for Hall effect measurements in chapter 5 were also purchased from Testbourne.

4.2.6 Photolithography

Photolithography is a nanofabrication process that uses UV light to selectively pattern a light sensitive resist layer. The most basic form of lithography is to use a shadow mask of the pattern which is placed in contact with the substrate and illuminated with UV light. The exposed resist will be cross-linked by the UV light and becomes insoluble in the developer, while the unexposed areas will be washed away by the developer. Masks can be either be etched into chrome or deposited on glass or plastic film. Contact photolithography using a chrome based mask is diffraction limited to 0.5 μm, however chrome masks are expensive and so plastic film masks are often used in research settings. The achievable resolution using contact based photolithography using a plastic film mask is approximately six μm, which is limited mainly by the spatial resolution used for printing of the plastic film mask. In semiconductor industry, contact based photolithography has long been superseded by techniques such as projection masking combined with deep UV light sources to achieve the seven nm feature resolution needed for modern microprocessor architectures.

Direct write photolithography uses a laser to expose the pattern in the resist, similar to electron beam lithography. While this is slower than masked based lithography, which exposes the whole sample at the same time, it does allow for rapid prototyping of different designs without the requirement of fabricating new masks for each design.

The Dilase 650 direct write laser system (Kloe) uses fixed beam moving stage configuration, where the sample is moved through the laser beam by an automated XY stage. The laser is modulated using pulse width modulation to change the laser power incident to the sample. The power can also be coarsely tuned by using optical filters at the laser output. The dose exposed to the sample is a function of the power modulation of the laser and the speed at which the stage is moved. The Dilase 650 has two beam lines giving a 10 μm and 0.5 μm beam spot, which can be further changed by using different magnification objectives and focal positions.

The writing time is also influenced by the stage overshoot. For scanning through a design the stage must move back and forth repeatedly. Reversing direction however requires arresting the forward momentum and accelerating the stage back to the desired movement speed. If this was performed within the boundaries of the pattern it would mean that the stage speed is not constant during writing. To solve this the stage moves further past the edge of the design before changing direction so that the stage can reach the required speed when the sample passes back through the laser. This leads to the majority of the stage movement not being used for
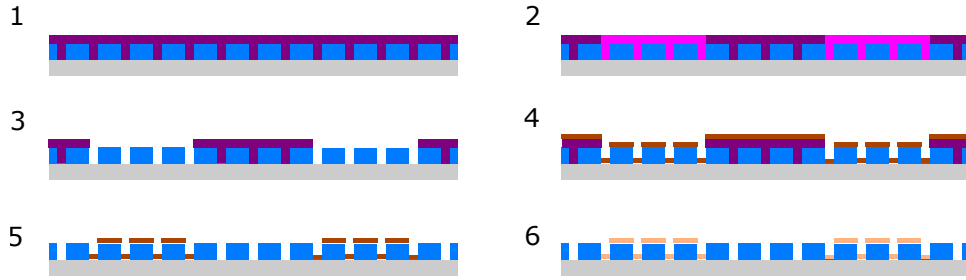
Figure 4.4: The photolithographic process for producing ITO electrodes on to the chirped GMR. 1) Spin coat S1811 2) Expose structure using direct write laser lithography 3) Develop resist with MF-319 4) Deposit ITO using electron beam evaporator 5) Lift off resist using acetone 6) Anneal ITO using a furnace.

writing of the pattern into the resist. Shortening the overshoot distance can reduce the writing time by reducing the total stage movement. This parameter was not optimised as the total write time for each of the structures used in chapter 6 was only 30 minutes, but for a sufficiently large design this could significantly reduce the overall write time.

Optical lithography was used for patterning the ITO electrodes on top of the ECGMR. The minimum feature size of the electrodes was 70 μm, well within the resolution limits of direct write laser lithography system. A GMR sensor fabricated using the process described in figure 4.1 was spin coated with S1818 photoresist at 6000 RPM for a film thickness of 1.6 μm. The resist was baked at 115°C for 60 seconds (Figure 4.4 1). For aligning the electrodes on to the GMR, alignment markers were included in the GMR design and etched into the Si_3N_4 during the RIE etching step. The electrode array was designed using the Kloe design software. The electrodes were exposed using a 385 nm laser with a 1 ND filter, 100% PWM at a stage speed of 9.5 mm/s (Figure 4.42). A x10 Olymypus objective was used to give a spot size of 10 μm.

After exposure the resist was developed for 90 seconds in microposit MF-319 developer. The substrate was dipped into clean MF-319 and then DI water to remove residual resist before drying with N_2. Plasma ashing using an O_2 plasma for five minutes was used for the removal of remaining resist after development in a process known as "descumming". Descumming assists the removal of undeveloped resist or resist that has resettled back on to the substrate when removing from the developer (Figure 4.4 3). ITO was deposited using electron beam evaporation described in section 4.2.5 (Figure 4.4 4). After deposition the unexposed resist was removed by soaking overnight in acetone and then briefly sonicating to remove any residual resist (Figure 4.4 5). The sample was then annealed using the annealing process described in section 4.2.5 (Figure 4.4 6) to give the completed ECGMR structure.

4.3 Rigorous Coupled-Wave Analysis

Rigorous coupled wave analysis is a semi-analytical computational method used for calculating diffraction efficiency in periodic structures. A structure is defined as number of separate layers each with their own complex permittivity and thickness. Simulation of a GMR sensor consists of three layers, the glass substrate, the periodic dielectric and the media. The glass substrate and the media have an infinite thickness while the dielectric thickness, period and filling fraction are defined as a user input. For a one dimensional grating the periodicity is considered to be infinite. The polarisation, incidence angle and wavelength of the incident can also be defined by the user as inputs.

To describe the method briefly, the electric field is calculated for each layer. For the glass substrate the total electric field is the incident light plus the reflected light from the structure. For the media layer the electric field is the transmitted light from the structure. The periodic permittivity of the grating region is described as a Fourier series expansion. By establishing boundary conditions between the layers, Maxwell's equations can be solved as coupled wave equations to give the reflectance and transmittance. The spectral response of the grating can be calculated by solving the electric field distributions at varying wavelengths in the spectra wavelengths. The full mathematical derivation of RCWA and its application to periodic grating structures has been described by Li [167].

All of the RCWA simulations in this thesis were made using the S^4 solver [168]. S^4 can be used for solving both one and two dimensional photonic structures. The main advantage of using RCWA over other methods such as finite difference time domain modelling is that the simulations less demanding in computational time with equivalent accuracy [169].

4.4 Optical Measurements

Two different optical measurement systems were used to measure the optical performance of the EGMR biosensors; a broadband white light measurement using a spectrometer, and a hyperspectral imaging system using a tunable monochromatic light source and a camera.
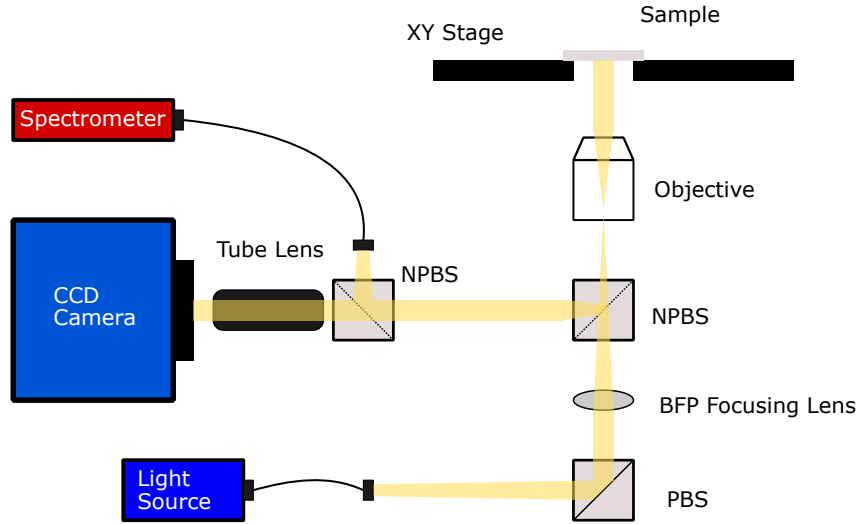
Figure 4.5: Schematic of the optical setup for measuring EGMR reflectance using white light.

4.4.1 Whitelight Reflectance

The simplest measurement of the GMR reflectance is to use a polarised white light source with a spectrometer as shown in figure 4.5. The output of a tungsten halogen light source (Ocean optics) is coupled using a fibre coupler into the optical system, resulting in collimated light needed for optimal GMR reflectance. If the light is not collimated other modes can be excited within the GMR structure, reducing resonance efficiency. The collimated light is S polarised by the polarising beam splitter (PBS). The incident light must be focused on to the back focal plane (BFP) of the objective to ensure that as much of the light as possible is collimated once it reaches the GMR surface. The sample is placed on a manually adjustable stage with XYZ control for alignment and focus. The tilt of the stage can also be adjusted to optimise the angle of incidence on to the GMR. The reflected light from the GMR is directed to the camera and spectrometer using a pair of non polarising beam splitters (NPBS).

Imaging of the GMR for alignment with in the incident was performed using a Cool-Snap Myo CCD camera (Photometrics) and the reflectance spectra was measured using a CCS175 spectrometer (Thorlabs). An Olympus X10 (NA = 0.25) objective was used for all of the experiments. Prior to each experiment a mirror reference was taken to the normalise the GMR reflectance.
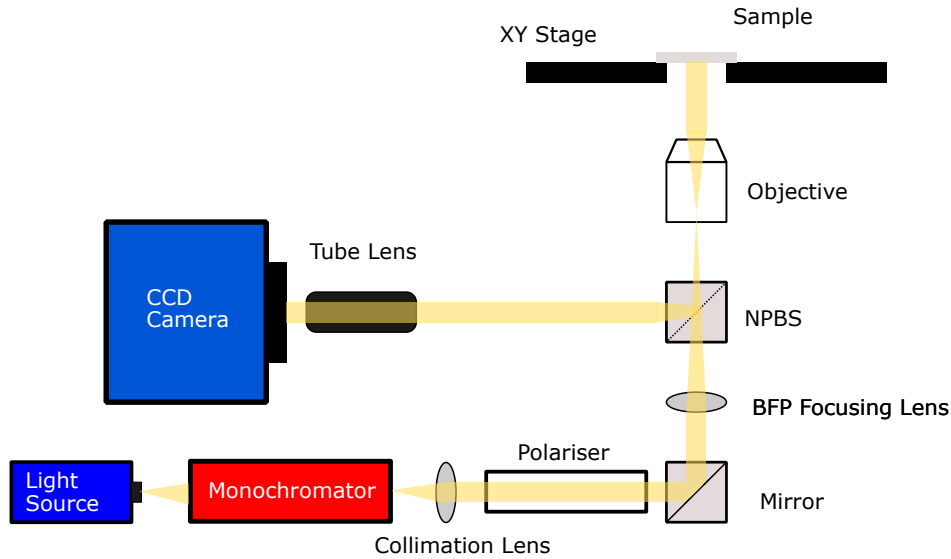
Figure 4.6: Schematic of the optical setup used for performing hyperspectral imaging and single wavelength measurements of the ECGMR.

4.4.2 Hyperspectral Imaging and Chirped GMR

For hyperspectral imaging of the GMR it is necessary to use a tunable light source to vary the illumination wavelength and then image the reflectance intensity with a CCD camera. Taking an image at each illumination wavelength produces a hyperspectral cube of reflectance for each incident wavelength. A hyperspectral image of the resonance wavelength across the grating can be generated by plotting the wavelength of maximum intensity for each pixel. The spectral resolution of hyperspectral images produced by plotting maximum intensityis limited by the spectral step size of the monochromator. Greater spectral resolution can be achieved by the applying the Fano equation, discussed in detail in chapter 5 per pixel across the entire hyperspectral image. A per pixel fit across hypersecptral cube currently has computational overhead so a region of interest (ROI) is defined to reduce the computational time.

In the first measurement setup used, the tunable illumination was performed using a custom built monochromator consisting of a diffraction grating mounted to a rotating stage where the first order diffracted was coupled into an optical fibre output. Due to the physical path length of almost 2 m this monochromater did have good spectral resolution (FWHM 1 nm) The use of the rotation stage meant that acquiring a hyperspectral cube consisting of 160 wavelengths from 830 - 870 nm at 0.5 nm steps would take several minutes.

During my PhD I assisted in constructing another measurement setup which has several advantages over the previous system shown in figure 4.6. First, Digicrom
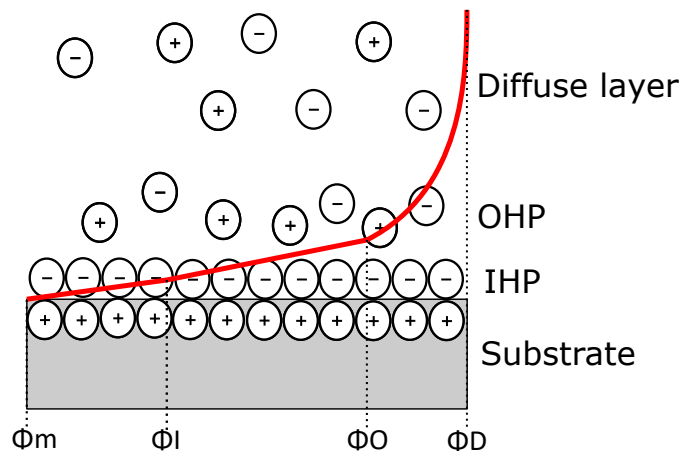
Figure 4.7: The electrochemical double layer that forms at a metal solution interface from ions in the solution. The electrochemical potential σ is shown in red and changes linearly across the inner Helmholtz plane (IHP) and outer Helmholtz plane (OHP) then decreases exponentially into the diffuse layer.

CM 110 Czerny-Turner monochromator using a 125 μm slit width was used to give a 1nm FWHM monochromatic light source but with a decreased physical pathlength. Second, the fixed polarising beam splitter has been replaced with a rotatable Glan-Thompson polariser to allow greater control over the polarisation. Finally the manual mechanical stage has been replaced with an automated stage, giving finer Z control for focusing the incident light and to allow the possibility of automated stage movements to measure multiple samples at once. The hyperspectral acquisition time was greatly improved compared to the original measurement setup, with the integration time of the camera now being the rate limiting step as opposed to the time required to move rotation stage.

The hyperspectral imaging set up was also used for measuring the ECGMR in chapter 6. The monochromator is set to a single wavelength to provide a constant monochromatic incident light source.

4.5 Electrochemical Measurements

4.5.1 Electrochemical Double Layer

The electrochemical double layer is a layer of ions that forms at a metal solution interface. There have been a number of theoretical models to explain the formation of this layer. The most basic is the Helmholtz model which assumes that when immersed in liquid the surface charge of the metal attracts ions of the opposite

charge towards the surface. A perfect layer of ions is formed at the metal surface to neutralise the surface charge known as the inner helmholtz plane (IHP). Counter ions are subsequently repelled from the surface by the formation of this layer The distribution of charge across the interface is exactly the same as a parallel plate capacitor and can be treated accordingly. The electrical potential therefore decreases linearly from the metal σ_m to the edge of the IHP σ_I

The Helmholtz model assumes that the ions at the surface are fixed when in fact they can diffuse throughout the solution. The Gouy-Chapman model describes the double layer as a diffuse cloud of ions at the metal solution interface. The concentration of the ions decreases further from the metal solution interface. The electrical potential decreases exponentially due to the decrease in ion concentration away from the metal surface. The Stern modification of the Gouy-Chapman model firstly treats the ions as having a finite size. Secondly it allows ions to be adsorbed on to the metal surface similar to the Helmholtz model known as the Stern layer. In terms of electrical potential there is a linear change in potential across the IHP and OHP and then an exponential decrease in potential in the diffuse layer σ_d.

4.5.2   The Electrochemical Cell

The most basic electrochemical cell consists of two electrodes, a working electrode and a reference electrode. The electrochemical reaction takes place at the surface of the electrode. The reference electrode holds a constant voltage to which the working electrode voltage. The difficulty of the two electrode system is that the reference voltage cannot be maintained when current flows from the working to reference electrode. The reference voltage has to change and so the measurement of the working electrode voltage is inaccurate.

The three electrode cell introduces a counter electrode. The flow of current in the cell goes from the working to the counter electrode. The reference voltage can now be maintained giving an accurate measure of the working electrode voltage. The three electrode system is also known as a "half cell" as the change in potential at the counter electrode electrode does not influence the measurement of the working electrode.

Working electrodes are made of inert materials such as Au, Pt, glassy carbon or ITO. Pt wire is a common counter electrode material as it can be easily shaped to fit any electrochemical cell. A standard reference electrode used for biosensing is the Ag/AgCl reference electrode. The reference consists of a Ag wire that has been

coated in AgCl and is housed in a KCl containing glass vial to maintain the AgCl concentration on the surface of the wire. A porous membrane allows access to the solution being tested to complete the electrochemical circuit. The drift of a double junction Ag/AgCl reference electrode will be in the order of a few millivolts over a period of several days.

The experiments in this thesis were all performed with a Ag wire pseudo reference. The pseudo reference was used as it is significantly smaller than a standard Ag/AgCl reference which made integration of the electrodes into the experimental setup simpler. Although not as stable compared to a Ag/AgCl reference the drift over 1 hour is less than 10mV. As the experiments were performed for less than an hour and the magnitude of the voltage change was hundreds of millivolts, the Ag wire is stable enough for this measurement [170]. The miniaturisation of reference electrodes is a very active area of research, there are a number of alternatives including AgCl coated wires or Ag/Ag_2SO_4 coated wires which have greater longer term stability compared to Ag wires [171][172][173].

Electrochemical measurements are performed using a potentiostat. The potentiostat controls the working electrode voltage with respect to the reference electrode and measures the respective current. Electrochemical measurements in this thesis were performed with a Biologic SP 300 and 200, the only difference between the instruments is that the SP 300 has two sensing channels.

4.5.3   Cyclic Voltammetry

Cyclic voltammetry (CV) is the most common electrochemical method of investigating redox reactions. Starting from the open circuit voltage V_{OC}, the bias voltage is first increased to voltage V_1 at a rate of x mV/s. The voltage then scans to V_2 and then back to V_{OC}, the absolute values of which are chosen to be greater than oxidation and reduction potential of the molecule of interest. The measured current in CV measurement is due to two processes; the non faradaic current which is due to the electrolyte ions in the solution and the faradaic current which is the generated by stimulating a redox reaction. Assuming that the solution is unstirred; the movement of a redox active molecule is limited by diffusion.

A schematic of a cyclic voltammogram is shown in figure 4.8, when the scan first begins the only current will be due to the non faradaic current i_{dl}. As the voltage reaches the reduction potential E_{pc} the magnitude of the current will increase to i_{pc} as electrons are gained by the molecules at the electrode surface. This creates a
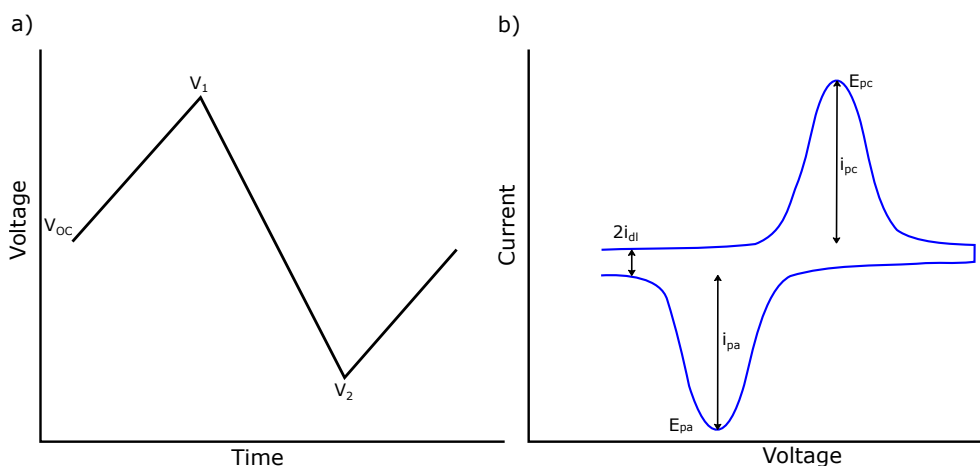
Figure 4.8: **a)** Voltage waveform for a CV measurement. **b)** CV plot of a fully reversible redox reaction.
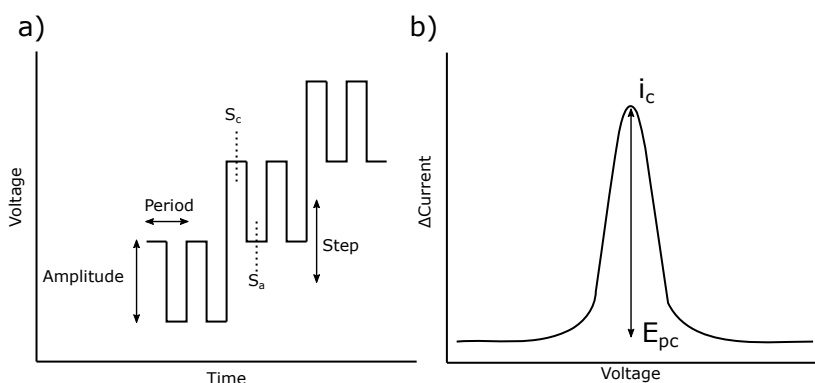
Figure 4.9: **a)** Voltage waveform for a SWV measurement. **b)** SWV plot of a fully reversible redox reaction.

diffusion layer of reduced molecules that prevents further diffusive transport of non reduced molecules towards the sensor. Electron tunnelling from the electrode to the solution is prevented, decreasing the measured current back to the non faradaic component. When the voltage is reversed back to E_{pa}, electrons tunnel from the reduced diffusion layer back to the electrode the resulting in the second peak i_{pa}.

Increasing the scan rate leaves less time for the diffusion layer to accumulate and therefore the peak oxidation and reduction currents will be higher, varying the scan rate can also be used to shown if the redox molecule is moving freely in solution or has been adsorbed on to the electrode surface: the peak current will be linear with the root of the scan rate for freely diffusing molecules.

4.5.4 Square Wave Voltammetry

CV is a powerful tool for analytical electrochemistry, but it is limited in terms of sensitivity by the capacitive background current i_{dl}. When the redox active molecule concentration is very low or the ion concentration of the media is very high, i_{dl} can mask the faradaic current due to the redox reaction so the CV peak cannot be determined. Square wave voltammetry (SWV) overcomes this limitation allowing for measurements at lower redox molecule concentration and at faster scan rates than CV. SWV is used extensively in electrochemical biosensors for these reasons

SWV uses a staircase voltage with a square wave superimposed on top of the staircase as shown in figure 4.9a. The amplitude of the square is typically tens of millivolts. The current is sampled at the points S_c and S_a of the square wave at each point in the staircase. Plotting $S_c - S_a$ against the applied staircase voltage gives the SWV voltammogram profile. When the staircase voltage is far from the reduction potential of the redox molecule the difference in the current at the top and the bottom of the square wave should be effectively zero, as the current is only due to the movement of the electrolyte ions that are able to freely move towards and away from the electrode surface. As the staircase voltage approaches the reduction potential, the redox molecule will be reduced at the top of square wave, generating faradaic current. There will be no faradaic current at the bottom of the square wave as the redox molecules have already been reduced. The difference between S_c and S_a is now no longer zero, resulting in a peak current proportional to the concentration of the redox molecule shown in figure 4.9b. Reduction of the redox molecule at the electrode forms a diffusion layer the same as when performing CV, preventing further electron transfer so Δi returns to zero.

The effective suppression of the non faradaic current results in greater sensitivity to lower concentrations of the redox active molecules compared to what can be achieved with CV. The complexity of the applied voltage does however make it more difficult to extract quantitative information from the voltammogram profiles compared to CV.

4.5.5 Electrochemical Impedance Spectroscopy (EIS)

The measure of a material's opposition to electrical current is known as its resistance which for direct current (DC) through an ohmic material is described by Ohms law $V = IR$. Ohms law can be then generalised to alternating current (AC) periodic
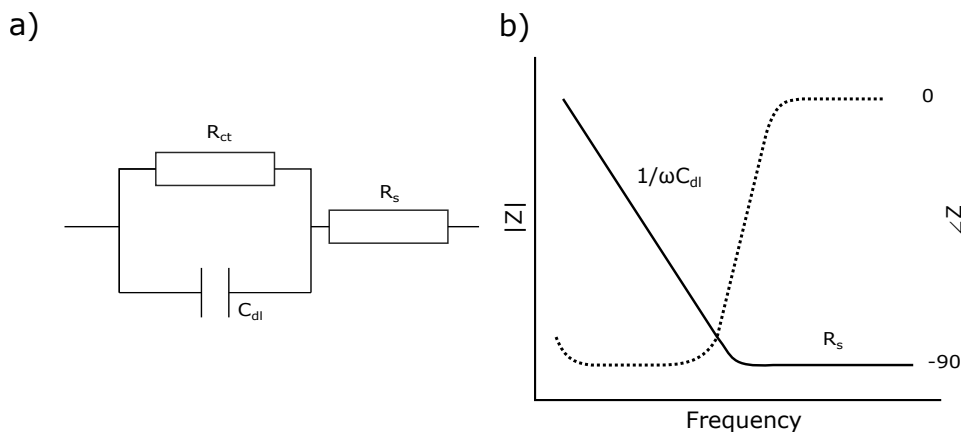
Figure 4.10: **a)** Circuit diagram of the simplified Randle's circuit. **b)** Bode plot of the simplified Randle's circuit.

signals, where the opposition to current is known as the impedance Z and can be represented in the complex expression $Z(\omega) = R + jX(\omega)$, where $\omega = 2\pi f$, R is the resistance, X is the reactance and j is $\sqrt{-1}$. Reactance can either be due to inductance or capacitance. Inductance is rarely seen in electrochemical systems therefore any reactance is due to capacitive elements. As the reactance is frequency dependent, a measure of impedance must be made using multiple frequencies to produce a "footprint" of the the system under test.

The value of the impedance can be calculated by measuring the output current I_{out} with respect to a known input voltage V_{in} as shown by equation 4.1 which illustrates that the impedance has two components $\frac{V_{in}}{I_{out}}$ which is known as the magnitude and ϕ which is the phase angle. In terms of measured signal the magnitude is the quotient of either the peak or RMS voltage and current while the phase angle in degrees is $360 \times \Delta T$,where ΔT is the difference in time between the peak voltage and peak current. In the case of a purely resistive load, the peak voltage and current are simultaneous, giving a phase angle of 0°, which reduces equation 4.1 to simply $\frac{V}{I}$, Ohms law for DC signals. For a purely capacitive load, the phase angle will be -90°.

$$Z(\omega) = \frac{V_{in}sin(\omega t)}{I_{out}sin(\omega t + \phi)} \tag{4.1}$$

The impedance of the interface between a metal electrode and a solution can be modelled in its most basic form by standard electrical components as shown in figure 4.10, where R_s is the solution resistance, R_{ct} is the charge transfer resistance and C_{dl} double layer capacitance. The parallel combination of the R_{ct} and C_{dl} is known as the simplified Randle's cell, more complex versions can include components known as constant phase elements (CPE) such as the Warburg impedance. These are used to account for the non perfect capacitive behaviour of the electrochemical behaviour

63

and effect charge transfer due to diffusion rather than electron transport.

$$Z = R_s + \frac{R_{ct}}{1 + j\omega R_{ct} C_{dl}}$$ (4.2)

The measured magnitude and phase can be fitted to the circuit in figure 4.10a and plotted on a Bode plot shown in figure 4.10b. An important assumption of Ohms law is that there is a linear relationship between the magnitude of the voltage and current. This however only occurs for very small voltages in an electrochemical system, which is known as pseudo linearity which means that the input voltage typically has an amplitude of 1 - 20mV.

Chapter 5

Characterisation of the Electrochemical Guided Mode Resonance Biosensor (EGMR)

Electrochemical and photonic biosensors have fundamentally opposite requirements. An electrochemical biosensor should be made from highly conductive materials to maximise electron transfer where as a photonic biosensor is ideally made of a loss-less dielectric material to reduce optical losses that will negatively affect the device resonance condition. An electrochemical photonic biosensor must balance these two opposing requirements to give maximum sensitivity for both modalities. This chapter discusses the development of the electrochemical GMR (EGMR) sensor which consists of a Si_3N_4 GMR grating coated with an ITO electrode shown schematically in figure 5.1.First the deposition of ITO thin films using electron beam evaporation is optimised. A theoretical study of the effect on the ITO layer on the GMR is then presented. The properties of the GMR resonance are quantified and the effect of applied bias voltage to the resonance wavelength is explored. The optical and electrical sensitivity is then quantified. Finally, optical electrochemical measurements of the redox active molecule performed in parallel using the EGMR are demonstrated.
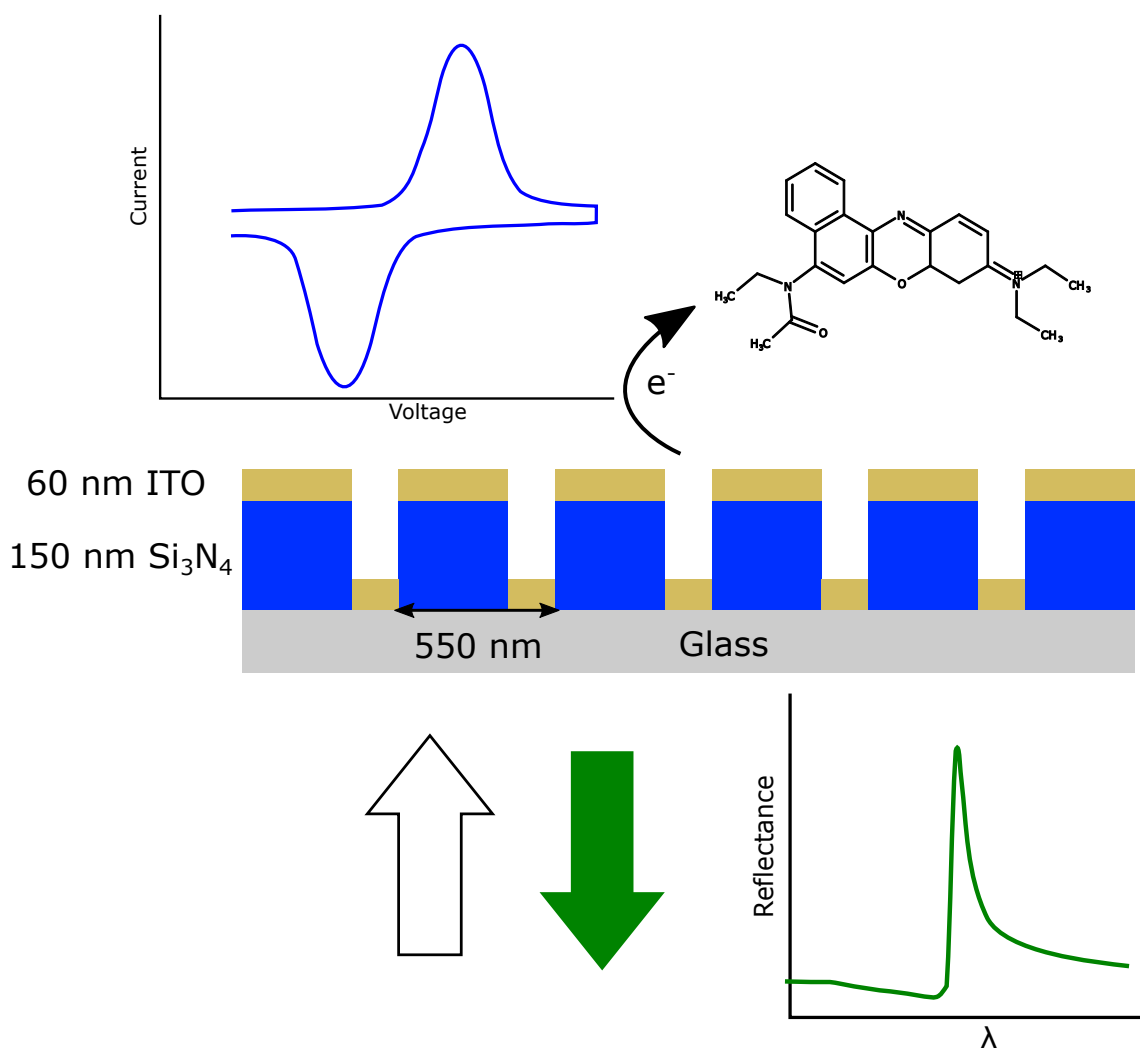
Figure 5.1: Schematic of the EGMR structure developed during this chapter. The GMR grating is fabricated into 150 nm thick Si_3N_4 layer deposited on to a glass substrate with a period of 550 nm an 80% filling fraction. 60 nm of ITO is deposited on top of the grating using electron beam evaporation to form a working electrode. The fabricated device allows for parallel electrochemical measurements and optical measurements, for example the measuring electrochemical and refractive index properties of a redox active molecule.

The SEM images in section 5.3 were acquired with the assistance of Dr. Casper Kunstmann.

5.1 Characterisation of Indium Tin Oxide Thin Films Deposited by Electron Beam Evaporation

Two deposition processes were available for the deposition of the ITO thin films, electron beam evaporation or DC magnetron sputtering. As discussed in chapter 4, there is little difference in terms of optical transmission and sheet resistance between the two techniques, though sputtered films are reported as having the lower surface roughness, electron beam evaporation was primarily used because it had an automated deposition controller, which would improve the repeatability of the film deposition.

Compared to other deposition techniques such as a sputtering, electron beam evaporation also has comparatively few parameters to optimise. The parameters that can be changed are: the electron beam voltage, the deposition rate and the O_2 concentration. The beam voltage was kept constant at 8 kV and the deposition controller was used to set a deposition rate of 0.5 Å/s for all of the films presented in this work.

5.1.1 Optimisation of O_2 Concentration

The O_2 concentration during deposition is the most important parameter for both the optical and electrical characteristics of ITO thin films. Borosilicate glass substrates were cleaned by UV ozone cleaning for 30 minutes then sonicated for 10 minutes in 2% Hellmanex followed by 17 MΩ DI water then ethanol. After sonication the glass wafers were dried using N_2. To optimise the O_2 concentration I initially deposited 100 nm thick ITO films at 5, 7.5, and 10 standard cubic centimeters per minute (SCCM) of O_2. After deposition the films were all dark brown and behaved as insulators with a sheet resistance of greater than 1 M Ω/sq. The films were annealed for one hour at 400°C in an O_2 atmosphere.

The optical transmission and reflectance were measured from 200 - 1000 nm using an F10-RT reflectometer (Filmetrics). The transmission and reflectance spectra of the films deposited at different O_2 concentrations are shown in figure 5.2. The films showed high adsorption in the UV below 300 nm after annealing, the high adsorption being characteristic of the large band gap of ITO. The transmission from 400 nm to 1000 nm was consistent between all the films, with a difference of 10% between the
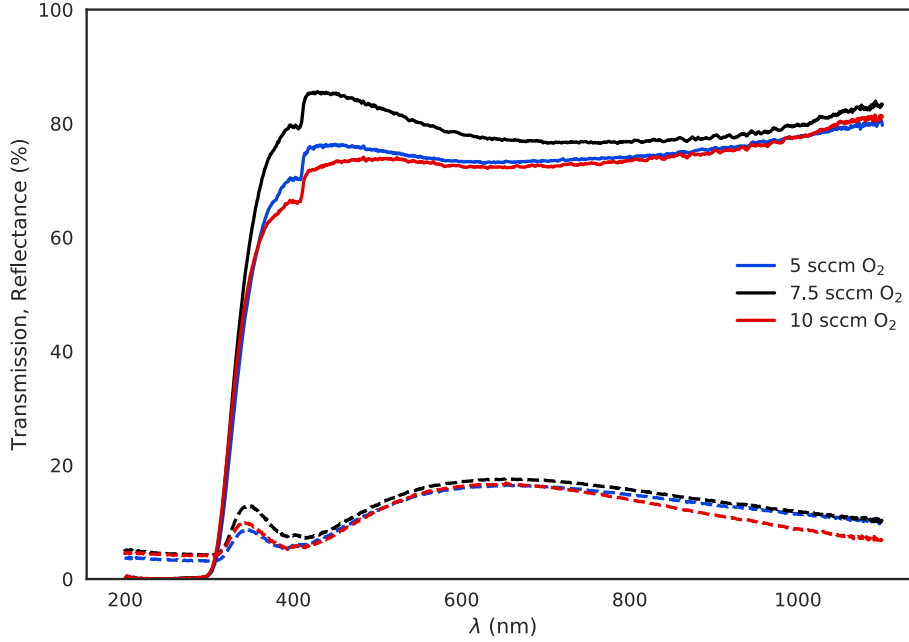
Figure 5.2: Transmission and reflectance of 100 nm ITO films deposited at 0.5 Å/s using O_2 rates of 5, 7.5 and 10 SCCM. Samples were annealed for 30 minutes at 400°C in an O_2 atmosphere after deposition.

transmission maxima and minima. The ITO deposited at 7.5 SCCM O_2 exhibited transmittance and lowest absorption at 850 nm of 76% and 8%, respectively.

The sheet resistance of the films was measured using a manual four point line probe system (Jandel). A four point probe measurement eliminates the contact resistance of the probes by passing a known current between the two outer probes then measuring the resulting voltage with the two inner probes, the sheet resistance of the film can the be calculated using Ohm's law. The sheet resistance of the ITO films deposited at varying O_2 concentrations is shown in figure 5.3. The ITO films deposited at 7.5 SSCM O_2 had the lowest sheet resistance of 300 Ωsq, a resistivity ρ of 3×10^{-3} Ωcm following annealing for 1 hour at 400°C. Increasing the annealing time to 3 hours improved the sheet resistance of both the 7.5 and 10 SCCM of O_2 films to approximately 90 Ω/sq ($\rho = 9 \times 10^{-4}$ Ωcm).

While it was possible to produce films with lower resistivity there was significant variation in the sheet resistance between different depositions, with the sheet resistance ranging from 60 to 150 Ω/sq. I did not discover the source of this variation but believe it to be a combination of positioning of the substrate on the rotating stage, error in the film thickness monitor and differences in the material when replacing the ITO pellets which changed the profile of the material deposition. Depositing
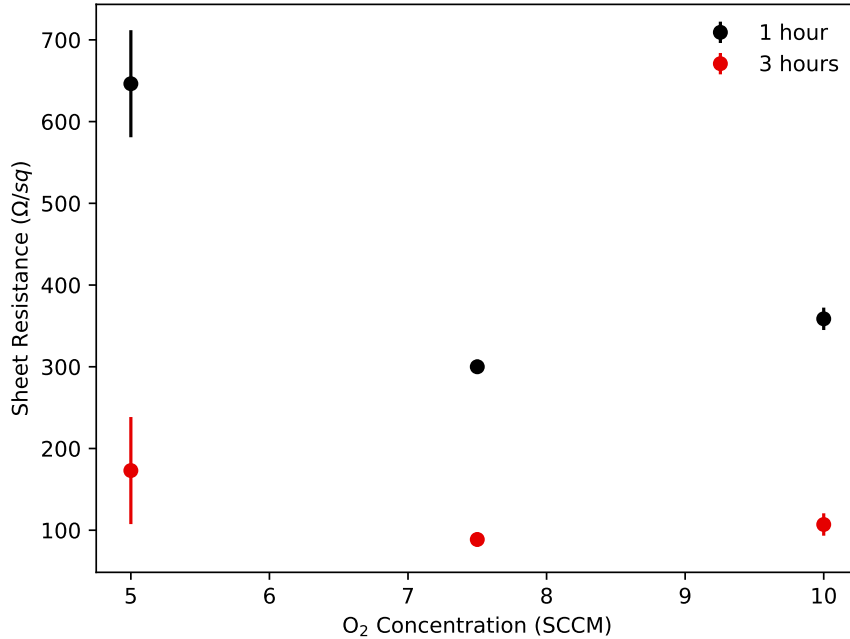
Figure 5.3: Sheet resistance of 100 nm ITO films deposited at 0.5 Å/s against O_2 concentration. The black markers show the sheet resistance with 1 hour annealing at 400°C, red marker shows sheet resistance after 3 hours annealing.

ITO using 7.5 SCCM of O_2 produced films with the highest transmission at 850 nm, the operating region of the GMR sensors. A three hour annealing time at 400°C produced the lowest sheet resistance at 7.5 SCCM of O_2 so these parameters were used for all subsequent ITO film depositions.

5.1.2 Thickness Dependence of ITO Thin Films

The electrical and optical properties of ITO have a strong dependence on the thickness of the films as discussed in chapter 4. The GMR sensor is sensitive to refractive index, deposition a high refractive material on top of the grating will consequently increase the resonance wavelength but also reduce the reflectivity due to the optical absorption of the ITO Understanding the properties of the deposited films was therefore crucial for later design choices when fabricating the EGMR.

The thickness of the ITO was calibrated by using a photolithography lift process to create features that could be measured using a Dektak stylus profileometer (Bruker). Although there are other methods of measuring the film thickness such as ellipsometry or SEM, characterising the film thickness using a lift off process and the profilometer was also useful for developing a photolithography protocol for the ITO

electrodes used in the ECGMR in chapter 6.

Sheet Resistance
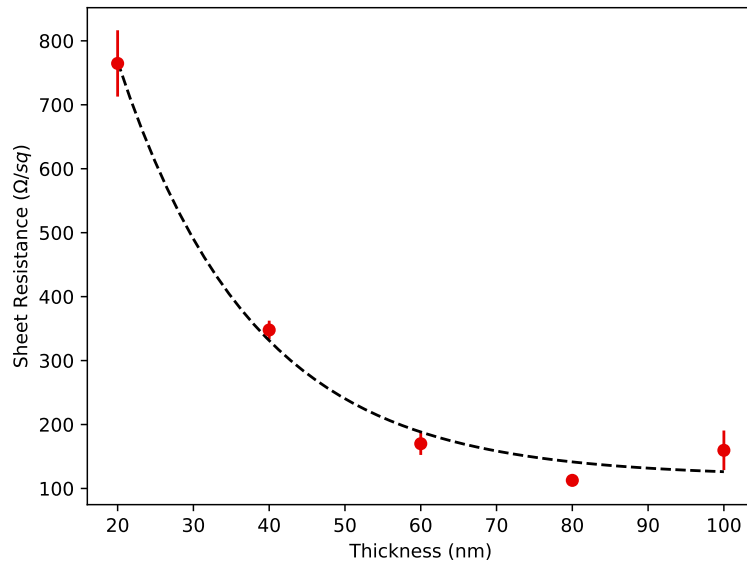
Figure 5.4: Sheet resistance of ITO films from 20 to 100 nm thick deposited at 0.5 Å/s with an O_2 of 7.5 SCCM. Samples were annealed for 3 hours at 400°C in an O_2 atmosphere after deposition. Error bars are the standard deviation (n =3). Dashed line shows the exponential fit, $R^2 = 0.991$.

To investigate the effect of the ITO film thickness on the optical and electrical properties, I deposited 20, 40, 60, 80, and 100 nm ITO films on to borosilicate glass that had been cleaned using the same glass cleaning protocol described in section 5.1.1. After annealing for three hours at 400°C the transmission and sheet resistance were measured as described in section 5.1.1. The sheet resistance of the ITO shown in figure 5.4 decreased rapidly from 770 Ω/sq at 20nm thick to 180 Ω/sq for the 60 nm sample and remained similar for the 80 and 100 nm samples. This result agrees well with previously published literature on how crystalline structure and consequently electron transport is dependent on the material thickness [174]. Importantly for designing the EGMR, it also shows that for maximum conductivity the ITO layer should be at least 60 nm thick.
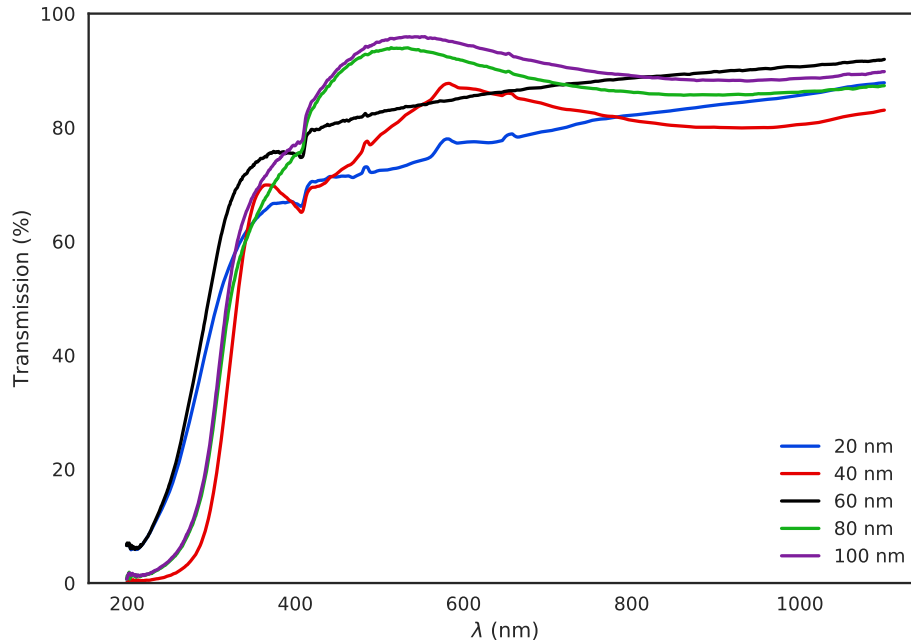
Figure 5.5: Transmission of ITO films from 20 to 100 nm thick deposited at 0.5 Å/s with an O_2 of 7.5 SCCM. Samples were annealed for 3 hours at 400°C in an O_2 atmosphere after deposition.

Optical Transmission

The optical transmission with respect to film thickness is shown in figure 5.5. Below 650 nm the transmission does depend on the ITO thickness, most clearly shown by the emergence of the peaks at 450 nm in the 80 nm and 100 nm samples. The notch in transmission at 400 nm for all samples is likely caused by the measurement system itself as two different light sources are used from 200 - 400 nm and 400 - 1100 nm. It is possible therefore that the illumination at 400 nm is not as consistent compared to the rest of the spectrum. The EGMR will operate at 850 nm however, where the transmission is less dependent on the thickness. The 40 nm sample had the lowest transmission of 80% at 850nm. Both the 60 nm and 100 nm sample had a transmission of 88% and there was only a standard deviation of 1.35% between the 60, 80 and 100nm samples.

Carrier Density and Mobility

I investigated the effect of film thickness on carrier density and electron mobility μ using a Ecopia 2000 Hall effect measurement system. The films were deposited on to 10 mm x 10 mm square borofloat glass substrates. An S1818 photoresist layer

was spin coated on top of the ITO at 5000 RPM. Ohmic contacts were defined using direct write laser lithography in the Van De Pauw configuration shown in figure 5.6a. Ten nm Ti and 100 nm Au was deposited using E-beam evaporation to create electrical contacts and the remaining resist was removed using acetone.
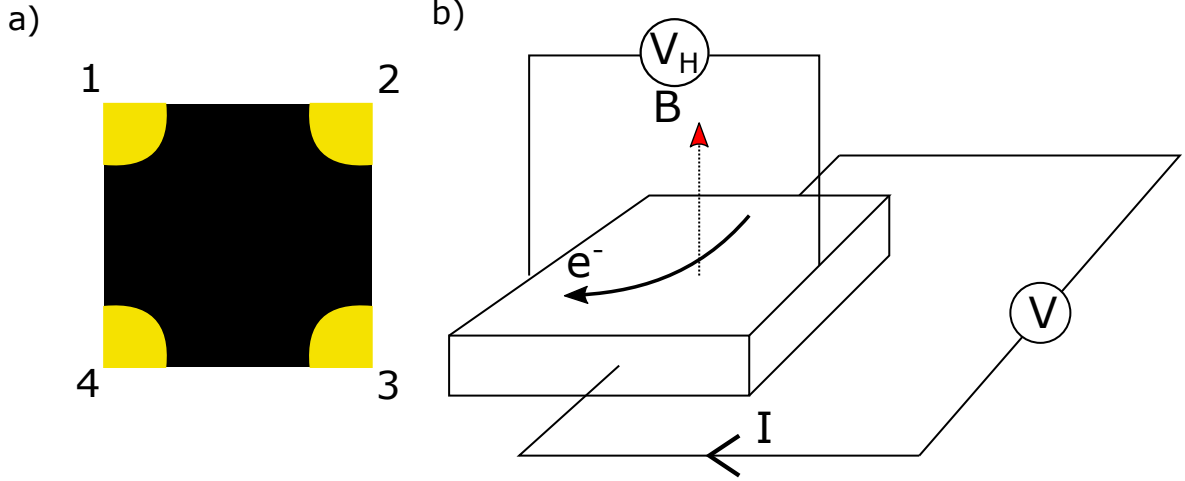
Figure 5.6: **a)** Schematic of a Van de Pauw electrical contact configuration. **b)** Schematic of a Hall effect measurement. A current I driven by voltage source V is applied to the film under test in the presence of a transverse magnetic field B. The Lorentz force due to the magnetic field deflects the charge carriers in the material, in this case electrons, causing a spatial distribution of charge across the material consequently leading to the Hall voltage V_H.

The Hall effect is the generation of the Hall Voltage by the deflection of charge carriers by a transverse magnetic field. The charge carriers are deflected due to the Lorentz force from the magnetic field. The direction of deflection is dependent on the charge of the carrier so holes and electrons are deflected in opposite directions. The deflection of the carrier leads to a distribution of charge at one side of the film, giving rise to the Hall voltage. To measure the Hall voltage in the Van de Pauw configuration, a DC current is applied between two of the contacts with the voltage in both directions e.g from contact one to contact three V_{13} and then from contact three to contact one V_{31}. The positive direction of the current is the conventional direction of current, opposite the direction of the electron movement. The resulting voltage due to the deflection of charge carriers across the opposite pair of contacts is measured with the magnetic field in both the positive and negative directions. The measurement is repeated between all of the pairs of the contacts giving a total of eight measurements. The Hall voltage V_H is then given by equation 5.1.

$$V_H = \frac{(V_{13p} - V_{13n}) + (V_{31p} - V_{31n}) + (V_{24p} - V_{24n}) + (V_{42p} - V_{42n})}{8} \qquad (5.1)$$
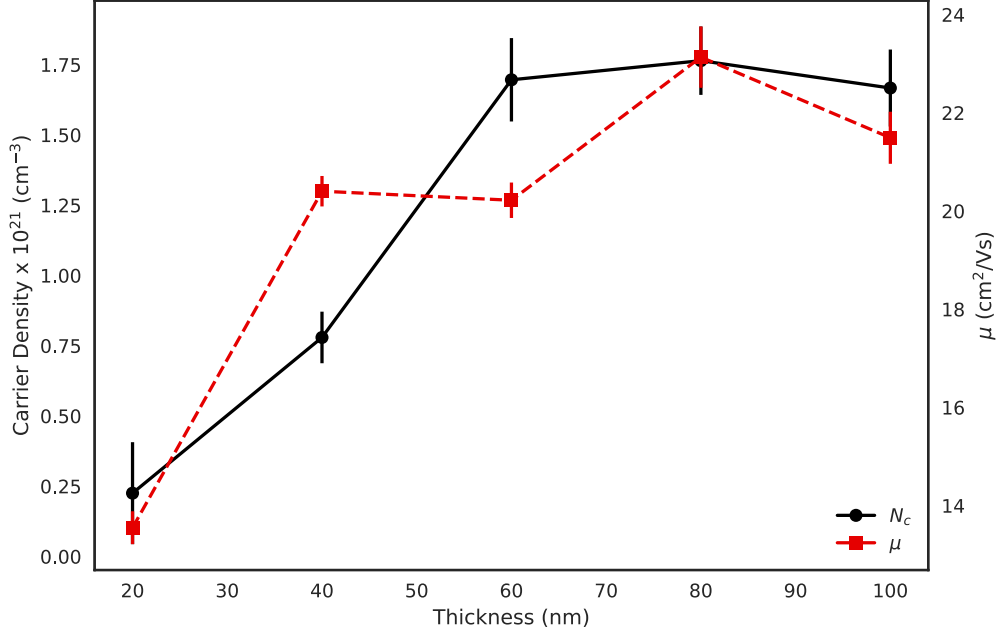
Figure 5.7: Mean carrier density N_c (black) and electron mobility μ (red) for different thicknesses of ITO. Error bars are the standard deviation (n=3).

If V_H is negative the thin film is n doped, and p doped if V_H is positive. The carrier density N_c can be calculated from equation 5.2 where I is the applied current, B is the applied magnetic field, t is the thickness of the thin film.

Once the carrier density is known the carrier mobility can be calculated using equation 5.3, where R_s is the sheet resistance, which can be calculated using Ohms law in the absence of the magnetic field. The Van de Pauw method of measuring sheet resistance assumes that there is no anisotropy in the film resistivity and gives a measurement of the average of the entire film. The advantage of using the Hall effect system is that there is clearly more information to be gained compared to the four point probe, but the measurement is also significantly more time consuming, requiring a lift off process for the Ohmic contacts and a more complicated measurement process.

$$N_c = \frac{IB}{qtV_H} \qquad (5.2)$$

$$\mu = \frac{1}{qnR_s} \qquad (5.3)$$

The measured carrier densities and electron mobilities at different film thicknesses

are shown in figure 5.7. The carrier density ranged from 2.5×10^{20} cm^{-3} for the 20 nm film to 1.6×10^{21} cm^{-3} for the 60, 80 and 100 nm films. The high carrier density of 10^{21} cm^{-3} suggests that there has been high incorporation of Sn into the film. There was little change in the carrier mobility for the 40 to 100 nm films, with the mobility being between 20 and 23 cm^2/Vs. The larger change of electron mobility was from 20 to 40 nm, from 13 cm^2/Vs to 20 cm^2/Vs, suggests that between 20 and 40 nm the film changes from being amorphous to polycrystalline. Dopant scattering is known to reduce the electron mobility in semiconductor films, the presence of the dopant atoms creating areas of charge that scatter the moving electrons, impeding electron mobility [175]. This may account for the lack of increase in electron mobility when the film is greater than 40 nm thick despite the decrease in sheet resistance due to the increase in carrier density as the measured carrier densities are consistent with the highest doped ITO films reported in the literature [176].

The measurements of sheet resistance, optical transmission, carrier mobility and carrier density all agree that the greatest change is seen from 0 -60 nm, with increases in thickness providing only minimal gains in terms of lowering sheet resistance and increasing optical transmission, carrier mobility and density.

5.2   RCWA Simulation of EGMR Structure

From the characterisation of the ITO in section 5.1, it is clear that both the optical and electrical performances depend significantly on the ITO thickness. To maximise the performance of the EGMR it is necessary to identify the best compromise between conductivity and optical loss of the GMR. GMR structures consisting of multiple layers of dielectric have not been widely studied however. RCWA was used to model to the reflectance spectra from the GMR for increasing ITO thicknesses and to understand the effect of the ITO layer on the GMR optical performance. A description of the RCWA method is provided in chapter 4.

The model of the EGMR is shown in figure 5.8, and consists of a glass substrate, a 150nm thick Si_3N_4 grating and an infinite media layer. The effect of depositing ITO on to the GMR grating can be simulated by including two extra layers into the simulation structure, one for the ITO deposited on the top of the grating and the other for the material in the grating trenches. The values of the wavelength dependent refractive index n and loss factor of ITO has been previously published. The values of n and k were fitted to polynomial equations shown in figure 5.9, allowing the wavelength dependence to be modelled within the simulation. While it would have
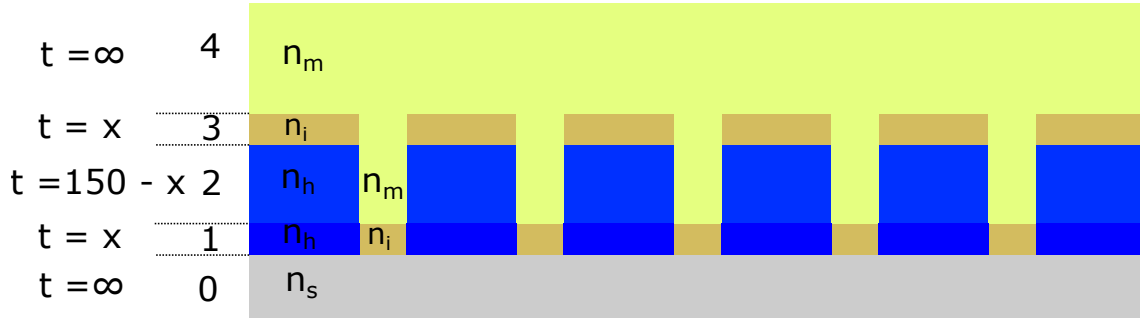
Figure 5.8: Geometry of EGMR used in RCWA simulations. The RCWA consists of 5 layers: layer 0, an infinitely thick glass substrate ($n_s = 1.46$; layer 1, a periodic structure of Si$_3$N$_4$ ($n_h = 2$) and ITO ($n_I = f(\lambda)$) of thickness x; layer 2, a periodic structure of Si$_3$N$_4$ and media ($n_m = 1.33$) with thickness $150 - x$; layer 3, a periodic structure of ITO and media of thickness x; layer 4, an infinitely thick layer of media. The refractive index of the ITO is calculated for each wavelength in the simulation. The grating period is 550nm, the filling fraction was 0.8 and the simulations were performed with normal incidence TE polarised light from 400 to 900 nm.
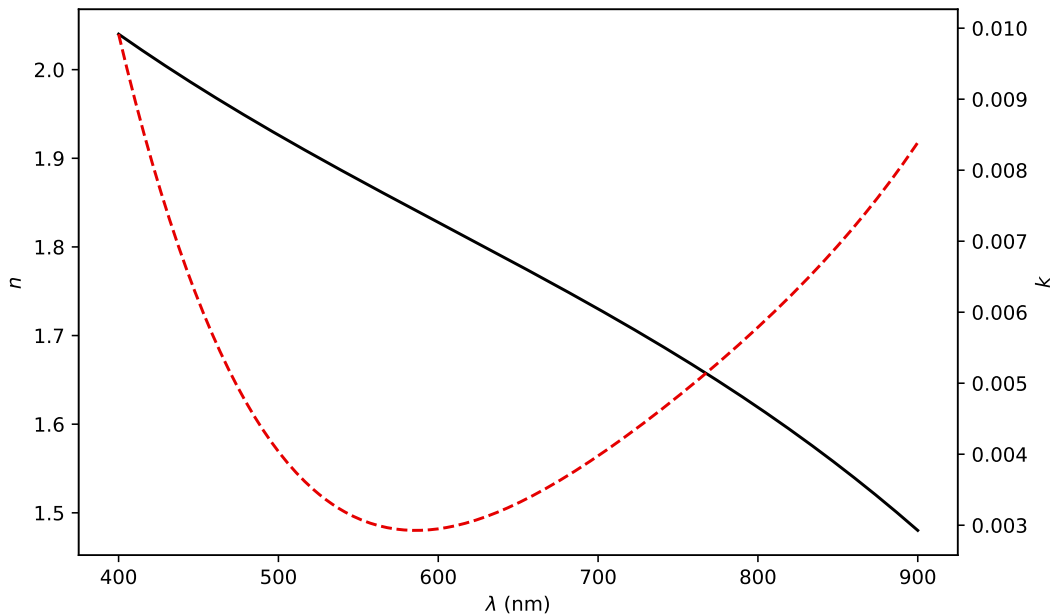
Figure 5.9: Simulated ITO n and k used in RCWA simulations. Black solid line is the refractive index n, red dashed line is the loss factor k. Data values were obtained from [177].

.
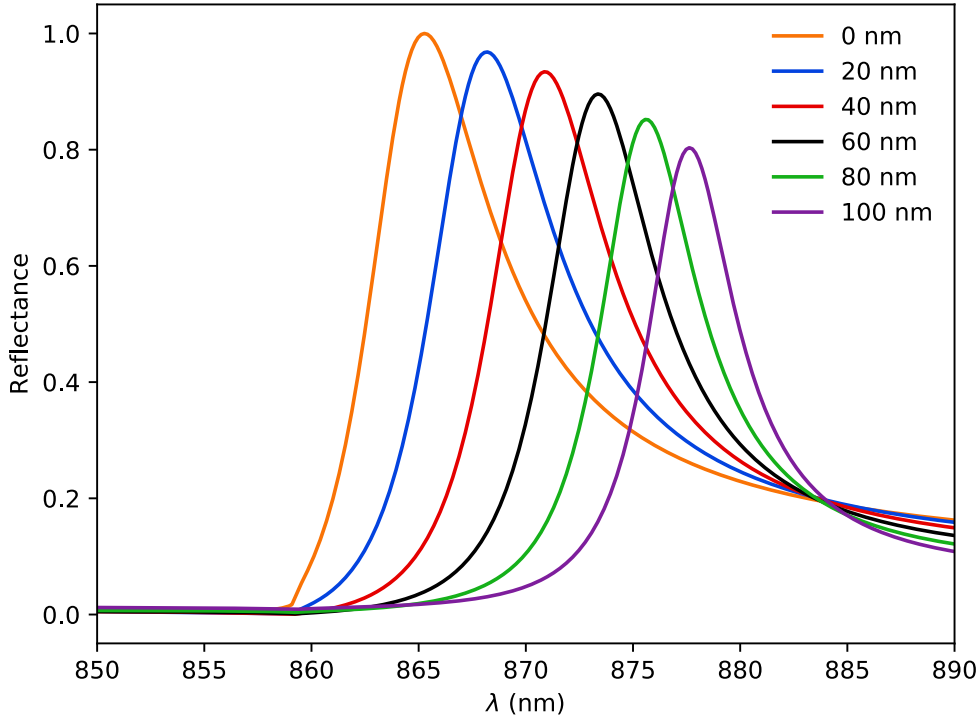
Figure 5.10: Simulated TE reflectance spectra of EGMR with different thicknesses of ITO. Period = 555, FF = 0.8 Si_3N_4 n = 2, glass n = 1.44, media n = 1.33.

been desirable to know the n and k of the deposited ITO films for the simulations, the other material properties of the ITO were consistent with previously published literature, so using n and k values from the literature was a sufficiently accurate estimation. I note, attempts to measure the values of n and k using an ellipsometer for all of the film thicknesses but could not be determined due to insufficient signal intensity from the films. This is a limitation of the ellipsometer that I had available and not a constraint of ellipsometry itself which can be used to measure n of films as thin as 5 nm [178]. The purpose of the simulation is to give a qualitative understanding of whether the GMR will still work with an ITO layer deposited on top. The ITO layer was assumed to be homogeneous, to have no surface roughness, no adherence to the side walls, and no anisotropy in n or k for the purpose of simplifying the model.

5.2.1 Effect of ITO Thickness

The reflectance spectra of the EGMR with increasing thickness of ITO is shown in figure 5.10. Increasing the ITO layer increases the resonance wavelength due to the
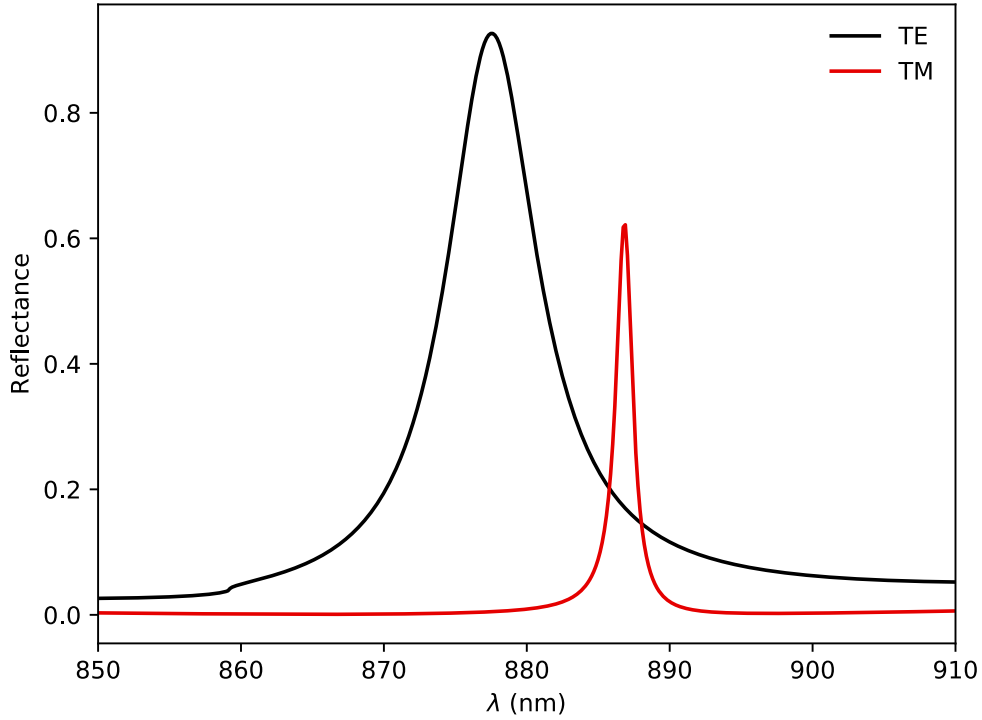
Figure 5.11: Simulated reflectance spectra of EGMR with a 60nm thick ITO layer showing the TE mode and TM mode.

greater refractive index at the surface of the grating, shifting from 867 nm for the Si_3N_4 GMR up to 878 nm for 100 nm of ITO. The increased adsorption due to the loss factor k decreases the reflectance peak intensity, from 1 for the Si_3N_4 GMR to 0.8 for the same structure capped with 100 nm of ITO. As expected the highest reflectance obtained when there is no ITO deposited on the top. While the reflectance decreased linearly with ITO thickness the experimental measurements of the ITO sheet resistance decreased exponentially, reaching a minimum for thicknesses greater than 60 nm. The Q factor of the resonance also increased with the increasing thickness ITO due to the enhanced confinement of the mode within the grating structure. To maximise reflectance and minimise the sheet resistance I chose to use 60 nm thick ITO films for the majority of the EGMR devices but also performed characterisation of a 20 nm layer as discussed in section 5.5.

5.2.2 Simulation of TE and TM modes

The TE and TM modes for a 60 nm thick ITO layer are viable as shown in figure 5.11. The TM mode has a Q factor of 600 but the peak reflectance is only 0.6. The
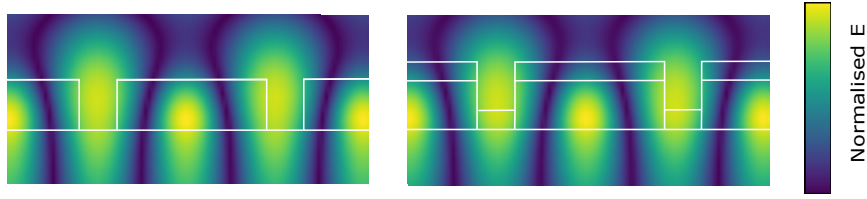
Figure 5.12: Field distribution of the TE mode of the Si_3N_4 GMR (Left) compared to an EGMR coated with 60nm of ITO (Right). Physical parameters are the same as the simulations in figure 5.10. The E field has been normalised to the maximum in the Si_3N_4 GMR plot.
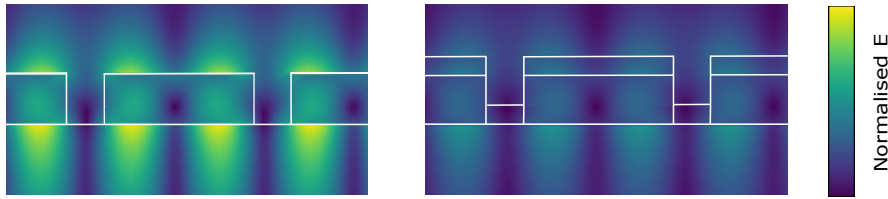
Figure 5.13: Field distribution of the TM mode of the Si_3N_4 GMR (Left) compared to an EGMR coated with 60nm of ITO (Right). Physical parameters are the same as the simulations in figure 5.10.The E field has been normalised to the maximum in the Si_3N_4 GMR plot.

sharper resonance of the TM mode has been shown to improve the RI sensitivity in comparison to the TE mode. As discussed in the chapter 3, the GMR resonance is an interaction between the Bragg resonance in the grating structure and the slowly varying thin film resonance. The interference between these two effects give rise to the Fano line shape of GMR resonance. The TE mode of a Si_3N_4 GMR sensor displays the asymmetry of the Fano lineshape more prominently, which is also observed in the EGMR. As with the Si_3N_4 GMR, the shape of the EGMR TM mode tends towards a standard Lorentzian shape due to the increased Q factor, where the high electric field intensity of the Bragg reflectance dominates the thin film resonance.

5.2.3   Electric Field Profile

The refractive index sensitivity of the GMR structure depends on how the evansecent field of the mode decays into the media as discussed in chapter 3. The mode profile for both the TE and the TM modes shows that the light is confined predominantly within the structure and the substrate, with only a fraction of the light present in media. For the TE mode shown in figure 5.12, the electric field distribution is similar with and without ITO, concentrating in the grooves and the centre of edge ridge although the field intensity is slightly weaker in the media in EGMR compared

to Si_3N_4 GMR. The sensitivity of the TE mode for EGMR should therefore be similar to that of a Si_3N_4 GMR. For the TM mode, the Si_3N_4 grating, shown in figure 5.13, there is a high intensity field confinement at the corners of the grating. The high electric field intensity at the Si_3N_4 media interface compared to the TE mode grating-media interface is what contributes to greater experimentally observed refractive index sensitivity of the TM mode. For the EGMR structure however, the electric field is distributed between both the ITO Si_3N_4 interface and the ITO media interface, reducing the overall maximum field intensity by half. The simulations suggests that the TM mode sensitivity for EGMR would be significantly lower than the the TM mode of the Si_3N_4 GMR.

5.3 Physical Characterisation

EGMR sensors were fabricated as discussed in chapter 4.1 using a 60 nm thick ITO layer deposited with a flow rate of 7.5 SCCM O_2. After fabrication the morphology of the EGMR structure was characterised using scanning electron microscopy with the assistance of Dr. Casper Kunstmann (Department of Electronic Engineering, University of York). Figure 5.14 shows the structure of the grating is still intact after deposition of the ITO on a GMR structure with a grating period of 550 nm. Although the ITO layer is conductive a layer of ARP-C was deposited by spin coating to prevent charging of the substrate during imaging, which will also have contributed to the surface roughness. Figure 5.15 shows that there has been deposition on the sidewalls of the grating and that the ITO within the grooves of the grating has greater thickness and surface roughness than that on the top of grating.

If the ITO surface roughness is only due to the deposition technique it would be expected that the roughness should be consistent across the entire grating. That it is confined to the grooves of the grating however suggests that the nanostructuring of the grating itself is affecting the deposition of the material. Formation of ITO nanostructures using both electron beam evaporation and DC magnetron sputtering has been reported, which is thought to be by a vapour liquid solid (VLS) growth mechanism. The mechanism of VLS for a metal oxide is due to the different melting temperatures of the oxide and the metal dopant, which then interact with each other during the deposition phase [179]. The growth of the nanostructures can be affected by controlling the substrate temperature. The electron beam evaporation system does not have a substrate temperature control, so the substrate may be being heated sufficiently to incite the VLS nanostructure growth. It would be interesting to compare the electron beam deposited films to those deposited by plasma sputtering,

which is performed closer to room temperature to investigate if this process is leads to the ITO roughness observed inside the grooves of the grating.
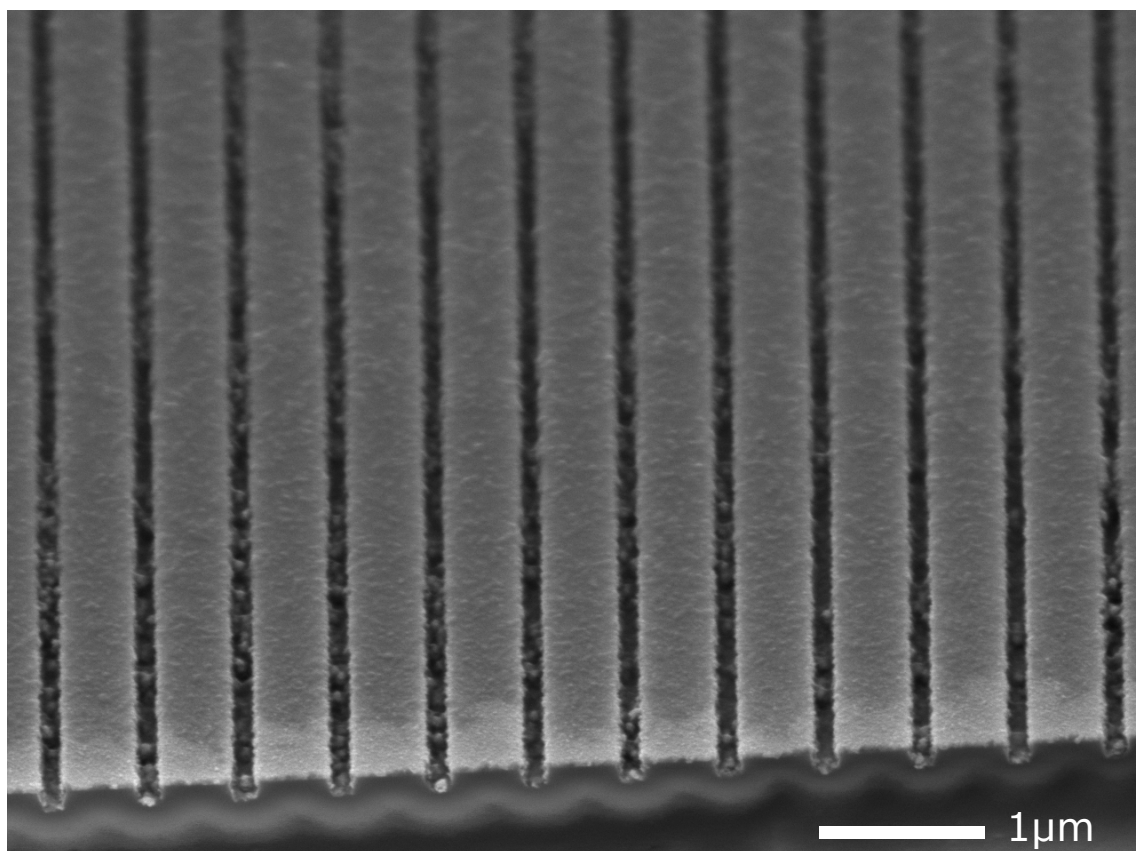
Figure 5.14: SEM image of EGMR grating which has been cleaved through to expose the profile of the grating. ITO thickness is 62 nm.
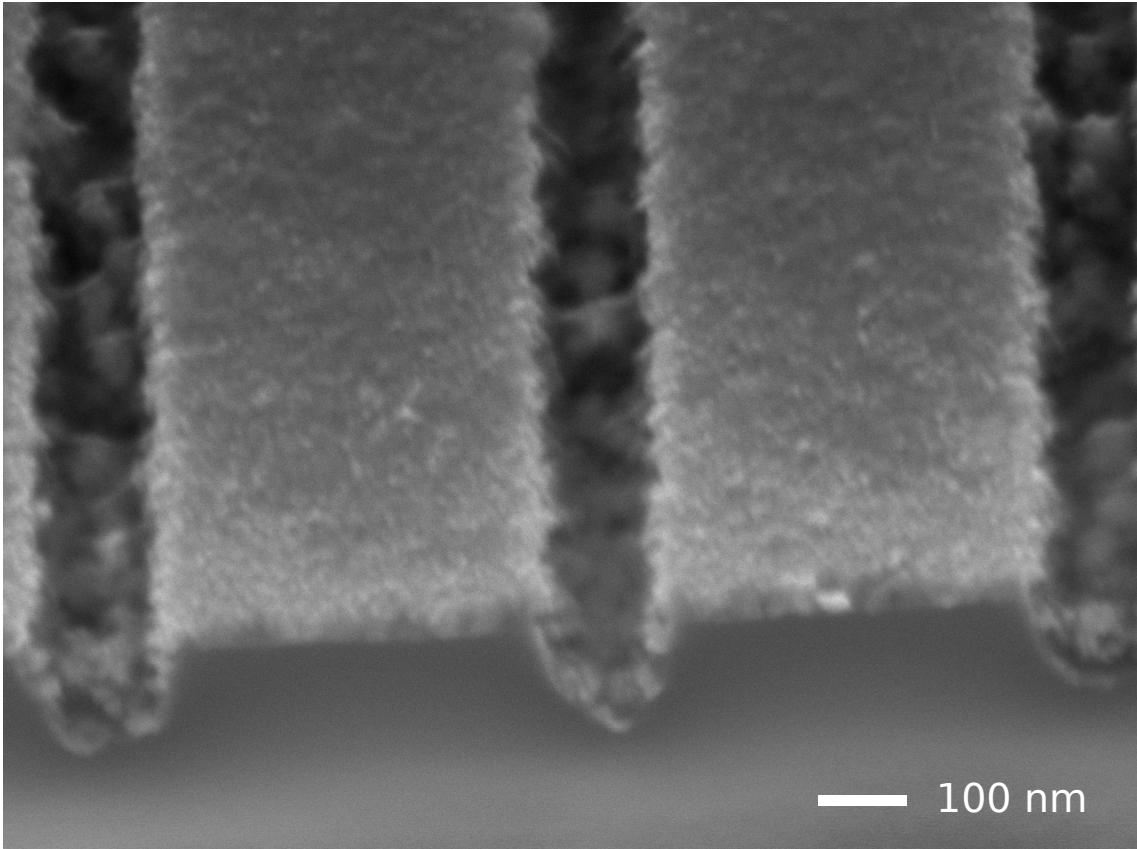
Figure 5.15: SEM image of EGMR grating grooves. The surface roughness of the ITO in the grooves is greater than that on the top.

5.4 Optical Resonance characterisation
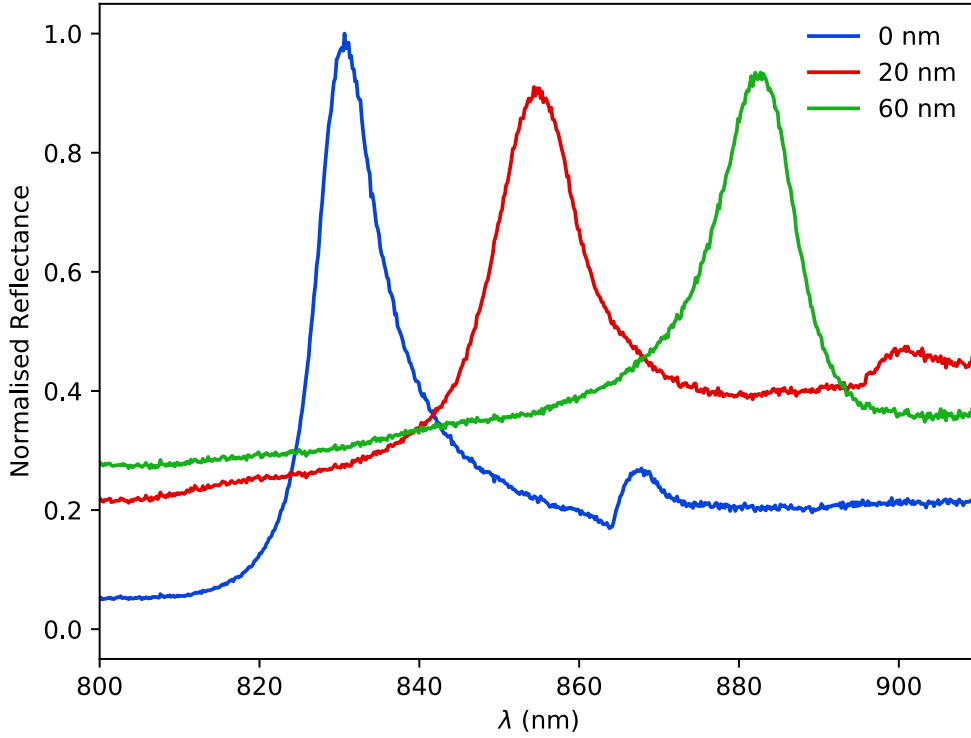
Figure 5.16: Reflectance spectra of the TE mode for the Si_3N_4 grating, 20 nm ITO EGMR grating and 60 nm EGMR grating. Reflectance has been normalised to a Ag mirror.

Table 5.1: Measured resonance parameters of Si_3N_4 GMR, 20 nm and 60 nm ITO EGMR sensors

Sample	λ_{res} (nm)	FWHM (nm)	Q factor	R^2
Si_3N_4	830	9.14	90	0.999
20 nm ITO	854	10.42	82	0.997
60 nm ITO	882	12.5	70	0.997

Characterising the resonance of the gratings is of fundamental importance for using the EGMR structures as a biosensor. To experimentally investigate the effect of the ITO on the resonance, I fabricated EGMR gratings coated with 20 nm and 60 nm thick ITO and a purely Si_3N_4 grating to act as a control. Using the white light reflectance optical setup described in chapter 4, I measured the resonance with DI water on top of the grating. The figures of merit from the three gratings are summarised in table 5.1.
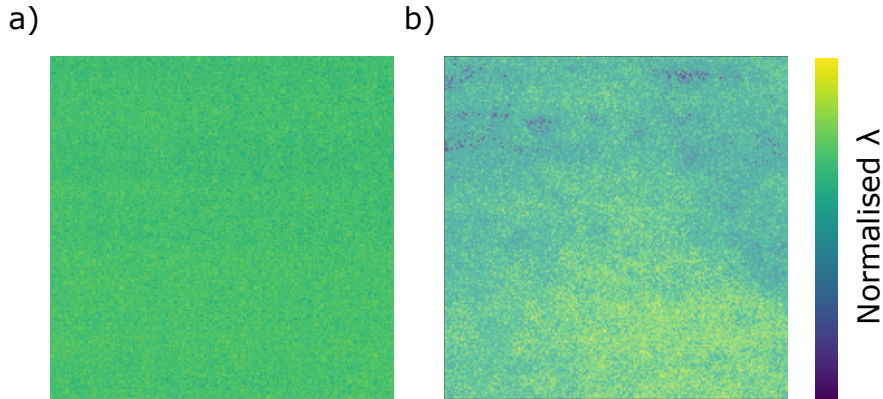
Figure 5.17: **a)** Hyperspectral image of resonance wavelengths for Si_3N_4 GMR grating **b)** Hyperspectral image of resonance wavelengths for EGMR with 60 nm thick ITO layer. The resonance wavelength has been normalised between 0 and 1 for both images. Image area is 181×181 μm.

All of the samples showed that they had a single resonance peak in the 800 - 900nm region when illuminated with a broadband white light source shown in figure 5.16. The resonance wavelength increases with ITO thickness as expected due to the deposition of the high refractive index material on the surface. The wavelength shift from the Si_3N_4 starting wavelength is approximately 5 times greater for both the 20 nm and 60 nm samples than predicted by the simulations of ITO thickness in section 5.2.1. The SEM images showed that there was adherence of ITO to the side walls of the grating and that the ITO was far from the smooth homogeneous film assumed in the models. Given the larger amount of material actually deposited, the greater resonance shift is expected. There will be also mismatch between the modelled refractive index and actual refractive index of the ITO film, so a difference between the simulated and experimental results was to be anticipated. For the purposes of a biosensing assay, it is the ability to measure the relative resonance wavelength shift not the absolute wavelength of the resonance that is important. Therefore as long as the resonance wavelength can be measured the EGMR can be considered functional. The simulated gratings show that the EGMR grating coated with 60 nm of ITO should support both the TE and the TM modes, however the TM mode was not observed in any of the structures that were measured.

The simulations also predicted an increase in Q factor with increasing ITO thickness, as the propagation length of the mode will be reduced by the optical losses introduced by the ITO. There was instead a broadening of the resonance with increasing thickness of ITO and subsequent decrease in Q factor compared to the Si_3N_4 grating. This is most likely caused by light scattering due to the inhomogeneity of the ITO film, with many additional randomly orientated surfaces from which the guided mode can scatter. The broadening of the resonance can also be understood
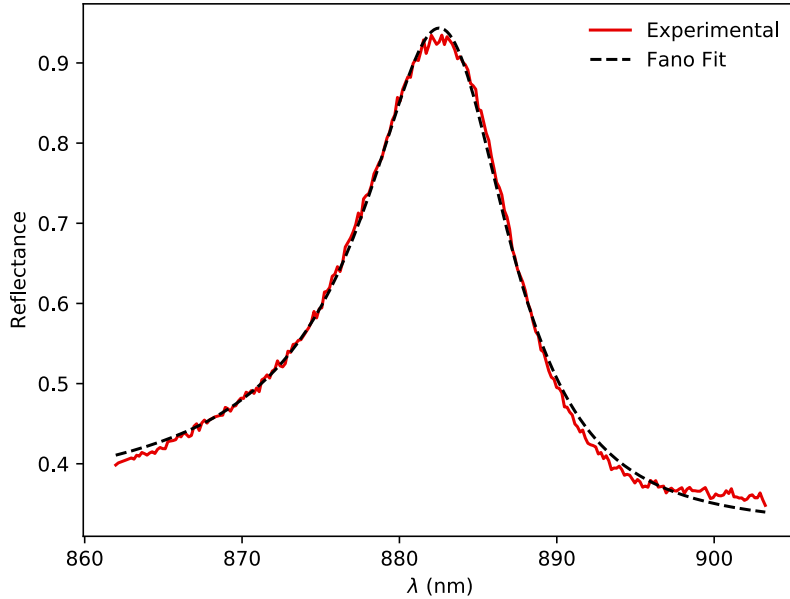
Figure 5.18: Reflectance spectra of 60 nm ITO EGMR in DI water (red line) fitted to the Fano equation.

by performing hyperspectral imaging of the gratings to visualise how homogeneous the resonance is across the entire grating. A hyperspectral image of an Si_3N_4 grating shown in figure 5.17a shows that the resonance wavelength is consistent across the entire area of the grating, with a standard deviation of 1.02 nm in resonance wavelength. In contrast, the standard deviation of the EGMR resonance is 1.54 nm, over 50% greater than the Si_3N_4 grating. Figure 5.17b also shows that this is not homogeneously distributed across the grating, but instead there are areas of higher and lower resonance contributing to the overall broadening of the reflectance peak. The broadening of the resonance will cause a decrease in refractive index sensitivity as the peak resonance cannot be determined as accurately.

It is crucial to be able to accurately monitor the resonance wavelength to use the EGMR as a biosensor. The simplest approach is to identify the resonance wavelength as the wavelength of maximum intensity from the measured reflectance spectra. This approach has limited accuracy due to the spectral resolution of the spectrometer which is limited by the grating constant of the diffraction grating, the size of the entrance slit and the number of pixels in the detector. Fitting the measured spectra to the Fano shape using equation 5.4 can increase the resolution beyond the physical limitations of the spectrometer. The fitting was performed using the scipy curve fit function to equation 5.4 where Γ is the FWHM, λ is the wavelength of light, a is the Fano asymmetry parameter, a is the background scaling factor and λ_{res} is the

Table 5.2: Measured parameters of 60 nm ITO EGMR fabricated independently

Sample	λ_{res} (nm)	Q Factor	FWHM (nm)
1	852.252	88.76	9.6
2	882.571	78.19	11.28
3	855.35	89.88	9.15
4	842.293	76.57	11.0
5	868.82	74.05	11.72

resonance wavelength using the non linear least squares method with the Leven-berg—Marquardt algorithm. Fitting the Fano equation to the reflectance spectra for the 60 nm ITO EGMR in figure 5.18 shows that the resonance of the EGMR matches the Fano shape well with an R^2 of 0.997.

$$R = b\frac{(a\Gamma + (\lambda - \lambda_{res}))^2}{\Gamma^2 + (\lambda - \lambda_{res})^2} \tag{5.4}$$

To evaluate the replicability of the EGMR fabrication process and the optical characteristic of the EGMR in terms of the resonance wavelength and Q factor of five different EGMRs with a 60 nm thick ITO layer were fabricated using the same process are shown in table 5.2. The fabrication process consistently results in EGMR sensors that successfully resonate (the total yield of EGMR that produce a resonance is estimated to be over 95%). There is clearly variation in the obtained resonance wavelength which is also observed in the varying ITO sheet resistance obtained in section 5.1. Variance in resonance wavelength is not critical for the application of the EGMR as a biosensor as all the measurements are relative with respect to the starting resonance. For expanding the future use of the EGMR technology however understanding and correcting the cause of the manufacturing variation would be desirable.

5.5   Electrical Modulation of the EGMR Resonance Wavelength

The optical resonance of combined electro-optical techniques has been repeatedly shown to be influenced by the application of bias voltages [91]. The change in resonance due to applied voltage must be characterised for performing analytical measurements to avoid erroneous experimental conclusions caused by the measurement system itself. To measure the effect of bias voltage on the EGMR resonance I monitored the resonance wavelength of a 20 nm and 60 nm thick ITO EGMR using

the broadband white light setup described in chapter 4 while applying increasing negative bias voltage to the EGMR in 100 mM potassium phosphate (KPi) buffer The KPi buffer was prepared by mixing 71.7 mL of 1M K_2HPO_4 with 28.3 mL 1M KH_2PO_4 dissolved in DI water. The 1M buffer was diluted 1:10 with DI to obtain a pH 7.2 100 mM KPi buffer, the pH was validated using a pH meter (Mettler Toledo). To apply bias voltage, I attached a wire to the EGMR using Ag epoxy resin to serve as the working electrode. A Pt wire was used as the counter electrode and a Ag wire was used as a pseudo reference electrode.

Bias voltage from 0 to -1 V was applied in -0.1V steps every 3 minutes using an SP200 (BioLogic) potentiostat. The voltage was limited to -1V to prevent damage to the ITO film. The bias voltage was held for 3 minutes to allow the electrochemical double layer to stabilise after application of the bias voltage.Reflectance spectra were measured every 2 seconds and the measured spectra were fitted to the Fano equation to extract the resonance wavelength and averaged to give the mean resonance wavelength at each bias voltage step.

Figure 5.19 shows the reflectance spectra for the EGMR coated in a 20 nm ITO layer in 100 mM KPi at increasing bias voltages. The resonance wavelength shifts negatively from 836.3 nm at 0V to 835 nm at -1V. This is accompanied by a decrease in reflectance intensity from 0.63 to 0.59. Comparing the bias induced resonance wavelength shift of the 20 and 60 nm EGMR in figure 5.20 shows that the 20 nm EGMR resonance wavelength shifted with -0.3V applied while for the 60 nm the resonance was stable until -0.8V was applied. The final wavelength shift at -1V was 0.35 nm for the 60 nm thick ITO and 1.35 nm for the 20 nm sample.

The bias-induced negative shift in resonance wavelength can be caused either by a reduction in refractive index of the media or the refractive index of the ITO. To investigate if the change in reflectance was affected by the double layer capacitance the experiments were repeated using the EGMR with a 20 nm thick layer of ITO in 100 mM, 1 mM and 10 μM KPi buffer. Changing the molarity of the buffer from 100 mM to 10 μM increases the Debye length from approximately 2 nm to 50 nm so if the change in resonance is dependent on the double layer capacitance, this would be evident in the voltage induced wavelength shift [180]. Figure 5.21 shows that there is a trend of resonance wavelength shift with changing the buffer molarity, with the 100 mM buffer showing the greatest wavelength shift. From this result alone however it is not clear what role the ITO itself has in the shift in resonance.

The permittivity of ITO can be described using the Drude model. The real and imaginary parts of the permittivity are described in equations 5.5 and 5.6, where ω
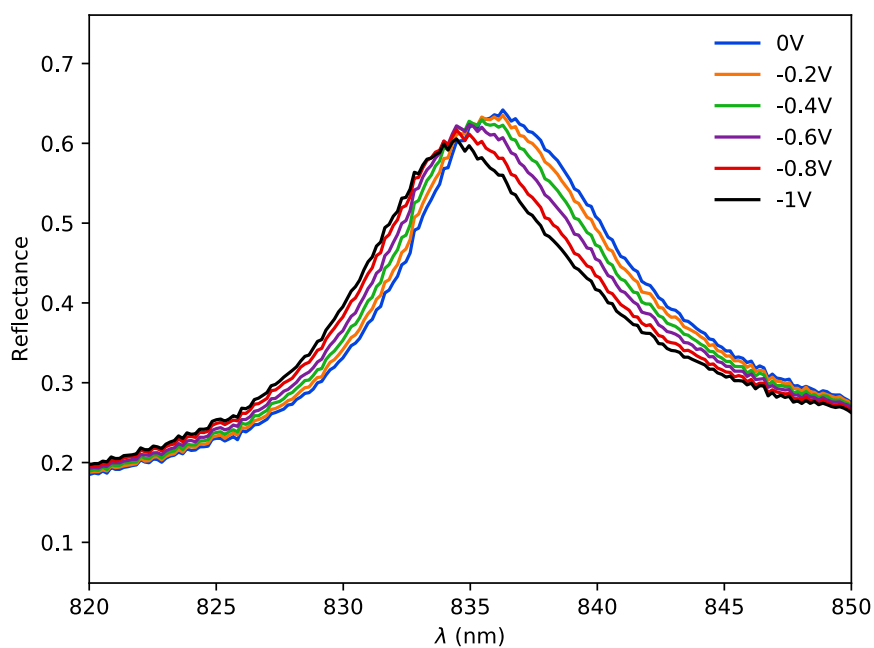
Figure 5.19: Reflectance spectra of EGMR with 20 nm thick ITO layer in 100 mM KPi buffer with increasing bias voltage.
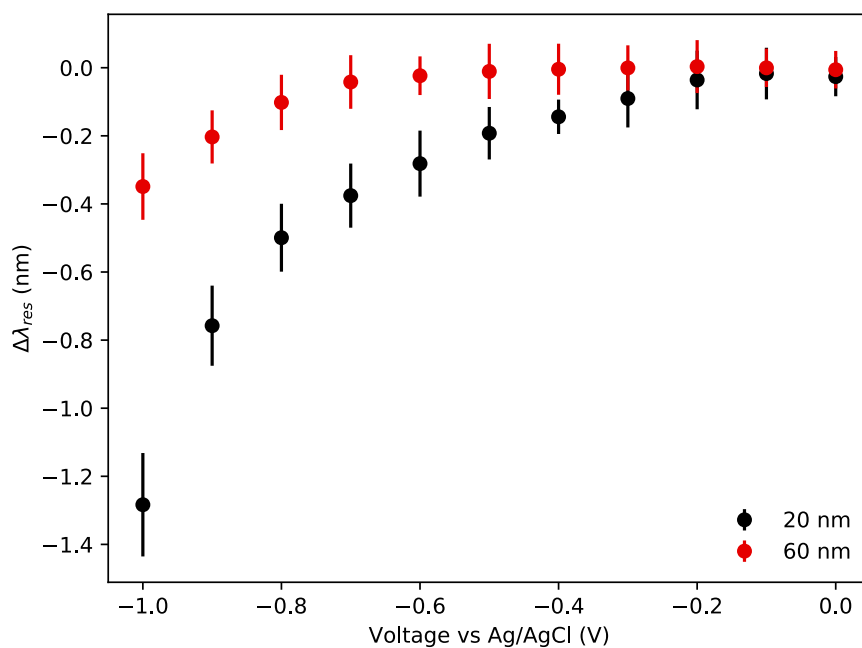
Figure 5.20: Change in resonance wavelength $\Delta\lambda_{res}$ with respect to applied bias voltage for EGMR with 20nm and 60 nm ITO layers.
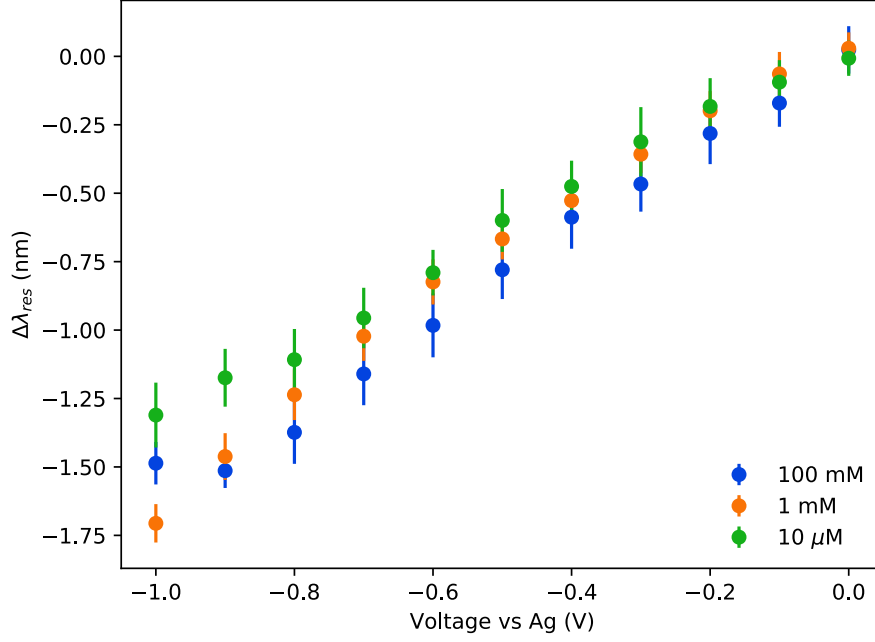
Figure 5.21: Change in resonance wavelength with applied voltage in 10 μM, 1 mM and 100 mM KPi buffer.

is the angular frequency, Γ is the damping constant and ω_p is the plasma frequency. The high frequency permittivity ϵ_∞ is approximated as $1 + \chi$. The real part of the permittivity is illustrative for understanding how ITO structures can be used for both plasmonic and photonic applications. When the incident wavelength is sufficiently long that $\omega^2 + \Gamma^2$ is greater than ω_p^2, the ITO will have a negative real permittivity and so is capable of meeting the conditions for SPR as discussed in chapter 2. When the wavelength is shorter however, the permittivity will be positive, so in the visible wavelengths the permittivity is large enough that the ITO can be used as a waveguide. This expression does not account for the band gap of ITO so while in theory the real permittivity will continue to increase into the UV, there will be also be significant adsorption of the light at these wavelengths.

$$\epsilon_{re} = \epsilon_\infty - \epsilon_\infty \frac{\omega_p^2}{\omega^2 + \Gamma^2} \tag{5.5}$$

$$\epsilon_{im} = \epsilon_\infty \frac{\Gamma}{\omega} \frac{\omega_p^2}{\omega^2 + \Gamma^2} \tag{5.6}$$

The dependence on the ITO carrier density n_c is seen in both the plasma frequency and damping constant in equations 5.7 and 5.8, where n_c is the carrier density, e is

the charge of the electron, m^* is the electron effective mass, ρ is the resistivity and the ϵ_0 is the permittivity of vacuum.

$$[H]\omega_p = \sqrt{\frac{n_c e^2}{m^* \epsilon_0}} \tag{5.7}$$

$$\Gamma = \frac{\rho n_c e^2}{m^*} \tag{5.8}$$
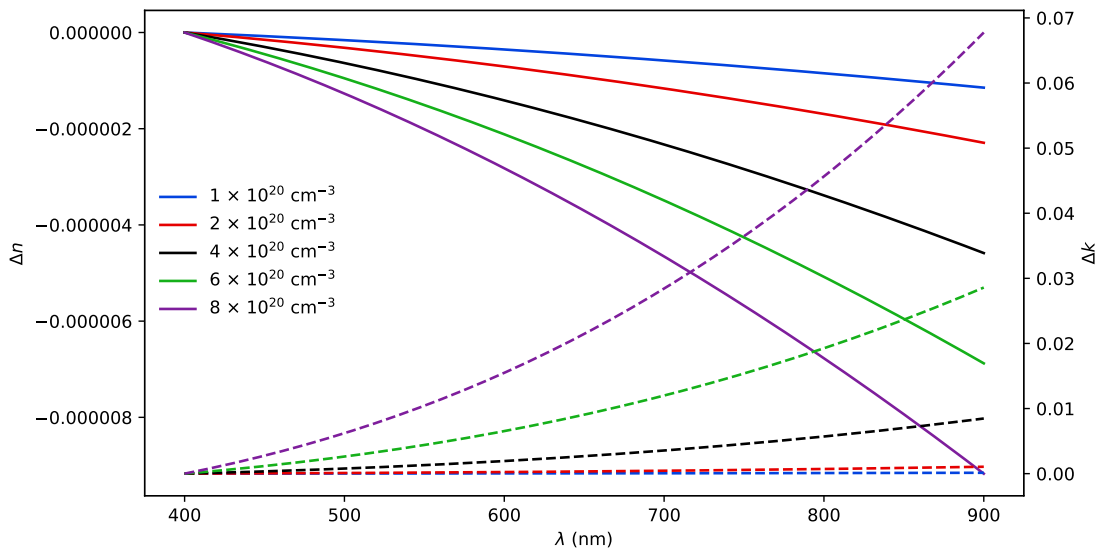
Figure 5.22: Simulated n and k of ITO using the Drude model.
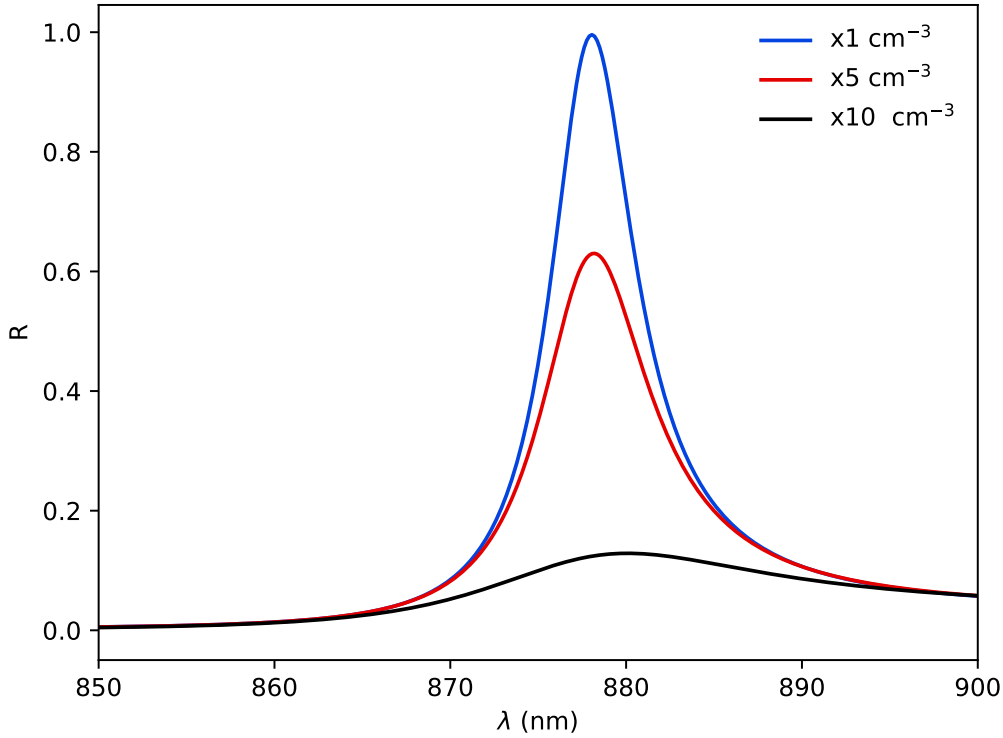
Figure 5.23: Simulated change in EGMR reflectance spectra with proportional increase in carrier density where the ITO n and k are obtained using the Drude model.

To investigate the charge dependence of the ITO refractive index and to attempt to uncouple the change in the media refractive index from the ITO refractive index, the ITO refractive index was modelled using equations 5.5 to 5.8. Figure 5.22 shows the change in the n and k with increasing carrier concentration, where the carrier concentrations are commensurate with those measured for the ITO thin films shown in figure 5.1, there is a 8×10^{-5} RIU decrease in n at 850 nm but a 0.05 increase in k. The resonance of the EGMR was simulated using the same EGMR geometry described in section 5.2 at increasing ITO carrier concentrations from the starting 10^{20}. The resonance wavelength shown in figure 5.23 increases by approximately 1 nm with the proportional increase in carrier density from the starting carrier density of 10^{20} cm^{-3} when the media refractive index is constant. The reflectance intensity decreases from 1 to 0.1 with a 10 fold increase in carrier concentration.

The simulation of the GMR reflectance with to respect increase in carrier concentration with application of bias voltage suggests that the negative resonance wavelength shift is due to the change in the electrochemical double layer and not due to the refractive index change of the ITO. The increase in electrons will repel negatively charged ions within the buffer solution, causing rearrangement of the double layer.

The change in electrochemical double layer has also been used to explain the same effect of changes in resonance wavelength in LMR fibre sensors [97]. The work in this thesis is the first time that the effect of the ITO layer itself has been investigated separately from the change in the media.

A further question that remains is the larger resonance wavelength shift observed the EGMR with the 20 nm thick ITO layer compared to the 60 nm layer in figure 5.20. There are two possible explanations. The first is that the Debye length is only a fraction of the length of the 150 - 200 nm evanescent wave decaying into the media. As there is still a large net contribution from the bulk media, which is unaffected by the applied voltage it is possible that the 20 nm ITO is simply more optically sensitive and therefore has a greater shift in resonance wavelength. Alternatively, the carrier concentration of the 60 nm ITO film has be shown to be an order of magnitude greater than 20 nm, causing a different surface charge for each film thickness.

5.6 Sensitivity Measurements

The sensitivity of a biosensor is fundamental to its performance. The bulk sensitivity of a refractive index sensor to changes in refractive index is typically expressed in nm/RIU. The limit of detection (LOD) is the smallest refractive index change that can be observed above the noise of the measurement, which is typically given as the three times the standard deviation 3σ. The sensitivity is an important figure of merit that informs biosensor applications.

5.6.1 Optical Sensitivity

To measure the sensitivity, an EGMR with a 60 nm thick ITO layer was integrated into a PDMS microfluidic channel, which was permanently bonded to the ITO surface using O_2 plasma bonding. The EGMR surface was subsequently exposed to increasing concentrations of NaCl from 1 to 20% w/v which were pumped through the PDMS microfluidic channel using a syringe pump at 20 μL/min. A wash step of 0.1% w/v NaCl was used between each NaCl solution in order to account for non specific adsorption of the NaCl on to the surface. The refractive index of the NaCl solutions was measured using a refractometer. The reflectance spectra was measured every two seconds and fitted to the Fano equation to extract the resonance wavelength.
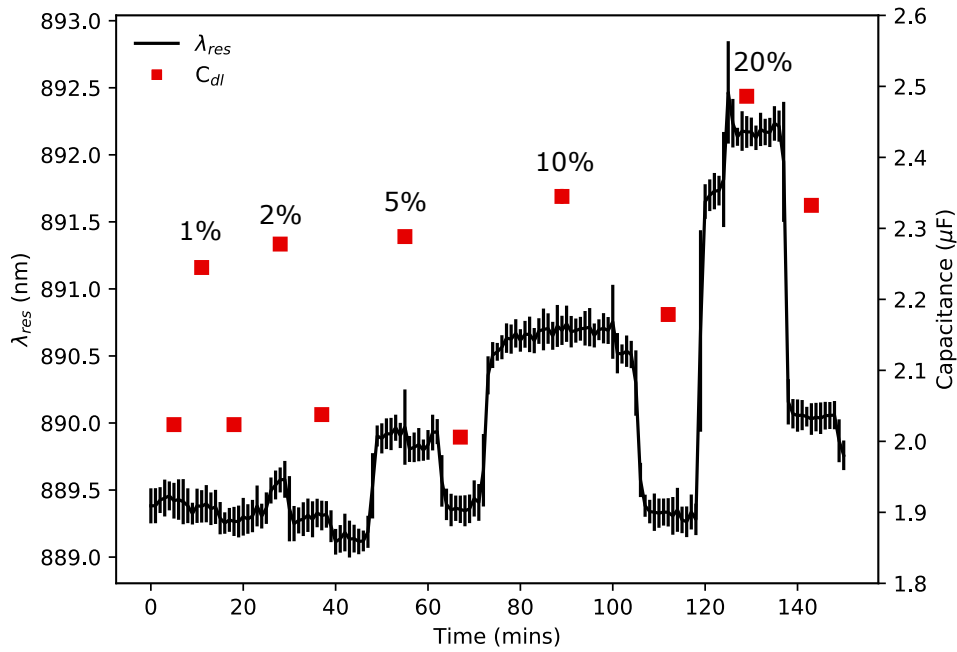
Figure 5.24: Sensitivity measurement of the EGMR using increasing concentrations of NaCl. Fitted resonance wavelength against time (black line). Red squares show the fitted double layer capacitance from CV scans taken at the same time.
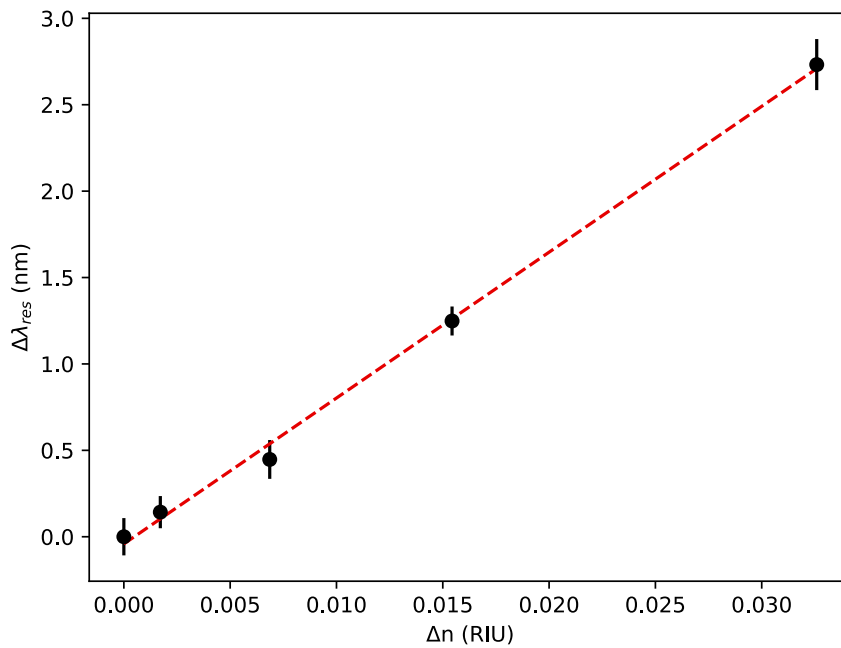
Figure 5.25: Change in resonance wavelength $\Delta\lambda_{res}$ with respect to NaCl refractive index. Linear fit $R^2 = 0.997$.

The resonance wavelength shift increases with NaCl concentration as shown in figure 5.24, starting at 889.5 nm at 0.1% Nacl to 892.5 nm at 20% NaCl reflecting the increasing refractive index of the solutions. Plotting the resonance wavelength shift against refractive index shown in figure 5.25 shows the linear relationship between refractive index and resonance wavelength shift. The slope of the straight line fit was 84.4 nm/RIU, previously reported GMR gratings have a bulk sensitivity in the range of 90-140 nm/RIU so the ITO layer has clearly compromised the sensitivity of the EGMR [14]. This loss in sensitivity is however offset by the gain of an entirely new modality (electrochemistry) which has not been reported before using GMR structures.
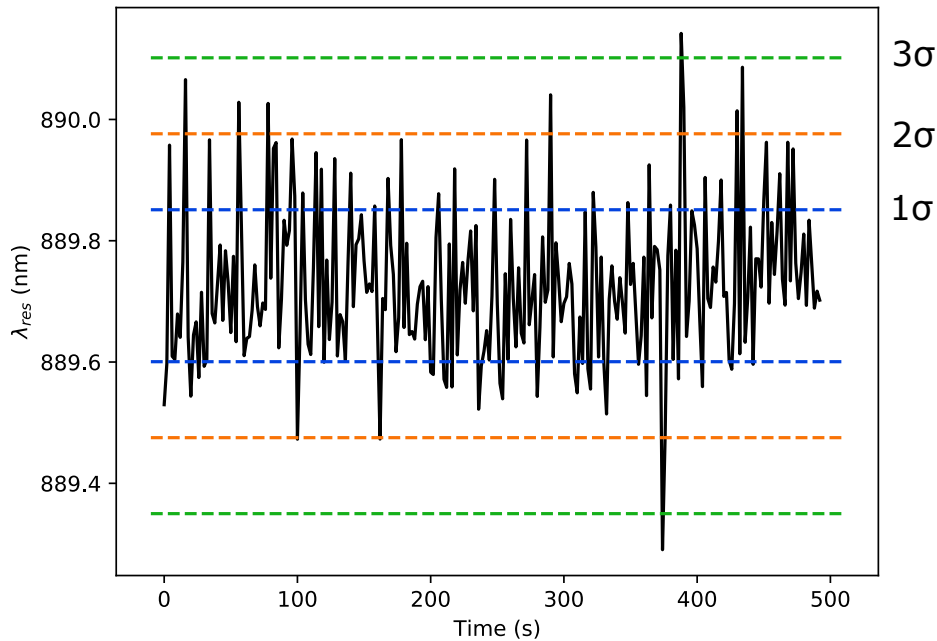
Figure 5.26: LOD measurement showing the fitted resonance wavelength over time. The blue, green and orange lines show the standard deviation σ, with the LOD being above the 3σ line.

To quantify the LOD, the wavelength was monitored every second for 500 seconds and the resonance wavelength fitted to the Fano resonance equation. The mean λ_{res} shown in figure 5.26 was 889.7 nm with a standard deviation σ of 0.125 nm. This leads to a 3σ of 0.37 nm giving a LOD of 4.4×10^{-3} nm/RIU. The optical noise is also greater than that of previously reported GMR sensors, which is likely due to the reduced Q factor which leads to errors in fitting of the resonance wavelength. The reduction in optical sensitivity was expected due to the introduction of the optically lossy ITO layer

5.6.2   Electrical Sensitivity
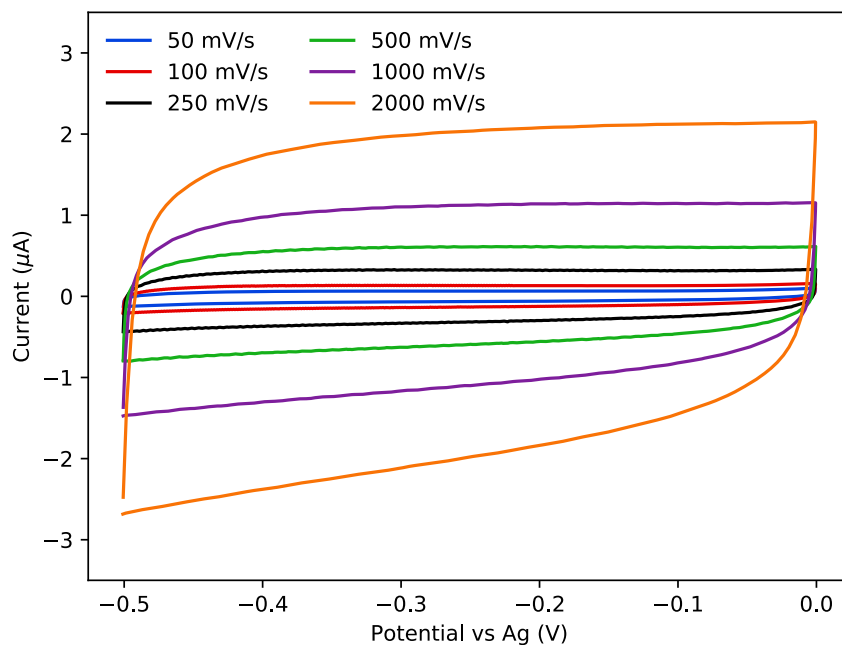
Figure 5.27: CV of EGMR with 0.1% NaCl solution at increasing scan rates.
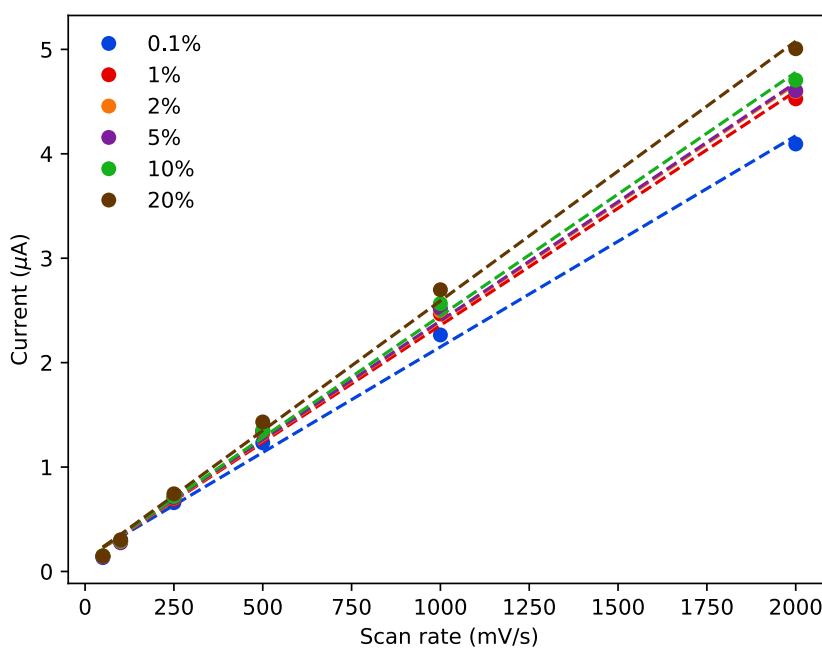
Figure 5.28: Peak current against scan rate for increasing concentrations of NaCl. Dashed lines show the line of best fit for each concentration. R^2 was greater than 0.995 for all concentrations.

As changing the concentration of NaCl will affect the size of the electrochemical double layer, I also performed cyclic voltammetry (CV) to measure the change in double layer capacitance C_{dl}. The ITO layer was used as the working electrode, the Pt counter electrode and Ag pseudo reference were placed in the waste outlet to complete the electrochemical cell. Cyclic voltammetry was performed in order to quantify C_{dl} from 0 to -0.5V, over which range the bias induced shift in resonance for a 60 nm thick ITO layer was shown to be negligible. In the absence of a redox active molecule in solution the non faradaic current is proportional to both C_{dl} and the voltage scan rate i.e. $i = C\frac{dV}{dt}$. Figure 5.27 shows a series of cyclic voltammograms recorded at a range of increasing scan rates for a 0.1% NaCl w/v solution. The double layer capacitance can be found by plotting the peak current against scan rate and the gradient of the resulting straight line gives the double layer capacitance C_{dl} This shown in figure 5.28 for each concentration of NaCl. The double layer capacitance for each NaCl concentration extracted from the straight line fit in figure 5.28 is shown in figure 5.24. As expected the double layer capacitance C_{dl} increased with NaCl concentration from 2 μF at 0.1% NaCl to 2.5 μF at 20% NaCl.

As shown in figure 5.24 the electrochemical measurement of capacitance is more sensitive than the equivalent photonic measure of the NaCl solution optically, with clear differences in capacitance observed from 0.1 to 1% NaCl, which cannot be observed optically. This highlights the advantage of multimodal biosensors.

5.7 Multimodal EGMR Characterisation of Redox Active Solutions

The final section of this chapter investigates the use of EGMR to perform characterisation of the refractive index and electrochemical properties of a solution of redox active molecules in parallel. Methylene blue (MB) is a redox active molecule commonly used in electrochemical biosensing applications [181]. Methylene blue reduces to leucomethylene blue in a two electron, one proton process. As the reduction is proton dependent MB can be used a pH sensor [182]. Optically, MB has a high absorbance peak around 600 nm, and has been shown to have non linear optical properties at high electric field intensities under laser illumination [183].

5.7.1 Concentration Dependence of Methylene Blue

Concentrations of methylene blue from 1 μM to 1 mM diluted in 10 mM KPi buffer were pipetted on to the EGMR sensor in a PDMS well adhered to the sensor surface. Using a static well as opposed to the microfluidic flow cell used in section 5.6 allows the reference electrode to be placed closer to the ITO working electrode, reducing the Ohmic drop between the working and reference electrode. The sensor was washed three times with KPi buffer between each concentration to remove MB and salts bound non-specifically to the surface. The reflectance was monitored every two seconds and the resonance wavelength was extracted by fitting the measured reflectance to the Fano equation. The redox activity of the MB was probed by CV and square wave voltammetry SWV using an SP200 potentiostat and a Pt wire counter electrode and an Ag wire pseudo reference electrode. The MB concentration was limited to 1 mM by the solubility of the MB, higher concentrations were found to precipitate out of the solution at the tested pHs.
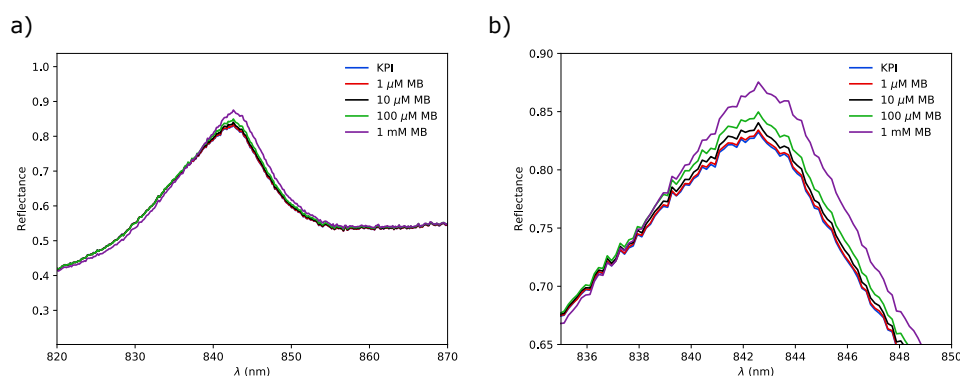
Figure 5.29: **a)** Reflectance spectra of EGMR in KPI buffer and MB concentrations from 1 μM to 1 mM. **b)** Zoomed in plot of a) to better show the change in reflectance spectra.
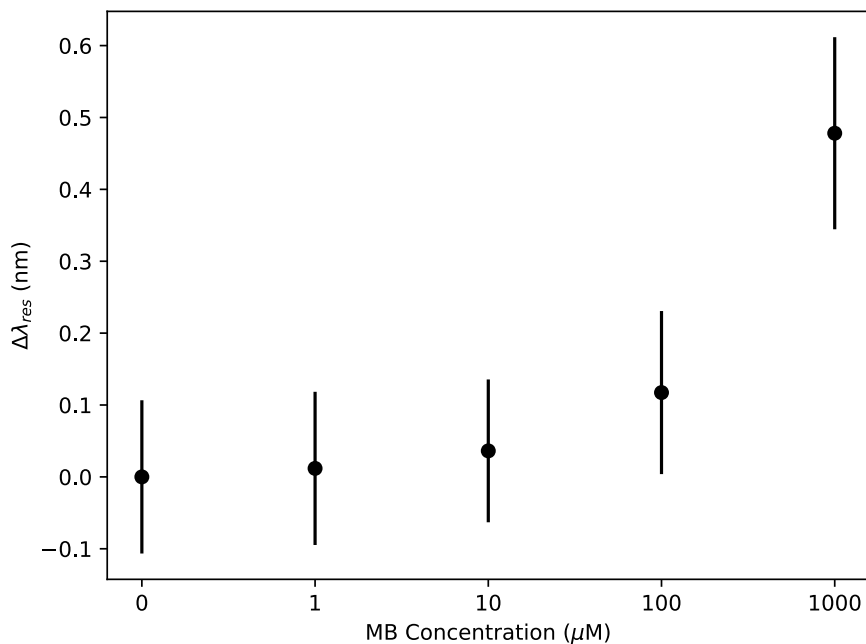
Figure 5.30: Mean change in resonance wavelength from KPi with increasing concentration of MB from 1μM to 1 mM in 10 mM KPi buffer. Resonance wavelength was recorded while the CV measurements were taking place. Error bars are standard deviation (n = 100).

The EGMR reflectance spectra in figure 5.29 shows the increase in resonance wavelength with increasing concentrations of MB reflecting the increase in solution refractive index. The increase in reflectance with concentration is due to the higher reflectance of MB solutions in the near infra red. Plotting the resonance peak shift over time with and without the CV voltage shows that the CV voltammogram does not influence the resonance wavelength significantly. Testing for normality in the data showed that the change in resonance wavelength over time with a constant refractive index is normally distributed indicating that the change is due to intrinsic noise in the experimental system rather than the applied bias voltage. This is true for all solutions independent of methylene blue concentrations showing that the electron transfer to/from the MB does not significantly affect the refractive index of the ITO layer. The fitted resonance wavelength increased exponentially with increasing concentrations of MB increasing 0.45 nm between the KPi electrolyte and 1 mM MB. The refractive index sensitivity of the EGMR for detecting changes in the MB is 60 μM, showing slight improvement over existing evanescent field methods for analysing redox molecules such as MB and has a larger dynamic range [184].
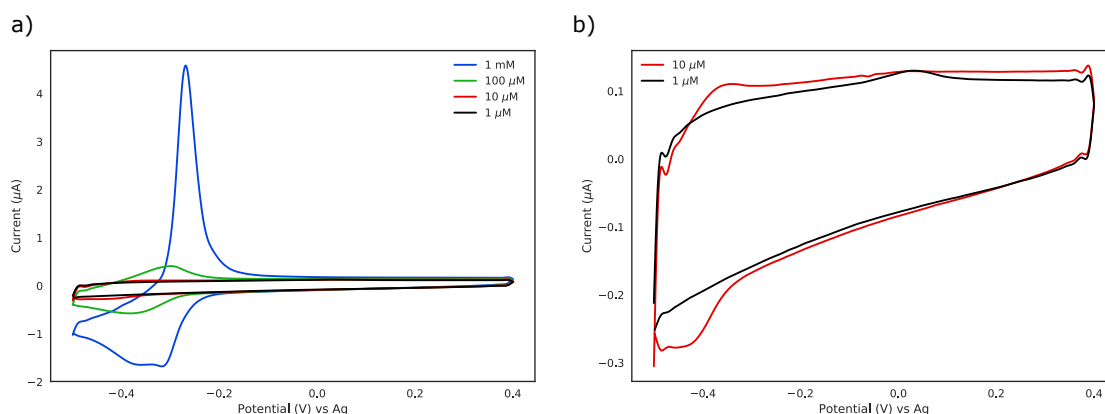
Figure 5.31: **a)** CV plot of MB concentrations from 1 μM to 1 mM in 10 mM KPi buffer. **b)** Plot of 10 μM and 1 μM MB trace from a). The ITO layer of the EGMR was used as the WE, a Pt wire as the CE and a Ag wire as the reference electrode. Scans were performed three times at a scan rate of 100 mV/s.
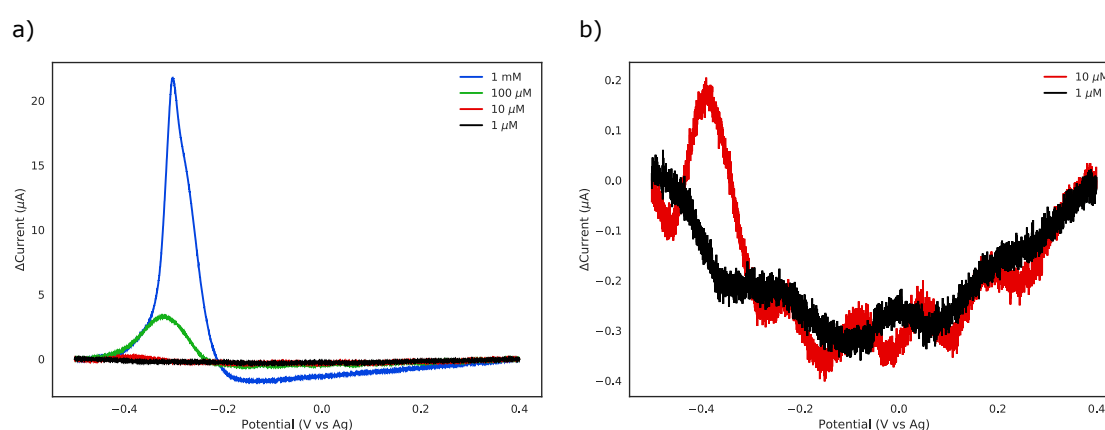
Figure 5.32: **a)** SWV plot of MB concentrations from 1μM to 1 mM in 10 mM KPi buffer. **b)** Plot of 10μM and 1 μM MB traces from a). The ITO layer of the EGMR was used as the WE, a Pt wire as the CE and a Ag wire as the reference electrode. Pulse height = 50 mV, pulse width = 10 ms, step height = 0.15 mV.

Figure 5.31 shows cyclic voltammograms at each concentration from 1 μM to 1 mM. These spectra were performed simultaneously with optical refractive index measurement demonstrating that the EGMR is able to perform electrochemical measurements of redox active molecules in solution can be conducted in parallel with refractive index sensing using the ITO GMR structure. While the redox peaks can be determined for the 1 mM and 100 μM concentrations using CV. The non faradaic background current is too large for the 10 μM and1 μM measurements and so masks the reduction and oxidation peaks at lower concentrations (Table 5.3). The redox potentials E_{pa} and E_{pc} show good agreement with values previously obtained in the literature for MB in phosphate buffer using a Ag/AgCl reference electrode [185]. The shift the peak potential and peak width with the increasing MB concentration

is likely due to the change in the composition of the buffer, with the addition of extra molecules of MB.

The peak separation value for the 1 mM and the 100 μM is greater than the ideal peak separation expected for a two electron redox reaction. Differences in the peak separation values can be attributed to the resistance of the working electrode limiting electron transfer. The decrease in peak separation with increasing concentration could also suggest that the MB is being adsorbed on to the ITO surface [186]. Square wave voltammetry (SWV) can be used to enhance the sensitivity of redox activity detection by reduction of non faradaic background current. Figure 5.32 shows square wave voltammograms for the MB solutions in which the redox peaks are observable at 10 μM, placing the minimum detectable concentration of MB between 1 and 10 μM.

$$i_p = nFAC(\frac{nFvD}{RT})^{\frac{1}{2}} \tag{5.9}$$

As shown in figure 5.31a, the peak current, i_p, of the oxidation reaction increases with voltage scan rate such that i_p is roughly proportional to the square root of the voltage scan rate. This is as predicted by the Randles-Sevcik equation (Eq. 5.9), for a freely diffusing molecule in solution. Here, i_p is the peak current, n is the number of electrons per redox molecule, F is the Faraday constant, A is the working electrode area, D is the diffusion coefficient, v is the scan rate, R is the gas constant and T is the temperature. The deviation from this relationship suggests that there is a contribution from both adsorbed and freely diffusing MB. Assuming a temperature of 25°C, the diffusion coefficient was calculated as 2.15 $\times 10^{-6}$ cm^{2}s^{-1}, which is comparable to the diffusion constants for MB from the literature [187].

Table 5.3: Parameters of MB extracted from CV measurements. CV peaks for 10 μM and 1 μM could not determined.

MB Concentration (μM)	E_{pa} (mV)	E_{pc} (mV)	Peak Separation (mV)
1000	-317	-268	49
100	-376	-295	81

Table 5.4: Parameters of MB extracted from SWV measurements. SWV peaks 1 μM MB could not determined.

MB Concentration (μM)	E_{pk} (mV)	Δi_{pk} (μA)
1000	-301	21.75
100	-320	3.27
10	-385	0.17

5.7.2 pH Dependence of Methylene Blue

To assess whether the pH sensitivity of MB can be observed using the EGMR, I measured the refractive index change and the CV profile of increasing concentrations of MB in the pH range 6-8. The proton dependence of the redox reaction can be observed by the increase in redox potential with respect to increasing pH and is shown in figure 5.33. Both the diffusion coefficient and peak separation also increased with the increasing pH as shown in table 5.5. The lower concentration of the protons in higher pH buffer means that the redox reaction become limited by proton diffusion and thus greater potential is required to attract hydronium ions towards the MB to complete the redox reaction. For each concentration of MB, the resonance wavelength shift apparently increases with reducing pH, as shown in figure 5.34. However, while there is an observable trend, the wavelength shift is within the noise of the measurement.

Table 5.5: Electrochemical parameters of MB at pH 6-8.

pH	E_{pa} (mV)	E_{pc} (mV)	Peak Separation (ΔmV)	$D \times 10^{-6}$ cm^{2}s^{-1}
6	-267	-307	40	1.422
7	-271	-314	43	1.717
8	-273	-321	49	2.139
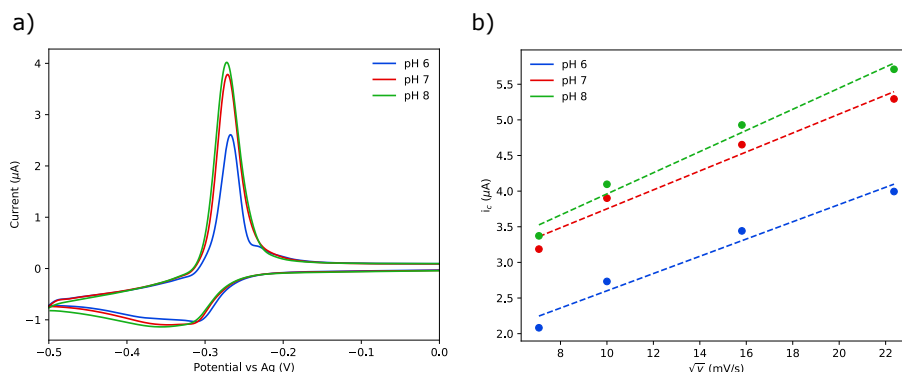
Figure 5.33: **a)** Cyclic voltamagrams of 100 μM MB in pH 6, 7, and 8. **b)** Plot of MB peak reduction current against the square root of the scan rate for different pH.

5.8 Summary

I have demonstrated that a conductive ITO layer can be integrated on to a GMR photonic crystal enabling refractive index sensing in parallel with electrochemical
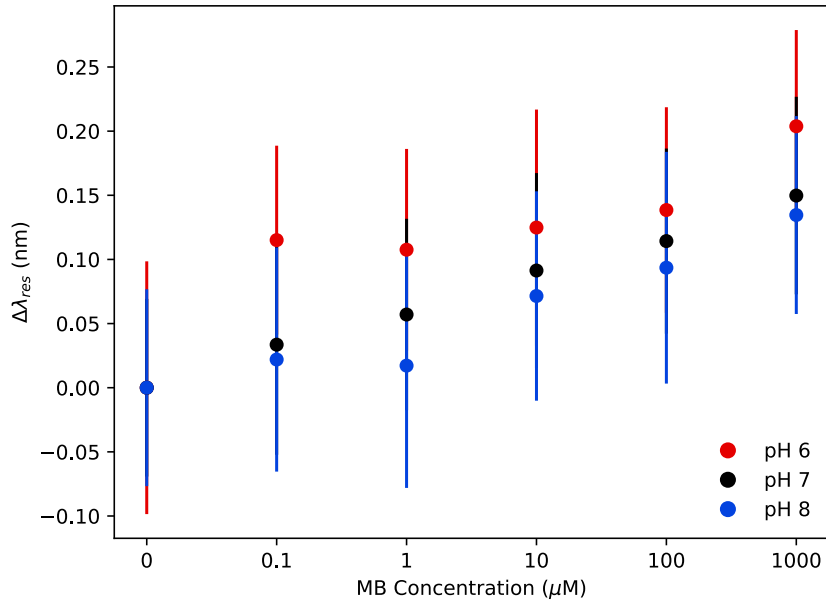
Figure 5.34: Change in EGMR resonance wavelength against MB concentration at pH 6 (red), pH 7 (black) and pH 8 (blue).

measurements. RCWA simulations and characterisation of the ITO thin film deposition were used to optimise the EGMR fabrication and inform the design of the EGMR where the best compromise of ITO thickness for minimum sheet resistance and maximum GMR reflectivity was found to be 60nm thick.

The experimental performance of the photonic characteristics of the EGMR agreed qualitatively with simulations, with the discrepancies being accounted by the large surface roughness of the ITO. The effect of bias voltage on the resonance wavelength was investigated and showed through experimental and theoretical work that the shift in resonance is due to changes in the electrochemical double layer and not the ITO refractive index. The optical sensitivity quantified using a range of NaCl solutions of differing concentrations, was found to be 84.1 nm/RIU. Finally the ability of the EGMR to perform combined optical and electrochemical measurements was confirmed through a study of the redox active molecule methylene blue. Ultimately however the ability to perform simultaneous electrochemical and refractive index sensing has come at the cost of sensitivity for both modalities, with the optical sensitivity in particular being lower than any other reported GMR grating. This does likely restrict the EGMR to applications that require a simultaneous electrochemical and refractive index measurements.

Chapter 6

Multiplexed Label Free Detection using Electrochemical Chirped Guided Mode Resonance (ECGMR) Biosensors

A clinician examining a patient will use a number of different physiological measures such as temperature, blood pressure, and blood oxygen saturation to inform their diagnosis. This decision making process is further supported by diagnostic tests capable of identifying and quantifying concentration of disease specific protein biomarkers. There is increasing interest in technologies capable of detecting multiple protein biomarkers simultaneously to improve diagnostic and prognostic accuracy and to better identify appropriate treatment options.

For example, infectious diseases including respiratory, gastrointestinal and nervous system infections can be caused by a wide variety of infectious agents including bacteria, viruses and fungi [188]. The multiplexed detection of diseases such as Dengue fever, Ebola hemorrhagic fever, and malaria is considered critical for the the future control of outbreaks in the developing world [189]. To test for all of these diseases can take many days, and combines multiple types of tests including phenotypic growth assays and molecular DNA identification.

Similarly, cancer diagnosis uses both protein and gene markers to differentiate between different cancer sub-types. Inflammatory and non-inflammatory breast cancer can be discriminated quantifiably measuring eleven protein biomarkers [190]. A six

protein marker bioassay is able to identify cancerous and non-cancerous tissues in the lungs without having to undergo any further invasive procedures [191]. Timely identification of cancer markers is important for beginning appropriate treatment as soon as possible.

The emergence of personalised and stratified medicine has further enhanced the need for multiplexed diagnostic technologies [192]. Conventional diagnosis and treatment regimes rely on averaged diagnostic data from many patients obtained over many years of medical practice. This does not reflect the disease heterogeneity displayed by individual patients, resulting in sub-optimal diagnosis and treatment. Personalised medicine is an approach which aims to treat patients based on their individual disease state. This new paradigm is underpinned by diagnostics assays, which are repeated at different time points throughout a treatment program to ensure that the treatment is effective for that particular individuals [192]. Changes in this finger print would then be an early indicator of disease, and if it can be improved such as monitoring the concentration of particular drug within the body. This type of diagnostic practice would require significant improvements in point of care diagnostic technology in terms of the number of biomolecules that can be monitored and the cost of each assay before it is practical reality [193].

Sepsis, a complex life threatening condition caused by the body's reaction to infection, is a disease where there is urgent need for multiplex diagnosis. Diagnosis and treatment of sepsis require the detection of multiple biomarkers within minutes of a patient being admitted to the hospital. Current diagnostic technology is too slow to meet this demand so treatment will be started without a complete diagnosis [194]. There is thus immediate need for rapid point of care diagnostics capable of performing multiplexed assays to improve the treatment of these conditions.

Here, I show an approach to multiplexed protein detection using the EGMR technology, focusing on sepsis as disease exemplary. The proposed technology uses electrically addressable array of ITO electrodes fabricated on top of a chirped GMR structure. The ECGMR was used here owing to potential for this device for POC applications. The electrodes are selectively functionalised with different antibodies using an electrochemical approach to direct immobilisation. The photonic resonance of each functionalised, ITO-coated ECMGR can be subsequently measured simultaneously to provided multiplexed detection capability.
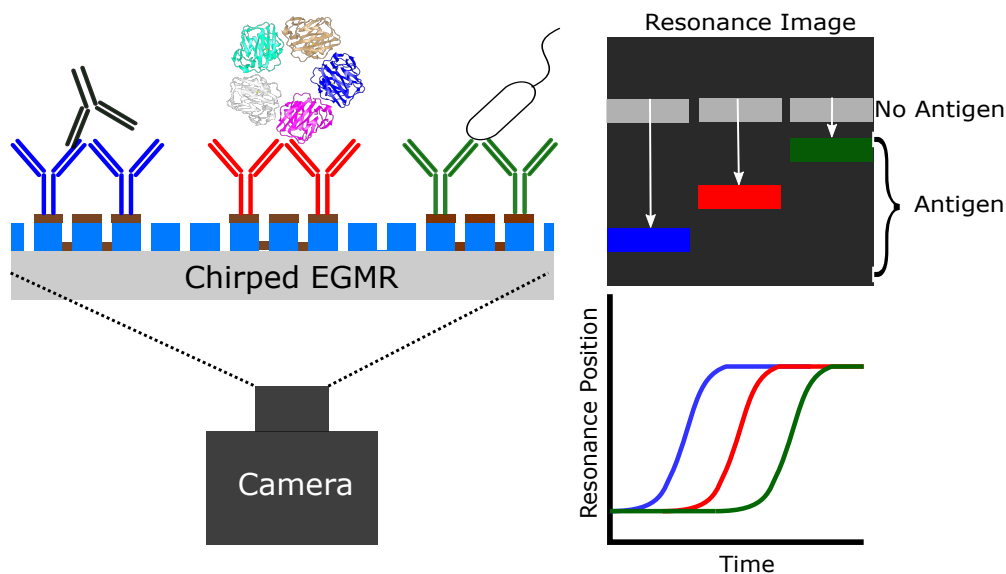
Figure 6.1: Schematic of the chirped EGMR. ITO electrodes are patterned on to the ECGMR. Antibodies are electrografted on to the ITO surface. The spatially separated resonance of the ITO electrodes allows for parallel detection of multiple analytes.

6.1 Methods of Multiplexing Surfaces

A significant challenge in fabricating a multiplexed biosensor is how to selectively functionalise the sensor surface with the different bioreceptors needed for the assay in a cheap and high throughput way. There are a number of methods that have been developed to address this problem that I will review briefly below.

6.1.1 Spotting

The most common way of fabricating a multiplexed diagnostic assay is to spot the different antibodies on to separate sections of the sensor. For a low density antibody array, this can be accomplished by hand using a standard pipette. For larger density arrays (and more repeatable results) there are number of automated robotic spotters that are available. Robotic spotters typically use arrays of micro-pins as the spotting element, with many variants on this geometry to improve spotting repeatability depending on the molecule being immobilised and viscosity of the media [195]. The tips of the micro-pin are immersed into wells containing different antibodies, drops of which form on the ends of the pin due to surface tension. The pins are then lowered on to the substrate allowing for the covalent binding of the bioreceptors to the prepared surface. The size of the spots is dependent on the the hydrophobicity

of sensor surface and so must be tuned for each substrate but is generally limited to the micron range [196]. Although providing high throughput, these systems are expensive, costing hundreds of thousands of dollars.

Spatial resolution in the order of nanometres using femtolitre sized spots of antibodies has been demonstrated using hollowed atomic force microscope tips [197]. The high spatial resolution leads to the possibly of the thousands of samples being immobilised within millimetre sized sensor errors. Creating multiplexed arrays this way however is extremely time consuming as the functionalisation must be performed serially. While research has been performed to multiplex this approach, atomic tip spotting is reserved for research applications for the foreseeable future.

One challenge of all spotting techniques is that evaporation of the material may cause the surface to dry out, which can affect the bioreceptor confirmation and consequently its performance as a sensing element.

6.1.2 Microfluidics

Microfluidic channels can be used to provide spatial separation of sensor regions for spatially controlled functionalisation. At its most basic, the microfluidic cell consists of separate channels that are adhered to the sensor surface. Solutions of different antibodies are then flowed through the channels in parallel to functionalise the sensor. After allowing time for the bioreceptors to covalently bind, the remaining unbound bioreceptors can be washed out of the channel leaving behind the functionalised surface.

The microfluidic chambers can be fabricated from multiple materials. The use of PDMS for research applications is common because it is cheap to process and new designs can be fabricated quickly using standard lithographic processes [198]. PDMS can also be easily bonded to Si and glass based biosensors using O_2 plasma bonding and other plasma free techniques are available as well. The use of 3D printed microfluidics has grown greatly since the advent of commercially available 3D printers [199]. The channel size of 3D printed microfluidics is generally restricted to tens of microns and sealing the the biosensor to such small channels can be potentially challenging. Glass microfluidic devices are also commonly used but are more difficult to fabricate due to the hydrofluoric acid etching step that is typically used for etching the channel into the substrate [200].

Microfluidic laminar flow patterning takes advantage of multiple laminar streams in-

herent to fluid flow in micrometre-scale fluidic channels. In the laminar flow regime there is no mixing between the different streams, so multiplexed functionalisation of the surface can be achieved without the need to define individual channels [201]. The direction of laminar flow has also been controlled electrically through the electroosmotic force effect, to create two dimensional arrays [202].

More complex microfluidic systems include fluidic channels that can be switched using air or mechanical pressure switches can be used to create addressable systems. However the complexity of the switching system would make them unsuitable candidates for point of care high density array diagnostic devices [203]. Multiplexed paper microfluidics have also been demonstrated for point of care diagnostics [204]. Although cheap to produce and easy to use, these paper devices suffer from the same limitations associated with lateral flow assays, namely, low sensitivity and quantification accuracy, limiting their future applications. Multiplexed paper fluidics is however an excellent choice for applications in low resourced settings that require only a yes/no answer and where there are no other forms of testing available.

6.1.3 Electrically Controlled Functionalisation

Electrically controlled surface functionalisation uses electrochemical reactions to graft molecules to an electrode surface. Early approaches to selective functionalisation via electrical control focussed on the binding of thiol self assembled monolayers (SAM) to Au surfaces. By selectively biasing the Au electrodes, the thiol adsorption could either be inhibited or promoted [205]. Alternatively a thiolated-SAM can be desorbed from a Au electrode by electrochemical reduction of the Au sulfur bond. For example, electrical removal of a thiolated poly ethylene glycol protective layer on Au electrodes has been used for the fabrication of protein aptamer microarrays[206].

Electrically controlled "click" chemistry using the binding of a thiol containing molecule to surface immobilised benzoquinone has been demonstrated on Au electrodes. Here, the application of bias voltage to a benzoquinone functionalised electrode enables the formation of a covalent bond between a thiol containing molecule and the benzoquinone. This approach has been demonstrated to direct the immobilisation of thiolated DNA on the Au surface of an SPR sensor [207]. Controllable azide-alkyne reactions have also been demonstrated using a redox active protective group. The protective group can be removed electrochemically leaving an exposed alkyne group which can bind covalently to an azide functionalised molecule using the click reaction [208].

Diazonium salts are a chemical group that has been used widely for spatially controlled functionalisation of metal and semiconductor surfaces [209]. A diazonium salt is formed from an aromatic amine. In order to enable electrografting, the amine group has to activated to form a diazonium ion. The process of forming a diazonium is called diazonisation and is shown schematically in figure 6.2. Diazonisation is typically achieved by combining the aromatic amine with sodium nitrite and HCl. The HCl and sodium nitrite react to make nitrosonium ions that attack the amine forming a radical aryl group. The reduction of this aryl radical can be used to attach the diazonium salt to the desired surface. The R group of the diazonium salt can be replaced with almost any functional group, including amines, azides, carboxylic acids or thiol groups for the binding of bioreceptors.
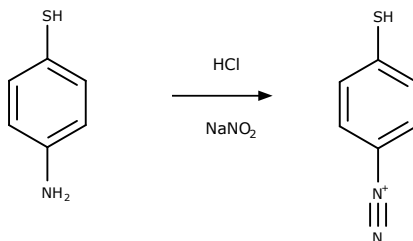
Figure 6.2: Diazonisation of the 4-aminothiolphenol from exposure to HCl and NaNO$_2$ to create a diazonium salt.

Electroreduction is the most common method of attaching diazonium salts to a surface. The diazonium ion is first formed *in situ* from the aromatic amine group after which negative bias voltage is applied to the surface using a standard electrochemical setup. This is typically performed by CV, but other techniques such as chronoamperometry have been demonstrated. On the first CV scan there will be large reduction peak associated with electron transfer from the electrode to the diazonium ion shown schematically in figure 6.3. The reduction leads to a covalent bonds between the diazonium ion amd the sensor surface. The formation of the diazonium layer on the surface prevents further electron transfer resulting in an absence of the reduction current peak in subsequent scans. The excess diazonium salt is washed off when the CV peak can no longer be observed, leaving only the functionalised surface. One challenge of immobilising diazonium salt is that diffusing radicals can attack the aryl groups that have already formed on the surface. This results in a multi-layer structure forming instead of a monolayer. The formations of these layers can be prevented by techniques such as radical scavenging, but this increases the complexity of the diazonium protocol [210].

There are many other methods of diazonium functionlisation, including photocat-

alytic chemical reduction, ultrasonication, heating and spontaneous reaction with the surface [211]. Chemical reduction of diazonium salts is primarily used to functionalise nanoparticles which cannot be contacted electrically. Photocatalysis offers the potential for patterning substrates directly with diazonium salts using photolithography masks.

There are two main advantages to using electrochemically directed reduction of diazonium salts as opposed to self assembled monolayers. First, the functionalisation process is very rapid, with several CV scans at 100 mV/s being performed in minutes as opposed to the several hours required for spontaneous SAM assembly. Secondly, as the reduction only occurs on the biased electrode, the functionalisation can be spatially controlled. This has been applied to multielectrode arrays to provide different surface functionalities on different electrodes [212]. The spatial resolution for patterning a single diazonium ion has been shown to be less than 1 μm although here spatial resolution was limited by the lithographic definition of the electrode [213]. For functionalisation of electrodes with different targets, the spatial resolution is instead limited by the amount of uncontrolled reduction of the diazonium salts on to adjacent unbiased electrodes. The spatial resolution in this case has been shown to be much lower, with values typically being in the tens of micrometer range [214].

The most widely reported method of using diazonim salts to functionalise surfaces with antibodies is to first electrograft the surface with diazoniums, then to covalently attach the antibody to the diazonium modified surface using a chemical linker such as NHS/EDC [215]. This method has the advantage that the antibodies are not exposed to the highly acidic conditions required for activation of the diazonium radical, which may impair their function. This method is not compatible with fabricating a multiplexed array however. After attaching the first antibody it must be then exposed to the reducing conditions for grafting the diazonium to the next electrode. Exposure to the high concentration of HCl would impair the antibody function reducing the device sensitivity or possibly destroying it entirely.

An alternative is to electrograft diazonium salts with different R groups to different electrodes, and then use the appropriate crosslinking techniques to bind the different antibodies simultaneously [104]. The disadvantage of this method is that this would require further modification of the antibodies to support these different crosslinker techniques. There are also only a limited number sufficiently different, orthogonal, crosslinking techniques for them to be performed in parallel.

It would be ideal instead if the antibodies can be linked to the diazonium salts prior to being grafted to the surface i.e. the antibodies can crosslinked to the diazonium

salt in solution then excess diazonium linker can then be removed from the solution using a spin column or other purification techniques. To achieve this requires the development of an antibody compatible diazonium electrografting protocol, which lowers the concentration HCl used for activating the diazonium [216]. The electrografting can also be performed more rapidly as there is no need to wash off excess diazonium salt first or to wait for the antibodies to bind to the surface, once the CV sweep is complete the antibodies are covalently bound to the surface via the diazonium.
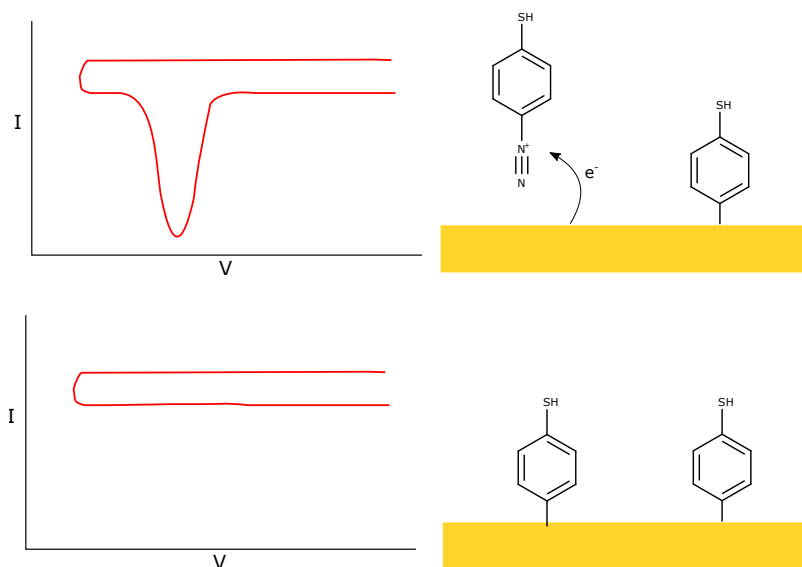
Figure 6.3: Electrografting of diazonised aminothiolphenol to a Au electrode. Electron transfer during the CV sweep from the electrode reduces the aryl radical forming a covalent bond with the electrode surface, which can be seen the by the current peak. On following scans the peak cannot be observed as there are no further binding sites the diazoniums to bind.

6.2 A Biocompatible Diazonium Electrografting Protocol

Diazonium functionalisation is undertaken in highly reducing conditions in an excess of HCl and nitric acid. These conditions are damaging to antibodies and could impair binding affinity once immobilised on the surface. To prevent this, the diazonium protocol was adapted to lower both the HCl and nitric acid concentration.

Optimisation of the biocompatible diazonium grafting protocol was first performed using planar ITO electrodes fabricated on glass substrates. Glass slides were cleaned using a UV ozone cleaner for 30 minutes followed by sonication for ten minutes in

2% Hellmanex glass cleaner, DI water, ethanol then dried with N_2. ITO surfaces for functionalisation were made by depositing 100 nm of ITO on to the cleaned glass slides using the ITO deposition process described in chapter 5. A contact wire was adhered to the ITO using silver epoxy resin and baked on a hotplate at 100°C for two hours. For electrografting of the diazonium ion, the ITO films were loaded into an electrochemical cell secured by a 5 mm diameter o-ring that included a Pt wire counter electrode and an Ag wire pseudo reference electrode. To verify the electrochemical cell was working correctly, electrochemical impedance spectroscopy (EIS) was performed from 1 mHz to 1 MHz using a 10mV amplitude sine wave in 10 mM KPi buffer. Electrografting was monitored using CV using an SP-300 potentiostat. The voltage was scanned from 0 to -1V at 100 mV/s.
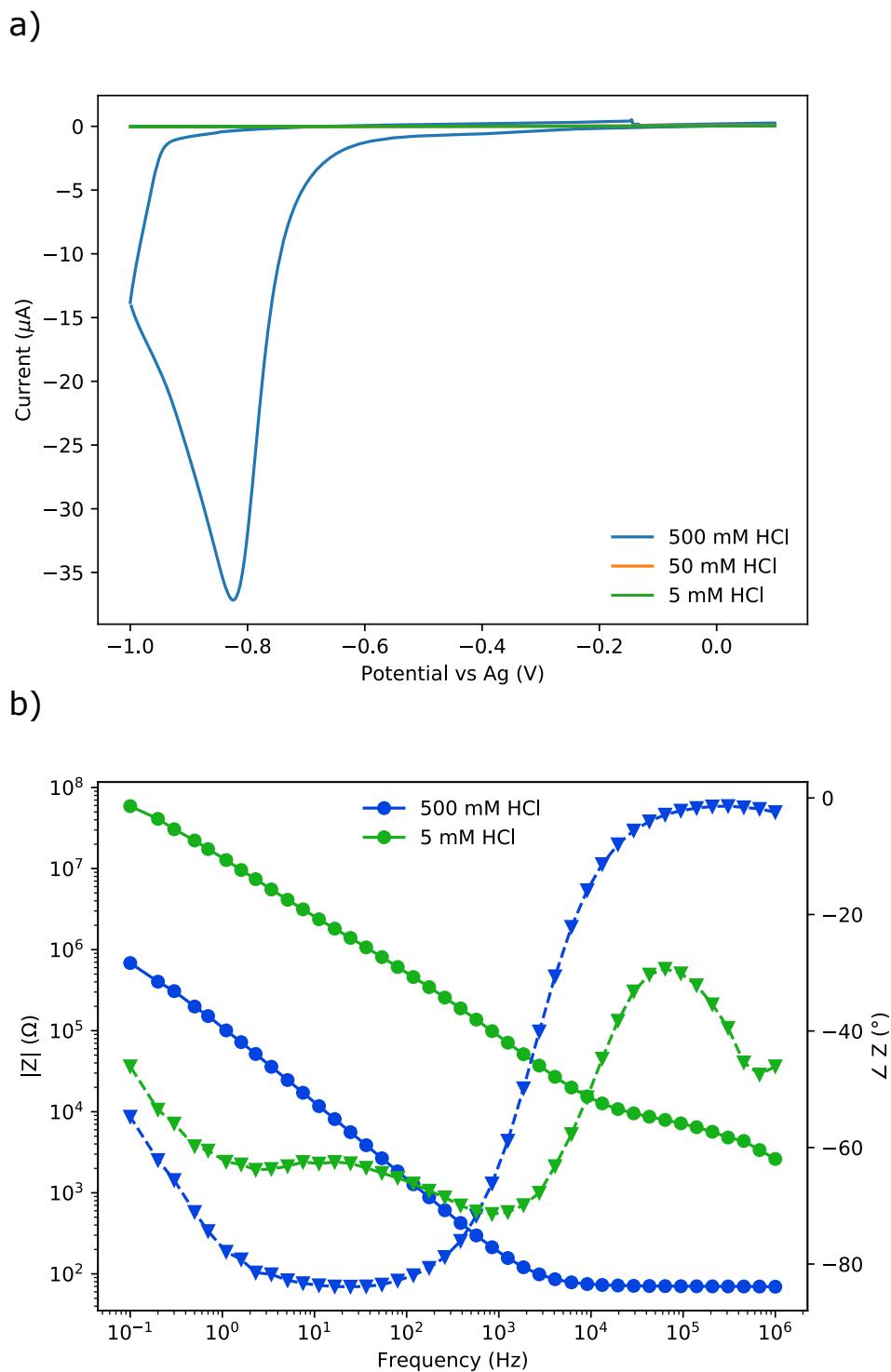
Figure 6.4: **a)** CV of aminothiolphenol using 500 mM, 50 mM and 5 mM HCl. **b)** EIS of aminothiolphenol using 500 mM and 5 mM HCl.

The typical protocol to activate the aminothiolphenol diazonium is to mix 20 μL of 100 mM aminothiolphenol diluted in methanol and 40 μL of 300 mM NaNO$_2$ in DI water and 2 mL 500 mM HCl that had been diluted from 2 M in DI water. The final concentrations of the aminothiolphenol was 0.97 μM. Using these conditions

with 500 mM HCl, the diazonium reduction peak of aminothiolphenol on ITO using 500 mM HCl can be observed at -0.82V as shown in figure 6.4a. No diazonium reduction was observed using the lower 50 mM and 5 mM HCl concentrations. Even at these dilutions the HCl solutions are far in excess compared to the concentration of aminothiolphenol so the reduction peak should have been evident. EIS of the 500 mM and 5 mM HCl solutions in figure 6.4b revealed that the solution resistance of the low HCl concentration solutions had increased by two orders of magnitude, limiting electron transfer to the diazonium.
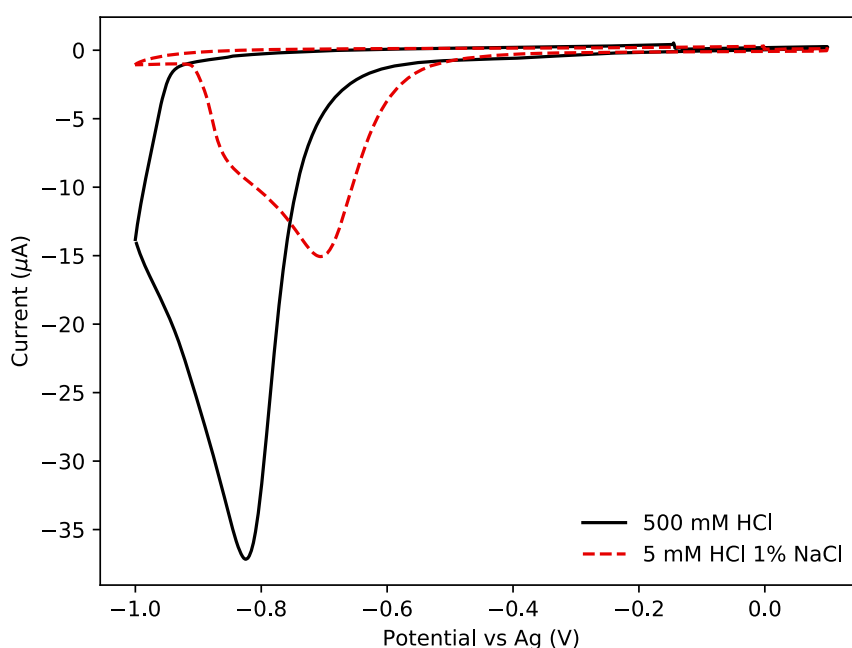
Figure 6.5: First CV scans of aminothiolphenol at 500 mM and 5 mM HCl with 1% NaCl w/v.

Supplementing the solution with 1%NaCl to increase the solution conductivity aided charge transfer to the aryl radical and restored the peak as shown in Figure 6.5. The difference in current suggests that the electrografting is not as efficient when performed in the 5 mM HCl supplemented with 1% NaCl compared to the 500 mM HCl protocol. CV sweeps without aminothiolphenol in solution confirmed that the reduction peak is due to diazonium reduction and not the undesired redox reactions in the buffer.

6.2.1 Nile Blue electrografting

To confirm if the aminothiolphenol using the reduced HCl protocol is bound to the surface I used the redox active molecule nile blue (NB) to label the aminothiolphenol. NB is a redox active molecule similar to methylene blue which was used in chapter 5, and undergoes a two electron two proton reduction [217]. The presence of redox activity after grafting from the NB would be confirmation of surface funcitonalisation. The NB was modified by Dr. Lisa Miller (Department of Chemistry, University of York) to include a maleimide group to crosslink to the thiol group of the aminothiolphenol as shown in figure 6.6.
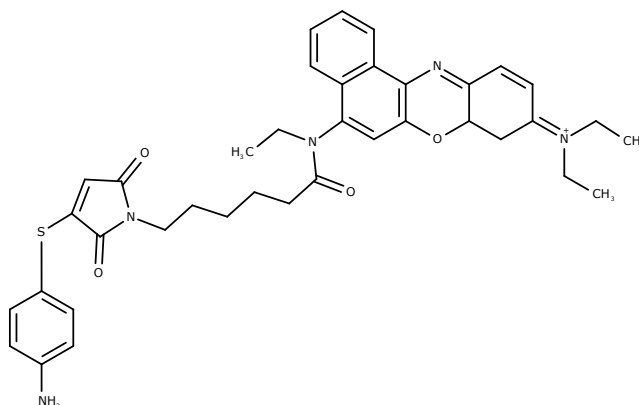
Figure 6.6: Chemical structure of aminothiolphenol crosslinked to maleimide modified nile blue.

To form the aminothiolphenol NB conjugate, 100 mM aminothiolphenol dissolved in methanol was mixed with 200 mM NB maleimide for two hours at room temperature. An excess of NB was used to maximise the concentration of aminothiolphenol crosslinking with the NB, the excess NB can be washed away after the electroreduction of the aminothiolphenol. After crosslinking 20 μL of the aminothiolphenol NB was activated using the 5 mM HCl protocol discussed in section 6.2.
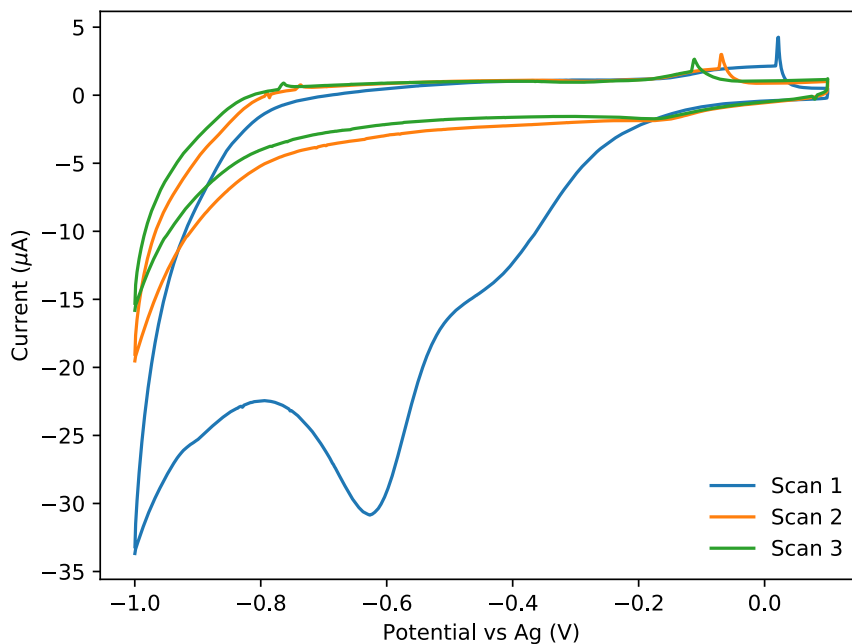
Figure 6.7: Electrografting of the aminothiolphenol nile blue conjugate to an ITO working electrode. CV scans performed from 0.1 to -1V at 100 mV/s. A Pt wire was used as the CE and an Ag wire as the RE.

The electrografting of the aminothiolphenol-NB to a 100 nm thick ITO surface is shown in figure 6.7. A large reduction peak is observed at -0.62V. This reduction peak is present only on the first CV scan suggesting the electrografting is complete after a single voltage scan to produce a dense aminothiolphenol-NB layer which blocks the electrode surface. I note, the small reduction peak at -0.15V is is believed to be associated with the NB reduction peak.

$$N = \frac{QN_A}{nF} \tag{6.1}$$

The number of molecules N immobilised on to the ITO surface can be obtained using equation 6.1 where Q is the total charge, n is the number of electrons involved in the reduction reaction per molecule, F is Faraday's constant and N_A is Avagadro's number. The total charge Q is found from the integral of the reduction peak with the non faradaic background subtracted. The diazonium surface coverage after the first CV sweep is approximately 5.1×10^{11} molecules per cm^2. The surface density is higher than that reported for a molecular monolayer of diazoniums, which are typically in the region of the 10^{10} mol/cm^2 indicating that there has been some polymerisation of diazoniums [218]
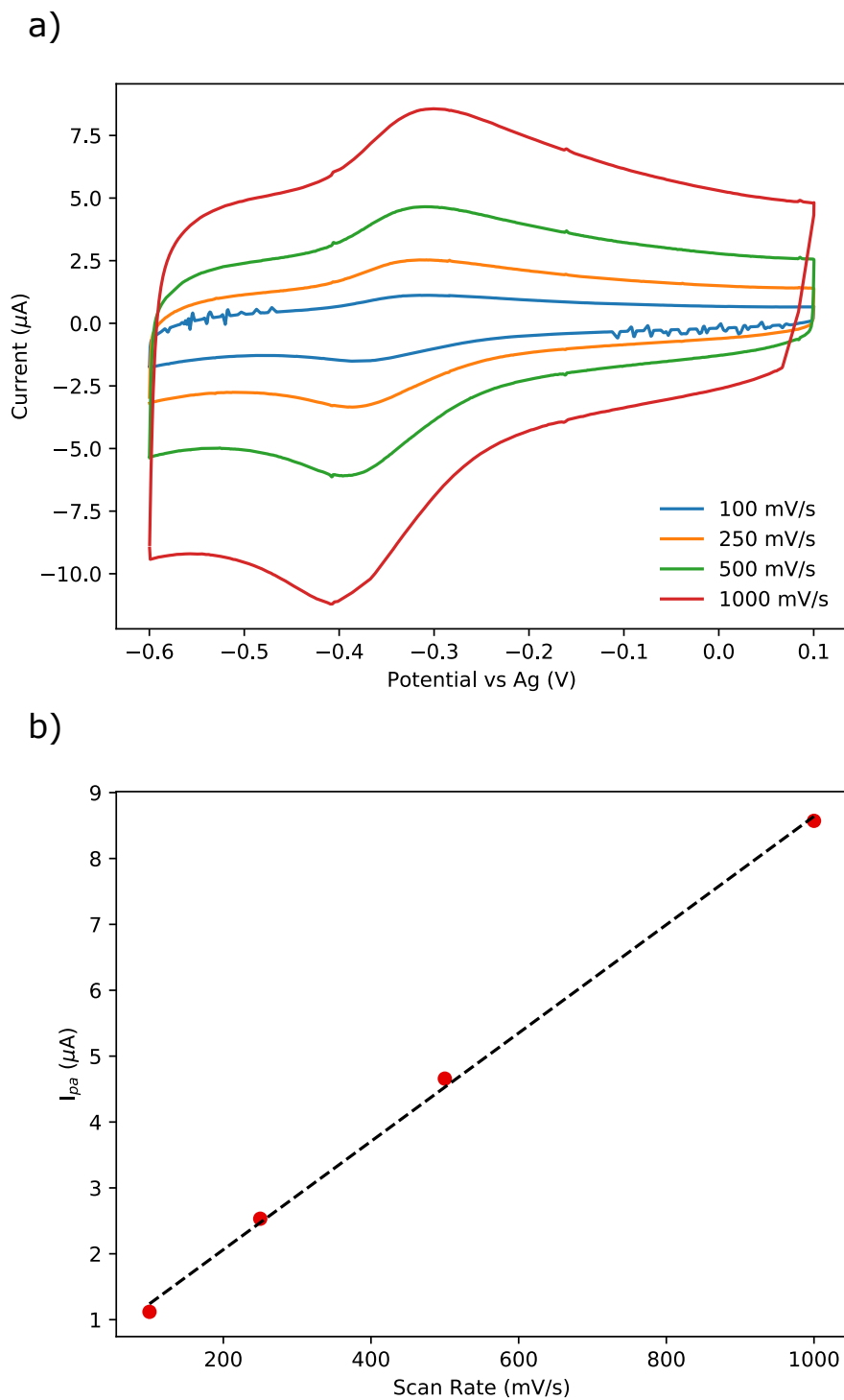
Figure 6.8: **a)** CV of nile blue immobilised to a 100 nm ITO electrode by electrografting at increasing scan rates. A Pt wire was used as the CE and Ag wire as the reference. Scans were performed in pH7 10 mM KPi buffer. **b)** Nile blue oxidation peak current I_{pa} against the scan rate of the surface immobilised. $R^2 = 0.998$.

After electrografting, the ITO surface was washed three times with 10 mM KPi buffer. Figure 6.8a shows CV scans of aminothiolphenol-NB functionalised ITO surface in pH 7.2 10 mM KPi buffer. Both oxidation and reduction peaks characteristic

of a redox reaction can be observed, demonstrating that the aminothiolphenol conjugated NB has been grafted to the ITO surface. The oxidation peak E_{pa} was at -0.31V and the reduction peak E_{pc} at -0.38V at 500 mV/s scan rate, the small difference in oxidation and reduction potential demonstrates that the aminothiolphenol-NB has been grafted to the electrode surface. The peak current was linear with respect to the scan rate as shown in figure 6.8b, confirming that the aminothiolphenol-NB has been successfully immobilised to the surface and is not freely diffusing in the solution. The FWHM of the reduction peak was approximately 100 mV. The theoretical FWHM of a redox reaction is $\frac{90.6}{x}$, where x is the number of electrons involved in the reaction. This indicates that the immobilised aminothiolphenol-NB undergoes a one-electron reduction rather than two typical for NB. The modification of the NB to include the maleimide group is achieved by the formation of an amide bond that removes one of the electrons from the electrochemical reaction [217]. The FWHM is therefore consistent with electrochemical properties of the NB. I note, reported values of FWHM from the literature for surface immobilised redox active molecules frequently differ from the exact theoretical value. This is attributed to the electrostatic interactions of between molecules within the film [182].
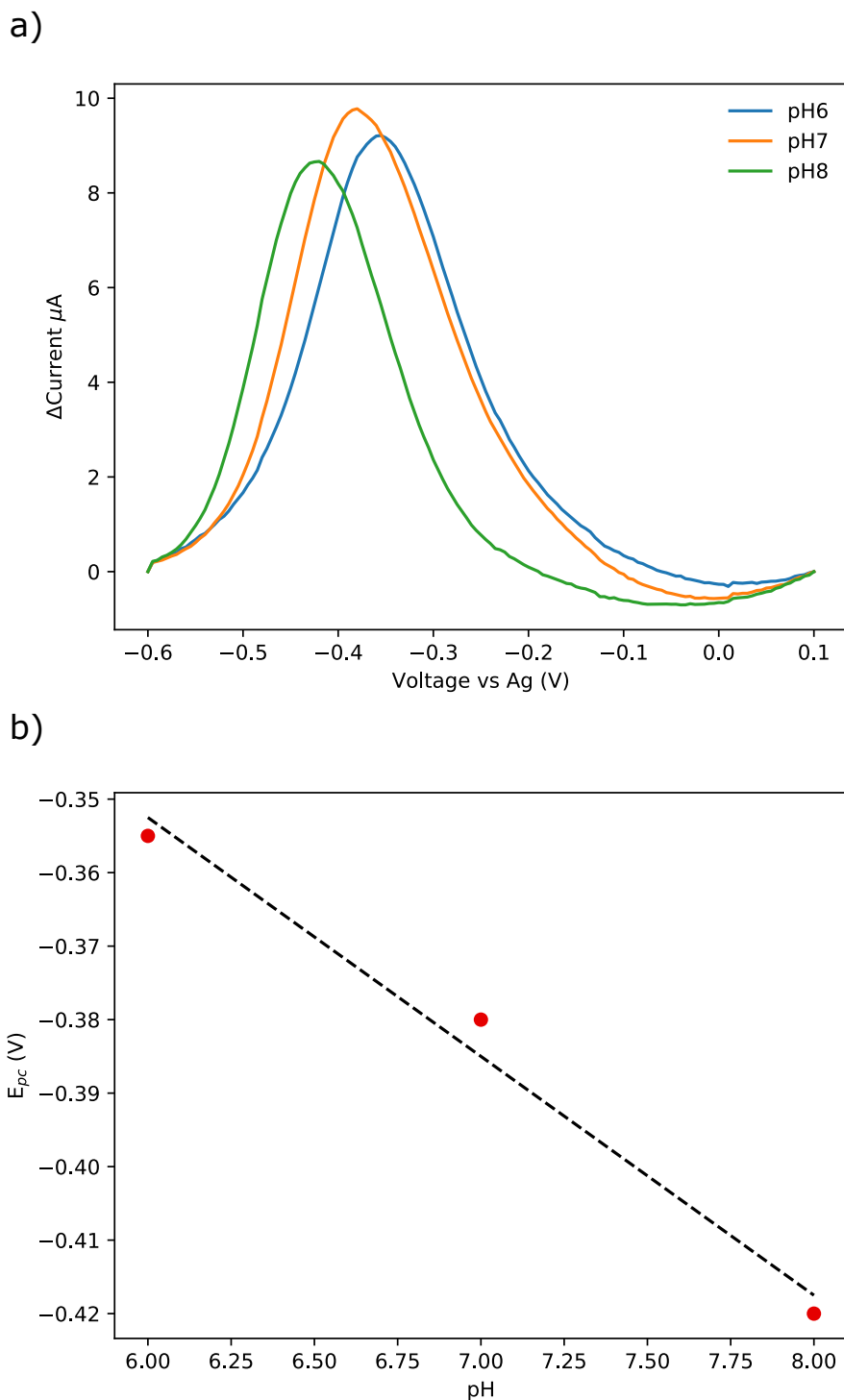
Figure 6.9: **a)** SWV of surface immobilised nile blue in 10 mM KPi buffer at pH 6-8. Pulse amplitude = 50 mV, pulse width = 10 ms, step height = 5mV. **b)** Nile blue SWV peak potential E_{pc} aginst pH. $\Delta E_{pc}/$pH = 32.5mV, R^2 = 0.983.

As the electrochemical activity of the aminothiolphenol-NB is proton dependent, the reduction potential will be sensitive to the pH of the buffer. Figure 6.9a shows SWV of the immobilised aminothiolphenol-NB. The buffers were changed in the order pH 7, pH 6, pH 8. The peak potential increases from -0.35V at pH 6 to -0.42V due to

reduced concentration of hydronium ions. The slope of the reduction potential E_{pc} against the pH shown in figure 6.9b reveals a 32.5 mV change in E_{pc} per pH change.

6.2.2 Diazonium functionalisation of antibodies

Having established a low HCl concentration protocol for functionalising surfaces using diazonium salts it was necessary to link the aminothiolphenol diazonium to an antibody.
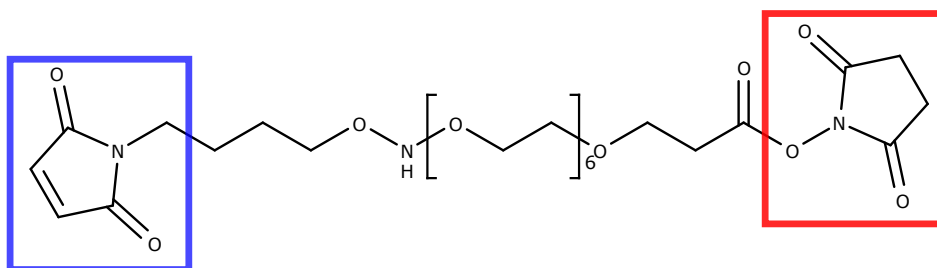
Figure 6.10: Chemical structure of the heterobifunctional PEG crosslinker. The malemide group highlighted in blue forms a thioether bond with the thiol group of the aminothiolphenol. The NHS ester highlighted in red forms an amine bond with an amine group on a lysine residue on the antibody.

A heterobifunctional maleimide NHS ester 6-poly ethylene glycol (PEG) linker, shown in figure 6.10, was used to cross-link the aminothiolphenol to lysine groups available on the antibody surface. The total length of the PEG linker is 31.7 angstroms. The malemide group reacts with the thiol group on the aminothiolphenol to form a thioether bond, while NHS ester and the available amine group on the lysine amino acid then form an amide bond, completing the functionalisation. It is important to note that at >pH 8.5 the malemide group will begin to react with the amine groups as well as the NHS ester. The pH was therefore controlled inhibit this unwanted reaction. Antibodies have over 30 thiol containing cysteine residues which could be crossed linked by the maleimide group. In a properly folded antibody however, these thiols should be all linked together into disulphide bonds as they are important for the structure of the proteins. Free sulphydryl groups may still be available in the variable region of the antibody, so there is a possibility of undesired thioether bonds between the PEG linker and the antibody.

PEG linkers have been widely used in biosensors and have been shown to aid specificity in surface immobilised antibody assays by inhibiting biofouling by increasing the hydrophilicity of the surface. PEG linkers have also been reported to increase sensitivity due to the increased flexibility of the antibody to re-orientate on the

surface to better expose the binding site of the antibody [219].

While the PEG linker will provide conformational flexibiltiy, the antibody orientation cannot be controlled precisely when immobilising via lysine groups. This can reduce the device sensitivity as it cannot be guaranteed that binding site of the antibody is accessible to the target biomolecule [220]. Controlling the antibody orientation can be be achieved in a number of different ways including:

- Labelling the C terminus of the antibody with a selective group such as as histidine tag.

- Using an intermediate protein such as a protein A or protein G that has a high affinity to the C terminus of the antibody.

- Cleaving the disulphide bonds at the centre of the antibody leaving available thiol groups for binding.

As a proof of concept however, crosslinking using the lysine groups is simple, quick and does not require any extra modification of the antibodies. Furthermore as lysine groups are available on all antibodies, the protocol can be changed to a different protein target by only changing the antibody.

Aminothiolphenol is insoluble in water and must be dissolved in organic solvents. Antibodies however must be kept in aqueous based buffers to retain their functionality and will quickly precipitate if exposed to excess organic solvents. The PEG linker is particularly important for linking of the aminothiolphenol and the antibody as the linker increases the hydrophilicity of the aminothiolphenol, allowing dilution of the organic solvent to levels that will not precipitate the antibody. Linking the aminothiolphenol and the PEG first in organic solvent also prevents degradation of the NHS ester while the thiolether bonds between the aminothiolphenol and PEG are formed. Once in aqueous solvent the NHS ester will only be reactive for 20 to 30 minutes at room temperature.

To form the antibody aminothiolphenol conjugate, 20 mM aminothiolphenol dissolved in DMSO was mixed with 2 mM PEG linker in DMSO for one hour to form the thioether bond. 40 μL of the PEG linked aminothiolphenol was subsequently diluted with 40 μL of 1% NaCl in DI water. Finally, 20 μL of 100 μg/mL of the desired antibody was added and allowed to incubate for 30 minutes. Initial research focused on an antibody against C reactive protein (anti-CRP)

After the crosslinking the excess diazonium was removed by centrifuging in a microcentrifuge at 13,000 RPM for 15 minutes using a 100 kDa protein spin column

to prevent blocking of the electrode with free PEG linkers. The filtered antibodies were collected by centrifuging at 4000 RPM for 4 minutes upside down into a fresh tube, giving a final volume of approximately 30 μL. To activate the antibody functionalised diazonium salt, 20 μL of the filtered antibodies were mixed with 20 μL of 60 mM NaNO$_2$, 20 μL of 50 mM HCl, and 140 μL 1% NaCl in DI water. The solution was left to react for 15 minutes to ensure complete diazonisation before electrografting .

To demonstrate that the diazonium modified antibodies can been successfully grafted to an ITO surface, I labelled the surface immobilised antibody using a secondary anti-IgG antibody labelled with horse radish peroxidase (HRP). HRP an enzyme commonly used in ELISA assays as a catalyst for oxidising a colorimetric dye such as tetramethyl benzidine (TMB) [221]. In the presence of the hydrogen donor H$_2$O$_2$ the TMB changes from colourless to blue. Measuring the absorbance at 650 nm enables quantification of the colour change, which is proportional to the concentration of HRP labelled secondary antibody and consequently the concentration of the primary antibody. Given the lack of information about the orientation of the surface immobilised antibodies, I deliberately used a polyclonal anti-IgG secondary antibody, to maximise the chance that there would be an available epitope present for the secondary antibody to bind to.

The activity of the HRP can also be measured electrochemically using chronoamperometry. Applying a voltage step reduces the TMB resulting in a pulse of current that decays exponentially over time. Measuring the activity of the HRP electrochemically has been shown to be more sensitive than absorbance based techniques, and it is also more convenient here given that the ITO electrode is already loaded into an electrochemical cell.

Aminothiolphenol crosslinked with the PEG linker only was used a non antibody control to quantify non specific adsorption of the secondary antibodies. The conjugates of aminothiolphenol-anti-CRP and aminothiolphenol-PEG were grafted 100nm thick planar ITO surfaces using CV performed from 0.1 to -1V at 100 mV/s. The voltage scan was repeated three times. Figure 6.11 shows the electrografting of the aminothiolphenol-anti-CRP conjguate to the ITO surface. A clear reduction peak at -0.81V associated with electroreduction of the aminothiolphenol-anti-CRP. While the magnitude of the reduction peak was largest for the first scan, clear electrografting was also observed in subsequent scans. This suggests that antibodies could be crosslinked to each other by further diazonium grafting or the reduced diffusion of the large molecular weight aminothiolphenol-anti-CRP conjugate compared to aminothiolphenol inhibits the rate of electrografting.
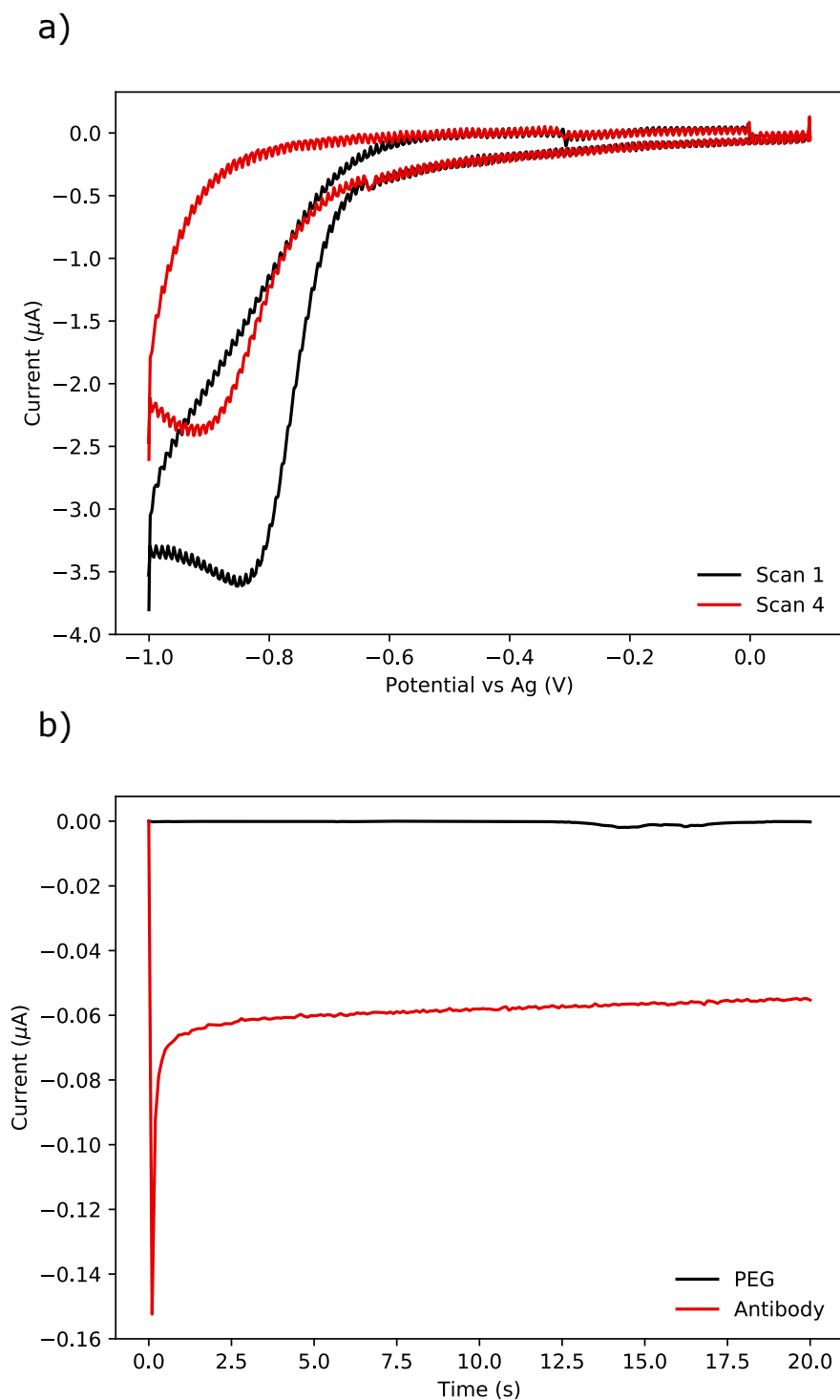
Figure 6.11: **a)** Electrografting of the aminothiolphenol-anti-CRP conjugate. CV scans were performed form 0.1 to -1V at 100mV/s. **b)** Chronoamperometry of the aminothiolphenol-PEG and aminothiolphenol-anti-CRP modified surfaces labelled with HRP. Voltage step was 0V vs Ag.

Following electrografting, the surface was washed three times in KPi buffer to remove any non covalently bound antibodies. Any remaining unfunctionalised surface regions were subsequently blocked with 1% caesin for 30 minutes to reduce

non specific binding of the secondary antibody. The aminothiolphenol-anti-CRP and aminothiolphenol-PEG functionalised surfaces were then exposed to 10 μg/mL HRP labelled anti-IgG for 30 minutes and then washed three times in KPi buffer to remove any unbound secondary antibody.

The reduction of TMB by HRP was measured using chronoamperometry at 0V versus the Ag pseudo reference electrode for 20 seconds. The current step followed by the exponential decay observed on the aminothiolphenol-anti-CRP electrode is characteristic of the enzymatic activity of HRP as shown in figure 6.11. In contrast there was no detectable current response in the aminothiolphenol-PEG functionalised surface, demonstrating the anti-fouling properties of the PEG and caesin functionalised surface.

6.3 Electrochemical Chirped GMR (ECGMR)

Having successfully demonstrated electrografting of antibodies on to ITO surfaces I now proceed to present a multiplexed protein array based on a EGMR using the chirped GMR structure, known as ECGMR, with individually addressable ITO electrodes to spatially control antibody electografting. A 500 μm chirped GMR was fabricated into a 150 nm thick Si_3N_4 substrate using the method and protocol described in chapter 4. Four individually addressable ITO electrodes were fabricated on top of the chirped GMR using optical lithography and a lift off process. The electrodes were 70 μm wide and separated by 20 μm. I previously showed in chapter 5 that the optimum thickness of the ITO to maximise both optical and electrochemical sensitivity was 60 nm. The ITO layer however was shown to reduce the optical sensitivity. For the low cost multiplexed protein sensor however the electrochemical activity of the ECGMR will be used for electrografting only and not as a characterisation tool. Instead it is the optical modality that will be critical to ensure assay sensitivity. As a result the thickness of the ITO electrodes was reduced to 15 nm in order to reduce the optical losses and consequently improve the sensitivity of the sensor.

Scanning electron microscopy of the four ITO electrodes patterned on to the chirped GMR are shown in figure 6.12. The chirping of the grating cannot be imaged directly as the period change is too long compared to the geometry of the GMR. I note, roughness at the edge of the electrodes was introduced due to a technical error in the laser writer design file. Figure 6.13 shows the grating structure in both the Si_3N4 and ITO areas. The grooves of the grating are clearly defined and the filling fraction

is constant across the length of the grating. The surface roughness is consistent on both the Si₃N4 and ITO sections suggesting that it is primarily due to the ARP-C charge dissipation layer.
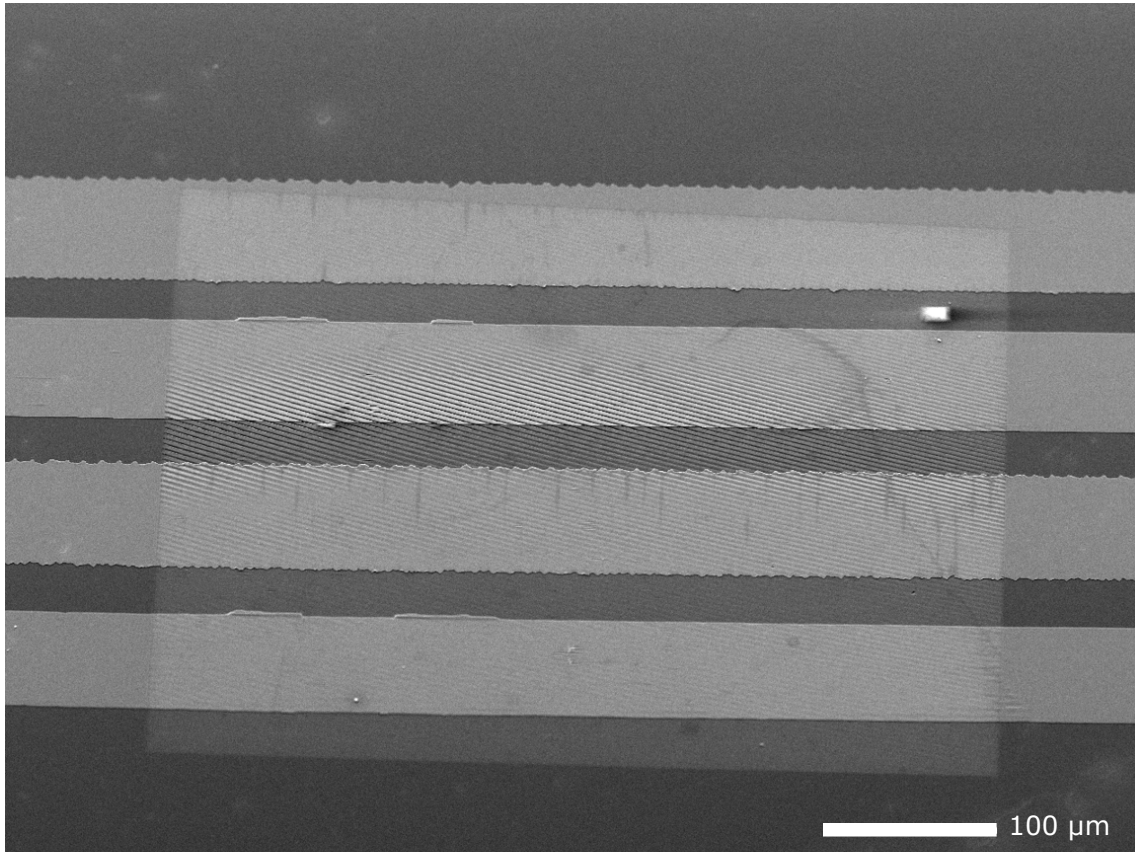
Figure 6.12: SEM image of the ECGMR with four ITO electrodes. The substrate was covered with a layer of ARP-C to prevent charging of the substrate during imaging.
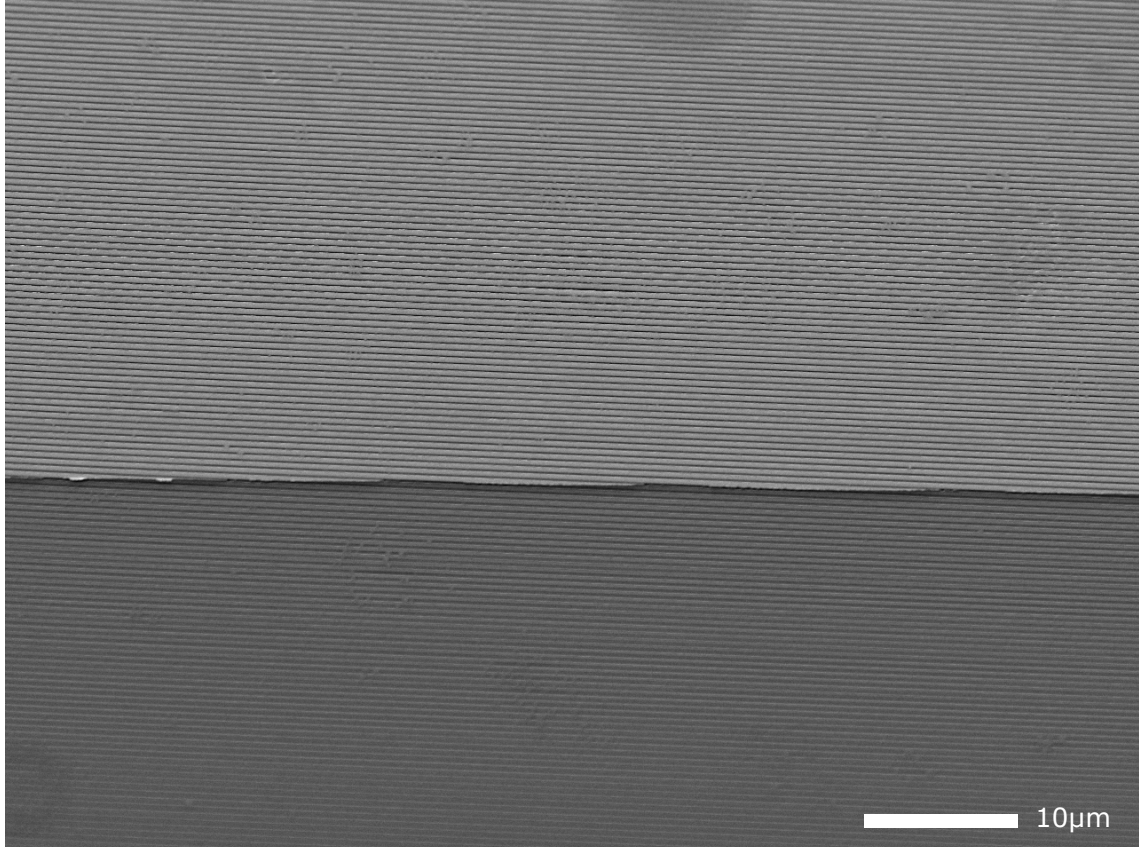
Figure 6.13: SEM image of the ITO electrode Si_3N_4 interface. The substrate was covered with a layer of ARP-C to prevent charging of the substrate during imaging.

6.3.1 Optical Characterisation

The change in resonance wavelength across the grating can be imaged using hyperspectral imaging which was performed using the optical setup described in chapter 4. Figure 6.14a shows the resonance wavelength of the ECGMR when immersed in DI water. The resonance wavelength varies from 820 to 848 nm across the length of the grating. The resonance wavelength across the length of one ITO electrode is shown in the figure 6.15a. The resonance wavelength is linear with respect to the change in period, increasing as the period of the grating increases as expected. The cross section of the four ITO electrodes shown in figure 6.15b shows the resonance wavelength is 20 nm longer between the Si_3N_4 and ITO sections.
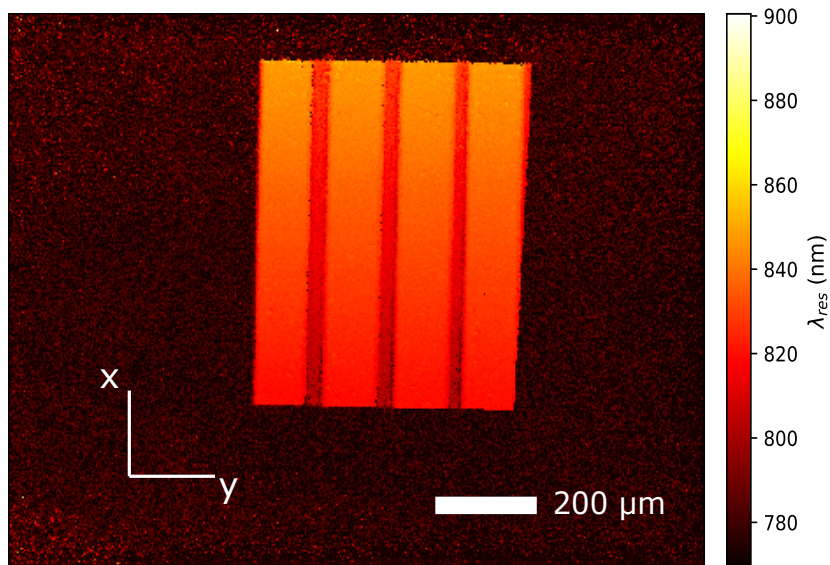
Figure 6.14: Hyperspectral image of the ECGMR. Four ITO electrodes of have been patterned on the surface to provide areas for selective functionalisation.

a)
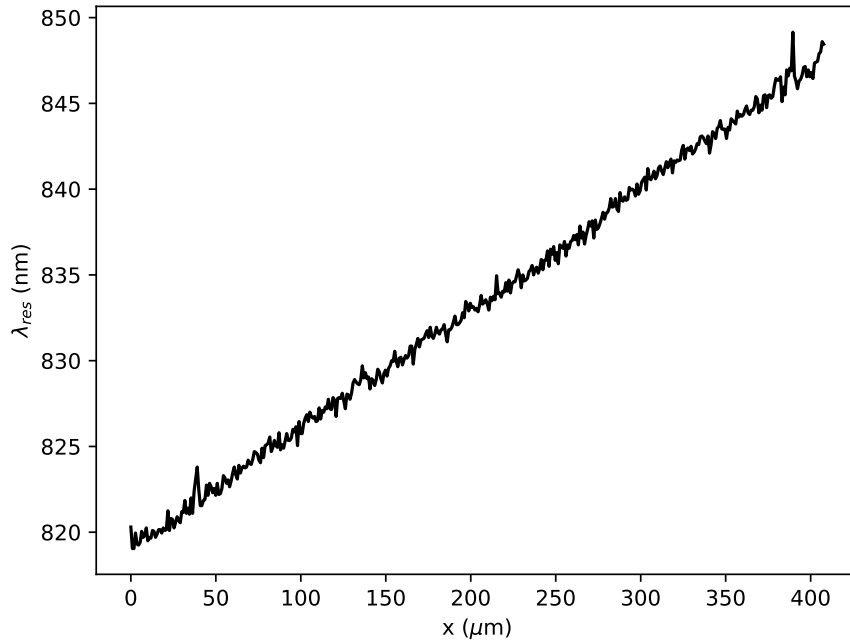
b)
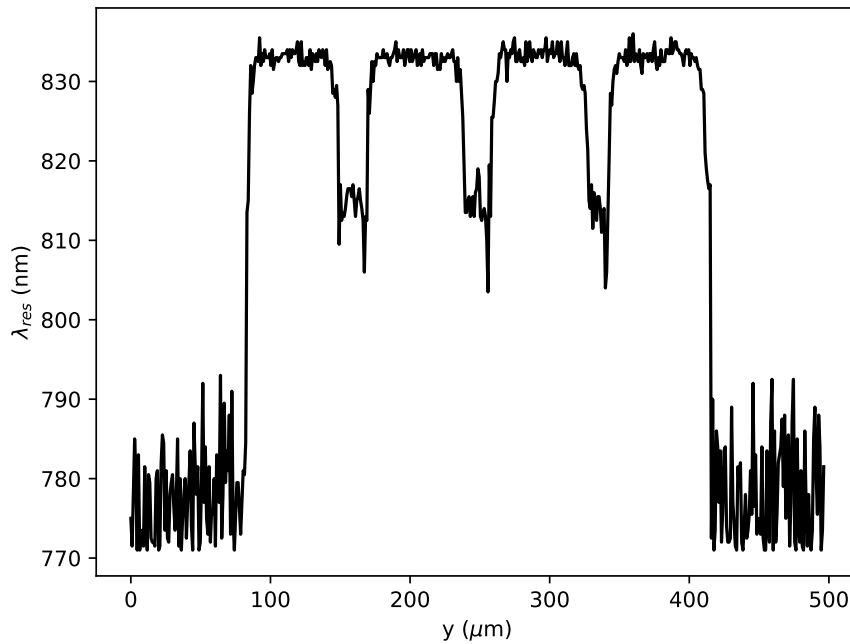
Figure 6.15: **a)** Resonance wavelength in the x direction of the ITO electrode. **b)** Resonance wavelength in the y direction across the grating.

The resonant section of the ECGMR when illuminated with monochromatic light is shown in figure 6.16a. For the conventional unchirped GMR the resonance peak is fitted to the Fano equation to determine the resonance wavelength and thus the refractive index. For the ECGMR, the change in refractive index is determined by

the resonance position. Figure 6.16b shows the intensity of the resonance peak across the ECGMR. The resonance peak is the combination of all the different periods of the grating and has a more Lorentzian lineshape compared to that of the standard GMR. The Fano equation can still be used to determine the resonance position, where the lack of asymmetry is accounted for by the Fano asymmetry parameter.

a)
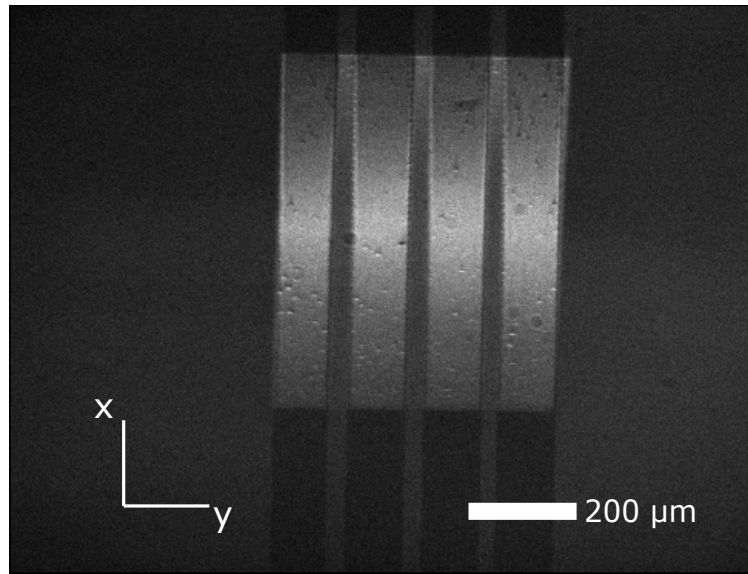
b)
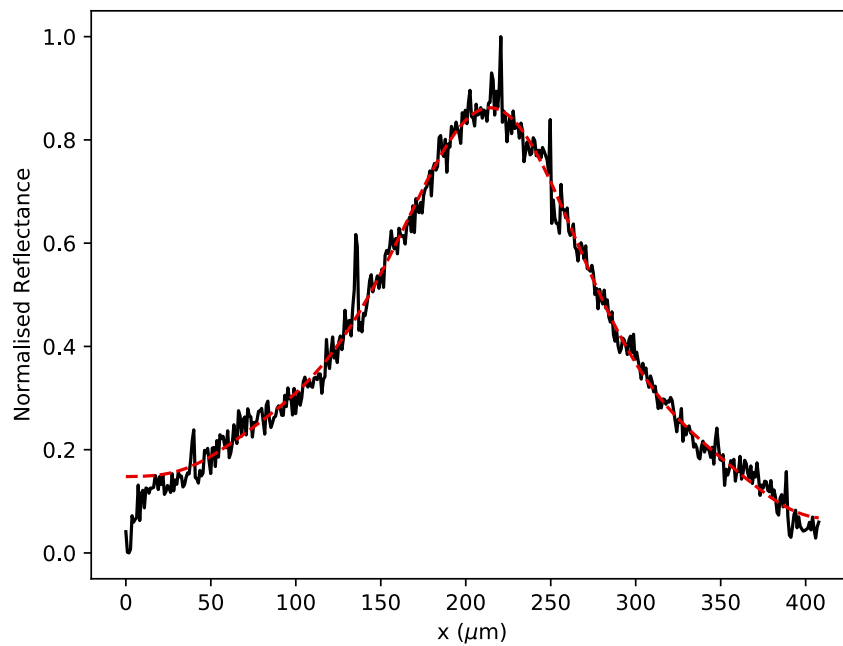
Figure 6.16: **a)** Resonance region of the ECGMR when illuminated with 830 nm monochromatic light. **b)** Resonant region of an ECGMR ITO microelectrode averaged across 30 pixels. Red dashed line shows the fit to the Fano resonance equation. $R^2 = 0.996$.

6.3.2 Electrical Characterisation of the Electrochemical Chirped GMR (ECGMR)

Due to the small size of the ITO electrodes it is difficult to measure their sheet resistance using the four point probe. Electrochemical impedance spectroscopy of an ITO microelectrode performed in 100 mM KPi buffer shown in figure 6.17 shows that the magnitude of the impedance has increased significantly compared the 100 nm thick ITO layer. Fitting the magnitude to the simplified Randles circuit discussed in chapter 4 and normalising to the electrode area shows that the charge transfer resistance R_{ct} is 705 Ω cm^2 for the ITO microelectrode and 60 Ω cm^2 for the 100 nm planar electrode.
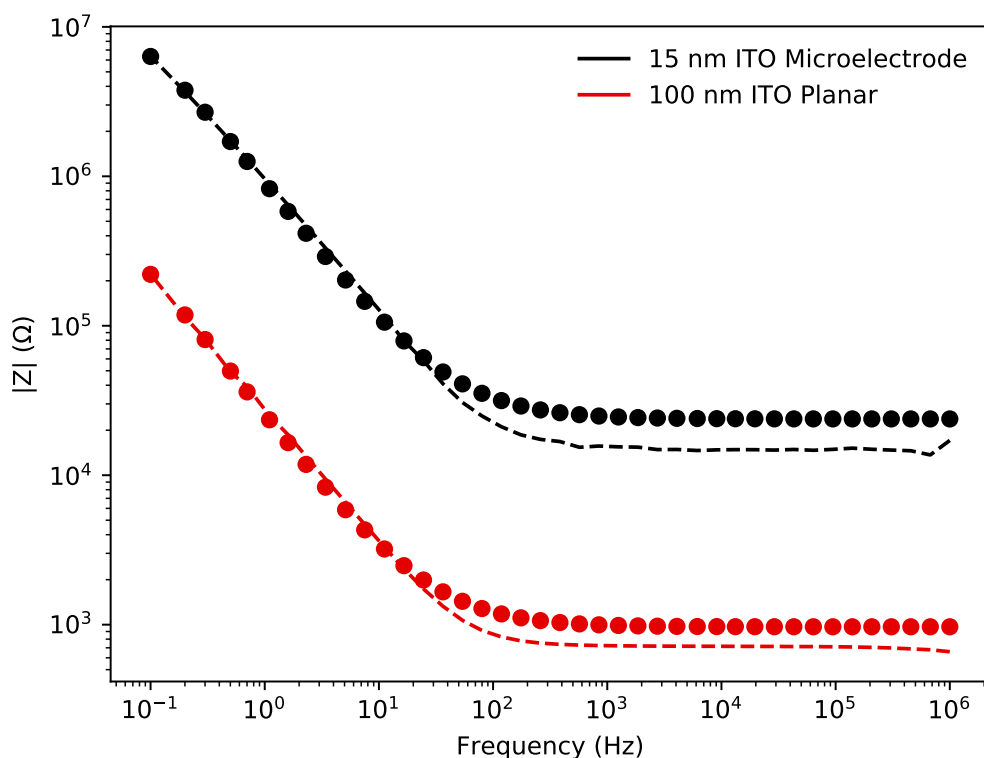
Figure 6.17: EIS of a 15 nm thick 70 μm wide ECGMR ITO microelectrode compared a 100 nm thick planar ITO electrode. Fitted data shown in dashed lines, measured data shown in circle markers.
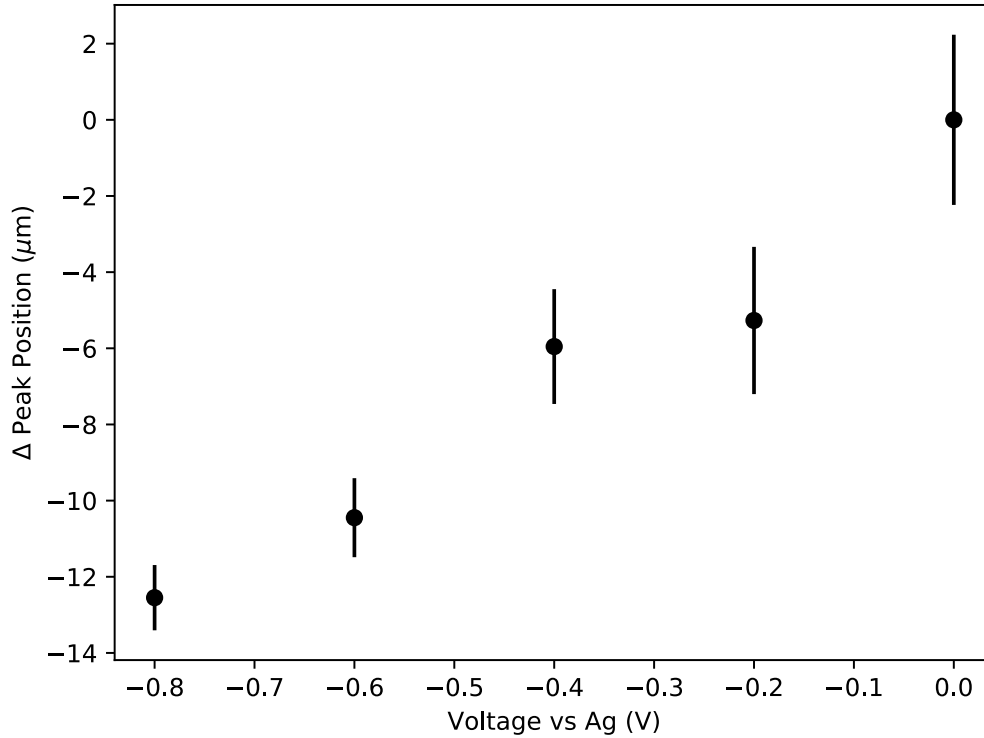
Figure 6.18: Mean resonance peak position with of the ECGMR against bias voltage (n =100).

To investigate the effect of applied voltage on the ECGMR resonance a bias voltage from 0 to -0.8V in -0.2V steps was applied using an SP300 potentionstat. The ECGMR was illuminated with 830 nm monochoromatic light at which wavelength the resonance occurs in the middle of the ECGMR. An image of the resonance position was taken every five seconds for three minutes after changing the bias voltage. An increase in the refractive index causes a shift towards a lower period and a decrease in refractive index causes a shift towards a higher period. The image was corrected for mechanical drift of the sensor and the resonance peak position was determined by fitting to the Fano equation. Figure 6.18 shows the change in resonance position against the applied bias voltage. As for the standard EGMRs a shift in the resonance peak position was observed as a function of applied bias voltage. Here, an increase in refractive index is defined as a positive Δ peak position, a decrease is a negative Δ peak position.

6.4 ECGMR for Multiplexed Protein Detection: Sepsis Exemplar

Sepsis is condition caused by the body's reaction to infection and is responsible for over 40,000 deaths in the UK annually. Sepsis is both difficult to diagnose and complex to treat due to the large number of symptoms that are shared with other conditions, as well as a wide range of possible causes. Sepsis is most commonly attributed to a bacterial infection in the bloodstream (bacteremia), but it can also be caused by viruses, fungi, or the body's own neutrophils as result of chemotherapy. The physical symptoms of sepsis include confusion, low blood pressure, and increased heart rate. These symptoms are generic and can be caused by many serious health conditions. If untreated, sepsis can lead rapidly to organ failure and death. Patients who survive may still be left with life-altering conditions.

Sepsis treatment is the guided by the "golden hour" rule, which states that intravenous fluids and antibiotics should be administered within one hour of a sepsis diagnosis [222]. The risk of death increases by 7.6% every hour after this, so immediate treatment will give patients the best chance of survival [223]. Diagnosis of sepsis is challenging and typically relies of the assessment of physical symptoms using the sequential organ failure assessment (SOFA) score coupled with testing for molecular diagnostic markers.

6.4.1 Sepsis Molecular Markers

There is no current gold standard marker for the molecular diagnosis of sepsis [224]. There are however over 150 different suggested sepsis molecular markers including acute phase proteins, inflammatory cytokines and immunoglobulin [225].

Acute phase proteins (APP) are a group of proteins involved in the immune system response and have a diverse array of roles such as trapping microrganisms, activating the production of antibodies and clearing damaged cell fragments. [226]. C reactive protein (CRP) is a pentameric APP that has been used for molecular diagnosis of sepsis for over 20 years. The exact role of CRP in the progression of sepsis is not fully understood. It is known that CRP is involved in the complement system, proteins that assist with the recruitment of immune cells, and that CRP itself can bind to bacteria cell membranes for presentation to immune cells. CRP expression is upregulated in response to the inflammatory cytokines interleukin 6 (IL-6), IL-1, and tumour necrosis factor α (TNFα) mainly in the liver tissue and has both

inflammatory and anti-inflammatory roles [227]. There is also some evidence that CRP contributes to coagulation in sepsis patients, which leads to organ failure, but these studies have been criticised for not controlling for endotoxins that can also cause organ failure so the role of CRP in this area is still unclear [228].

In response to a bacterial infection, CRP load in blood serum can increase from 1 μg/mL to 500 μg/mL and will return back to the uninfected level within 20 hours of the infection being cleared [229]. As CRP is cleared rapidly with the removal of infection is also monitored to inform when to cease antibiotic treatment for improved antimicrobial stewardship. CRP sepsis assays have a sensitivity of 60-98% and a specificity of 45-75%, with most studies showing a 60-70% sensitivity and specificity [230]. Inflammation is a very general response however and CRP levels can reach similar levels sepsis patients as those found after performing exercises such weight lifting.

Procalcitonin (PCT) is a 14 kDa APP that is particular associated with bacterial infection and so is being increasingly used for the diagnosis of bacterial sepsis [231]. PCT is not expressed in healthy patients so it can be considered a clear marker of infection, however the concentration of PCT can be very low with the clinical cutoff being 1 pg/mL [232]

Cytokines are a group of small protein signalling molecules used for inter cell communication. There are a number of cytokines involved in the process of inflammation for example IL-4, IL-6, IL-18 and TNFα [233]. Cytokine based diagnostics are attractive as their upregulation preempts many of the physical symptoms associated with sepsis such as the acute phase proteins. IL-6 and IL-10 in particular have been shown promise as a rapid biomarker in neonatal sepsis [234]. The challenge of using cytokines is that the concentrations are lower and their molecular half life is shorter than acute phase proteins making the detection more challenging.

Immunoglobulin or antibodies are a part of the adaptive immune system that are used to specifically bind antigens that are the cause of an immune response. Antibodies are Y shaped proteins that have a variable region of 110 to 130 amino acids at the tips of the Y. The variable region gives the antibody its specificity towards the antigen.

Given the role of antibodies in protecting us from infections immunoglobulin levels have been investigated as a marker of sepsis. Clinical trials using a single antibody as a clinical marker, such as IgG, have shown that the level of immunoglobulin on admission had little correlation with patient survival. Low levels of IgM, IgA, and IgG levels on admission in patients suspected of having sepsis has been linked with

increased mortality. Furthermore, monitoring levels of IgM over time has also been shown to be a strong indicator of patient mortality, with the IgM levels lowering further when progressing into septic shock [235].

A challenge of using molecular markers for sepsis is that they are not specific for diagnosing sepsis alone. A study that the used six different biomarkers including CRP, PCT, cytokines and neutrophil counts showed that individually only CRP and PCT where diagnostically useful for detecting sepsis, but that combined the six markers were more accurate than any single marker [236].

6.4.2 State of the art: Molecular POC Sepsis Diagnostics

Given the importance of rapid diagnosis of sepsis, there have been significant efforts to bring sepsis testing to the point of care. Detection of cytokines at clinically relevant levels for sepsis has been demonstrated using biosensors developed for the point of care. A magnetoelectrochemical approach integrated into a smartphone based sensor was used to detect IL-3 with a LOD of < 10 pg/mL in less than one hour in blood plasma [237]. IL-3 causes upregulation of inflammatory cytokines such as IL-6, IL-1 and TNFα and so can in theory serve as an early marker of inflammation. Electrochemical detection of IL-6 was demonstrated on a needle based microelectrode at 25 pg/mL within 2.5 minutes [238]. The mechanism of the enhanced sensitivity is not understood for this technique however as it was reported that the charge transfer resistance went down on binding with IL-6, contrary to the expected result that antigen binding should increase the charge transfer resistance.

A multiplexed lens free interferometric assay using an extraordinary optical transmission nanohole array was developed to show μg levels of sensitivity for parallel detection of CRP and IL-6 along with μM sensitivity for the detection of the miRNA [239]. The sensitivity of this device is insufficient to be clinically relevant. It has been shown however that labelling the proteins with Au nanoparticles enhanced the sensitivity for CRP detection to detect 40 pg/mL within two hours [240]. A GMR based sensor for CRP with an integrated on chip filtration system demonstrated a LOD of 6.4 ng/mL in blood plasma and demonstrated that CRP could be detected from whole blood using the filter to remove red blood cells [241].

A microfluidic cell counter has been used to measure CD64 expression on neutrophils from whole blood. The cells are electrically counted entering and exiting a capture chamber where the CD64 expressing cells are immobilised on to an anti-CD-64 surface [242]. The difference between the cells entering and exiting correlates with

the number of CD-64 expressing cells.

6.4.3 Current Techniques for Bacterial Detection

It is vital not just to detect the presence of sepsis but the agent that is causing it. Microbiological techniques are used for identifying if sepsis is caused by a bacterial infection. The current gold standard in clinical microbiology is to use growth based methods on selective growth media plates, which can take from 24 hours to five days. Growing a microbial culture from a blood sample is challenging as the starting concentration of bacteria is only 1 - 10^2 CFU/mL. The diagnosis of paediatric sepsis in particular in difficult as the amount of blood withdrawn is less than 1 mL, so growth assays can be incorrect by virtue of not collecting enough blood to find a single bacteria [243]. The species of bacteria can be identified by the positive growth combined with staining techniques such as Gram staining. Alternatively, 16S ribosomal RNA sequencing, which sequences the highly conserved 16s RNA gene, has recently been used for the identification of bacterial pathogens causing sepsis directly from whole blood [244].

Whole genome sequencing (WGS) is also seeing increasing use within a clinical setting, with WGS being used to perform epidemiological studies of *Staphylococcus aureus* within a single hospital to show how seemingly unrelated outbreaks of infection can have the same cause [245]. The use of matrix-assisted laser desorption/ionisation-time of flight mass spectrometry (MALDI-TOF MS) is being used increasingly for the identification of bacteria strains from blood samples in 30 minutes. MALDI-TOF MS has also been used for the identification of antibiotic resistance mechanisms such as the expression of β-lactamases that break down β-lactam antibiotics or the presence of the *mecA* gene used for methicillin resistance in methicillin resistant *S. aureus* (MRSA) [246].

6.4.4 Biosensing Approaches to Bacteria Detection

The rapid detection of bacteria from clinical and environmental applications using POC biosensors has been studied extensively, and there have been some excellent reviews on bacterial biosensors [247][248][249][250]. A number of strategies including microfluidic filtration or trapping of the cells, electrochemical monitoring using redox molecules or light scattering have been proposed.

The rapid detection of bacteria for a number of applications including sepsis using

photonic/plasmonic affinity biosensors has been reported. A Mach-Zendher inferometer integrated into an optical fibre was able to detect 10^2 CFU/mL *E. coli* within ten minutes, using surface immobilised anti-*E. coli* antibodies [251]. A multiplexed plasmonic nanohole array was able to detect *Nisseria gonorrhoeae* and *Chlamydia trachomatis* from a simulated clinical urine sample [252]. A SPR assay using surface immobilised polymxin B, an antibiotic that targets Gram negative bacteria, to detect bacteria in blood plasma with a LOD of 10^2 CFU/mL within 2 hours [253]. Inferometric bimodal waveguides have been able to detect bacteria from spinal fluid at 4 CFU/mL [254].

An advantage of using affinity based detection of bacteria is that the bacteria detection can be integrated within a multiplexed protein assay. The availability of antibodies and other biorecognition molecules for detecting sepsis causing pathogens must be considered however. Antibodies for the main pathogens such as *E. coli*, *S. aureus*, *Pseudomonas aeruginosa* and *Klebsiella pneumonia* are widely available. There are many other sepsis causing bacteria however such as *Finegoldia magna*, a commensal skin bacteria that acts as an opportunistic pathogen and is most commonly found in post operative sepsis [255]. Antibodies for these other species are either limited or non existent so currently the use of an antibody based bacteria identification strategy is limited to the most prevalent forms of bacteria. Being able to rapidly identify the most common causes of sepsis is extremely valuable of course, and would improve the care of the majority of sepsis patients. The point merely is that even with rapid POC diagnostics, conventional microbiology will still have a role to play in sepsis diagnosis for some time to come.

6.5 ECGMR for the Label Free Multiplexed Detection of Sepsis Biomarkers and Bacteria

For this work I have chosen to use C reactive protein and IgG as the main molecular markers of sepsis coupled with antibody based detection of *E. coli*. Both CRP and IgG molecules have high molecular weights of >100 kDa and are expressed in higher levels compared to other APPs such as procalcitonin or cytokines such as IL-6.

E. coli is a common sepsis pathogen, with up to 25% of sepsis patients contracting the condition from progression of urinary tract infections caused by *E. coli*. The anti-*E. coli* antibodies are selected against components of the outer membrane that confer a particular serotype, the lipopolysacharide (O serotype), acidic capsular polysaccharide (K antigen serotype) or the flagella (H antigen serotype). There

are antibodies that also target other membrane components such as the β barrel assembly machine but the serotype specific antibodies are most common [256]. Given the wide availability of antibodies and the clinical relevance of *E. coli* in sepsis, I chose to use *E. coli* MG1655, as the model sepsis causing bacteria for this work.

6.5.1 Detection of CRP using ECGMR

The ECGMR sensor was prepared by attaching wires to the four ITO electrodes using silver expoxy resin and baked on a hot plate at 100°C for one hour. The sensor was cleaned for 30 minutes using a UV ozone cleaner before adhering an o-ring fludic well with cynaoacrylate glue. The sensor was mounted on to a 3D printed holder to secure it to the optical setup.

The aminothiolphenol-anti-CRP conjugates were prepared using the protocol described in section 6.2.2 and 100 μL of the activated diazonium solution was pipetted on the sensor. Activated diazonium salts will spontaneously bind to the metal surfaces over time. To prevent non specific binding to the ITO microelectrodes a voltage of +0.1V was applied to all of the electrodes that were not to be functionalised. The aminothiolphenol-anti-CRP conjugate was electrografted to one ITO microelectrod using CV from 0.1 to -1V at 100 mV/s. After each CV sweep the electrodes were biased at 0V for three minutes to stabilise the electrochemical double layer prior to measuring the resonance position.
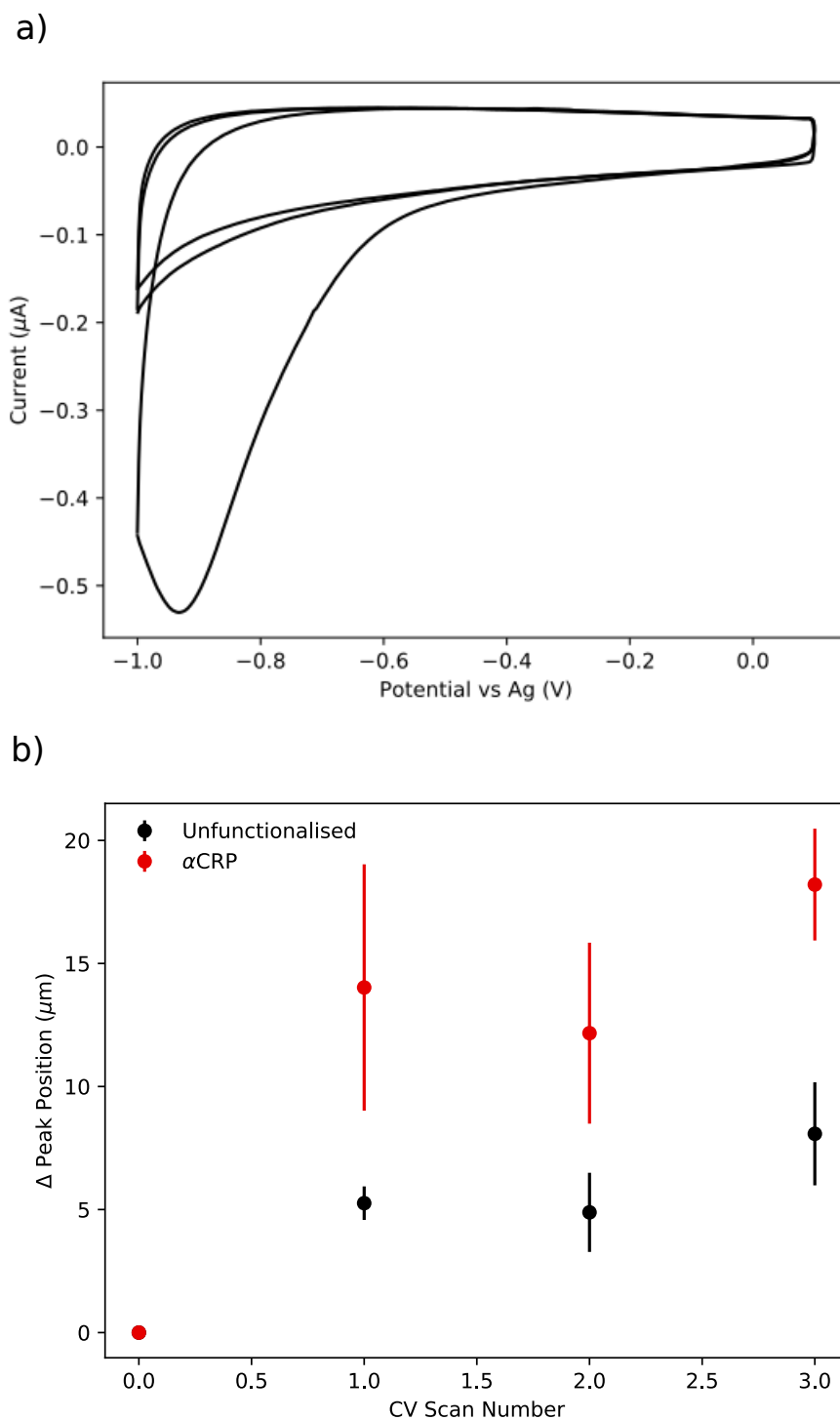
Figure 6.19: **a)** Electrografting of aminothiolphenol-anti-CRP to an ECGMR ITO microelectrode. **b)** Mean resonance position of the aminothiolphenol-anti-CRP functionalised electrode (red) and an unfunctionalised ECGMR ITO microelectrode with 0.1V bias voltage applied (black).

The electrografting reduction peak can be observed at -0.9V, in the cyclic voltammogram of figure 6.19a. This current peak was only observed for the first voltage scan. The increase in reduction potential required for diazonium reduction compared to

the 100 nm ITO electrodes is due to the increased sheet resistance of the 15 nm ITO microelectrodes.

In parallel, the optical resonance of the ECGMR was used to optically monitor the deposition of aminothiolphenol-anti-CRP conjugates on to the ITO surface in parallel. Figure 6.19b shows that after the first voltage sweep the peak resonance position increased by 14 μm, indicate of a local increase in refractive index. The resonance position remained within the standard deviation of the resonance after the first voltage sweep. Combining this with the lack of reduction peak suggest that there is no subsequent binding to the electrode from the electrografting. The resonance position on the other ITO microelectrodes was also seen to shift, but only by 5 μm for the unmodified antibodies electrode suggesting that there has been some fouling of the electrode the density of the antibodies is lower.
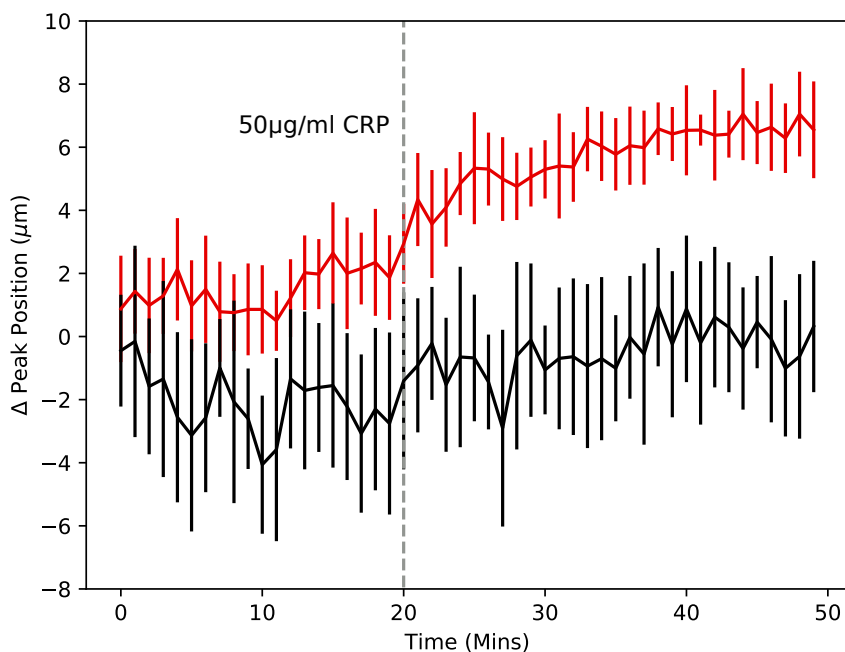
Figure 6.20: Resonance position shift against time of the anti-CRP functionalised electrode (red) and an unfunctionalised electrode in response to the 50 μg/mL CRP (black).

After functionalisation, the ECGMR sensor was exposed to 10 mM KPi buffer to establish a baseline then the incidence wavelength was tuned to 835 nm to bring the resonance position back to the centre of the grating. After 20 minutes the ECGMR was challenged with 50 μg/mL CRP in 10 mM KPi buffer. An image of the ECGMR was taken every five seconds, the mean resonance on both the aminothiolphenol-anti-CRP and unfunctionalised electrodes was fitted to the Fano equation to extract the

resonance position. The change in resonance position as a function of time is shown in figure 6.20. The resonance position of the aminothiolphenol-anti-CRP functionalised electrode shifted by 8 μm with the introduction of the CRP. In contrast, the unfunctionalised electrode did not show any positive shift with the addition of the CRP. This confirms the ability to specifically detect the binding of CRP to the anti-CRP functionalised electrode.

6.5.2   Parallel Detection of CRP and IgG

Having demonstrated that a single protein could be detected using the ECGMR I next investigated if the ECGMR could be used to detect two proteins, CRP and IgG in parallel.

IgG and CRP antibodies were prepared using the same protocol described in section 6.5.1 to create aminothiolphenol-anti-CRP and aminothiolphenol-anti-IgG conjugates. CV (0.1 to -1V) was used to graft aminothiolphenol-anti-IgG on to one ITO microelectrode, after which aminothiolphenol-anti-CRP was grafted to a second electrode. During electrografting all other ITO electrodes were biased to 0.1V. Figure 6.21a shows the grafting of the anti-IgG antibodies to the electrode, the reduction peak was a at -0.7V with a peak current of -0.33μA. The CRP antibody electrografting is shown in figure 6.21b, the reduction peak was also at -0.7V with a peak current of -23μA.
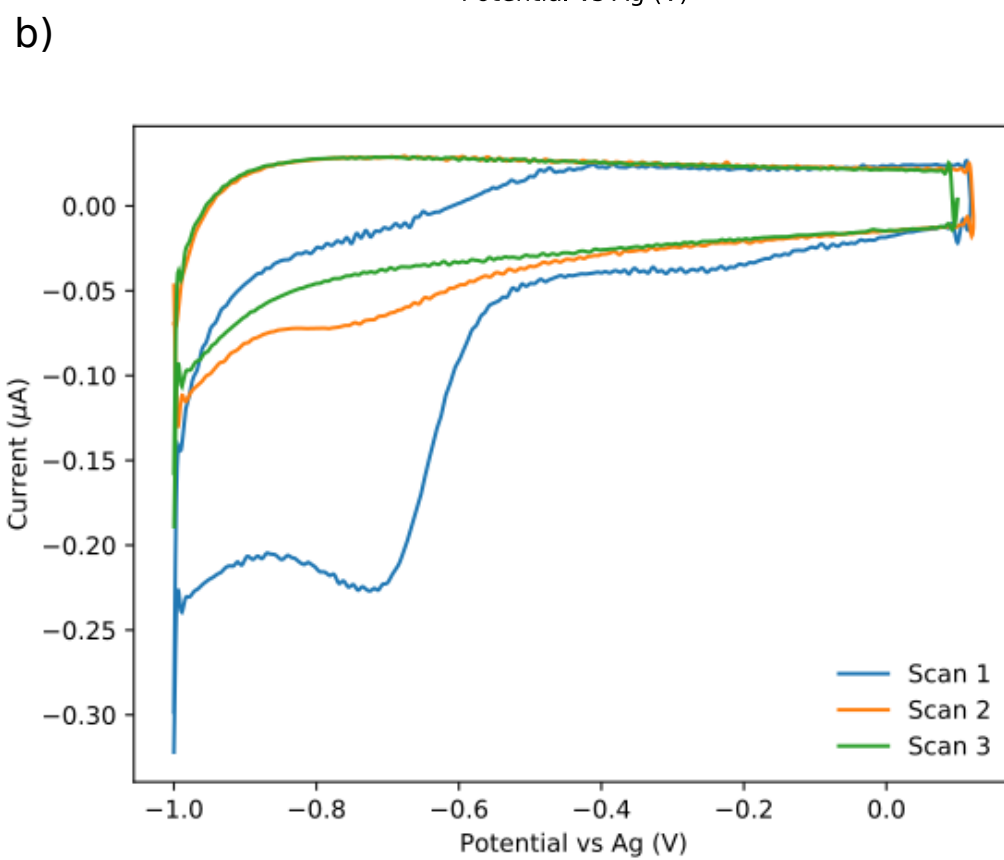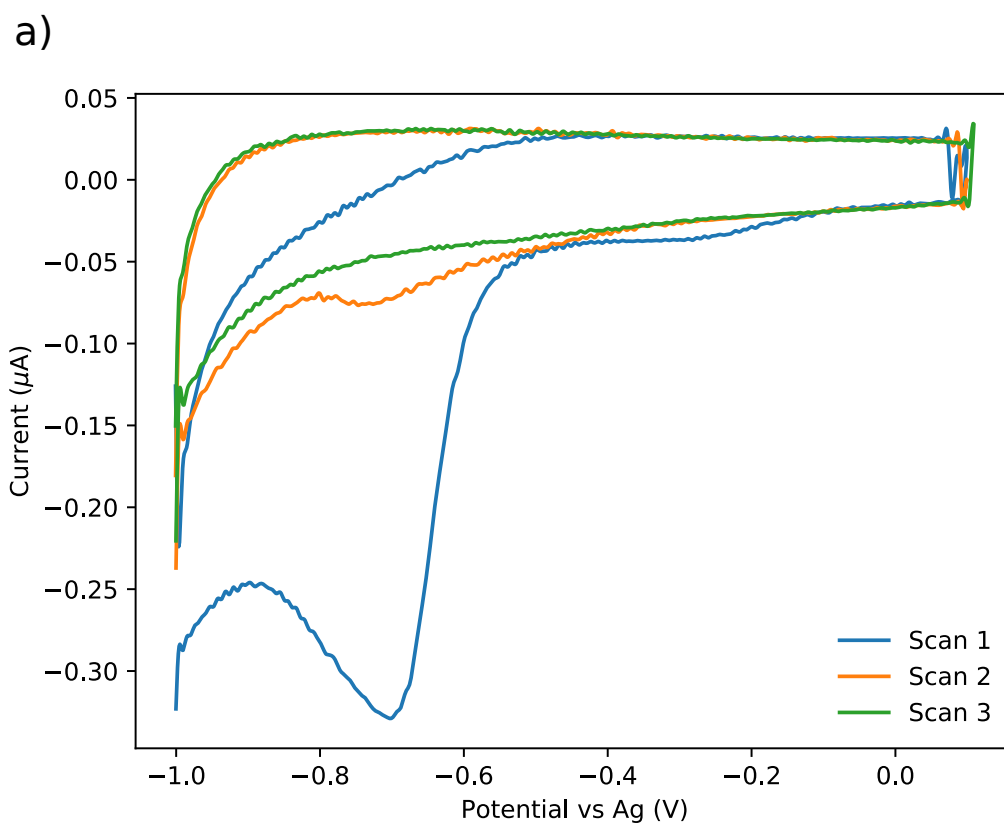
Figure 6.21: **a)** Electrografting of aminothiolphenol conjugated anti-IgG antibodies to an ITO ECGMR microelectrode. **b)** Electrografting of aminothiolphenol conjugated anti-CRP antibodies to an ITO ECGMR microelectrode.
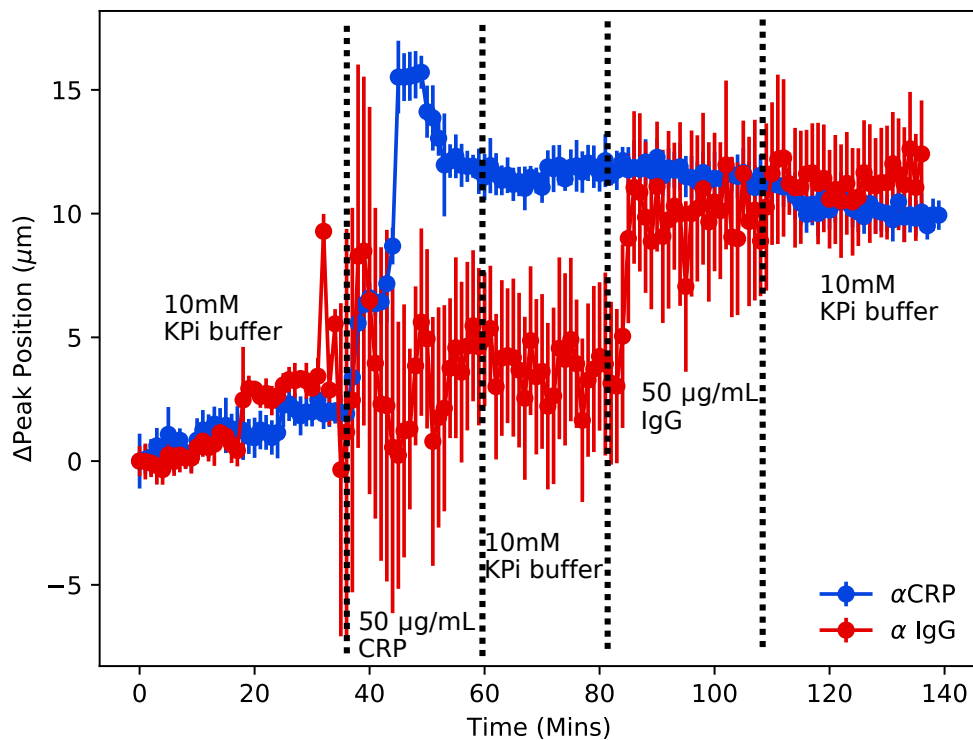
Figure 6.22: Parallel detection of 50 μg/mL CRP and IgG to anti-CRP (blue) and anti-IgG functionalised ITO electrodes using the ECGMR. Black lines indicate when the buffer was changed during the assay.

Again, the ECGMR was illuminated with 835 nm The sensor was exposed to 10 mM KPI buffer to establish a baseline. After 30 minutes 50 μg/mL CRP in 10 mM KPi buffer was pipetted on to the sensor and left for 30 minutes, after which the sensor was washed three times with 10 mM KPi buffer. The sensor was then exposed to 50 μg/mL IgG in 10 mM KPi buffer for 20 minutes before a final wash with 10 mM KPi buffer. An image of the sensor was taken every five seconds, corrected for the mechanical movement of the sensor then the peak position was determined by the fitting the resonance profile to the Fano equation.

Figure 6.22 shows the time dependent change in resonance peak position for both the aminothiolphenol-anti-CRP and aminothiolphenol-anti-IgG functionalised microelectrodes. A 11 μm shift was observed on the aminothiolphenol-anti-CRP functionalised electrode after the introduction of the CRP which remained after the wash step. Despite significant amount of noise on the aminothiolphenol-anti-IgG functionalised electrode the resonance peak position did return to the baseline after the wash step suggesting suggesting the initial step following exposure to CRP was due to non-specific binding. After the sensor was exposed to the IgG there was a

10.6 μm shift in the resonance peak position for anti-IgG functionalised electrode while the anti-CRP electrode remained stable. After the final wash step the resonance peak position remained stable on both microelectrodes demonstrating that both of the antigens have bound to their respective antibodies. This experiment has demonstrated that the diazonium based antibody surface immobilisation combined with the ECGMR can be used to perform parallel detection of at least two different protein targets.

6.5.3 CRP Sensitivity

Measuring the sensitivity of the ECGMR is vital for establishing whether it can be be applied for its target application. As CRP is the more standard clinical marker for sepsis compared to IgG my research focused on quantifying the assay sensitivity to CRP.

One of the challenges of making an accurate and quantifiable biosensor is developing approaches to account for drifts in the sensor signal due to non specific binding or environmental effects such as a change in temperature. A common solution to this challenge is to use a control antibody as reference to account for these changes. The aim of the control antibody is to provide a replica of surface chemistry used to create the detection signal but which does not specifically bind to any biomolecule in the media. Any changes in signal due to environmental effects will be observed in both the reference and target signals can be removed. Choosing a reference antibody for more complex media such as whole blood can be challenging due to the high protein content and the variation in blood composition different patients [257]. As a proof of principle I used an anti bovine serum albumin (BSA) antibody as the control as there would be no BSA present in the buffer solution.

a)

b)
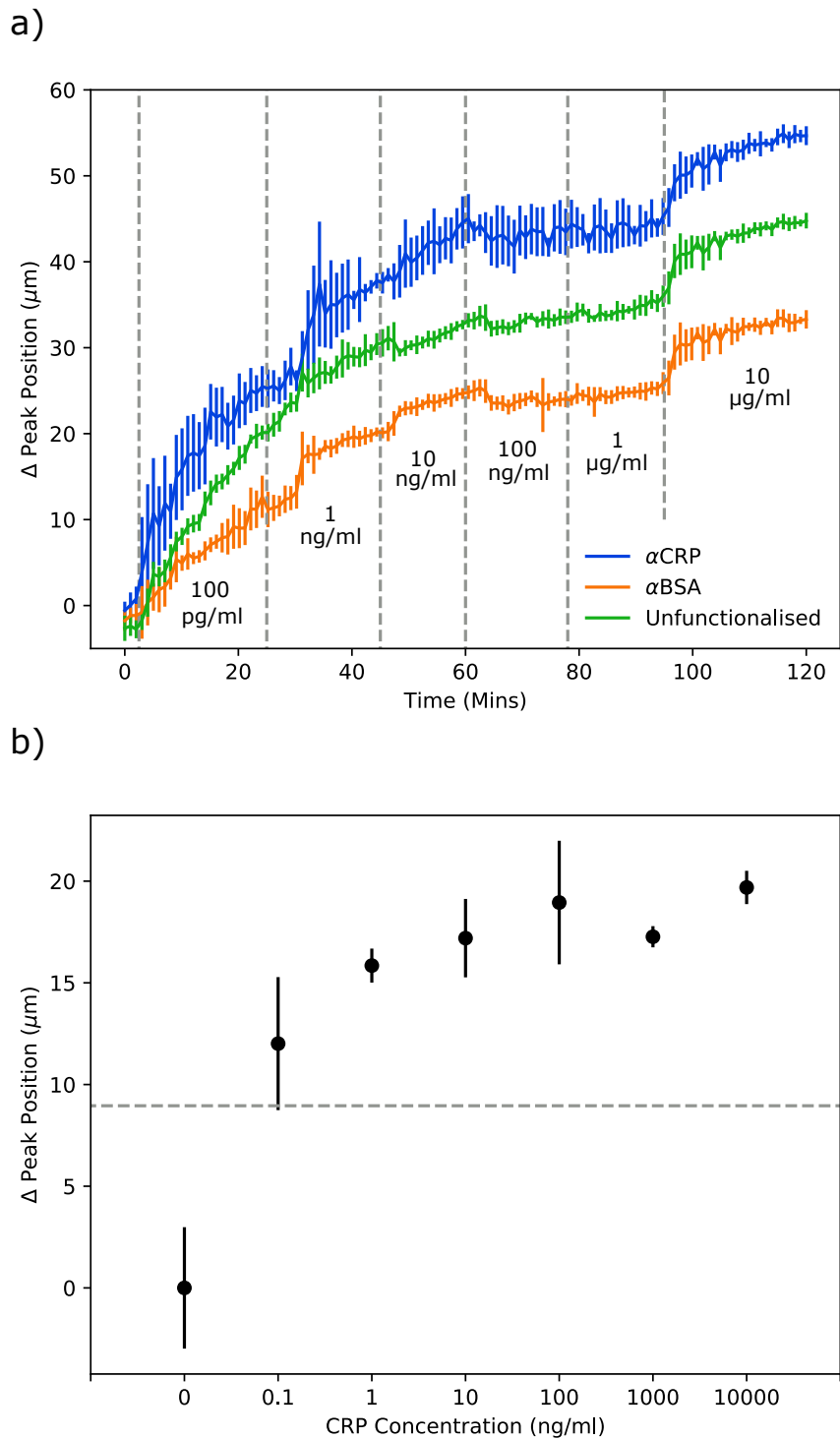
Figure 6.23: **a)** Change in peak resonance position over time for increasing concentrations of CRP in KPi buffer. Grey lines indicate when each concentration was added to the sensor. **b)** Change in peak resonance position against concentration of CRP. The grey dashed line indicates the 3σ LOD.

Following the same antibody functionalisation protocol described in section 6.5.1 anti-CRP and anti-BSA antibodies were electrografted on to separate microelectrodes using CV from 0.1 to -1V at 100 mV/s for four scans until the reduction peak

could not be observed. One of the electrodes was left unfunctionalised to investigate the effectiveness of the anti-BSA antibody control against non specific binding, To quantify the sensitivity, the functionalised ECGMR was challenged with increasing concentrations of the CRP diluted into 10 mM KPi buffer starting at 100 pg/mL up to 10 μg/mL. The sensor was washed three times with 10 mM KPi after each CRP solution. The ECGMR was illuminated with monochromatic light at 830 nm and an image taken every five seconds. The images were processed to remove physical drift from the movement of the stage and the resonance position of each electrode was fitted using the Fano resonance equation. Figure 6.23a shows the change in resonance position over time for three electrodes. Drifts due to non-specific binding and environmental factors, particular temperature, are evident on all three electrodes. This highlights the value of including a reference channel functionalised with a control antibody.

Figure 6.23b plots the resonance position shift of the CRP functionalised electrode following subtraction of the BSA reference channel. The resonance shift is seen to increase with CRP concentration which saturates for solutions > 10 ng/mL. Ideally the plot should resemble the S curve of a langmuir isotherm, which would require lower concentrations of CRP. However the noise floor is sufficiently large that it would not be possible to reduce to CRP concentration further. The LOD for CRP detection was 60 pg/mL, well below the required LOD for detecting sepsis however increasing the dynamic range of the sensor would be required as it currently saturates at 10 ng/mL of CRP while the level of CRP in a sepsis patient can routinely be in the hundreds of micrograms.

6.5.4   *E. coli* Sensitivity

The ideal sepsis biosensor would identify not only if a patient has sepsis but also the cause of infection. *E. coli* was used here as the model organism as it is one of the most common causes of the sepsis.

E. coli MG1655 was grown overnight in lysogeny broth (LB) media at 37°C shaking at 200 RPM. The cells were washed three times by centrifuging at 7000 RPM in a microcentrifuge for three minutes and then resuspending the pellet in 10 mM KPi buffer. The optical density was measured using a spectrophotometer (Jenway) and the cells diluted to an OD_{650} of 0.1, which is approximately 10^8 colony forming units (CFU)/mL.

Lysing bacteria in a sample prior to measurement has been shown to improve the

sensitivity of an antibody based photonic bionsensor [258]. Bacteria antibodies are selected against outer membrane components. The bacteria cells are much larger than the antibodies so once a whole cell is bound to the surface there is a large proportion of the bacteria outer membrane that now cannot come into contact with the cell. Lysing the cells makes more of the antigen available to the sensing region, increasing the device sensitivity. The cells were lysed by heating the media to 90°C for ten minutes before serially diluting from 10^8 to 10^2 CFU/mL.
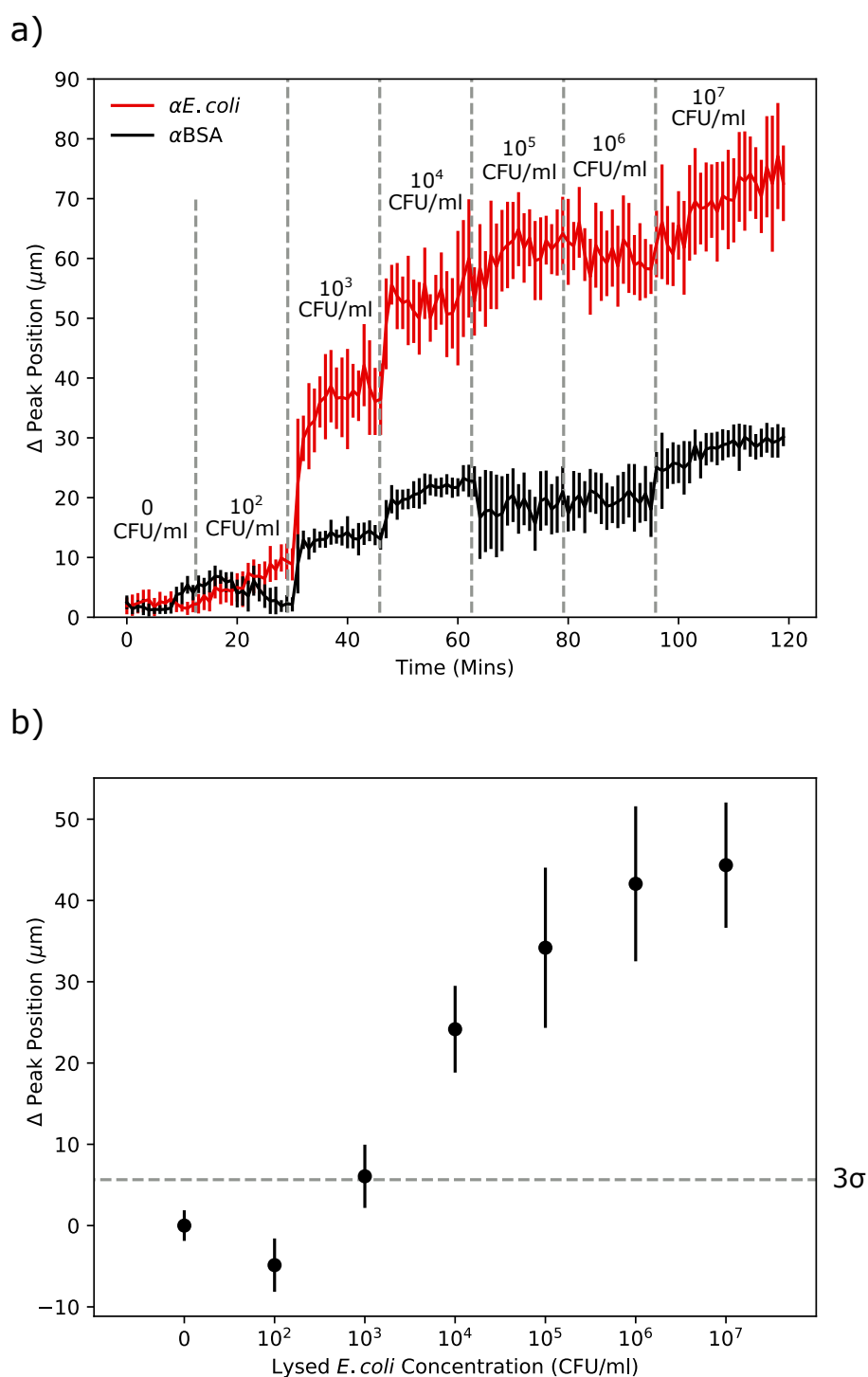
Figure 6.24: **a)** Change in peak resonance position over time for increasing concentrations of lysed *E. coli* MG1655 in KPi buffer. Grey lines indicate when each concentration was added to the sensor. **b)** Change in peak resonance position against concentration of *E. coli*. The grey dashed line indicates the 3σ LOD.

The anti-*E. coli* and anti-BSA antibodies were electrografted on to independent ITO microelectrodes using the protocol described in section 6.5.3. The ECGMR was illuminated with 830 nm monochromatic light. The resonance wavelength was

measured every five seconds and fitted to the Fano equation to extract the resonance position. The serially diluted bacterial lysate was pipetted on to the sensor and left to incubate for 20 minutes. The sensor was washed three times with KPi between each sample. The change in resonance position over time is shown in figure 6.24a. The resonance position on the anti-*E. coli* functionalised electrodes increases by 30 μm with the 10^3 CFU/mL sample, then saturating at 10^5 CFU/mL compared to the anti-BSA reference. The sensitivity plot of resonance position against concentration after subtraction of the anti-BSA reference measurement is shown in figure 6.24b. The LOD is approximately 5×10^2 CFU/mL, close to the levels of clinical relevance, which for sepsis, is between 1 - 10^2 CFU/mL. These measurements were conducted in buffer however so upon moving to clinical samples it is likely that matrix effects that will decrease the specificity and sensitivity of the assay so the LOD will be lower. The measured results however are promising for future development of this method as a sepsis biosensor.

6.6   Summary

In this chapter I have developed a proof of concept multiplexed biosensor for sepsis using the electrochemical GMR. Selective functionalisation of individual ITO microelectrodes fabricated on a single ECGMR sensor was achieved by diazonium salt based electrografting. The optimised electrografting protocol allows for sequential functionalisation of spatially separated microelectrodes without the loss of antibody function. I have successfully fabricated a chirped EGMR so that changes in refractive index can be measured using a monochromatic light source and a camera instead of a spectrometer. The ECGMR consisted of four separate ITO electrodes, each independently addressable for selective functionalisation. Finally I have applied the developed technology for detection of CRP, IgG and *E. coli*. I have demonstrated that two proteins CRP and IgG can be detected in parallel using this label free multiplexed biosensor and shown a LOD of 60 pg/mL for CRP and 5×10^2 CFU/mL for lysed *E. coli*.

This work is the first example of a multiplexed photonic antibody based biosensor where functionalisation was achieved by the diazonium grafting. The relative simplicity of the optical setup compared to other photonic biosensor techniques also means that there is potential for the technology to be used as a low cost POC diagnostic technology. The LOD for CRP is well below the clinically relevant level for diagnosis of sepsis, however the dynamic range of the measurement would need to be improved to provide a quantitative measurement of the CRP level. The LOD for

the lysed *E. coli* is approximately 5 times above clinically bacteria levels in blood for diagnosis of sepsis however there is still scope for optimising the surface chemistry to improve the LOD further.

Chapter 7

Conclusions and Future Work

Here, I have demonstrated a multimodal electrochemical and optical biosensor that consists of a Si_3N_4 GMR grating with an ITO working electrode deposited on the top of the grating surface. The advantage of using a GMR grating is that it can be illuminated with normally incident light, reducing the complexity of the experimental setup compared to other photonic biosensors. Multimodal sensing has not been demonstrated using GMR sensors previously so this work shows that combined electrochemical and refractive index sensing can be performed.

The optimum thickness of the ITO layer was designed by characterisation of the ITO material properties and simulation of the GMR reflectance using RCWA. Using a 60 nm ITO layer the EGMR had a TE resonance was originally shown at 880 nm however there was significant variation of the resonance wavelength between different sensors. The resonance wavelength was shown to be tunable by applying bias voltage to the ITO layer, where the resonance wavelength shifted by -1.25 nm with -1V of applied bias voltage. Combining experimental measurements and theoretical simulations showed that the change in resonance was primarily due to changes in the electrochemical double layer and not the ITO itself. This experiment also highlighted the range of the voltages which could be used for true parallel sensing where the applied bias voltage does not affect the resonance wavelength which for a 60 nm ITO layer was up to -0.6V. Optical and electrochemical measurements of different concentrations of NaCl solutions were used to investigate the sensitivity of the GMR, real time sensing of both refractive index and the surface double layer capacitance was demonstrated. The measured optical sensitivity of 83 nm/RIU is lower than previously published GMR sensors but not entirely unexpected given the addition of the lossy ITO layer. The loss in optical sensitivity is of course balanced

by the gain in an entirely new mode of sensing. Finally the refractive index and electrochemical properties of the redox active molecule methylene blue were characterised in parallel suing the EGMR. Using square voltammetry the electrochemical sensitivity was between 1 and 10 μM and the optical LOD for MB was 63 μM. The pH dependent electrochemical behaviour of MB was measured simultaneously with refractive index, showing a 32.5mV/pH shift.

The electrical and optical properties of the EGMR have been extensively characterised. Further work should of course look to apply the developed technology to more advanced problems than the simple characterisation tests currently demonstrated. There are many microbiological systems that could be investigated using the EGMR technology, for example the gram negative bacteria *Pseudomonas aeruginosa* is known to produce the redox active quorum sensing molecule pyocyanin. The presence of pyocyanin is important for biofilm formation in clinically relevant strains of *P. aeruginosa* isolated from cystic fibrosis patients. The concentration of pyocyanin produced by biolfilms is within the sensitivity of the EGMR leading to the opportunity of parallel refractive index sensing of bacterial growth and electrochemical analysis of the pyocyanin molecule over time. Another potentially interesting species is *Shewanella* which has been used for the making microbial fuel cells. Future work would look to make measurements of *Shewanella* growth on the EGMR surface using the optical modality while simultaneously measuring the the electrical output. I performed preliminary work on using the EGMR for investigating electrically active bacteria by developing a surface chemistry based on the sugar D-mannose to promote bacteria adherence to the ITO substrate. Bacterial adhesion to glycosylated surfaces is well characterised for species such as *E. coli* however surprisingly little is known about other species. The surface sensitivity of the EGMR technology provides opportunities for studying how surface chemistry can affect the growth and formation of bacterial biofilms.

In chapter 6, I modified the EGMR to use the chirped GMR structure, known as ECGMR. The ECGMR was applied to developing a multiplexed label free biosensor for sepsis markers. To make the sensor compatible with a low cost point of care device, I used the chirped GMR structure which can be measured using only an LED and a camera. By tuning the structure period the resonance wavelength varies spatially across the length of the grating. When illuminated with a monochromatic light source, the binding of biomolecules can be observed from movement of a region of high reflectance across the surface of grating as the resonance condition for each period of the grating is met. ITO microelectrodes were fabricated on to the chirped GMR to provide electrically addressable electrodes for surface functionalisation. The resonance of the chirped EGMR ITO electrodes was characterised optically using

hyperspectral imaging and shown to the be linear with the grating period. Electrical tuning of the resonance peak position was shown to be consistent with the results obtained in chapter 5 for the standard EGMR.

An antibody functionalisation protocol based on diazonium electrograting was optimised that allows direct sequential immobilisation of antibodies on to an electrode array. Verification of covalent diazonium grafting to ITO surfaces was performed by grafting a redox active label to the ITO surface. The binding of antibody diazonium conjugates to the ITO surface was verified using secondary anti-IgG antibodies labelled with HRP. The diazonium protocol was used for selective functionalisation of the chirped EGMR. Antibodies for CRP, IgG and *E. coli* were successfully grafted to the chirped EGMR surface. The binding of antibodies to the chirped EGMR was verified by combined optical and electrochemical measurements, the loss of the diazonium reduction peak and increase in the EGMR resonance position showing that antibodies had been grafted to the surface. Parallel label free detection of IgG and CRP was demonstrated. The LOD of CRP and lysed *E. coli* when measured against an anti-BSA reference was shown to be 60 pg/mL and 5×10^2 CFU/mL respectively.

The ECGMR biosensor is a promising proof of concept for multiplexed label free detection using a cheap point of care diagnostic platform. There is room for optimisation and improvement at every level in fabricating the assay however.

A new chirped structure using a Si nanohole array has recently been demonstrated within the group. Initial results suggest that along with increased optical sensitivity compared to the GMR the resonance is also less sensitive to polarisation. This could lead to being able to remove the polariser entirely from the optical measurement system which would assist with later miniaturisation for point of care applications. The optical noise from the chirped EGMR can be over five times the noise levels measured for the previously published chirped GMR, which reduces the limit of detection. The most likely source of the optical noise is the quality of the ITO layer forming the electrodes. The surface roughness of the electrodes has been shown to be high which will impact the performance of the sensor optically. Given that the conductivity of the electrodes is now no longer a priority, exploring other methods of depositing the ITO such as plasma sputtering may improve the surface roughness and correspondingly decrease the optical noise.

The ECGMR was designed to have a 20 nm shift in resonance wavelength across the grating. The expected resonance wavelength shift for a biomolecule binding is less than 2 nm so the ECGMR period is much larger than it needs to be. Currently

the ECGMR has the same change in period across the sensor, meaning the dynamic range is also nominally the same for each analyte. The dynamic range of the ECGMR when was actually limited by the amount of available binding sites, not the resonance position of the ECGMR. The multiplexing of the ECGMR is also limited by the number of electrodes that can be placed within the field of view of the camera. Investigation of the physical grating parameters to optimise the dynamic range and to determine the minimum functional width of the ITO electrodes is important to identify the multiplexing potential of the ECGMR.

The diazonium protocol currently appears to suffer from unwanted binding to other sensors despite the application of bias voltage to prevent this. Investigation of the the applied bias voltage along with the concentration of the antibodies could be investigated as a route for reducing the non specific binding. Alternatively the protocol could be change to use electrically controllable click chemistry discussed in chapter 6. The diazonium chemistry was chosen because it is a well established chemistry and there was existing experience in the research group. Having demonstrated the electrical functionalisation of the ECGMR is viable however these methods could provide greater spatial control to compared to the diazonium chemistry.

The PEG linker was relied upon entirely for preventing biofouling of the surface with no use of any other blocking agents. This was done purely to eliminate a potential parameter of optimisation at the time, as both the diazonium based functionalisation and the chirped EGMR were still in the early phases of characterisation. Improving the blocking using caesin or other blocking proteins could help further improve the sensitivity. Improvement for preventing biofouling is also essential for moving to simulated clinical samples, which would be the next stage of device testing.

The ECGMR has been tested using a research level optical experimental setup. Recent work within the group has developed a low cost version of the ECGMR measurement using a minimum number of optical components with the aim of having a materials cost of less than £100. Testing the ECGMR within this device is essential for demonstrating that it is compatible with the more cost effective optical components needed for a commercial product. Finally integration of the chirped ECGMR within a microfluidic device for sample preparation such as the filtration of red blood cells or the pre-concentration of analytes would demonstrate that the ECGMR has the potential for a true sample in/answer out device. To my knowledge this would be the first demonstration of a multimodal μTAS, which would be an important step forward for developing a versatile and robust point of care diagnostic tool.

Bibliography

[1] N. Bhalla, P. Jolly, N. Formisano, and P. Estrela, "Introduction to biosensors.," *Essays in biochemistry*, vol. 60, no. 1, pp. 1–8, 2016.

[2] S. Aydin, "A short history, principles, and types of ELISA, and our laboratory experience with peptide/protein analyses using ELISA," *Peptides*, vol. 72, pp. 4–15, 10 2015.

[3] K. M. Koczula and A. Gallotta, "Lateral flow assays.," *Essays in biochemistry*, vol. 60, pp. 111–20, 6 2016.

[4] A. C. Carpenter, I. T. Paulsen, and T. C. Williams, "Blueprints for Biosensors: Design, Limitations, and Applications.," *Genes*, vol. 9, 7 2018.

[5] X. Zeng, Z. Shen, and R. Mernaugh, "Recombinant antibodies and their use in biosensors," *Analytical and Bioanalytical Chemistry*, vol. 402, pp. 3027–3038, 4 2012.

[6] S. Sharma, H. Byrne, and R. J. O'Kennedy, "Antibodies and antibody-derived analytical biosensors.," *Essays in biochemistry*, vol. 60, no. 1, pp. 9–18, 2016.

[7] J. Zhou, M. R. Battig, and Y. Wang, "Aptamer-based molecular recognition for biosensor development," *Analytical and Bioanalytical Chemistry*, vol. 398, pp. 2471–2480, 11 2010.

[8] C. Chen, Q. Xie, D. Yang, H. Xiao, Y. Fu, Y. Tan, and S. Yao, "Recent advances in electrochemical glucose biosensors: a review," *RSC Advances*, vol. 3, p. 4473, 3 2013.

[9] E. Luan, H. Shoman, D. M. Ratner, K. C. Cheung, and L. Chrostowski, "Silicon Photonic Biosensors Using Label-Free Detection.," *Sensors (Basel, Switzerland)*, vol. 18, 10 2018.

[10] L. Laplatine, E. Luan, K. Cheung, D. M. Ratner, Y. Dattner, and L. Chrostowski, "System-level integration of active silicon photonic biosensors using

Fan-Out Wafer-Level-Packaging for low cost and multiplexed point-of-care diagnostic testing," *Sensors and Actuators B: Chemical*, vol. 273, pp. 1610–1617, 11 2018.

[11] Y. Tan and D. Dai, "Silicon microring resonators," *Journal of Optics*, vol. 20, p. 054004, 5 2018.

[12] D. Duval, J. Osmond, S. Dante, C. Dominguez, and L. Lechuga, "Grating couplers integrated on Mach-Zehnder interferometric biosensors operating in the visible range," *IEEE Photonics Journal*, vol. 5, pp. 3700108–3700108, 4 2013.

[13] H. Inan, M. Poyraz, F. Inci, M. A. Lifson, M. Baday, B. T. Cunningham, and U. Demirci, "Photonic crystals: emerging biosensors and their promise for point-of-care applications.," *Chemical Society reviews*, vol. 46, pp. 366–388, 1 2017.

[14] G. Pitruzzello and T. F. Krauss, "Photonic crystal resonances for sensing and imaging Related content Recent advances and progress in photonic crystal-based gas sensors Photonic crystal resonances for sensing and imaging," *Journal of Optics*, vol. 20, 2018.

[15] D. Grieshaber, R. MacKenzie, J. Vörös, and E. Reimhult, "Electrochemical Biosensors - Sensor Principles and Architectures.," *Sensors (Basel, Switzerland)*, vol. 8, pp. 1400–1458, 3 2008.

[16] A. A. Pupim Ferreira, C. Venturini, M. d. Souza Castilho, N. Canaverolo, M. Vinicius, G. P. dos Santos, C. Sadao, A. Vicente, and H. Yamanak, "Amperometric Biosensor for Diagnosis of Disease," in *State of the Art in Biosensors - Environmental and Medical Applications*, InTech, 3 2013.

[17] L. C. C. Wong, P. Jolly, and P. Estrela, "Development of a Sensitive Multiplexed Open Circuit Potential System for the Detection of Prostate Cancer Biomarkers," *BioNanoScience*, vol. 8, pp. 701–706, 6 2018.

[18] E. B. BahadÄśr and M. K. Sezgintürk, "A review on impedimetric biosensors," *Artificial Cells, Nanomedicine, and Biotechnology*, vol. 44, pp. 248–262, 1 2016.

[19] V. P. Rachim and W.-Y. Chung, "Multimodal Wrist Biosensor for Wearable Cuff-less Blood Pressure Monitoring System," *Scientific Reports*, vol. 9, p. 7947, 12 2019.

[20] S. Johnson and T. F. Krauss, "Label-free affinity biosensor arrays: novel technology for molecular diagnostics," *Expert Review of Medical Devices*, vol. 14, pp. 177–179, 3 2017.

[21] C. G. Siontorou, S. Bratakou, S. Karapetis, and N. Tzamtzis, "Biosensors Based on Microfluidic Devices Lab-on-a-Chip and Microfluidic Technology," *Nanotechnology and Biosensors*, pp. 375–394, 1 2018.

[22] D. E. W. Patabadige, S. Jia, J. Sibbitts, J. Sadeghi, K. Sellens, and C. T. Culbertson, "Micro Total Analysis Systems: Fundamental Advances and Applications," *Analytical Chemistry*, vol. 88, pp. 320–338, 1 2016.

[23] K. Scholten and E. Meng, "A review of implantable biosensors for closed-loop glucose control and other drug delivery applications," *International Journal of Pharmaceutics*, vol. 544, pp. 319–334, 6 2018.

[24] C. G. Siontorou, G.-P. D. Nikoleli, D. P. Nikolelis, S. Karapetis, N. Tzamtzis, and S. Bratakou, "Point-of-Care and Implantable Biosensors in Cancer Research and Diagnosis," in *Next Generation Point-of-care Biomedical Sensors Technologies for Cancer Diagnosis*, pp. 115–132, Singapore: Springer Singapore, 2017.

[25] F. S. Rodrigues Ribeiro Teles, L. A. Pires de Távora Tavira, and L. J. Pina da Fonseca, "Biosensors as rapid diagnostic tests for tropical diseases," *Critical Reviews in Clinical Laboratory Sciences*, vol. 47, pp. 139–169, 6 2010.

[26] H. Chen, K. Liu, Z. Li, and P. Wang, "Point of care testing for infectious diseases," *Clinica Chimica Acta*, vol. 493, pp. 138–147, 6 2019.

[27] S. K. Vashist, "Point-of-Care Diagnostics: Recent Advances and Trends.," *Biosensors*, vol. 7, 12 2017.

[28] C. I. L. Justino, A. C. Duarte, and T. A. P. Rocha-Santos, "Recent Progress in Biosensors for Environmental Monitoring: A Review.," *Sensors (Basel, Switzerland)*, vol. 17, 12 2017.

[29] S. Kröger and R. J. Law, "Biosensors for marine applications," *Biosensors and Bioelectronics*, vol. 20, pp. 1903–1913, 4 2005.

[30] S. Neethirajan, V. Ragavan, X. Weng, and R. Chand, "Biosensors for Sustainable Food Engineering: Challenges and Perspectives," *Biosensors*, vol. 8, p. 23, 3 2018.

[31] J. Juan-Colás, S. Johnson, and T. Krauss, "Dual-Mode Electro-Optical Techniques for Biosensing Applications: A Review," *Sensors*, vol. 17, p. 2047, 9 2017.

[32] M. D. M. Dryden and A. R. Wheeler, "DStat: A Versatile, Open-Source Potentiostat for Electroanalysis and Integration," *PLOS ONE*, vol. 10, p. e0140349, 10 2015.

[33] M. C. Dixon, "Quartz crystal microbalance with dissipation monitoring: enabling real-time characterization of biological materials and their interactions.," *Journal of biomolecular techniques : JBT*, vol. 19, pp. 151–8, 7 2008.

[34] E. Briand, M. Zäch, S. Svedhem, B. Kasemo, and S. Petronis, "Combined QCM-D and EIS study of supported lipid bilayer formation and interaction with pore-forming peptides," *Analyst*, vol. 135, no. 2, pp. 343–350, 2010.

[35] S. Nilsson, F. Björefors, and N. D. Robinson, "Electrochemical quartz crystal microbalance study of polyelectrolyte film growth under anodic conditions," *Applied Surface Science*, vol. 280, pp. 783–790, 9 2013.

[36] N. Jung, D. Kim, C. Yim, J. Y. Park, B. Y. Chang, and S. Jeon, "Quartz Resonator for Simultaneous Measurement of Changes in Mass and Electrical Impedance during Protein Adsorption," *Journal of the Electrochemical Society*, vol. 161, no. 2, pp. B3107–B3110, 2014.

[37] Z. Guo, M. Shams, C. Zhu, Q. Shi, Y. Tian, M. H. Engelhard, D. Du, I. Chowdhury, and Y. Lin, "Electrically Switched Ion Exchange Based on Carbon-Polypyrrole Composite Smart Materials for the Removal of ReO 4- from Aqueous Solutions," *Environmental Science and Technology*, vol. 53, pp. 2612–2617, 3 2019.

[38] D. Hao, C. Hu, J. Grant, A. Glidle, and D. R. Cumming, "Hybrid localized surface plasmon resonance and quartz crystal microbalance sensor for label free biosensing," *Biosensors and Bioelectronics*, vol. 100, pp. 23–27, 2 2018.

[39] E. M. Larsson, M. E. M. Edvardsson, C. Langhammer, I. Zorić, and B. Kasemo, "A combined nanoplasmonic and electrodeless quartz crystal microbalance setup," *Review of Scientific Instruments*, vol. 80, p. 125105, 12 2009.

[40] J. Zhu, S. Huang, J. Ye, X. Zhang, and G. Liu, "Design of a quartz crystal with transparent electrode used for both QCM-D and LSPR technology," *Sensors and Actuators A: Physical*, vol. 229, pp. 141–146, 6 2015.

[41] E. Reimhult, C. Larsson, B. Kasemo, and F. Höök, "Simultaneous Surface Plasmon Resonance and Quartz Crystal Microbalance with Dissipation Monitoring Measurements of Biomolecular Adsorption Events Involving Structural Transformations and Variations in Coupled Water," *Analytical Chemistry*, vol. 76, no. 24, pp. 7211–7220, 2004.

[42] A. R. Ferhan, J. A. Jackman, and N.-J. Cho, "Investigating how vesicle size influences vesicle adsorption on titanium oxide: a competition between steric packing and shape deformation âĂă," *Phys. Chem. Chem. Phys*, vol. 19, p. 2131, 2017.

[43] B. Veigas, E. Fortunato, and P. V. Baptista, "Field effect sensors for nucleic acid detection: Recent advances and future perspectives," 5 2015.

[44] N. Al-Hardan, M. Abdul Hamid, N. Ahmed, A. Jalar, R. Shamsudin, N. Othman, L. Kar Keng, W. Chiu, and H. Al-Rawi, "High Sensitivity pH Sensor Based on Porous Silicon (PSi) Extended Gate Field-Effect Transistor," *Sensors*, vol. 16, p. 839, 6 2016.

[45] Y. Li, X. Yang, and W. Zhao, "Emerging Microtechnologies and Automated Systems for Rapid Bacterial Identification and Antibiotic Susceptibility Testing," 2017.

[46] H.-J. Jang, J. Ahn, M.-G. Kim, Y.-B. Shin, M. Jeun, W.-J. Cho, and K. H. Lee, "Electrical signaling of enzyme-linked immunosorbent assays with an ion-sensitive field-effect transistor," *Biosensors and Bioelectronics*, vol. 64, pp. 318–323, 2 2015.

[47] I. Lee, S.-W. Lee, K.-Y. Lee, C. Park, D. Kim, J.-S. Lee, H. Yi, and B. Kim, "A Reconfigurable and Portable Highly Sensitive Biosensor Platform for ISFET and Enzyme-Based Sensors," *IEEE Sensors Journal*, vol. 16, pp. 4443–4451, 6 2016.

[48] M. A. Al-Rawhani, C. Hu, C. Giagkoulovits, V. Annese, B. Chong Cheah, J. M. Beeley, S. Velugotla, C. Accarino, J. Grant, S. Mitra, M. Barrett, S. Cochran, and D. Cumming, "Multimodal Integrated Sensor Platform for Rapid Biomarker Detection," *IEEE Transactions on Biomedical Engineering*, pp. 1–1, 6 2019.

[49] M. E. Abdelsalam, P. N. Bartlett, J. J. Baumberg, S. Cintra, T. A. Kelf, and A. E. Russell, "Electrochemical SERS at a structured gold surface," *Electrochemistry Communications*, vol. 7, pp. 740–744, 7 2005.

[50] D.-Y. Wu, J.-F. Li, B. Ren, and Z.-Q. Tian, "Electrochemical surface-enhanced Raman spectroscopy of nanostructures," *Chemical Society Reviews*, vol. 37, pp. 1025–1041, 2008.

[51] S. D. Bindesri, D. S. Alhatab, and C. L. Brosseau, "Development of an electrochemical surface-enhanced Raman spectroscopy (EC-SERS) fabric-based plasmonic sensor for point-of-care diagnostics," *The Analyst*, vol. 143, pp. 4128–4135, 8 2018.

[52] A. Campu, L. Susu, F. Orzan, D. Maniu, A. M. Craciun, A. Vulpoi, L. Roiban, M. Focsan, and S. Astilean, "Multimodal Biosensing on Paper-Based Platform Fabricated by Plasmonic Calligraphy Using Gold Nanobypiramids Ink.," *Frontiers in chemistry*, vol. 7, p. 55, 2019.

[53] J. Park, D. Bang, K. Jang, E. Kim, S. Haam, and S. Na, "Multimodal label-free detection and discrimination for small molecules using a nanoporous resonator," *Nature Communications*, vol. 5, p. 3456, 5 2014.

[54] J. Vörös, J. Ramsden, G. Csúcs, I. Szendrő, S. De Paul, M. Textor, and N. Spencer, "Optical grating coupler biosensors," *Biomaterials*, vol. 23, pp. 3699–3710, 9 2002.

[55] A. Székács, N. Adányi, I. Székács, K. Majer-Baranyi, and I. Szendrő, "Optical waveguide light-mode spectroscopy immunosensors for environmental monitoring," *Applied Optics*, vol. 48, p. B151, 2 2009.

[56] R. Horváth, G. Fricsovszky, and E. Papp, "Application of the optical waveguide lightmode spectroscopy to monitor lipid bilayer phase transition," *Biosensors and Bioelectronics*, vol. 18, pp. 415–428, 4 2003.

[57] N. Adányi, K. Majer-Baranyi, M. Berki, B. Darvas, B. Wang, I. Szendrő, and A. Székács, "Development of immunosensors based on optical waveguide lightmode spectroscopy (OWLS) technique for determining active substance in herbs," *Sensors and Actuators B: Chemical*, vol. 239, pp. 413–420, 2 2017.

[58] J. P. Bearinger, J. Vörös, J. A. Hubbell, and M. Textor, "Electrochemical optical waveguide lightmode spectroscopy (EC-OWLS): A pilot study using evanescent-field optical sensing under voltage control to monitor polycationic polymer adsorption onto indium tin oxide (ITO)-coated waveguide chips," *Biotechnology and Bioengineering*, vol. 82, pp. 465–473, 5 2003.

[59] Michelle A. Brusatori, Y. Tie, , and P. R. V. Tassel*, "Protein Adsorption Kinetics under an Applied Electric Field:âĂŔ An Optical Waveguide Lightmode Spectroscopy Study," *Langmuir*, vol. 19, no. 12, pp. 5089–5097, 2003.

[60] P. A. Ngankam and P. R. V. Tassel*, "In Situ Layer-by-Layer Film Formation Kinetics under an Applied Voltage Measured by Optical Waveguide Lightmode Spectroscopy," *Langmuir*, vol. 21, no. 13, pp. 5865–5871, 2005.

[61] I. Szendrő, K. Erdélyi, M. Fábián, Z. Puskás, N. Adányi, and K. Somogyi, "Combination of the optical waveguide lightmode spectroscopy method with electrochemical measurements," *Thin Solid Films*, vol. 516, pp. 8165–8169, 9 2008.

[62] N. Matsuda, H. Okabe, T. Nagamura, A. Omura, M. Nakano, and K. Miyake, "In Situ Observation of Desorption and Direct Electron Transfer Reaction of Cytochrome c on Bare ITO Electrode with Electrochemical Slab Optical Waveguide Spectroscopy," *Journal of Nanoscience and Nanotechnology*, vol. 19, pp. 4350–4354, 7 2019.

[63] K. Sugihara, M. Delai, I. Szendro, O. Guillaume-Gentil, J. Vörös, and T. Zambelli, "Simultaneous OWLS and EIS monitoring of supported lipid bilayers with the pore forming peptide melittin," *Sensors and Actuators B: Chemical*, vol. 161, pp. 600–606, 1 2012.

[64] N. Adányi, E. Németh, A. Halász, I. Szendrő, and M. Váradi, "Application of electrochemical optical waveguide lightmode spectroscopy for studying the effect of different stress factors on lactic acid bacteria," *Analytica Chimica Acta*, vol. 573-574, pp. 41–47, 7 2006.

[65] J. HomolaâĂă, "Surface Plasmon Resonance Sensors for Detection of Chemical and Biological Species," *Chemical Reviews*, vol. 108, pp. 462–493, 2008.

[66] H. N. Daghestani, B. W. Day, H. N. Daghestani, and B. W. Day, "Theory and Applications of Surface Plasmon Resonance, Resonant Mirror, Resonant Waveguide Grating, and Dual Polarization Interferometry Biosensors," *Sensors*, vol. 10, pp. 9630–9646, 11 2010.

[67] B. Prabowo, A. Purwidyantri, K.-C. Liu, B. A. Prabowo, A. Purwidyantri, and K.-C. Liu, "Surface Plasmon Resonance Optical Sensor: A Review on Light Source Technology," *Biosensors*, vol. 8, p. 80, 8 2018.

[68] K. Kurihara and K. Suzuki, "Theoretical Understanding of an Absorption-Based Surface Plasmon Resonance Sensor Based on Kretchmann's Theory," *Pockrand, I. Surf. Sci*, vol. 32, no. 1, pp. 696–701, 1991.

[69] H. Nguyen, J. Park, S. Kang, M. Kim, H. H. Nguyen, J. Park, S. Kang, and M. Kim, "Surface Plasmon Resonance: A Versatile Technique for Biosensor Applications," *Sensors*, vol. 15, pp. 10481–10510, 5 2015.

[70] A. Olaru, C. Bala, N. Jaffrezic-Renault, and H. Y. Aboul-Enein, "Surface Plasmon Resonance (SPR) Biosensors in Pharmaceutical Analysis," 4 2015.

[71] R. Schasfoort, F. Abali, I. Stojanovic, G. Vidarsson, L. Terstappen, R. B. M. Schasfoort, F. Abali, I. Stojanovic, G. Vidarsson, and L. W. M. M. Terstappen, "Trends in SPR Cytometry: Advances in Label-Free Detection of Cell Parameters," *Biosensors*, vol. 8, p. 102, 10 2018.

[72] A. B. Dahlin, B. Dielacher, P. Rajendran, K. Sugihara, T. Sannomiya, M. Zenobi-Wong, and J. Vörös, "Electrochemical plasmonic sensors," *Analytical and Bioanalytical Chemistry*, vol. 402, pp. 1773–1784, 2 2012.

[73] A. Baba, P. Taranekar, R. R. Ponnapati, W. Knoll, and R. C. Advincula, "Electrochemical Surface Plasmon Resonance and Waveguide-Enhanced Glucose Biosensing with N-Alkylaminated Polypyrrole/Glucose Oxidase Multilayers," *ACS Applied Materials & Interfaces*, vol. 2, pp. 2347–2354, 8 2010.

[74] S. Sriwichai, R. Janmanee, S. Phanichphant, K. Shinbo, K. Kato, F. Kaneko, T. Yamamoto, and A. Baba, "Development of an electrochemical-surface plasmon dual biosensor based on carboxylated conducting polymer thin films," *Journal of Applied Polymer Science*, vol. 135, p. 45641, 1 2018.

[75] A. Blidar, B. Feier, M. Tertis, R. Galatus, and C. Cristea, "Electrochemical surface plasmon resonance (EC-SPR) aptasensor for ampicillin detection," *Analytical and Bioanalytical Chemistry*, vol. 411, pp. 1053–1065, 2 2019.

[76] D. Pallarola, M. Schneckenburger, J. P. Spatz, and C. Pacholski, "Real-time monitoring of electrochemical controlled protein adsorption by a plasmonic nanowire based sensor," *Chemical Communications*, vol. 49, p. 8326, 8 2013.

[77] J. Zhang, Y. Wang, T. I. Wong, X. Liu, X. Zhou, and B. Liedberg, "Electrofocusing-enhanced localized surface plasmon resonance biosensors," *Nanoscale*, vol. 7, pp. 17244–17248, 10 2015.

[78] L. L. Zhang, X. Chen, H. T. Wei, H. Li, J. H. Sun, H. Y. Cai, J. L. Chen, and D. F. Cui, "An electrochemical surface plasmon resonance imaging system targeting cell analysis," *Review of scientific instruments*, vol. 84, 2013.

[79] S. Patskovsky, A.-M. Dallaire, and M. Meunier, "Electrochemical surface plasmon resonance sensing with absorptive redox mediator film," *Sensors and Actuators B: Chemical*, vol. 222, pp. 71–77, 1 2016.

[80] Y. Mei, C. Zhong, L. Li, J. Nong, W. Wei, and W. Hu, "Single-layer graphene-coated gold chip for electrochemical surface plasmon resonance study," *Analytical and Bioanalytical Chemistry*, vol. 411, pp. 4577–4585, 7 2019.

[81] M. Atighilorestani, D. P. dos Santos, R. F. V. V. Jaimes, M. M. Rahman, M. L. A. Temperini, and A. G. Brolo, "Electrochemical Control of Light Transmission through Nanohole Electrode Arrays," *ACS Photonics*, vol. 3, pp. 2375–2382, 12 2016.

[82] Q. Wang and W.-M. Zhao, "A comprehensive review of lossy mode resonance-based fiber optic sensors," *Optics and Lasers in Engineering*, vol. 100, pp. 47–60, 1 2018.

[83] I. Del Villar, M. Hernaez, C. R. Zamarreño, P. Sánchez, C. Fernández-Valdivielso, F. J. Arregui, and I. R. Matias, "Design rules for lossy mode resonance based sensors," *Applied Optics*, vol. 51, p. 4298, 7 2012.

[84] D. Kaur, V. Sharma, and A. Kapoor, "High sensitivity lossy mode resonance sensors," *Sensors and Actuators B: Chemical*, vol. 198, pp. 366–376, 7 2014.

[85] F. J. Arregui, I. Del Villar, C. R. Zamarreño, P. Zubiate, and I. R. Matias, "Giant sensitivity of optical fiber sensors by means of lossy mode resonance," *Sensors and Actuators B: Chemical*, vol. 232, pp. 660–665, 9 2016.

[86] I. Del Villar, C. R. Zamarreño, M. Hernaez, F. J. Arregui, and I. R. Matias, "Generation of Lossy Mode Resonances With Absorbing Thin-Films," *Journal of Lightwave Technology*, 12 2010.

[87] D. Kaur, V. K. Sharma, and A. Kapoor, "Effect of prism index on sensitivity of lossy mode resonance sensors operating in visible region," *Journal of Nanophotonics*, vol. 9, p. 093042, 10 2015.

[88] I. Del Villar, F. J. Arregui, C. R. Zamarreño, J. M. Corres, C. Bariain, J. Goicoechea, C. Elosua, M. Hernaez, P. J. Rivero, A. B. Socorro, A. Urrutia, P. Sanchez, P. Zubiate, D. Lopez, N. De Acha, J. Ascorbe, and I. R. Matias, "Optical sensors based on lossy-mode resonances," *Sensors and Actuators B: Chemical*, vol. 240, pp. 174–185, 3 2017.

[89] A. Ozcariz, M. Dominik, M. Smietana, C. Zamarreño, I. Del Villar, and F. Arregui, "Lossy mode resonance optical sensors based on indium-gallium-zinc oxide thin film," *Sensors and Actuators A: Physical*, vol. 290, pp. 20–27, 5 2019.

[90] X.-Z. Wang, Q. Wang, X.-Z. Wang, and Q. Wang, "Theoretical Analysis of a Novel Microstructure Fiber Sensor Based on Lossy Mode Resonance," *Electronics*, vol. 8, p. 484, 4 2019.

[91] M. Smietana, M. Sobaszek, B. Michalak, P. Niedzialkowski, W. Bialobrzeska, M. Koba, P. Sezemsky, V. Stranak, J. Karczewski, T. Ossowski, and R. Bogdanowicz, "Optical Monitoring of Electrochemical Processes With ITO-Based Lossy-Mode Resonance Optical Fiber Sensor Applied as an Electrode," *Journal of Lightwave Technology*, vol. 36, pp. 954–960, 2 2018.

[92] M. Sobaszek, M. Dominik, D. Burnat, R. Bogdanowicz, V. Stranak, P. Sezemsky, and M. Śmietana, "Optical monitoring of thin film electro-polymerization on surface of ITO-coated lossy-mode resonance sensor," in *25th Optical Fiber Sensors Conference* (Y. Chung, W. Jin, B. Lee, J. Canning, K. Nakamura, and L. Yuan, eds.), p. 103234W, 4 2017.

[93] M. Sobaszek, D. Burnat, P. Sezemsky, V. Stranak, R. Bogdanowicz, M. Koba, K. Siuzdak, MateuszÂťsmietana, , and M. MateuszÂťsmietana, "Enhancing electrochemical properties of an ITO-coated lossy-mode resonance optical fiber sensor by electrodeposition of PEDOT:PSS," *Optical Materials Express*, vol. 9, no. 7, 2019.

[94] S. W. James and R. P. Tatam, "Optical fibre long-period grating sensors: characteristics and application," *Measurement Science and Technology*, vol. 14, pp. 49–61, 2003.

[95] D. A. González, J. L. Arce-Diego, and A. Cobo, "Tilted short-period fibre-Bragg-grating-induced coupling to cladding modes for accurate refractometry Related content Spectralmodelling of fibre gratings," *Measurement Science and Technology*, vol. 12, no. 7, 2001.

[96] S. Bandyopadhyay, P. Biswas, F. Chiavaioli, T. K. Dey, N. Basumallick, C. Trono, A. Giannetti, S. Tombelli, F. Baldini, and S. Bandyopadhyay, "Long-period fiber grating: a specific design for biosensing applications," *Applied Optics*, vol. 56, p. 9846, 12 2017.

[97] M. Janczuk-Richter, M. Piestrzyńska, D. Burnat, P. Sezemsky, V. Stranak, W. J. Bock, R. Bogdanowicz, J. Niedziółka-Jönsson, and M. Śmietana, "Optical investigations of electrochemical processes using a long-period fiber grating functionalized by indium tin oxide," *Sensors and Actuators B: Chemical*, vol. 279, pp. 223–229, 1 2019.

[98] R. Bogdanowicz, P. Niedziałkowski, M. Sobaszek, D. Burnat, W. Białobrzeska, Z. Cebula, P. Sezemsky, M. Koba, V. Stranak, T. Ossowski, and M. Śmietana, "Optical Detection of Ketoprofen by Its Electropolymerization on an Indium Tin Oxide-Coated Optical Fiber Probe," *Sensors*, vol. 18, p. 1361, 4 2018.

[99] W. Bogaerts, P. De Heyn, T. Van Vaerenbergh, K. De Vos, S. Kumar Selvaraja, T. Claes, P. Dumon, P. Bienstman, V. Thourhout, and R. Baets, "Silicon microring resonators," *Laser Photonics Rev*, vol. 6, no. 1, pp. 47–73, 2012.

[100] R. Guider, D. Gandolfi, T. Chalyan, L. Pasquardini, A. Samusenko, C. Peder-zolli, G. Pucker, and L. Pavesi, "Sensitivity and Limit of Detection of biosen-sors based on ring resonators," *Sensing and Bio-Sensing Research*, vol. 6, pp. 99–102, 12 2015.

[101] P. Steglich, M. Hülsemann, B. Dietzel, and A. Mai, "Optical Biosensors Based on Silicon-On-Insulator Ring Resonators: A Review.," *Molecules (Basel, Switzerland)*, vol. 24, 1 2019.

[102] S. TalebiFard, S. Schmidt, W. Shi, W. Wu, N. A. F. Jaeger, E. Kwok, D. M. Ratner, and L. Chrostowski, "Optimized sensitivity of Silicon-on-Insulator (SOI) strip waveguide resonator sensor.," *Biomedical optics express*, vol. 8, pp. 500–511, 2 2017.

[103] J. Juan-Colas, A. Parkin, K. E. Dunn, M. G. Scullion, T. F. Krauss, and S. D. Johnson, "The electrophotonic silicon biosensor," *Nat Commun*, vol. 7, 2016.

[104] J. Juan-Colás, T. F. Krauss, and S. D. Johnson, "Real-Time Analysis of Molec-ular Conformation Using Silicon Electrophotonic Biosensors," *ACS Photonics*, vol. 4, pp. 2320–2326, 9 2017.

[105] W.-k. Kuo, C.-j. Hsu, A.-l. Fehrembach, O. Gauthier-Lafaye, K. Chan Shin Yu, A. Monmayrant, S. Bonnefont, E. Daran, P. Arguel, F. Lozes-Dupuy, A. Sen-tenac, R. Yukino, P. K. Sahoo, J. Sharma, T. Takamura, J. Joseph, and A. Sandhu, "Implementation of guided-mode resonance optical filter using two-step nanoimprinting process," *IEEE Photonics Technol. Lett*, vol. 61, no. 2, p. 29642, 1992.

[106] K. J. Lee, J. Giese, L. Ajayi, R. Magnusson, and E. Johnson, "Resonant grating polarizers made with silicon nitride, titanium dioxide, and silicon: Design, fabrication, and characterization," *Optics Express*, vol. 22, p. 9271, 4 2014.

[107] T. Kondo, S. Ura, and R. Magnusson, "Design of guided-mode resonance mirrors for short laser cavities," *Journal of the Optical Society of America A*, vol. 32, p. 1454, 8 2015.

[108] K. Kintaka, J. Nishii, J. Ohmori, Y. Imaoka, M. Nishihara, S. Ura, R. Satoh, and H. Nishihara, "Integrated waveguide gratings for wavelength-demultiplexing of free space waves from guided waves," *Optics Express*, vol. 12, p. 3072, 7 2004.

[109] G. Quaranta, G. Basset, O. J. F. Martin, and B. Gallinet, "Recent Advances in Resonant Waveguide Gratings," *Laser & Photonics Reviews*, vol. 12, p. 1800017, 9 2018.

[110] S. S. Wang and R. Magnusson, "Theory and applications of guided-mode resonance filters," *Applied Optics*, vol. 32, p. 2606, 5 1993.

[111] B. Cunningham, P. Li, B. Lin, and J. Pepper, "Colorimetric resonant reflection as a direct biochemical assay technique," *Sensors and Actuators B: Chemical*, vol. 81, pp. 316–328, 1 2002.

[112] Q. Wang, D. Zhang, H. Yang, C. Tao, Y. Huang, S. Zhuang, and T. Mei, "Sensitivity of a label-free guided-mode resonant optical biosensor with different modes.," *Sensors (Basel, Switzerland)*, vol. 12, no. 7, pp. 9791–9, 2012.

[113] R. Magnusson, D. Wawro, S. Zimmerman, and Y. Ding, "Resonant Photonic Biosensors with Polarization-Based Multiparametric Discrimination in Each Channel," *Sensors*, vol. 11, pp. 1476–1488, 1 2011.

[114] A. S. Gangnaik, Y. M. Georgiev, and J. D. Holmes, "New Generation Electron Beam Resists: A Review," *Chemistry of Materials*, vol. 29, pp. 1898–1917, 3 2017.

[115] S. Sarkar, S. Poulose, P. K. Sahoo, and J. Joseph, "Flexible and stretchable guided-mode resonant optical sensor: single-step fabrication on a surface engineered polydimethylsiloxane substrate," *OSA Continuum*, vol. 1, no. 4, pp. 1277–1286, 2018.

[116] M. A. Bader, C. Kappel, A. Selle, J. Ihlemann, M. L. Ng, and P. R. Herman, "F_2-laser-machined submicrometer gratings in thin dielectric films for resonant grating waveguide applications," *Applied Optics*, vol. 45, p. 6586, 9 2006.

[117] A. Micco, A. Ricciardi, M. Pisco, V. La Ferrara, and A. Cusano, "Optical fiber tip templating using direct focused ion beam milling," *Scientific Reports*, vol. 5, p. 15935, 12 2015.

[118] B. Kwon and J. H. Kim, "Importance of Molds for Nanoimprint Lithography: Hard, Soft, and Hybrid Molds," *Journal of Nanoscience*, vol. 2016, pp. 1–12, 6 2016.

[119] L. Liu, H. A. Khan, and J. Li, "One-step sol-gel imprint lithography for guided-mode resonance structures," *Nanotechnology*, vol. 27, no. 9, 2016.

[120] Y. Nazirizadeh, V. Behrends, A. Prósz, N. Orgovan, R. Horvath, A. M. Ferrie, Y. Fang, C. Selhuber-Unkel, and M. Gerken, "Intensity interrogation near cutoff resonance for label-free cellular profiling," *Scientific Reports*, vol. 6, p. 24685, 7 2016.

[121] W.-K. Kuo, N.-C. Huang, H.-P. Weng, and H.-H. Yu, "Tunable phase detection sensitivity of transmitted-type guided-mode resonance sensor in a heterodyne interferometer," *Optics Express*, vol. 22, p. 22968, 9 2014.

[122] P. K. Sahoo, S. Sarkar, and J. Joseph, "High sensitivity guided-mode-resonance optical sensor employing phase detection," *Scientific Reports*, vol. 7, 2017.

[123] G. J. Triggs, Y. Wang, C. P. Reardon, M. Fischer, G. J. O. Evans, and T. F. Krauss, "Chirped guided-mode resonance biosensor," *Optica*, vol. 4, p. 229, 2 2017.

[124] C.-W. Chang, S.-T. Chen, Y.-M. Lin, and C.-S. Huang, "Resonant Wavelength Shift Detection System Based on a Gradient Grating Period Guided-Mode Resonance," *IEEE Photonics Journal*, vol. 10, pp. 1–10, 8 2018.

[125] C.-T. Hsiung and C.-S. Huang, "Refractive Index Sensor Based on Gradient Waveguide Thickness Guided-Mode Resonance Filter," *IEEE Sensors Letters*, vol. 2, pp. 1–4, 12 2018.

[126] J. Juan-Colás, I. S. Hitchcock, M. Coles, S. Johnson, and T. F. Krauss, "Quantifying single-cell secretion in real time using resonant hyperspectral imaging.," *Proceedings of the National Academy of Sciences of the United States of America*, vol. 115, pp. 13204–13209, 12 2018.

[127] I. D. Block, P. C. Mathias, S. I. Jones, L. O. Vodkin, and B. T. Cunningham, "Optimizing the spatial resolution of photonic crystal label-free imaging," *Applied Optics*, vol. 48, p. 6567, 12 2009.

[128] G. J. Triggs, M. Fischer, D. Stellinga, M. G. Scullion, G. J. O. Evans, and T. F. Krauss, "Spatial Resolution and Refractive Index Contrast of Resonant Photonic Crystal Surfaces for Biosensing," *IEEE Photonics Journal*, vol. 7, pp. 1–10, 6 2015.

[129] Y. Zhuo, H. Hu, W. Chen, M. Lu, L. Tian, H. Yu, K. D. Long, E. Chow, W. P. King, S. Singamaneni, and others, "Single nanoparticle detection using photonic crystal enhanced microscopy," *Analyst*, vol. 139, no. 5, pp. 1007–1015, 2014.

[130] W. Chen, K. D. Long, M. Lu, V. Chaudhery, H. Yu, J. S. Choi, J. Polans, Y. Zhuo, B. A. C. Harley, and B. T. Cunningham, "Photonic crystal enhanced microscopy for imaging of live cell adhesion," *The Analyst*, vol. 138, p. 5886, 9 2013.

[131] Y. Wang, C. P. Reardon, N. Read, and T. F. Krauss, "Guided mode resonance imaging: A novel sensing technique to study bacterial biofilm antibiotic resistance (Conference Presentation)," in *Biophysics, Biology and Biophotonics III: the Crossroads* (A. Wax and V. Backman, eds.), vol. 10504, p. 13, SPIE, 3 2018.

[132] I. Molina-Fernández, J. Leuermann, A. Ortega-Moňux, J. Gonzalo Wangüemert-Pérez, and R. Halir, "Fundamental limit of detection of photonic biosensors with coherent phase read-out," 2019.

[133] S.-F. Lin, T.-J. Ding, J.-T. Liu, C.-C. Lee, T.-H. Yang, W.-Y. Chen, and J.-Y. Chang, "A Guided Mode Resonance Aptasensor for Thrombin Detection," *Sensors*, vol. 11, pp. 8953–8965, 9 2011.

[134] W.-J. Kim, B. K. Kim, A. Kim, C. Huh, C. S. Ah, K.-H. Kim, J. Hong, S. H. Park, S. Song, J. Song, and G. Y. Sung, "Response to Cardiac Markers in Human Serum Analyzed by Guided-Mode Resonance Biosensor," *Analytical Chemistry*, vol. 82, pp. 9686–9693, 12 2010.

[135] G. Y. Sung, W.-J. Kim, H. Ko, B. K. Kim, K.-H. Kim, C. Huh, and J. Hong, "Portable guided-mode resonance biosensor platform for point-of-care testing," vol. 8460, p. 84600F, International Society for Optics and Photonics, 10 2012.

[136] Y.-K. Tu, M.-Z. Tsai, I.-C. Lee, H.-Y. Hsu, and C.-S. Huang, "Integration of a guided-mode resonance filter with microposts for in-cell protein detection," *The Analyst*, vol. 141, pp. 4189–4195, 6 2016.

[137] D. Wawro, P. Koulen, Y. Ding, S. Zimmerman, and R. Magnusson, "Guided-mode resonance sensor system for early detection of ovarian cancer," vol. 7572, p. 75720D, International Society for Optics and Photonics, 2 2010.

[138] D. Wawro, Y. Ding, S. Gimlin, S. Zimmerman, C. Kearney, K. Pawlowski, and R. Magnusson, "Guided-mode resonance sensors for rapid medical diagnostic testing applications," vol. 7173, p. 717303, International Society for Optics and Photonics, 2 2009.

[139] B. Seeleang, C. Promptmas, S. Boonruang, W. S. Mohammed, and R. Jolivot, "Label-free Guided Mode Resonance Sensor for Detection of Glycated Hemoglobin," in *Conference on Lasers and Electro-Optics Pacific Rim*, 2017.

[140] H. Shafiee, E. A. Lidstone, M. Jahangir, F. Inci, E. Hanhauser, T. J. Henrich, D. R. Kuritzkes, B. T. Cunningham, and U. Demirci, "Nanostructured Optical Photonic Crystal Biosensor for HIV Viral Load Measurement," *Scientific Reports*, vol. 4, p. 4116, 5 2015.

[141] Y. Chen, Y.-B. Wang, L.-Y. Su, C.-S. Fu, C.-Y. Huang, C.-S. Huang, and W. Hsu, "Integration of photonic crystal and magnetic bead aggregation technique for fluorescence enhancement," in *CLEO Pacific Rim Conference*, (Washington, D.C.), p. Tu3K.5, OSA, 7 2018.

[142] P. C. Mathias, N. Ganesh, and B. T. Cunningham, "Application of Photonic Crystal Enhanced Fluorescence to a Cytokine Immunoassay,"

[143] P. Saengdee, W. Chaisriratanakul, W. Bunjongpru, W. Sripumkhai, A. Srisuwan, W. Jeamsaksiri, C. Hruanun, A. Poyai, and C. Promptmas, "Surface modification of silicon dioxide, silicon nitride and titanium oxynitride for lactate dehydrogenase immobilization," *Biosensors and Bioelectronic*, vol. 67, pp. 134–138, 2015.

[144] H. S. Dow, W. S. Kim, and J. W. Lee, "Thermal and electrical properties of silicon nitride substrates," *AIP Advances*, vol. 7, p. 095022, 9 2017.

[145] Z. Mao, Y. Zhu, Y. Zeng, F. Xu, Z. Liu, G. Ma, Z. Du, and W. Geng, "Investigation of Al-doped silicon nitride-based semiconductor and its shrinkage mechanism," *CrystEngComm*, vol. 14, p. 7929, 10 2012.

[146] E. B. AydÄśn and M. K. Sezgintürk, "Indium tin oxide (ITO): A promising material in biosensing technology," *TrAC Trends in Analytical Chemistry*, vol. 97, pp. 309–315, 12 2017.

[147] K. Suzuki, N. Hashimoto, T. Oyama, J. Shimizu, Y. Akao, and H. Kojima, "Large scale and low resistance ITO films formed at high deposition rates," *Thin Solid Films*, vol. 226, pp. 104–109, 4 1993.

[148] M. Bender, W. Seelig, C. Daube, H. Frankenberger, B. Ocker, and J. Stollenwerk, "Dependence of oxygen flow on optical and electrical properties of DC-magnetron sputtered ITO films," *Thin Solid Films*, vol. 326, pp. 72–77, 8 1998.

[149] M. Mizuno, T. Miyamoto, T. Ohnishi, and H. Hayashi, "Effects of Tin Doping and Oxygen Vacancies on the Electronic States of Indium Oxide," *Japanese Journal of Applied Physics*, vol. 36, pp. 3408–3413, 6 1997.

[150] A. Chen, K. Zhu, H. Zhong, Q. Shao, and G. Ge, "A new investigation of oxygen flow influence on ITO thin films by magnetron sputtering," *Solar Energy Materials and Solar Cells*, vol. 120, pp. 157–162, 1 2014.

[151] Z. Chen, Y. Zhuo, Y. Pei, G. Wang, D. J. Seo, J. P. Shim, S. B. Choi, T. H. Seo, E. K. Suh, U. Fiedeler, C. Karcher, T. N. D Tibbits, E. Oliva, G. Siefer, M. Schachtner, A. Wekkeli, A. W. Bett, R. Krause, M. Piccin, N. Blanc, C. Drazek, E. Guiot, B. Ghyselen, T. Salvetat, A. Tauzin, T. Signamarcheix, A. Dobrich, T. Hannappel, K. Schwarzburg, J. H. Yoo, M. Matthews, P. Ramsey, A. C. Barrios, A. Carter, A. Lange, J. Bude, S. Elhadj, H. Peng, W. Dang, J. Cao, Y. Chen, D. Wu, W. Zheng, H. Li, Z. X. Shen, Z. Liu, M. Marus, A. Hubarevich, H. Wang, A. Smirnov, X. Sun, W. Fan, L. Zhang, Y. Zhou, L. Guo, W. Zhao, A. Barnes, H. T. Zhang, C. Eaton, Y. Zheng, M. Brahlek, H. F. Haneef, N. J. Podraza, M. H. Chan, V. Gopalan, K. M. Rabe, R. Engel-Herbert, X. Du, J. M. Logan, J. Sippel, M. Nikolou, K. Kamaras, J. R. Reynolds, D. B. Tanner, A. F. Hebard, A. G. Rinzler, T. M. Barnes, M. O. Reese, J. D. Bergeson, B. A. Larsen, J. L. Blackburn, M. C. Beard, and J. Bult, "Past achievements and future challenges in the development of optically transparent electrodes," *5. F. Dimroth, M. Grave, P*, vol. 6, no. 12, p. 22123, 2012.

[152] M. Marikkannan, M. Subramanian, J. Mayandi, M. Tanemura, V. Vishnukanthan, and J. M. Pearce, "Effect of ambient combinations of argon, oxygen, and hydrogen on the properties of DC magnetron sputtered indium tin oxide films," *AIP Advances*, vol. 5, p. 17128, 2015.

[153] N. M. Ahmed, F. A. Sabah, H. Abdulgafour, A. Alsadig, A. Sulieman, and M. Alkhoaryef, "The effect of post annealing temperature on grain size of

indium-tin-oxide for optical and electrical properties improvement," *Results in Physics*, vol. 13, p. 102159, 6 2019.

[154] A. Klein, C. Körber, A. Wachau, F. Säuberlich, Y. Gassenbauer, S. P. Harvey, D. E. Proffit, and T. O. Mason, "Transparent Conducting Oxides for Photovoltaics: Manipulation of Fermi Level, Work Function and Energy Band Alignment.," *Materials (Basel, Switzerland)*, vol. 3, pp. 4892–4914, 11 2010.

[155] J. Park, C. Buurma, S. Sivananthan, R. Kodama, W. Gao, and T. Gessert, "The effect of post-annealing on Indium Tin Oxide thin films by magnetron sputtering method," *Applied Surface Science*, vol. 307, pp. 388–392, 7 2014.

[156] S. Song, T. Yang, J. Liu, Y. Xin, Y. Li, and S. Han, "Rapid thermal annealing of ITO films," *Applied Surface Science*, vol. 257, pp. 7061–7064, 6 2011.

[157] M. Mazur, D. Kaczmarek, J. Domaradzki, D. Wojcieszak, S. Song, and F. Placido, "Influence of thickness on transparency and sheet resistance of ITO thin films," in *The Eighth International Conference on Advanced Semiconductor Devices and Microsystems*, pp. 65–68, IEEE, 10 2010.

[158] V. Senthilkumar, P. Vickraman, M. Jayachandran, and C. Sanjeeviraja, "Structural and optical properties of indium tin oxide (ITO) thin films with different compositions prepared by electron beam evaporation," *Vacuum*, vol. 84, pp. 864–869, 2 2010.

[159] C. A. Pan and T. P. Ma, "High quality transparent conductive indium oxide films prepared by thermal evaporation," *Applied Physics Letters*, vol. 37, pp. 163–165, 7 1980.

[160] L. Kerkache, A. Layadi, E. Dogheche, and D. Rémiens, "Physical properties of RF sputtered ITO thin films and annealing effect," *Journal of Physics D: Applied Physics*, vol. 39, pp. 184–189, 1 2006.

[161] H. Kim, J. S. Horwitz, G. Kushto, A. Piqué, Z. H. Kafafi, C. M. Gilmore, and D. B. Chrisey, "Effect of film thickness on the properties of indium tin oxide thin films," *Journal of Applied Physics*, vol. 88, p. 6021, 11 2000.

[162] X. Fang, C. L. Mak, S. Zhang, Z. Wang, W. Yuan, and H. Ye, "Pulsed laser deposited indium tin oxides as alternatives to noble metals in the near-infrared region," *Journal of Physics: Condensed Matter*, vol. 28, p. 224009, 6 2016.

[163] Z. Chen, W. Li, R. Li, Y. Zhang, G. Xu, and H. Cheng, "Fabrication of Highly Transparent and Conductive IndiumâĂŞTin Oxide Thin Films with a High Figure of Merit via Solution Processing," 2013.

[164] A. T. Poortinga, R. Bos, and H. J. Busscher, "Reversibility of Bacterial Adhesion at an Electrode Surface," 2001.

[165] K. N. Tonny, R. Rafique, A. Sharmin, M. S. Bashar, and Z. H. Mahmood, "Electrical, optical and structural properties of transparent conducting Al doped ZnO (AZO) deposited by sol-gel spin coating," *AIP Advances*, vol. 8, p. 065307, 6 2018.

[166] R. Dylewicz, R. De, L. Rue, F. Rahman, and S. Lis, "Electron Beam Lithography of Bulk Zinc Oxide Wafers using a Polythiophene-based Charge Dissipation Layer," tech. rep.

[167] L. Li and L. Li Fourier, "Fourier Modal Method," tech. rep., 2014.

[168] V. Liu and S. Fan, "S4 : A free electromagnetic solver for layered periodic structures," *Computer Physics Communications*, vol. 183, pp. 2233–2244, 10 2012.

[169] M. Paulsen, L. T. Neustock, S. Jahns, J. Adam, and M. Gerken, "Simulation methods for multiperiodic and aperiodic nanostructured dielectric waveguides," *Optical and Quantum Electronics*, vol. 49, p. 107, 3 2017.

[170] M. R. Majidi, Y. Omidi, P. Karami, and M. Johari-Ahar, "Reusable potentiometric screen-printed sensor and label-free aptasensor with pseudo-reference electrode for determination of tryptophan in the presence of tyrosine," *Talanta*, vol. 150, pp. 425–433, 4 2016.

[171] C. L. Bentley, D. Perry, and P. R. Unwin, "Stability and Placement of Ag/AgCl Quasi-Reference Counter Electrodes in Confined Electrochemical Cells," *Analytical Chemistry*, vol. 90, pp. 7700–7707, 6 2018.

[172] M. Velický, K. Y. Tam, and R. A. W. Dryfe, "On the stability of the silver/silver sulfate reference electrode," *Analytical Methods*, vol. 4, p. 1207, 5 2012.

[173] B. Huber and B. Roling, "Development of a Ag/Ag+ micro-reference electrode for electrochemical measurements in ionic liquids," *Electrochimica Acta*, vol. 56, pp. 6569–6572, 7 2011.

[174] D.-H. Kim, M.-R. Park, H.-J. Lee, and G.-H. Lee, "Thickness dependence of electrical properties of ITO film deposited on a plastic substrate by RF magnetron sputtering," *Applied Surface Science*, vol. 253, pp. 409–411, 11 2006.

[175] K. Ellmer, "Past achievements and future challenges in the development of optically transparent electrodes," *Nature Photonics*, vol. 6, no. 12, pp. 809 – 817, 2012.

[176] H. Kim, C. M. Gilmore, A. Piqué, J. S. Horwitz, H. Mattoussi, H. Murata, Z. H. Kafafi, and D. B. Chrisey, "Electrical, optical, and structural properties of indiumâĂŞtinâĂŞoxide thin films for organic light-emitting devices," *Journal of Applied Physics*, vol. 86, pp. 6451–6461, 12 1999.

[177] R. J. Moerland and J. P. Hoogenboom, "Subnanometer-accuracy optical distance ruler based on fluorescence quenching by transparent conductors," *Optica*, vol. 3, p. 112, 2 2016.

[178] J. N. Hilfiker, M. Stadermann, J. Sun, T. Tiwald, J. S. Hale, P. E. Miller, and C. Aracne-Ruddle, "Determining thickness and refractive index from free-standing ultra-thin polymer films with spectroscopic ellipsometry," *Applied Surface Science*, vol. 421, pp. 508–512, 11 2017.

[179] H. K. Yu and J.-L. Lee, "Growth mechanism of metal-oxide nanowires synthesized by electron beam evaporation: A self-catalytic vapor-liquid-solid process," *Scientific Reports*, vol. 4, p. 6589, 5 2015.

[180] J. Lee, M. Shin, C.-G. Ahn, C. S. Ah, C. W. Park, and G. Y. Sung, "Effects of pH and Ion Concentration in Phosphate Buffer Solution on the Sensitivity of the Silicon Nanowire BioFETs," *Journal of the Korean Physical Society*, vol. 55, pp. 1621–1625, 10 2009.

[181] E. González-Fernández, N. Avlonitis, A. F. Murray, A. R. Mount, and M. Bradley, "Methylene blue not ferrocene: Optimal reporters for electrochemical detection of protease activity," *Biosensors and Bioelectronics*, vol. 84, pp. 82–88, 10 2016.

[182] E. Koutsoumpeli, J. Murray, D. Langford, R. S. Bon, and S. Johnson, "Probing molecular interactions with methylene blue derivatized self-assembled monolayers," *Sensing and Bio-Sensing Research*, vol. 6, pp. 1–6, 2015.

[183] X. Q. Zhang, X. W. Fan, D. Z. Shen, a. , M. Fontalvo, A. Garcia, S. Valbuena, and F. Racedo, "Measurement of nonlinear refractive index of organic materials," in *Journal of Physics: Conference Series*, 2016.

[184] M. Duan, J. Wu, Y. Xiong, S. Fang, and J. Chen, "Characterization and differentiation of the adsorption behavior of crystal violet and methylene blue at the silica/water interface using near field evanescent wave," *Soft Matter*, vol. 14, pp. 7516–7525, 9 2018.

[185] S. O. Kelley, J. K. Barton, N. M. Jackson, and M. G. Hill, "Electrochemistry of Methylene Blue Bound to a DNA-Modified Electrode," Tech. Rep. 96, 1997.

[186] J. M. Godwin and R. Evitts, "Polypyrrole/Poly(Methylene Blue) Composite Electrode Films on Stainless Steel," in *ECS Transactions*, vol. 33, pp. 181–188, The Electrochemical Society, 3 2011.

[187] K. L. Kostka, M. D. Radcliffe, and E. Von Meerwall, "Diffusion coefficients of methylene blue and thioflavin T dyes in methanol solution," *The Journal of Physical Chemistry*, vol. 96, pp. 2289–2292, 3 1992.

[188] K. E. Hanson and M. R. Couturier, "Multiplexed Molecular Diagnostics for Respiratory, Gastrointestinal, and Central Nervous System Infections," *Clinical Infectious Diseases*, vol. 63, pp. 1361–1367, 11 2016.

[189] A. Deshpande, B. McMahon, A. R. Daughton, E. L. Abeyta, D. Hodge, K. Anderson, and S. Pillai, "Surveillance for Emerging Diseases with Multiplexed Point-of-Care Diagnostics," *Health Security*, vol. 14, pp. 111–121, 6 2016.

[190] E. Cohen, G. Jayachandran, H. Gao, S. Tin, R. Alvarez, V. Valero, B. Lim, W. Woodward, N. Ueno, and J. Reuben, "Abstract P2-02-04: Circulating protein biomarker profile for inflammatory breast cancer using a multiplexed proximity extension assay," in *Poster Session Abstracts*, vol. 78, pp. 2–02, American Association for Cancer Research, 2 2018.

[191] A. Fish, A. Vachani, P. Massion, S. Antic, N. Trivedi, J. Brown, T. Rubenstein, A. Rostykus, M. Beggs, H. Yu, L. Carbonell, and M. Arjomandi, "Novel Multiplexed Plasma Biomarkers and Clinical Factors Augment Risk Assessment for Indeterminate Pulmonary Nodules in Former Smokers," in *C110. THE FUTURE OF LUNG CANCER BIOMARKERS: WHERE SHOULD WE LOOK?*, pp. A7452–A7452, American Thoracic Society, 5 2019.

[192] C. Dincer, R. Bruch, S. Wirth, S. Schumann, and G. A. Urban, "Biosensors and personalized drug therapy: what does the future hold?," *Expert Review of Precision Medicine and Drug Development*, vol. 2, pp. 303–305, 11 2017.

[193] A. Romeo, T. S. Leung, and S. Sánchez, "Smart biosensors for multiplexed and fully integrated point-of-care diagnostics," *Lab on a Chip*, vol. 16, pp. 1957–1961, 5 2016.

[194] D. Harpaz, E. Eltzov, R. C. S. Seet, R. S. Marks, and A. I. Y. Tok, "Point-of-Care-Testing in Acute Stroke Management: An Unmet Need Ripe for Technological Harvest.," *Biosensors*, vol. 7, 8 2017.

[195] T. M. Dias, E. Fernandes, S. Cardoso, G. Monteiro, and P. P. Freitas, "One-step trapping of droplets and surface functionalization of sensors using gold-patterned structures for multiplexing in biochips," *RSC Advances*, vol. 7, pp. 43273–43282, 9 2017.

[196] G. Blagoi, S. Keller, A. Johansson, A. Boisen, and M. Dufva, "Functionalization of SU-8 photoresist surfaces with IgG proteins," *Applied Surface Science*, vol. 255, pp. 2896–2902, 12 2008.

[197] A. Meister, J. Polesel-Maris, P. Niedermann, J. Przybylska, P. Studer, M. Gabi, P. Behr, T. Zambelli, M. Liley, J. Vörös, and H. Heinzelmann, "Nanoscale dispensing in liquid environment of streptavidin on a biotin-functionalized surface using hollow atomic force microscopy probes," *Microelectronic Engineering*, vol. 86, pp. 1481–1484, 4 2009.

[198] B. Gale, A. Jafek, C. Lambert, B. Goenner, H. Moghimifam, U. Nze, and S. Kamarapu, "A Review of Current Methods in Microfluidic Device Fabrication and Future Commercialization Prospects," *Inventions*, vol. 3, p. 60, 8 2018.

[199] C. M. B. Ho, S. H. Ng, K. H. H. Li, and Y.-J. Yoon, "3D printed microfluidics for biological applications," *Lab on a Chip*, vol. 15, pp. 3627–3637, 8 2015.

[200] Z. Qi, L. Xu, Y. Xu, J. Zhong, A. Abedini, X. Cheng, and D. Sinton, "Disposable silicon-glass microfluidic devices: precise, robust and cheap," *Lab on a Chip*, vol. 18, pp. 3872–3880, 12 2018.

[201] R. S. Kane, S. Takayama, E. Ostuni, D. E. Ingber, and G. M. Whitesides, "Patterning proteins and cells using soft lithography," *Biomaterials*, vol. 20, pp. 2363–2376, 12 1999.

[202] D. Kohlheyer, S. Unnikrishnan, G. A. J. Besselink, S. Schlautmann, and R. B. M. Schasfoort, "A microfluidic device for array patterning by perpendicular electrokinetic focusing," *Microfluidics and Nanofluidics*, vol. 4, pp. 557–564, 6 2008.

[203] F. Volpetti, J. Garcia-Cordero, and S. J. Maerkl, "A Microfluidic Platform for High-Throughput Multiplexed Protein Quantitation," *PLOS ONE*, vol. 10, p. e0117744, 2 2015.

[204] C. Carrell, A. Kava, M. Nguyen, R. Menger, Z. Munshi, Z. Call, M. Nussbaum, and C. Henry, "Beyond the lateral flow assay: A review of paper-based microfluidics," *Microelectronic Engineering*, vol. 206, pp. 45–54, 2 2019.

[205] M. Riepl, V. M. Mirsky, and O. S. Wolfbeis, "Electrical Control of Alkanethiols Self-Assembly on a Gold Surface as an Approach for Preparation of Microelectrode Arrays," *Microchimica Acta*, vol. 131, pp. 29–34, 6 1999.

[206] D. Evans, S. Johnson, S. Laurenson, G. Davies, P. Ko Ferrigno, and C. Walti, "Electrical protein detection in cell lysates using high-density peptide-aptamer microarrays," *Journal of Biology*, vol. 7, p. 3, 1 2008.

[207] A. Hammami, N. Raouafi, and V. M. Mirsky, "Electrically controlled Michael addition: Addressing of covalent immobilization of biological receptors," *Biosensors and Bioelectronics*, vol. 121, pp. 72–79, 12 2018.

[208] M. Hellstern, M. Gantenbein, L. Le Pleux, G. Puebla-Hellmann, E. Lörtscher, and M. Mayor, "Electrochemical Multiplexing: Control over Surface Functionalization by Combining a Redox-Sensitive Alkyne Protection Group with âĂIJClickâĂİ-Chemistry," *Advanced Materials Interfaces*, vol. 6, p. 1801917, 3 2019.

[209] S. Mahouche-Chergui, S. Gam-Derouich, C. Mangeney, and M. M. Chehimi, "Aryl diazonium salts: a new class of coupling agents for bonding polymers, biomacromolecules and nanoparticles to surfaces," *Chem. Soc. Rev*, vol. 40, pp. 4143–4166, 2011.

[210] T. Menanteau, E. Levillain, and T. Breton, "Electrografting via Diazonium Chemistry: From Multilayer to Monolayer Using Radical Scavenger," *Chemistry of Materials*, vol. 25, pp. 2905–2909, 7 2013.

[211] W. Zheng, R. van den Hurk, Y. Cao, R. Du, X. Sun, Y. Wang, M. McDermott, S. Evoy, W. Zheng, R. Van den Hurk, Y. Cao, R. Du, X. Sun, Y. Wang, M. T. McDermott, and S. Evoy, "Aryl Diazonium Chemistry for the Surface Functionalization of Glassy Biosensors," *Biosensors*, vol. 6, p. 8, 3 2016.

[212] K. Levrie, K. Jans, R. Vos, N. Ardakanian, N. Verellen, C. Van Hoof, L. Lagae, and T. Stakenborg, "Multiplexed site-specific electrode functionalization for multitarget biosensors," *Bioelectrochemistry*, vol. 112, pp. 61–66, 12 2016.

[213] J. Charlier, S. Palacin, J. Leroy, D. Del Frari, L. Zagonel, N. Barrett, O. Renault, A. Bailly, and D. Mariolle, "Local silicon doping as a promoter of patterned electrografting of diazonium for directed surface functionalization," *Journal of Materials Chemistry*, vol. 18, p. 3136, 6 2008.

[214] A.-M. J. Haque and K. Kim, "Aldehyde-Functionalized Benzenediazonium Cation for Multiprobe Immobilization on Microelectrode Array Surfaces," *Langmuir*, vol. 27, pp. 882–886, 2 2011.

[215] P. Yáñez-Sedeño, S. Campuzano, and J. M. Pingarrón, "Integrated Affinity Biosensing Platforms on Screen-Printed Electrodes Electrografted with Diazonium Salts.," *Sensors (Basel, Switzerland)*, vol. 18, 2 2018.

[216] R. Polsky, J. C. Harper, D. R. Wheeler, S. M. Dirk, D. C. Arango, and S. M. Brozik, "Electrically addressable diazonium-functionalized antibodies for multianalyte electrochemical sensor applications," *Biosensors and Bioelectronics*, vol. 23, pp. 757–764, 1 2008.

[217] A. J. Wilson, N. Y. Molina, and K. A. Willets, "Modification of the Electrochemical Properties of Nile Blue through Covalent Attachment to Gold As Revealed by Electrochemistry and SERS," 2016.

[218] A. Mattiuzzi, I. Jabin, C. Mangeney, C. Roux, O. Reinaud, L. Santos, J.-F. Bergamini, P. Hapiot, and C. Lagrost, "Electrografting of calix[4]arenediazonium salts to form versatile robust platforms for spatially controlled surface functionalization," 2012.

[219] B. Zhang, J. Yu, C. Liu, J. Wang, H. Han, P. Zhang, and D. Shi, "Improving detection sensitivity by oriented bioconjugation of antibodies to quantum dots with a flexible spacer arm for immunoassay," *RSC Advances*, vol. 6, pp. 50119–50127, 5 2016.

[220] A. K. Trilling, J. Beekwilder, and H. Zuilhof, "Antibody orientation on biosensor surfaces: a minireview," *The Analyst*, vol. 138, p. 1619, 2 2013.

[221] A.-C. Lee, G. Liu, C.-K. Heng, S.-N. Tan, T.-M. Lim, and Y. Lin, "Sensitive electrochemical detection of horseradish peroxidase at disposable screen-printed carbon electrode.," *Electroanalysis*, vol. 20, p. 2040, 8 2008.

[222] L. R. Kodan, K. J. C. Verschueren, H. H. H. Kanhai, J. J. M. van Roosmalen, K. W. M. Bloemenkamp, and M. J. Rijken, "The golden hour of sepsis: An in-depth analysis of sepsis-related maternal mortality in middle-income country Suriname.," *PloS one*, vol. 13, no. 7, p. e0200281, 2018.

[223] A. Kumar, D. Roberts, K. E. Wood, B. Light, J. E. Parrillo, S. Sharma, R. Suppes, D. Feinstein, S. Zanotti, L. Taiberg, D. Gurka, A. Kumar, and M. Cheang, "Duration of hypotension before initiation of effective antimicrobial therapy is the critical determinant of survival in human septic shock*," *Critical Care Medicine*, vol. 34, pp. 1589–1596, 6 2006.

[224] M. Sinha, J. Jupe, H. Mack, T. P. Coleman, S. M. Lawrence, and S. I. Fraley, "Emerging Technologies for Molecular Diagnosis of Sepsis," *Clinical Microbiology Reviews*, vol. 31, pp. 00089–17, 4 2018.

[225] S.-Y. Cho and J.-H. Choi, "Biomarkers of sepsis.," *Infection & chemotherapy*, vol. 46, pp. 1–12, 3 2014.

[226] S. Jain, V. Gautam, and S. Naseem, "Acute-phase proteins: As diagnostic tool.," *Journal of pharmacy & bioallied sciences*, vol. 3, pp. 118–27, 1 2011.

[227] C. Lelubre, S. Anselin, K. Zouaoui Boudjeltia, P. Biston, and M. Piagnerelli, "Interpretation of C-reactive protein concentrations in critically ill patients.," *BioMed research international*, vol. 2013, p. 124021, 10 2013.

[228] M. B. Pepys, P. N. Hawkins, M. C. Kahan, G. A. Tennent, J. R. Gallimore, D. Graham, C. A. Sabin, A. Zychlinsky, and J. de Diego, "Proinflammatory Effects of Bacterial Recombinant Human C-Reactive Protein Are Caused by Contamination With Bacterial Products, Not by C-Reactive Protein Itself," *Circulation Research*, vol. 97, 11 2005.

[229] N. R. Sproston and J. J. Ashworth, "Role of C-Reactive Protein at Sites of Inflammation and Infection.," *Frontiers in immunology*, vol. 9, p. 754, 2018.

[230] S. Pradhan, A. Ghimire, B. Bhattarai, B. Khanal, K. Pokharel, M. Lamsal, and S. Koirala, "The role of C-reactive protein as a diagnostic predictor of sepsis in a multidisciplinary Intensive Care Unit of a tertiary care center in Nepal.," *Indian journal of critical care medicine : peer-reviewed, official publication of Indian Society of Critical Care Medicine*, vol. 20, pp. 417–20, 7 2016.

[231] J. Whicher, J. Bienvenu, and G. Monneret, "Procalcitonin as an Acute Phase Marker," *Annals of Clinical Biochemistry: An international journal of biochemistry and laboratory medicine*, vol. 38, pp. 483–493, 9 2001.

[232] M. Jin and A. I. Khan, "Procalcitonin: Uses in the Clinical Laboratory for the Diagnosis of Sepsis," *Laboratory Medicine*, vol. 41, pp. 173–177, 3 2010.

[233] H. Chaudhry, J. Zhou, Y. Zhong, M. M. Ali, F. McGuire, P. S. Nagarkatti, and M. Nagarkatti, "Role of cytokines as a double-edged sword in sepsis.," *In vivo (Athens, Greece)*, vol. 27, no. 6, pp. 669–84, 2013.

[234] Y. A. Leal, J. Álvarez-Nemegyei, A. I. Lavadores-May, J. L. Girón-Carrillo, R. Cedillo-Rivera, and J. R. Velazquez, "Cytokine profile as diagnostic and prognostic factor in neonatal sepsis," *The Journal of Maternal-Fetal & Neonatal Medicine*, vol. 32, pp. 2830–2836, 9 2019.

[235] E. J. Giamarellos-Bourboulis, E. Apostolidou, M. Lada, I. Perdios, N. K. Gatselis, I. Tsangaris, M. Georgitsi, M. Bristianou, T. Kanni, K. Sereti, M. A.

Kyprianou, A. Kotanidou, A. Armaganidis, and Hellenic Sepsis Study Group, "Kinetics of circulating immunoglobulin M in sepsis: relationship with final outcome.," *Critical care (London, England)*, vol. 17, p. R247, 10 2013.

[236] K. Kofoed, O. Andersen, G. Kronborg, M. Tvede, J. Petersen, J. Eugen-Olsen, and K. Larsen, "Use of plasma C-reactive protein, procalcitonin, neutrophils, macrophage migration inhibitory factor, soluble urokinase-type plasminogen activator receptor, and soluble triggering receptor expressed on myeloid cells-1 in combination to diagnose infections: a prospective study," *Critical Care*, vol. 11, no. 2, p. R38, 2007.

[237] J. Min, M. Nothing, B. Coble, H. Zheng, J. Park, H. Im, G. F. Weber, C. M. Castro, F. K. Swirski, R. Weissleder, and H. Lee, "Integrated Biosensor for Rapid and Point-of-Care Sepsis Diagnosis," *ACS Nano*, vol. 12, pp. 3378–3384, 4 2018.

[238] C. Russell, A. C. Ward, V. Vezza, P. Hoskisson, D. Alcorn, D. P. Steenson, and D. K. Corrigan, "Development of a needle shaped microelectrode for electrochemical detection of the sepsis biomarker interleukin-6 (IL-6) in real time," *Biosensors and Bioelectronics*, vol. 126, pp. 806–814, 2 2019.

[239] N. Fabri-Faja, O. Calvo-Lozano, P. Dey, R. A. Terborg, M.-C. Estevez, A. Belushkin, F. Yesilköy, L. Duempelmann, H. Altug, V. Pruneri, and L. M. Lechuga, "Early sepsis diagnosis via protein and miRNA biomarkers using a novel point-of-care photonic biosensor," *Analytica Chimica Acta*, vol. 1077, pp. 232–242, 10 2019.

[240] A. Belushkin, F. Yesilkoy, and H. Altug, "Nanoparticle-Enhanced Plasmonic Biosensor for Digital Biomarker Detection in a Microarray," *ACS Nano*, vol. 12, pp. 4453–4461, 5 2018.

[241] M.-Z. Tsai, C.-T. Hsiung, Y. Chen, C.-S. Huang, H.-Y. Hsu, and P.-Y. Hsieh, "Real-time CRP detection from whole blood using micropost-embedded microfluidic chip incorporated with label-free biosensor," *The Analyst*, vol. 143, pp. 503–510, 1 2018.

[242] U. Hassan, T. Ghonge, B. Reddy, M. Patel, M. Rappleye, I. Taneja, A. Tanna, R. Healey, N. Manusry, Z. Price, T. Jensen, J. Berger, A. Hasnain, E. Flaugher, S. Liu, B. Davis, J. Kumar, K. White, and R. Bashir, "A point-of-care microfluidic biochip for quantification of CD64 expression from whole blood for sepsis stratification," *Nature Communications*, vol. 8, p. 15949, 8 2017.

[243] K. Patel and E. McElvania, "Diagnostic Challenges and Laboratory Considerations for Pediatric Sepsis," *The Journal of Applied Laboratory Medicine*, vol. 3, pp. 587–600, 1 2019.

[244] N. Watanabe, K. Kryukov, S. Nakagawa, J. S. Takeuchi, M. Takeshita, Y. Kirimura, S. Mitsuhashi, T. Ishihara, H. Aoki, S. Inokuchi, T. Imanishi, and S. Inoue, "Detection of pathogenic bacteria in the blood from sepsis patients using 16S rRNA gene amplicon sequencing analysis.," *PloS one*, vol. 13, no. 8, p. e0202049, 2018.

[245] G. Durand, F. Javerliat, M. Bes, J.-B. Veyrieras, G. Guigon, N. Mugnier, S. Schicklin, G. Kaneko, E. Santiago-Allexant, C. Bouchiat, P. Martins-SimÃţes, F. Laurent, A. Van Belkum, F. Vandenesch, and A. Tristan, "Routine Whole-Genome Sequencing for Outbreak Investigations of Staphylococcus aureus in a National Reference Center," *Frontiers in Microbiology*, vol. 9, p. 511, 3 2018.

[246] G. Vrioni, C. Tsiamis, G. Oikonomidis, K. Theodoridou, V. Kapsimali, and A. Tsakris, "MALDI-TOF mass spectrometry technology for detecting biomarkers of antimicrobial resistance: current achievements and future perspectives.," *Annals of translational medicine*, vol. 6, p. 240, 6 2018.

[247] S. M. Yoo and S. Y. Lee, "Optical Biosensors for the Detection of Pathogenic Microorganisms," *Trends in Biotechnology*, vol. 34, no. 1, pp. 7–25, 2016.

[248] Y. Wang and J. K. Salazar, "Culture-Independent Rapid Detection Methods for Bacterial Pathogens and Toxins in Food Matrices," *Comprehensive Reviews in Food Science and Food Safety*, vol. 15, pp. 183–205, 1 2016.

[249] G. Maugeri, I. Lychko, R. Sobral, and A. C. A. Roque, "Identification and Antibiotic-Susceptibility Profiling of Infectious Bacterial Agents: A Review of Current and Future Trends," *Biotechnology Journal*, vol. 14, p. 1700750, 1 2019.

[250] A. Ahmed, J. V. Rushworth, N. A. Hirst, and P. A. Millner, "Biosensors for whole-cell bacterial detection.," *Clinical microbiology reviews*, vol. 27, pp. 631–46, 7 2014.

[251] M. Janik, M. Koba, A. Celebańska, W. J. Bock, and M. Śmietana, "Live E. coli bacteria label-free sensing using a microcavity in-line Mach-Zehnder interferometer," *Scientific Reports*, vol. 8, p. 17176, 12 2018.

[252] M. Soler Aznar, X. Li, A. Belushkin, H. Altug, and F. Yesilköy, "Towards a point-of-care nanoplasmonic biosensor for rapid and multiplexed detection of pathogenic infections," in *Plasmonics in Biology and Medicine XV* (T. Vo-Dinh and J. R. Lakowicz, eds.), vol. 10509, p. 17, SPIE, 2 2018.

[253] Ã. Pardoux, A. Roux, R. Mathey, D. Boturyn, and Y. Roupioz, "Antimicrobial peptide arrays for wide spectrum sensing of pathogenic bacteria," *Talanta*, vol. 203, pp. 322–327, 10 2019.

[254] J. Maldonado, A. B. González-Guerrero, C. Domínguez, and L. M. Lechuga, "Label-free bimodal waveguide immunosensor for rapid diagnosis of bacterial infections in cirrhotic patients," *Biosensors and Bioelectronics*, vol. 85, pp. 310–316, 2016.

[255] C. Arsene, A. Saste, M. Somiah, J. Mestrovich, and G. Berger, "A Case of Septic Arthritis of the Wrist due to Finegoldia magna.," *Case reports in infectious diseases*, vol. 2014, p. 793053, 4 2014.

[256] K. M. Storek, M. R. Auerbach, H. Shi, N. K. Garcia, D. Sun, N. N. Nickerson, R. Vij, Z. Lin, N. Chiang, K. Schneider, A. T. Wecksler, E. Skippington, G. Nakamura, D. Seshasayee, J. T. Koerber, J. Payandeh, P. A. Smith, and S. T. Rutherford, "Monoclonal antibody targeting the β-barrel assembly machine of Escherichia coli is bactericidal.," *Proceedings of the National Academy of Sciences of the United States of America*, vol. 115, pp. 3692–3697, 4 2018.

[257] M. L. Sin, K. E. Mach, P. K. Wong, and J. C. Liao, "Advances and challenges in biosensor-based diagnosis of infectious diseases," *Expert Review of Molecular Diagnostics*, vol. 14, pp. 225–244, 3 2014.

[258] F. Abbasian, E. Ghafar-Zadeh, and S. Magierowski, "Microbiological Sensing Technologies: A Review," *Bioengineering*, vol. 5, no. 1, 2018.